

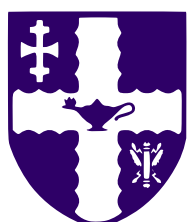
Doctoral Thesis

QUANTITATIVE  
ELECTROLUMINESCENCE  
MEASUREMENTS OF PV DEVICES

By

Karl Georg Bedrich

April 2017



Loughborough  
University

Centre for Renewable Energy  
Systems Technology (CREST)



Centre for Renewable Energy Systems Technology (CREST),  
The Wolfson School of Mechanical, Electrical  
and Manufacturing Engineering,  
Loughborough University, LE11 3TU

*THIS PAGE INTENTIONALLY LEFT BLANK*



## Certificate of Originality Thesis Access Conditions and Deposit Agreement

Students should consult the guidance notes on the electronic thesis deposit and the access conditions in the University's Code of Practice on Research Degree Programmes

**Author**.....

**Title**.....

I [Please insert name and address], "the Depositor", would like to deposit [Please insert title of dissertation], hereafter referred to as the "Work", once it has successfully been examined in Loughborough University Institutional Repository

**Status of access** OPEN / RESTRICTED / CONFIDENTIAL

**Moratorium Period**..... years, ending...../.....20.....

**Status of access approved by (CAPITALS)**:.....

**Supervisor (Signature)**.....

**School of**.....

**Author's Declaration** *I confirm the following :*

### CERTIFICATE OF ORIGINALITY

This is to certify that I am responsible for the work submitted in this thesis, that the original work is my own except as specified in acknowledgements or in footnotes, and that neither the thesis nor the original work therein has been submitted to this or any other institution for a degree

### NON-EXCLUSIVE RIGHTS

The licence rights granted to Loughborough University Institutional Repository through this agreement are entirely non-exclusive and royalty free. I am free to publish the Work in its present version or future versions elsewhere. I agree that Loughborough University Institutional Repository administrators or any third party with whom Loughborough University Institutional Repository has an agreement to do so may, without changing content, convert the Work to any medium or format for the purpose of future preservation and accessibility.

### DEPOSIT IN LOUGHBOROUGH UNIVERSITY INSTITUTIONAL REPOSITORY

I understand that open access work deposited in Loughborough University Institutional Repository will be accessible to a wide variety of people and institutions - including automated agents - via the World Wide Web. An electronic copy of my thesis may also be included in the British Library Electronic Theses On-line System (EThOS).

I understand that once the Work is deposited, a citation to the Work will always remain visible. Removal of the Work can be made after discussion with Loughborough University Institutional Repository, who shall make best efforts to ensure removal of the Work from any third party with whom Loughborough University Institutional Repository has an agreement. Restricted or Confidential access material will not be available on the World Wide Web until the moratorium period has expired.

- That I am the author of the Work and have the authority to make this agreement and to hereby give Loughborough University Institutional Repository administrators the right to make available the Work in the way described above.

- That I have exercised reasonable care to ensure that the Work is original, and does not to the best of my knowledge break any UK law or infringe any third party's copyright or other Intellectual Property Right. I have read the University's guidance on third party copyright material in theses.
- The administrators of Loughborough University Institutional Repository do not hold any obligation to take legal action on behalf of the Depositor, or other rights holders, in the event of breach of Intellectual Property Rights, or any other right, in the material deposited.

*The statement below shall apply to ALL copies:*

**This copy has been supplied on the understanding that it is copyright material and that no quotation from the thesis may be published without proper acknowledgement.**

**Restricted/confidential work:** All access and any copying shall be strictly subject to written permission from the University Dean of School and any external sponsor, if any.

**Author's signature.....Date.....**

<b>user's declaration:</b> for signature during any Moratorium period (Not Open work): <i>I undertake to uphold the above conditions:</i>			
Date	Name (CAPITALS)	Signature	Address

# ABSTRACT

Electroluminescence (EL) imaging is a fast and comparatively low-cost method for spatially resolved analysis of photovoltaic (PV) devices. A Silicon CCD or InGaAs camera is used to capture the near infrared radiation, emitted from a forward biased PV device. EL images can be used to identify defects, like cracks and shunts but also to map physical parameters, like series resistance.

The lack of suitable image processing routines often prevents automated and setup-independent quantitative analysis. This thesis provides a tool-set, rather than a specific solution to address this problem. Comprehensive and novel procedures to calibrate imaging systems, to evaluate image quality, to normalize images and to extract features are presented.

For image quality measurement the signal-to-noise ratio (SNR) is obtained from a set of EL images. Its spatial average depends on the size of the background area within the EL image. In this work the SNR will be calculated spatially resolved and as (background independent) averaged parameter using only one EL image and no additional information of the imaging system.

This thesis presents additional methods to measure image sharpness spatially resolved and introduces a new parameter to describe resolvable object size. This allows equalising images of different resolutions and of different sharpness allowing artefact-free comparison.

The flat field image scales the emitted EL signal to the detected image intensity. It is often measured through imaging a homogenous light source such as a red LCD screen in close distance to the camera lens. This measurement however only partially removes vignetting - the main contributor to the flat field. This work quantifies the vignetting correction quality and introduces more sophisticated vignetting measurement methods.

Especially outdoor EL imaging often includes perspective distortion of the measured PV device. This thesis presents methods to automatically detect and correct for this distortion. This also includes intensity correction due to different irradiance angles.

Single-time-effects and hot pixels are image artefacts that can impair the EL image quality. They can conceivably be confused with cell defects. Their detection and removal is described in this thesis.

The methods presented enable direct pixel-by-pixel comparison for EL images of the same device taken at different measurement and exposure times, even if imaged by different contractors.

EL statistics correlating cell intensity to crack length and PV performance parameters are extracted from EL and dark I-V curves. This allows for spatially resolved performance measurement without the need for laborious flash tests to measure the light I-V- curve.

This work aims to convince the EL community of certain calibration- and imaging routines, which will allow setup independent, automatable, standardised and therefore comparable results.

Recognizing the benefits of EL imaging for quality control and failure detection, this work paves the way towards cheaper and more reliable PV generation.

The code used in this work is made available to public as library and interactive graphical application for scientific image processing.

# ACKNOWLEDGEMENTS

I would like to thank Martin Bliss (CREST) for supporting me during my first months at CREST, Ralph Gottschalg (CREST), Tom Betts (CREST) and Brian Goss (CREST) for being critical and earnest, Mike Walls (SuperSolar) for funding my trips, Peter Hacke (NREL) for questioning immature results, Matevž Bokalič (LPVO) for his images and insight and John Raguse (CSU) for granting shelter. Many thanks also to my external examiner Uwe Rau (FZ Jülich) and my internal examiner Gianfranco Claudio (CREST).

# CONTENTS

CERTIFICATE OF ORIGINALITY .....	III
ABSTRACT .....	V
ACKNOWLEDGEMENTS .....	7
CONTENTS .....	8
LIST OF ABBREVIATIONS AND ACRONYMS .....	13
CONVENTIONS FOR FUNCTIONAL EXPRESSIONS .....	14
COMMONLY USED IMAGE PROCESSING TERMS .....	14
<b>1 INTRODUCTION .....</b>	<b>15</b>
1.1 PROBLEM .....	16
1.2 THESIS .....	16
1.3 OBJECTIVES .....	18
<b>2 BACKGROUND .....</b>	<b>19</b>
2.1 PHOTOVOLTAIC DEVICES .....	19
2.1.1 <i>The Photovoltaic Effect</i> .....	20
2.1.2 <i>The Single-Diode-Model</i> .....	20
2.2 DARK I-V MEASUREMENT (DIV) .....	21
2.3 LIGHT I-V MEASUREMENT (LIV) .....	22
2.4 ELECTROLUMINESCENCE IMAGING .....	23
2.4.1 <i>Principles of Radiative Recombination</i> .....	23
2.4.2 <i>Principal Setup</i> .....	25
2.4.3 <i>Camera Types</i> .....	27
2.4.4 <i>Physical Parameters</i> .....	28
2.4.5 <i>Comparison to Other Camera-Based Methods</i> .....	31
<b>3 CAMERA CALIBRATION .....</b>	<b>33</b>
3.1 DARK CURRENT MEASUREMENT .....	34
3.1.1 <i>Dark Current from Background Image Average</i> .....	35
3.1.2 <i>Dark Current as Function of Exposure Time</i> .....	36
3.1.3 <i>Dark Current Level Estimation without Background Image</i> .....	38
3.2 SIGNAL-TO-NOISE RATIO (SNR) .....	43
3.2.1 <i>Introduction</i> .....	43

3.2.2	<i>What is ‘Noise’?</i> .....	45
3.2.3	<i>What is ‘Signal’?</i> .....	53
3.2.4	<i>SNR Averaging</i> .....	55
3.2.5	<i>SNR Comparison</i> .....	57
3.2.6	<i>Section Summary</i> .....	61
3.3	BEST FOCUS DETERMINATION.....	62
3.4	IMAGE SHARPNESS .....	65
3.4.1	<i>Introduction</i> .....	65
3.4.2	<i>Sharpness Functions</i> .....	67
3.4.3	<i>Sharpness Parameters</i> .....	70
3.4.4	<i>Sharpness Measurement</i> .....	72
3.4.5	<i>Comparing Sharpness Measurement Methods</i> .....	83
3.4.6	<i>Comparing Images at Different Sharpness Levels</i> .....	90
3.4.7	<i>Sharpness Estimation from Image Comparison</i> .....	94
3.4.8	<i>Section Summary</i> .....	95
3.5	LENS DISTORTION .....	96
3.6	IN-PLANE FLAT FIELD MEASUREMENT.....	98
3.6.1	<i>Introduction</i> .....	98
3.6.2	<i>Vignetting Measurement</i> .....	100
3.6.3	<i>Post Processing</i> .....	110
3.6.4	<i>Vignetting Comparison</i> .....	113
3.6.5	<i>Sensitivity Measurement</i> .....	120
3.6.6	<i>Section Summary</i> .....	122
3.7	SETUP DEPENDENCY OF THE EFFECTIVE FLAT FIELD .....	123
3.7.1	<i>Emission Waveband</i> .....	124
3.7.2	<i>Camera Setup</i> .....	125
3.7.3	<i>Perspective</i> .....	130
3.7.4	<i>Section Summary</i> .....	138
3.8	CHAPTER SUMMARY .....	139
<b>4</b>	<b>IMAGE CORRECTION .....</b>	<b>141</b>
4.1	SINGLE-TIME-EFFECTS .....	142
4.1.1	<i>STE Measurement and Statistics</i> .....	143
4.1.2	<i>STE Removal</i> .....	148

4.1.3	<i>Section Summary</i>	149
4.2	BACKGROUND REMOVAL	150
4.3	FLAT FIELD REMOVAL	150
4.4	IMAGE ARTEFACTS	151
4.5	IMAGE RESTORATION	152
4.5.1	<i>Unsharp Masking</i>	152
4.5.2	<i>Richardson-Lucy Deconvolution</i>	152
4.5.3	<i>Wiener Deconvolution</i>	153
4.5.4	<i>Unsupervised Wiener Deconvolution</i>	153
4.5.5	<i>Comparison</i>	153
4.5.6	<i>Section Summary</i>	157
4.6	LENS DISTORTION REMOVAL	158
4.7	PERSPECTIVE CORRECTION	158
4.7.1	<i>Rectification without Reference Image</i>	160
4.7.2	<i>Rectification with Reference Image</i>	165
4.7.3	<i>Correction Example</i>	166
4.8	SUB-PIXEL ALIGNMENT	168
4.9	INTENSITY NORMALISATION	172
4.10	CHAPTER SUMMARY	174
<b>5</b>	<b>EXTRACTING FEATURES FROM DIFFERENCE IMAGES</b>	<b>175</b>
5.1	INTRODUCTION	175
5.2	PARTLY AND FULLY INACTIVE AREAS	176
5.3	CRACKS DETECTION	177
5.3.1	<i>Limitations</i>	179
5.3.2	<i>Deriving Quantitative Parameters</i>	180
5.3.3	<i>Deriving Electrical Characteristics from Detected Cracks</i>	184
5.4	CHAPTER SUMMARY	186
<b>6</b>	<b>UNCERTAINTY ANALYSIS</b>	<b>188</b>
6.1	INTENSITY UNCERTAINTY	188
6.1.1	<i>Signal Quantisation</i>	188
6.1.2	<i>Image Noise</i>	190
6.1.3	<i>Image Correction</i>	190
6.1.4	<i>EL Signal Stability</i>	191

6.1.5	<i>Intensity Uncertainty Averaging</i>	211
6.1.6	<i>Section Summary</i>	211
6.2	POSITION UNCERTAINTY	212
6.2.1	<i>Image Sharpness</i>	213
6.2.2	<i>Re-Projection Error</i>	213
6.2.3	<i>Depth-of-Field Blur</i>	213
6.2.4	<i>Pixel Deflection</i>	216
6.2.5	<i>Neglected Position Uncertainty Factors</i>	217
6.2.6	<i>Calculating Uncertainty <math>U_{pos}</math> from <math>\sigma_{pos}</math></i>	217
6.2.7	<i>Example Position Uncertainty of a Perspective and Lens-Corrected EL image</i>	218
6.2.8	<i>Position Uncertainty Averaging and Validation</i>	220
6.2.9	<i>Satisfying Object Resolution Requirements</i>	223
6.2.10	<i>Section Summary</i>	224
6.3	UNCERTAINTY ESTIMATION	224
7	CASE STUDIES	226
7.1	THERMO-MECHANICAL LOAD EXPERIMENT AT NREL	226
7.1.1	<i>Measurement Setup</i>	226
7.1.2	<i>Measurement Results</i>	230
7.1.3	<i>Snail Trails</i>	254
7.1.4	<i>Section Summary</i>	257
7.2	FIRST INTERNATIONAL ROUND ROBIN ON EL IMAGING	257
7.2.1	<i>Image Quality Analysis</i>	260
7.2.2	<i>Calibration Image Analysis</i>	273
7.2.3	<i>Image Comparison</i>	277
7.2.4	<i>Section Summary</i>	299
CONCLUSIONS		302
FUTURE RESEARCH AVENUES		304
REFERENCES		305
APPENDIX		318
1	RESEARCH OUTPUT	319
2	HUGE LUMINESCENCE CHAMBER ‘HULC’	321
2.1	OPERATION	322

<b>2.2 TEST PROCEDURE .....</b>	<b>324</b>
<b>2.2.1 Device Storage.....</b>	<b>324</b>
<b>2.2.2 Preparation (Hours before Measurement) .....</b>	<b>325</b>
<b>2.2.3 Imaging .....</b>	<b>325</b>
<b>2.2.4 Image Analysis and Post Processing .....</b>	<b>328</b>
<b>3 SCIENTIFIC IMAGE PROCESSING WITH ‘DATAARTIST’ .....</b>	<b>329</b>
<b>3.1 IMPORTING DATA.....</b>	<b>331</b>
<b>3.2 PROGRAM LAYOUT .....</b>	<b>332</b>
<b>3.2.1 Program Components .....</b>	<b>333</b>
<b>3.2.2 Import and Representation of EL Images .....</b>	<b>335</b>
<b>3.2.3 Image Rectification using Camera Calibration File .....</b>	<b>337</b>
<b>4 ADDITIONAL MATERIAL .....</b>	<b>339</b>
<b>4.1 THERMO-MECHANICAL LOAD EXPERIMENT AT NREL.....</b>	<b>339</b>
<b>4.2 FIRST INTERNATIONAL ROUND ROBIN ON EL IMAGING .....</b>	<b>339</b>
<b>4.3 V-CUT SHARPNESS MEASUREMENT (METHOD B) .....</b>	<b>339</b>
<b>4.3.1 Influence of Measurement Number .....</b>	<b>340</b>
<b>4.3.2 Influence of Opening Angle .....</b>	<b>340</b>
<b>4.3.3 Scaling xMTF to Align with Theoretical MTF Slope .....</b>	<b>341</b>

# LIST OF ABBREVIATIONS AND ACRONYMS

AM	Air mass (characterizing solar irradiance spectrum)
BG	Background
CCD	Charge coupled device (camera sensor type)
CIS	Copper indium selenide (PV technology)
c-Si	Crystalline Silicon (PV technology)
DUT	Device under test
DIV	Current-voltage characteristics of dark DUT
DLIT	Dark lock-in thermography (measurement method)
EFG	Edge-defined Film-fed Growth (Si wafer type)
EL	Electroluminescence (measurement method)
HF	Humidity-freeze test (durability stress test)
HOG	Histogram of oriented gradients (image processing)
InGaAs	Indium-Gallium-Arsenide (camera sensor type)
LBIC	Light (or laser) beam induced current (measurement method)
LIV	Current-voltage characteristics of illuminated DUT
PID	Potential-induced degradation
PL	Photoluminescence (measurement method)
PV	Photovoltaic
px	Pixel
SNR	Signal-to-Noise Ratio (image quality)
STE	Single-Time-Effect (image artefact)
RMSE	Root mean square error
ROI	Region of interest (image section)
RR	Round Robin
UV	Ultra violet (light waveband)

# CONVENTIONS FOR FUNCTIONAL EXPRESSIONS

$I$	Image
$x, y$	Horizontal and vertical image dimensions / pixel index
$\phi, \varphi$	EL signal / image intensity or pixel value at $(x, y)$
$I[10:20,30:40]$	Example sub-image of $I$ from $x=10$ and $y=30$ to $x=20$ and $y=40$

## COMMONLY USED IMAGE PROCESSING TERMS

Kernel ( $k$ )	A two-dimensional matrix of size $(u, v)$ .
Convolution of image ( $I$ ) with $k$	Result is an image ( $I_{conv}$ ) of the same resolution as $I$ , where every pixel at $x, y$ equals: $I_{conv}[x, y] = I[x - \frac{u}{2} : x + \frac{u}{2}, y - \frac{v}{2} : y + \frac{v}{2}] \cdot k$
Gaussian filter with $k$	Two-dimensional convolution of an image with a Gaussian function, discretized for $(u, v)$
Median filter with $k$	Result is an image ( $I_{med}$ ) of the same resolution as $I$ , where every pixel at $x, y$ equals: $I_{med}[x, y] = \text{median}(I[x - \frac{u}{2} : x + \frac{u}{2}, y - \frac{v}{2} : y + \frac{v}{2}])$

# 1 INTRODUCTION

The Global Market Outlook for Solar Power 2016-2020 predicts a worldwide installed solar power of 700 GW<sub>p</sub>. Currently more than seven percent of the annual domestic consumption in Germany, Greece and Italy are covered with this clean and sustainable energy source [1]. The sheer number of installed photovoltaic panels demands a highly automated monitoring to measure produced electricity and to assess the device condition. PV module defects, such as cracks, can be introduced during module shipment or installation. If these defects have a minor influence on PV performance, defect diagnosis is difficult using traditional I-V curve measurements.

Electroluminescence (EL) imaging enables to detect and localise these extrinsic defects. It is often used to judge presumed warranty cases and to control quality during production. Though capturing the near infrared emission from a forward or reverse biased PV device, it enables non-destructive mapping of intrinsic and extrinsic features of PV devices within seconds. Only a camera and a power supply are needed. However, to date EL imaging focusses mostly on manual and qualitative analysis.

Since Fuyuki et al. [2] introduced EL, more than a decade has passed since science and industry adopted EL imaging for PV measurement.

EL is found suitable for qualitative analysis including identification of shunts, pre-breakdown sites, cracks, broken fingers and interconnectors. Regarding quantitative analysis, diffusion length, local voltage and series resistance mapping for solar cells [3-6] as well as modules [7, 8] have been presented. Even an extensive analysis of module performance can be found [9]. Nowadays, EL can be applied using contact-less experimental setups [10] and even under daylight [11].

## 1.1 Problem

EL images are not really comparable across different laboratories. Device position and orientation, resolution, sharpness, intensity distribution and vignetting are just a few causes for diverting results. Figure 1.1 shows three unprocessed EL images of the same PV device, imaged by different camera systems and laboratories. Although the device roughly aligns, an evaluation of image differences would include manual adjustment of image brightness and contrast. Further, features have to be manually detected and compared. The supposedly low investment costs for an EL system conceal the problem that to date most analysis is performed manually and by the human eye. This causes delays and subjective results.

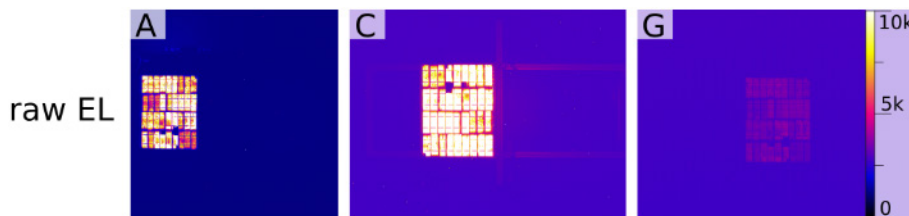


**Figure 1.1: Unprocessed example images from EL Round Robin (Section 7.2) of the same device (ID ‘Mod6’) taken by three camera systems (A, C, G); Image intensity range same for all images**

## 1.2 Thesis

This thesis provides not a specific solution but rather a tool-set to standardize EL measurements, to normalize their output, to calculate difference images and to assess measurement uncertainty. Figure 1.2a displays images from Figure 1.1 after the proposed image correction routine. The routine aligns every device and the same position and therefore allows a direct pixel-by-pixel comparison (Figure 1.2b). The quality of the corrected images is mainly influenced by noise and sharpness of the raw images. It can be evaluated through spatially resolved uncertainty maps (Figure 1.2c).

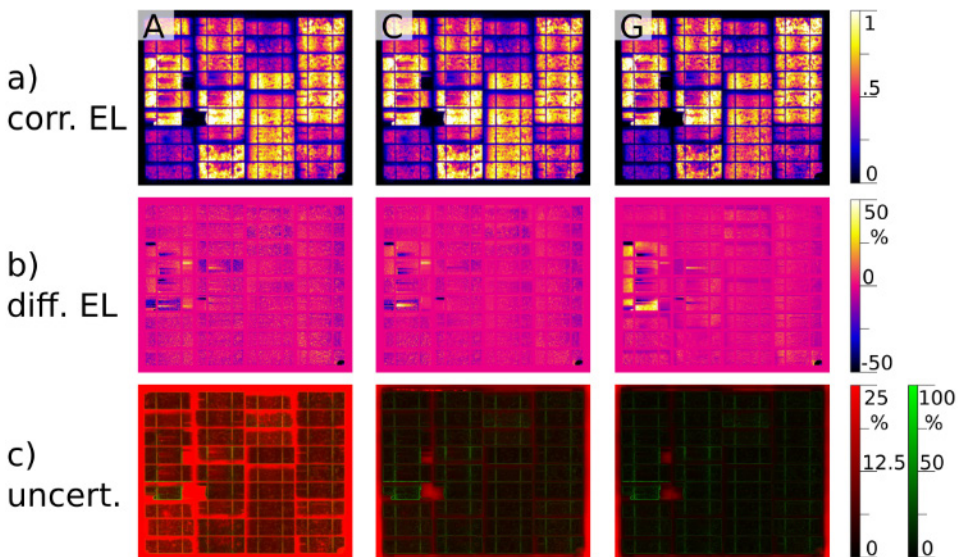


**Figure 1.2:** a) Same EL images as in Figure 1.1 after the proposed image correction routine; b) relative difference image to camera 'I' (not shown); c) Image uncertainty from image noise (red) and sharpness (green)

Difference images, calculated from corrected EL images, will be used to extract features, such as cracks and inactive areas (Figure 1.3).

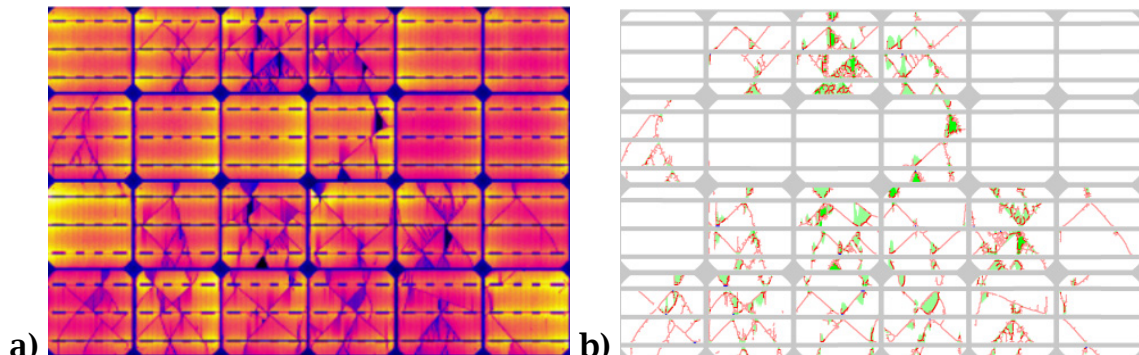


**Figure 1.3:** a) Corrected EL image of a PV module (ID 'M1' from Section 7.1); b) Extracted features of the same device (red: cracks, green: inactive areas)

These feature maps will be used for statistical analysis and to quantify breakage. In Figure 1.4 cell averages of 40 individual EL measurements were analysed. Figure 1.4a shows a correlation between the length of introduced cracks and EL intensity decrease of the affected cell. Figure 1.4b shows that this intensity decrease is around three times larger in EL images, captured at 10% short circuit current, relative to those at 100%.

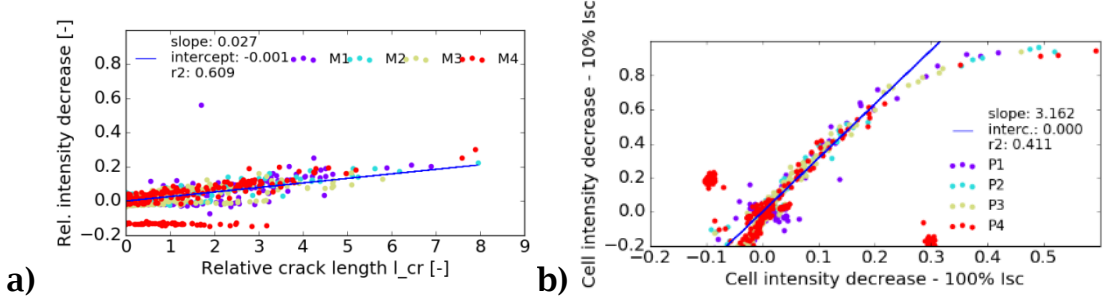


**Figure 1.4: Example statistical analysis of 10 EL measurements for every cell of four modules (ID ‘M1’-‘M4’ from Section 7.1); a) EL intensity decrease vs relative crack length; b) EL intensity decrease of EL image at 10%  $I_{sc}$  (short circuit current) vs 100%  $I_{sc}$**

### 1.3 Objectives

After a brief background on the photovoltaic effect and the EL measurement method (Chapter 2), camera calibration routines to measure dark current, lens distortion and flat field are described (Chapter 3). Therein methods to estimate image quality and image sharpness are provided.

An integral image correction procedure aims to remove the influence from camera and perspective (Chapter 4). The detection of micro-cracks and inactive areas from EL difference images is discussed in Chapter 5. The spatially resolved measurement uncertainty assigns every pixel of an EL image a standard deviation (Chapter 6). The introduced image correction routine is subsequently applied to two test cases (Chapter 7). Section 7.1 analyses EL images obtained the same measurement system of eight modules after different treatment steps. In a statistical analysis, a link between EL signal and device performance is established.

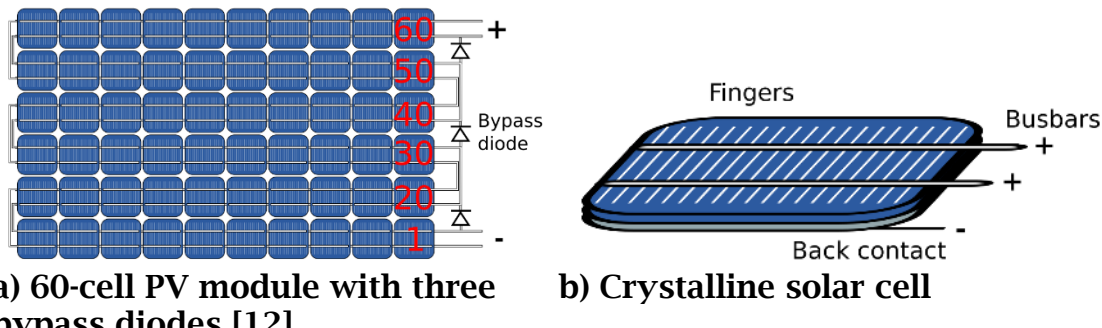
Section 7.2 analyses EL images of ten modules and five one-cell mini modules from 14 different imaging systems. The imaging systems are rated regarding image quality and the visibility of features, relative to image resolution and sharpness.

# 2 BACKGROUND

This chapter covers the physical principle of photovoltaic devices and EL. It describes extraction of PV performance parameters and compares EL measurement to other imaging-based measurements.

## 2.1 Photovoltaic Devices

Most commercially available crystalline silicon PV modules consists of a single string of solar cells connected in series, typically 60 or 72 cells (Figure 2.1a). Commonly, three bypass diodes across cells 1-20, 30-40 and 50-60 are connected to reduce the self-damage potential and the influence of partial shading or defective cells on the overall power generation. The cells used to manufacture one module are pre-sorted in the factory, into bins of similar current generation. Most solar cells consist of a back contact, an n or p-type silicon base, screen-printed fingers for current collection and busbars for cell-to-cell interconnection (Figure 2.1b). To create the diodes (positive to negative) p-n junction, dopants such as phosphorus and boron and used. Boron used in the Silicon base causes a scarcity of free electrons. Boron-doped Si wafers are therefore labelled p-type.



a) 60-cell PV module with three bypass diodes [12]

b) Crystalline solar cell

Figure 2.1: Schematic of a PV device

### 2.1.1 THE PHOTOVOLTAIC EFFECT

If the energy of a photon absorbed by the PV device is larger than the band gap energy of the device's semiconductor, electrons in the valence band can break free and excite into the conduction (valence) band (Figure 2.2). An electron-hole pair is generated. For silicon the average time between electron-hole-generation and recombination is typically 1  $\mu\text{s}$ . An externally applied voltage supports carrier separation. Current can be extracted from the device, if the carriers are 'collected' by the fingers before recombination. [13]

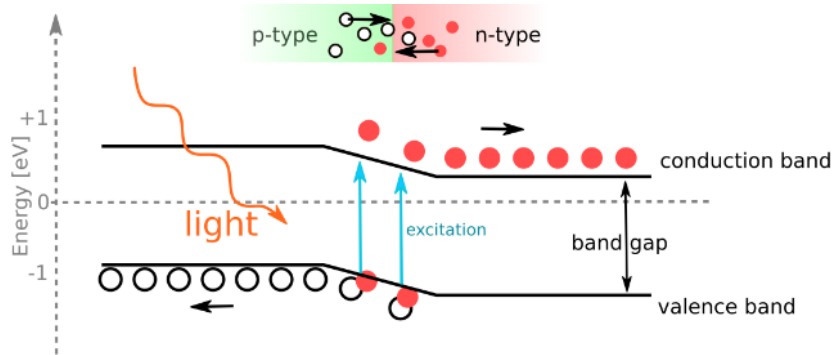


**Figure 2.2:** Electron-hole pair generation from light absorption; red circles: electrons; white circles: holes

### 2.1.2 THE SINGLE-DIODE-MODEL

In this thesis, cells are electrically modelled using the single-diode model (Figure 2.3).

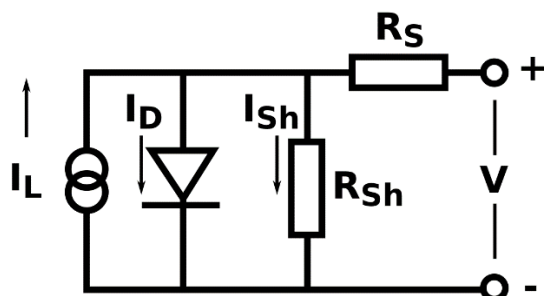


**Figure 2.3:** Equivalent circuit diagram of a solar cell according to the 'single-diode model'

This model depends on five parameters, namely photo-generated current ( $I_L$ ), reverse saturation current ( $I_0$ ), series resistance ( $R_s$ ), shunt resistance ( $R_{Sh}$ ) and modified ideality factor ( $a$ ). The current-voltage relationship is defined as:

$$I(V) = I_L - I_D - I_{Sh}; \quad (2.1)$$

$$I_D = I_0 \left[ e^{\frac{V+IR_S}{a}} - 1 \right]; \quad I_{Sh} = \frac{V + IR_S}{R_{Sh}}; \quad a = \frac{N_S n_I k_b T_c}{q} \quad (2.2)$$

Where:

---

$N_S$	Number of cells in series
$I_D$	Current lost due to recombination
$I_{Sh}$	Current lost due to shunt resistances
$n_I$	Ideality factor
$T_c$	Cell temperature
$k_b$	Boltzmann constant
$q$	Electrical charge on an electron

---

The five model parameters in Equation 2.2 are found numerically following the fitting routine described in [14].

## 2.2 Dark I-V Measurement (DIV)

In principle, a solar cell in the dark behaves as a large flat diode. Its diode properties can be measured by injecting carriers in forward bias. For this, a power supply is connected to the device. It causes current flow from positive to negative contact. For DIV measurements, voltage is increased gradually from zero to an upper limit (such as the DUT's open-circuit voltage when illuminated) [15]. Both current and voltage are measured simultaneously either with two- or with four-wire measurement to eliminate lead resistance [16].

## 2.3 Light I-V Measurement (LIV)

Under illumination, current is generated in a solar cell. This shifts the DUT's I-V curve into the fourth quadrant of the I-V coordinate system (Figure 2.4a). Power can be extracted from the device under these conditions. Commonly the light I-V (LIV) curve is displayed in its inverted form (Figure 2.4b). LIV measurements enable not just extraction of the DUT's diode properties but also measurement of PV performance characteristics (Table 2.1).

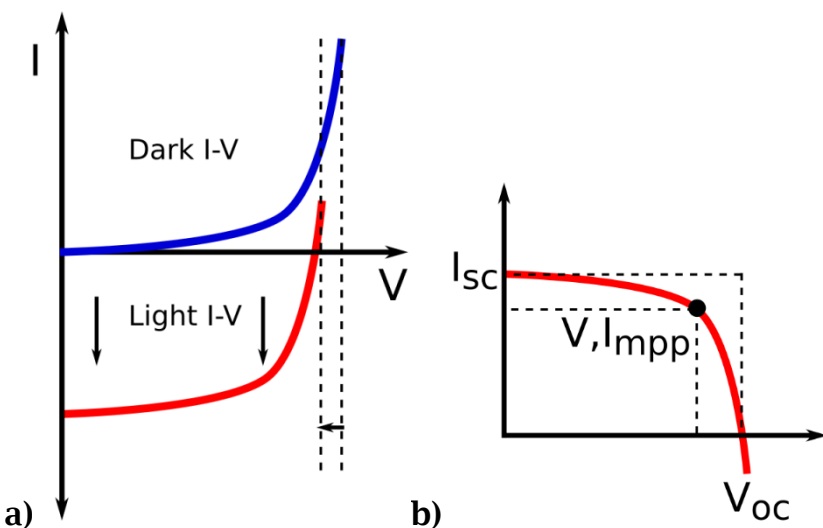


**Figure 2.4: a) Shift of dark I-V curve due to photo-generated current; b) representation of light I-V curve and position of common performance parameters**

The position of open-circuit voltage ( $V_{oc}$ ), short-circuit current ( $I_{sc}$ ) and voltage and current at maximum power point ( $mpp$ ) is shown in Figure 2.4b. A common method for measuring the LIV curve includes a pulsed light source (flasher), which aims to reproduce the suns spectrum at AM1.5 with a homogenous illumination across the measurement area. The effective irradiance is usually  $1000 \frac{W}{m^2}$  and the pulse length in the range of 2-10 ms [17]. During illumination, the DUT's I-V characteristic is measured, similar to DIV measurement.

**Table 2.1: PV performance parameters used in this work**

Parameter	Name	Description
$V_{oc}$ [V]	Open-circuit voltage	Voltage at zero current
$I_{sc}$ [A]	Short-circuit current	Current at zero voltage
MPP	Maximum power point	Peak of power ( $= V \cdot I$ ) vs voltage plot
$P_{mpp}$ [W]	Power at MPP	
$V_{mpp}$ [V]	Voltage at MPP	
$I_{mpp}$ [A]	Current at MPP	
FF [%]	Fill factor	$= \frac{V_{mpp} \cdot I_{mpp}}{V_{oc} \cdot I_{sc}}$

## 2.4 Electroluminescence Imaging

### 2.4.1 PRINCIPLES OF RADIATIVE RECOMBINATION

PV devices enable conversion of incoming light to electrical energy. Under electrical excitation, the PV device acts as light emitting diode (LED) with an emission invisible to the human eye. The LED quantum efficiency of the device is reciprocal to its electrical efficiency [18]. The radiative electron-hole recombination inside the device emits near infrared light: luminescence. Photoluminescence (PL) and electroluminescence (EL) can be separated depending on the excitation method. For EL, current is injected into the device through electrical contacts. Thus, EL can only be applied to PV devices with metallisation. If a minimum energy (defined by the semiconductor's band gap) is absorbed, electrons in the valence band, can be excited into a higher energy state (conduction band, Figure 2.5). After diffusion from the n-type side, electrons recombine with holes from the diodes p-type side at the p-n junction. The thereby released energy is mainly passed on to lattice vibration but also causes photon emission (EL).

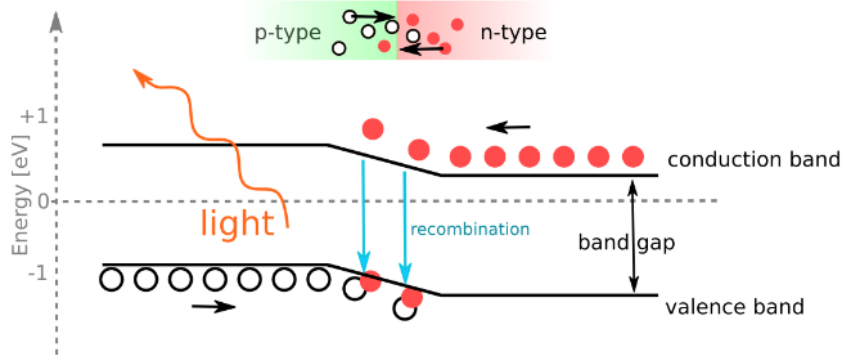


**Figure 2.5: Schematic and band diagram of radiative electron-hole recombination under external bias; red circles: electrons; white circles: holes**

The emitted photon energy is equivalent to the minority carrier's local band gap energy. In crystalline Si solar cells, the photon energy is around 1.1 eV or equivalent wavelength 1150 nm with a distribution from 950 to 1250 nm due to the nature of an indirect band gap. The indirect band gap if Si causes a large mismatch of momentum between available electron and hole states, which reduces the probability of EL emission. [19]

The emitted light can be detected using an external sensor such as a Silicon CCD or InGaAs. These devices are sensitive in the corresponding wavelengths from 900 nm upwards [2]. Areas with reduced carrier density such as shunts, interrupted interconnections, dangling bonds and contamination reduce the possibility of radiative recombination and are therefore distinguishable in EL images [20–23].

The local luminescence emission ( $\phi$ ) at a point ( $x$ ) is a function of the local junction voltage ( $V(x)$ ) [18]:

$$\phi(E, x) = C(E, x) \cdot \left[ \exp\left(\frac{V(x)}{V_T}\right) - 1 \right] \quad (2.3)$$

$$V_T = \frac{k_b T}{q} \quad (2.4)$$

With the local calibration factor  $C(E, x)$ :

$$C(E, x) = [1 - R(E, x)] \cdot Q_i(E, x) \cdot \phi_{bb}(E) \quad (2.5)$$

Including the black body radiation  $\phi_{bb}(E)$ :

$$\phi_{bb}(E) = \frac{2 \cdot \pi \cdot E^2 / (h^3 \cdot c^2)}{\exp(E/k_b T) - 1} \approx \frac{2 \cdot \pi \cdot E^2}{h^3 \cdot c^2} \cdot \exp\left(\frac{-E}{k_b T}\right) \quad (2.6)$$

Where:

---

$C(E, x)$	Local calibration factor based on the measurement setup
$E$	Photon energy
$x$	Surface coordinate
$V_T$	Thermal voltage
$k_b$	Boltzmann constant
$T$	Temperature
$q$	Electrical charge of an electron
$R(E, x)$	Reflectance of the cell surface
$Q_i(E, x)$	Internal quantum efficiency
$h$	Planck's constant
$c$	Vacuum speed of light

---

The local calibration factor  $C(E, x)$  is a combination of quantum efficiency, reflectance and black body radiation. In case of series resistance imaging,  $C(E, x)$  is obtained from a low current EL image (Subsection 2.4.4.1)

## 2.4.2 PRINCIPAL SETUP

A typical setup for EL imaging (Figure 2.6) consists of an infrared sensitive camera, a power supply connected to the DUT and a dark chamber. Under normal test conditions the DUT is forward biased in the dark to admit a current similar to the illuminated short-circuit current ( $I_{sc}$ ) [21]. The light emitted from the DUT as a result of radiative recombination is captured by the camera.

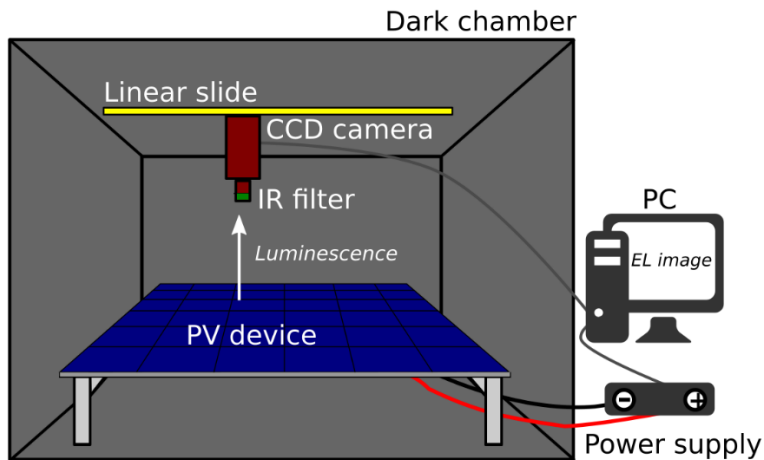


**Figure 2.6: Typical setup for electroluminescence imaging, based on CRESTs EL measurement system 'HuLC' (Appendix 2)**

The DUT temperature can be monitored to ensure thermally stable measurements. Placing the DUT in a dark room decreases the influence of environmental radiation [22]. Filters in front of the camera lens can additionally reduce the disturbance of environmental (stray) light.

For c-Si devices, IR long pass filters with a cut-off wavelength of 850 nm can be used. EL images can be taken under different conditions to extract the physical properties of the DUT:

- EL images can be resolved by spectrum [8, 21] or polarization [24] using a variety of filters. This allows for example determination of operation voltage and selection of high recombination areas.
- EL images taken at different DUT temperatures (such as room temperature to 100 °C) allow the extraction of intrinsic defects such as crystallographic defects and grain boundaries [21].
- EL images taken at different injected currents can be used for series resistance mapping (Subsection 2.4.4.1).

The image acquisition time is dependent on a range of factors, such as the optics, aperture, field of view, signal-to-noise ratio and the camera quantum efficiency. It can vary from less than a second up to multiple minutes.

The EL image acquired by the camera differs from the actual EL signal emitted by the DUT. These distortions need to be corrected for to allow

quantitative analysis. Scattered light generated by the PV device can lead to signal overestimation at points of lower emission. It is reported that the apparent EL signal from the middle of the DUT may decrease by about 2% just due to the use of low-reflective test chamber walls that absorb 96% of the incident light [25]. Inactive areas within a DUT can still indicate EL signal due to blur and pixel-smearing caused by camera lens and sensor [26].

### 2.4.3 CAMERA TYPES

Three different types of camera sensors are commonly used for EL imaging: silicon charge-coupled devices (CCD), indium gallium arsenide (InGaAs) and the less common mercury cadmium telluride (MCT). They differ in spectral response and cost. CCD detectors are often cheaper than InGaAs or MCT, however for c-Si DUTs they detect only a small part of the wave band of the DUT's EL, whilst InGaAs sensors cover the entire EL spectrum (Figure 2.7).

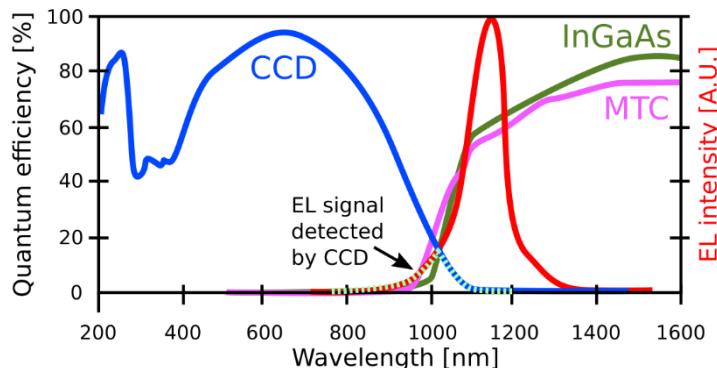


**Figure 2.7: Quantum efficiency of common camera sensors (CCD, InGaAs, MCT) in comparison to a typical emission spectrum of a c-Si DUT (red) [20, 21]**

In comparison, this allows largely reduced exposure times but also causes differences in the captured EL images (Subsection 7.2.3.3). However, CCD cameras are often seen as the preferable choice of EL imaging due to lower price and higher resolution [20]. If it can be assumed, that the CCD well accumulates charge linearly, the image intensity at pixel  $[x, y]$  is a product

of the cameras quantum efficiency ( $QE_{cam}$ ), exposure time ( $t_{exp}$ ) and local EL flux ( $\phi(i, j, E)$ ):

$$I[x, y] = QE_{cam}[x, y](E) \cdot t_{exp} \cdot \phi(x, y, E) \quad (2.7)$$

## 2.4.4 PHYSICAL PARAMETERS

The measured EL image contains superimposed information of the DUT material, optical and electrical properties. This makes a separation of the different influence factors in the captured image difficult [27]. However, EL imaging under different operation conditions and with different optical filters can be used to extract multiple parameters [8, 25], such as minority carrier diffusion length [6].

### 2.4.4.1 SERIES RESISTANCE IMAGING

The spatial distribution of PV performance parameters can vary strongly due to shunts, contact/sheet resistance, grain boundaries, dislocations, cracks and other non-uniform defects. Their measurement is either destructive (such as contact resistance using CORESCAN [28]) and/or time consuming like LBIC used for current- [29] or CELLO for series resistance ( $R_s$ ) mapping [30]. Therefore, there is strong motivation to replace these measurements using contactless, fast and cheap imaging methods, such as EL, PL or DLIT (Subsection 2.4.5). To date, several approaches exist to measure the local effective series resistance of cells and modules ( $R_{s,i}$ ). On cell level, a method using two PL images together with different light intensities and terminal voltages has been demonstrated [31]. Methods using EL images taken at two different biases are manifold [32–34]. The similarity with other measurement methods is reported from good [35] to ‘hardly visible’ [36]. Reasons can be partly found in the application of the Fuyuki approximation [2]. This approximation links the local current density to local luminescence and requires cell thickness to be larger than the diffusion length.

In this thesis, series resistance mapping is conducted for module-scale PV (Subsection 7.2.3.4). It is based on Breitenstein's method [32] to obtain  $R_{s,i}$  together with the Potthoff assumption [8], wherein the brightest image pixel of a cell is linked to the cells junction voltage. This allows measurements on modules as a network of in series connected cells [8]. The following description aims to provide a short overview of equations needed to calculate  $R_s$ .

A detailed physical interpretation is out of the scope of this work.

Two EL images ( $\phi_{i1}, \phi_{i2}$ ) are captured at 10%  $I_{sc}$  (#<sub>1</sub>) and 100%  $I_{sc}$  (#<sub>2</sub>). Background is subtracted from both images following the procedure described in Section 4.2. Further measurement parameters are listed in Table 2.2. Parameters are scalar, 2d arrays at EL image resolution (#<sub>i</sub>) or 2d arrays with resolution defined by number of rows and columns (for example {6,10}) of the PV module (#<sub>a</sub>). The calculation of  $R_{s,i}$  requires the following assumptions:

- The cells ideality factor equals 1.
- Lateral currents in the low current image are sufficiently small so that the local voltage ( $U_{i,1}$ ) equals the external applied voltage ( $U_1$ ) and series resistance can be neglected.

**Table 2.2: Input for series resistance imaging**

Param.	Unit	Description
$U_1, U_2$	[V]	Operation voltage, averaged during measurement time
$I_2$	[A]	Applied current, averaged during measurement time
$T_1, T_2$	[K]	Module temperature, averaged during measurement t.
$t_1, t_2$	[s]	Exposure time for capturing $\phi_{i1}, \phi_{i2}$
$n_{cell}$	[-]	Number of cells in the PV module (for example 60)

If both EL images are captured at different exposure times,  $\phi_{i1}$  is scaled as follows:

$$\phi_{i1}^* = \phi_{i1} \frac{t_1}{t_2} \quad (2.8)$$

From the module temperatures ( $T_1, T_2$ ) the thermal voltage ( $V_{T1}, V_{T2}$ ) is calculated using Equation 2.4. Following the Potthoff assumption, the brightest pixels within every cell area in  $\phi_{i2}$  ( $\phi_{a2,max}$ ) should be taken to estimate the cell voltage. This method however includes the risk of selecting defective or otherwise not representative values. Therefore the maximum criterion is modified in this work and  $\phi_{a2,max}$  is obtained from the median of the brightest 10% in every cell instead. To exclude the effect of intrinsic defects and to scale the EL signal, a calibration image ( $C_{i1}$ ) is calculated. Following the proportionality  $\phi_{i1} \sim \exp(\frac{U_1}{V_T})$  (Equation 2.3) and assuming no voltage gradients at 10%  $I_{sc}$ ,  $C_{i1}$  can be calculated as follows [34, 37]:

$$C_{i1} = \frac{\phi_{i1}}{c} \quad (2.9)$$

$$c = \exp\left(\frac{U_1}{n_{cell} \cdot U_{T1}}\right) \quad (2.10)$$

The same proportionality then leads to the local voltage map at 100%  $I_{sc}$  [37]:

$$U_{i2} = U_{T2} \cdot \ln(\phi_{i2} - \ln(C_{i1})) \quad (2.11)$$

The global module series resistance ( $R_{s,gl}$ ) is measured from the voltage drop ( $U_2 - U_{\Sigma cell,2}$ ) across the module and the module current:

$$R_{s,gl} = \frac{U_2 - U_{\Sigma cell,2}}{I_2} \quad (2.12)$$

Following the Potthoff assumption [8] the sum of all cell voltages can be calculated using: [37]

$$U_{\Sigma cell,2} = \sum_{cells} (U_{T2} \cdot \ln(\frac{\phi_{a2,max}}{C}))$$

$$C = \left( \frac{\prod(\phi_{a2,max})}{c} \right)^{\frac{1}{n_{cell}}} \quad (2.13)$$

Following Fuyuki et al. [2], the diffusion length and therefore the local dark current saturation current ( $I_{0,i}$ ) is indirect proportional to the EL signal [37]:

$$I_{0,i} = \frac{f}{C_{i1}} \quad (2.14)$$

The scaling factor ( $f$ ) thereby ensures that the arithmetic mean of  $R_{s,i}$  equals  $R_{s,gl}$  [34, 37]:

$$f = \frac{\text{mean}(U_i^* \cdot C_{i1})}{R_{s,gl}} \quad (2.15)$$

$$U_i^* = \frac{\frac{U_2}{n_{cell}} - U_{i2}}{\exp(\frac{U_{i2}}{U_{T2}})} \quad (2.16)$$

Finally the local series resistance ( $R_{s,i}$ ) is calculated as follows [37]:

$$R_{s,i} = \frac{U_i^*}{I_{0,i}} \quad (2.17)$$

#### 2.4.5 COMPARISON TO OTHER CAMERA-BASED METHODS

Although this thesis focusses on quantification of the electroluminescence method, it is assumed that the methods introduced to describe image quality, to calibrate the camera and to correct images

can be adapted to other camera-based measurement methods. Two of them are detailed as follows.

#### 2.4.5.1 PHOTOLUMINESCENCE (PL)

Both EL and PL measurements capture near infrared (IR) radiation. In contrast to EL, PL imaging is contactless and does not require current injection to the device from an external supply. This enables measurement on Si wafers without metallisation. A light source (such as a scanning or expanded laser beam) illuminates the DUT at a wave band below the DUT's emission (for instance 815 nm for c-Si). The irradiating light (and not an external power supply) provides the energy required for excitation of electrons into the conduction band [38]. In contrast to EL images, carrier generation is homogenous [39]. Therefore, electrically disconnected areas and apparent intensity deviations due to series resistance effects are not visible in PL [10]. Shunts are visible in both methods, because luminescence is still related to the local junction voltage [40].

#### 2.4.5.2 LOCK-IN THERMOGRAPHY (LIT)

Thermography captures far IR emission with a suitable thermo camera. Emission in this band is caused by radiative recombination, thermalisation and Peltier effects. Depending on the energy source, two lock-in technologies are popular: In dark lock-in thermography (DLIT) a pulsed forward bias is applied to the DUT. In illuminated lock-in thermography (ILIT) a pulsed light source is used. Thermal diffusion in the DUT is limited and spatial resolution is increased by high frequency modulation (multiple Hz) of the energy source [41]. It is found that lifetime, bulk defect and series resistance imaging are preferably done with EL or PL but LIT is superior when mapping current, weak Ohmic shunts and trapping centres [39].

# 3 CAMERA CALIBRATION

This chapter describes the methods executed prior to the actual EL imaging procedure. These methods are used to calibrate the camera according to the imaging setup. Camera calibration optimizes image quality versus measurement time and allows correction of camera dependent distortions.

Camera calibration includes correcting for or minimising the impact of the following seven problems (Figure 3.1):

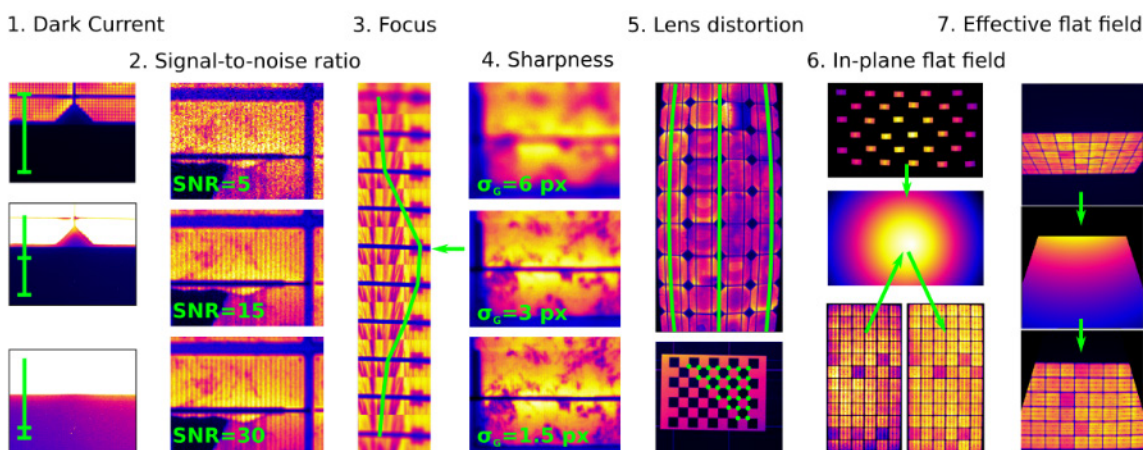


**Figure 3.1: Overview of Chapter 3**

**1:** Thermal noise, environmental stray- and reflected EL light can offset the measured signal. This problem is commonly solved by subtracting an additional (background or dark current) image from every EL image taken of the unbiased device. Section 3.1 discusses options to improve this method by defining a one-off calibration. This makes sequential background image capturing redundant.

**2:** The calculation of an averaged and spatially resolved signal-to-noise ratio (SNR) is described in Section 3.2. An SNR average enables minimizing exposure time in accordance to given image quality requirements. A

spatially resolved SNR can be used to determine part of the overall measurement uncertainty (Section 6.1).

**3:** No cameras dedicated to EL imaging of PV devices were found which were able to automatically focusing the imaged scene. Instead, the best focal point is often defined intuitively by the operator after inspecting multiple images taken at different focal settings. Section 3.3 introduces a parameter that helps to quantify this procedure.

**4:** Methods to measure absolute image sharpness are presented and compared in Section 3.4. Knowing the image sharpness helps to indicate whether an imaging setup is capable of resolving certain features and to calculate part of the position based uncertainty (Section 6.2). When quantitatively comparing images from different setups, measured image sharpness also helps to adjust the sharpness before calculating difference images.

**5:** Every system using a camera lens suffers lens distortion. The commonly known barrel distortion (and others) causes spatial displacement of the EL signal. Their calibration is detailed in Section 3.5.

**6-7:** The final two Sections 3.6 and 3.7 investigate methods to measure the flat field at different exposure times, apertures, wavebands and perspective orientations. The flat field describes the spatial intensity distribution of a homogenous EL signal as captured by the camera sensor.

## 3.1 Dark Current Measurement

The removal of environmental stay light and thermal noise intrinsic to the CCD (dark current) is often done by subtracting from the EL image another image of the unbiased device at the same exposure time (background image) [8, 25, 33, 42, 43].

A lock-in technology together with a highly sensitive camera (such as InGaAs) introduced background removal even during daylight [11].

Background subtraction removes the offset between usable EL signal and zero as well as defective ('hot' or 'dead') pixels, if their intensity is the

same on both images. Dark current subtraction requires an additional image to be taken and adds an additional noise layer to the EL image [44]. This section firstly shows how noise can be reduced by averaging multiple background images. Then a method is presented to make background image capturing redundant. Finally, algorithms to estimate average background levels in the absence of a background image will be discussed and compared. The first two methods are limited to controlled and fixed imaging conditions as provided by a (dark) measurement chamber.

When performing a calibration for background subtraction, it should be noted that single-time-effects (STE, Section 4.1) should be filtered first. Otherwise, bright spots created by STE in the background image will result in dark spots in the corrected EL image. In certain circumstances, these spots could be easily confused with shunts or other cell defects.

### 3.1.1 DARK CURRENT FROM BACKGROUND IMAGE AVERAGE

Averaging multiple background images, taken at the same exposure time, can reduce thermal noise and therefore improve the image quality [45]. Figure 3.2 shows the relative signal-to-noise ratio (SNR) improvement of one EL image after subtracting background averages, obtained from 1-10 individual images. Two different camera systems and different exposure times within the usual range of EL imaging (Subsection 7.2.1.2) were analysed for this method. The SNR was calculated with options ‘NLF, xBG’, as detailed in Subsection 3.2.5.1.

Looking at Figure 3.2, the shape resembles a  $\sqrt{n}$  increase, as can be expected when averaging Gaussian distributions. The improvement is highest for small exposure times because of the similarly higher influence of noise. For the shortest exposure time of 3 s the SNR could be increased by over 20% by using an average of 10 background images instead of one.

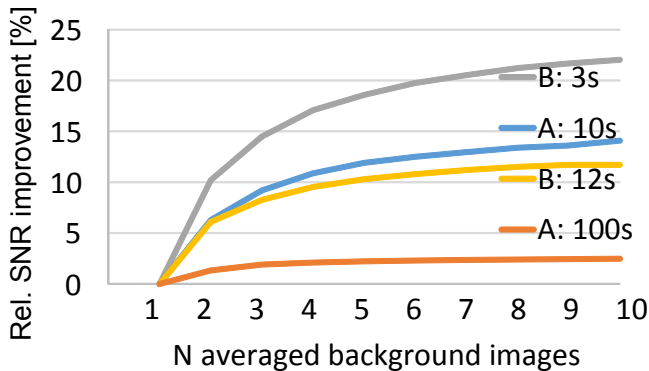


**Figure 3.2: Relative SNR improvement [%] for two cameras (A: Apogee Alta F, B: CoolSamba 830HR) and different exposure times**

### 3.1.2 DARK CURRENT AS FUNCTION OF EXPOSURE TIME

If environmental light can be neglected (light-tight or dark chamber) or assumed to be constant, it is possible to calculate a background image for a specific exposure time from two calibration images: dark current intercept and slope (Figure 3.4 b,c). If the CCD well is assumed to accumulate charge linearly, pixel intensities will either increase linearly or (at saturation) stagnate over time. Both behaviours will also be superimposed by thermal noise. To obtain both calibration maps, the following algorithm is proposed:

1. Capture background images at multiple (recommended nine) equidistantly distributed exposure times. For each exposure time at minimum two images should be taken for single-time-effect removal (Section 4.1) and noise averaging. The calibration quality depends on the numbers of images used and is camera dependent.
2. Apply a linear regression using the exposure times and the per exposure time averaged background images (Figure 3.3). Saturated pixels should be excluded from the regression to retain linearity. This returns the dark currents slope ( $a$ ) and intercept ( $b$ ).
3. Assume a minimum slope of defective ('hot') pixels and filter values below that threshold from the acquired slope map. Multiply the filtered values by the mean exposure time and add the result to the offset map. This decreases noise close to the minimum and

maximum exposure times and ensures positive intensity values on the resulting background image.

4. Calculate background image ( $BG$ ) for an exposure time ( $\tau_{exp}$ ) using:

$$BG(\tau_{exp}) = a \cdot \tau_{exp} + b \quad (3.1)$$

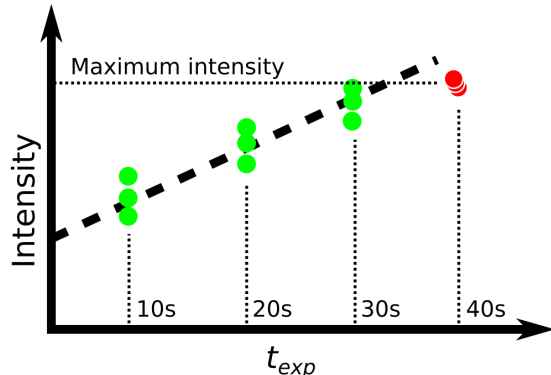


Figure 3.3: Schematic of linear regression applied on one image pixel; dots: measured image intensities of three measurements at four exposure times; green: valid values; red: saturated pixels that are excluded from linear regression

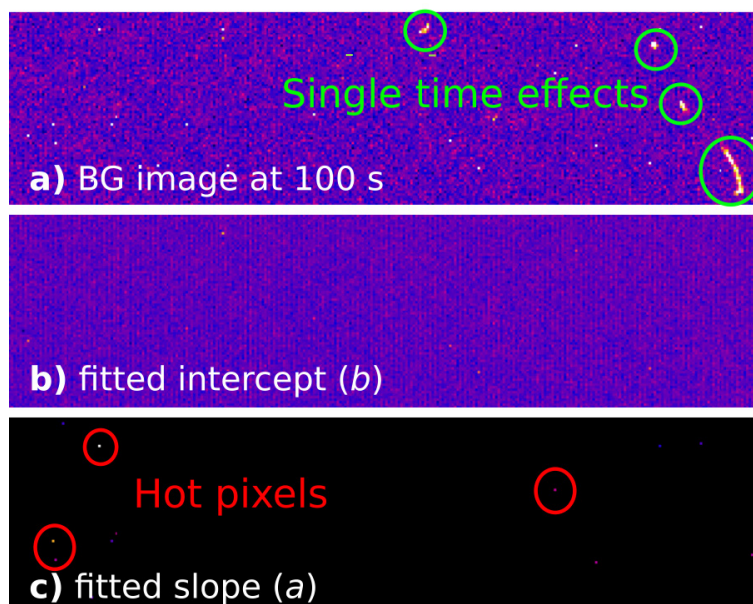
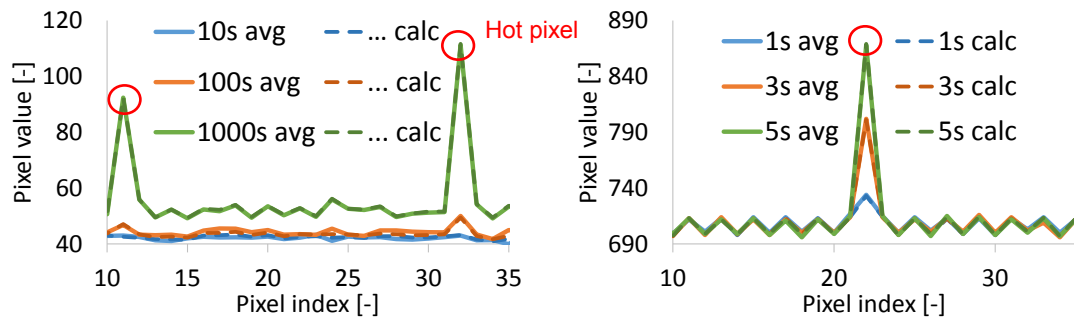


Figure 3.4: a) Example dark current image with hot pixels and single-time-effects; b) fitted intercept including static camera noise; c) fitted slope including hot pixels and environmental light (if existent)

A comparison of averaged and calculated (Equation 3.1) background images is shown in Figure 3.5. For each exposure time, 10 (a) resp. 50 (b) background images were used.



**a) Camera: Apogee Alta F**      **b) Camera: CoolSamba 830HR**  
**Figure 3.5: Comparison of averaged ('avg') to calculated ('calc') background image (line plot at positions including hot pixels) for different exposure times (1 - 1000 s)**

The offset level of the camera in Figure 3.5b fluctuates between two different intensity levels. The offset in Figure 3.5a appears random however. Offset as well as intensity of the two (a) or one (b) hot pixels can be almost exactly reproduced using only one intercept and slope map.

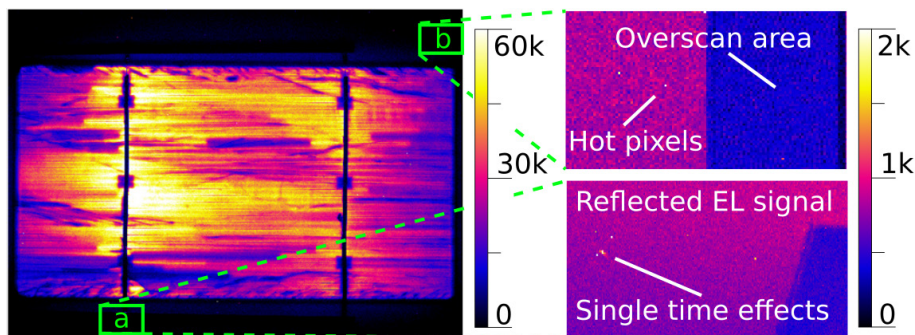
This allows the conclusion that, in the case of unchanging background and camera conditions, no extra background image (Equation 3.1) for each exposure time is necessary. The background image can be calculated using two calibration maps. Because multiple background images were used for calibration, the resulting calculated image has a lower noise level. The uncertainty of this method will depend on the linearity of the camera and its defects as well as the number of averaged images used to fit the linear equation as well as the time between creating the two calibration maps and their usage for background removal. New hot pixels, generated between camera calibration and EL imaging, will remain uncorrected.

### 3.1.3 DARK CURRENT LEVEL ESTIMATION WITHOUT BACKGROUND IMAGE

This subsection covers the estimation of a background level if no background image is available. All methods will treat the background level as spatially invariant. Setting the background level to the average of a representative background area can lead to contradictory results.

Although it might not be clearly visible within the overall image, areas around PV devices are often influenced by scattered or reflected EL signal (Figure 3.6). Some camera sensors have an overscan area not influenced by incoming radiation (area b in Figure 3.6, top right).

Choosing a representative background area requires a manual inspection regarding the existence of these features. This cannot be easily automated. Therefore, this method will not be discussed here. The following methods of background level estimation are compared.



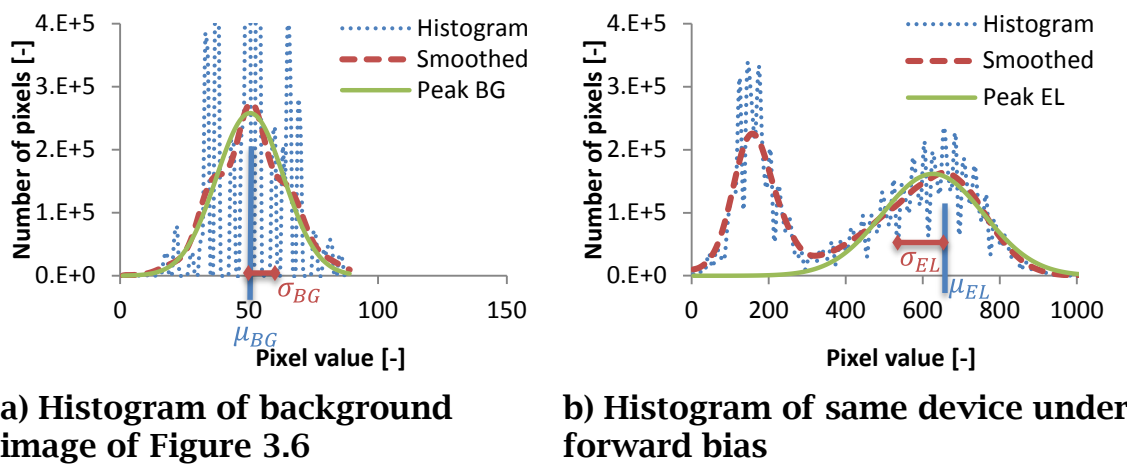
**Figure 3.6:** EL image of an EFG mini-module with two different background areas, which are not suitable for background level- or noise estimation

Image minima: Setting the background level to the image minimum is not sufficient. Non-sensitive or ‘dead’ pixels as well as environmental and reflected EL light create the need for more extensive methods. The influence of defective pixels at specific areas (such as image border), can be reduced if the respective area is excluded from the minimum. A median filter can also average noise and remove defective pixels. Minimum-based parameters, used for the evaluation below are listed in Table 3.1.

**Table 3.1: Minimum-based parameters**

Parameter	Description
‘min’	The minimum value of the entire image
‘Med3, min’	The minimum of a median filtered image (kernel size=3 px)
‘NB, Med3, min’	Same as above, but initially excluding an image border of 10 px

First peak in image intensity histogram: The background level can also be identified by investigating the intensity histogram of the EL image. The histogram of EL images enables the separation of signal and background due to the two distinct intensity levels. For this purpose, the image has to include an area that is not influenced by the EL signal. Figure 3.7 shows a histogram of an EL image under open (a) and short circuit conditions (b). By comparing both images, it appears that the lower of the two peaks represents the background and so the background level can therefore be extracted from the lower peak within the EL image. However, in this example, scattered and reflected EL light influenced the majority of background areas. Therefore the mean of the Gaussian  $\mu_{BG}$  is with 150 about 90 counts higher in (b) than in the background image (a).



**a) Histogram of background image of Figure 3.6**

**b) Histogram of same device under forward bias**

**Figure 3.7: Example image intensity histogram**

Cumulative distribution function of image intensity histogram: Instead of fitting a function to the intensity histogram, the integral of the histogram can be evaluated. Divided by its sum, the resulting cumulative distribution function (CDF) describes the probability of a pixel being brighter than or equal to a given intensity. By choosing an intensity with a probability of for instance 1%, darker (defective) pixels, which occur less often, will be filtered. In order to define the correct probability, different parameters are examined (Table 3.2).

**Table 3.2: CDF-based parameters**

Parameter	Description
'1%CDF', '0.5%CDF', '0.1%CDF'	Intensity value occurring with a probability of more than 1%, 0.5% or 0.1%.
'NB, 0.1%CDF'	Same as above, but 10 px of the image border were excluded from the CDF
'NB, Med3, 0.1%CDF'	Same as above but the image was median filtered before calculation of the CDF

Local minimum of standard deviation: The minimum of the spatial standard deviation can point to the most homogenous area in an image. The background level can be obtained as the median value at that point.  
Comparison of different background level parameters: 12 different EL images and their corresponding background images were used for the comparison (Figure 3.8). The EL images were selected as representing a broad spectrum of different PV module sizes, exposure times and cameras.

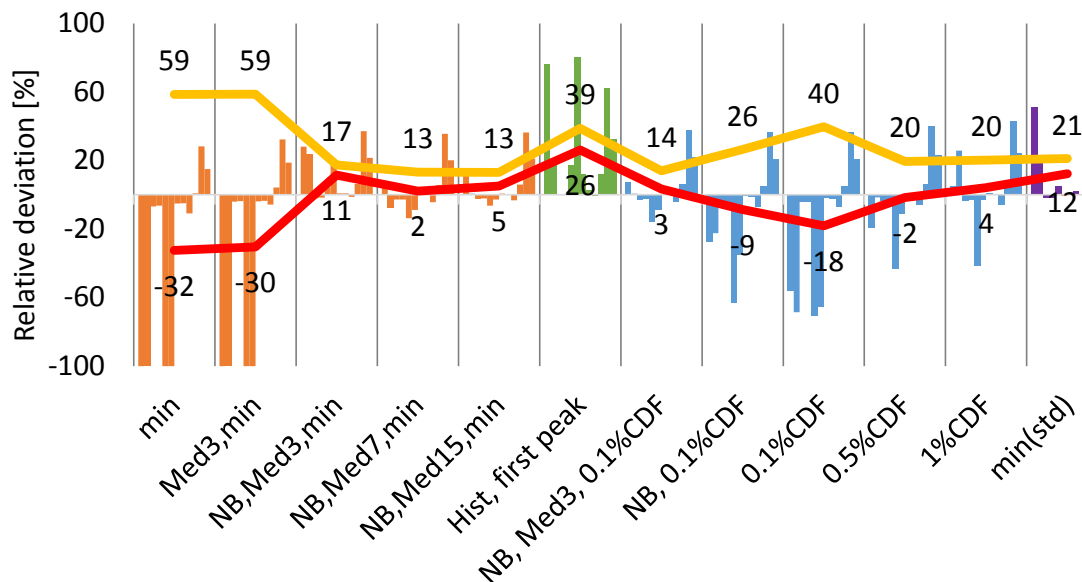


**Figure 3.8: Relative deviation between estimated and real background level for 12 different EL images; average (red) and RMSE (yellow)**

The RMSE (yellow) of all parameters was compared against the average of the corresponding background image. The average of the background image was representative for the background level due to the absence of environmental light.

A RMSE between 10 and 20 % was reached by only five parameters:

Orange: The relatively simple parameters ‘min’ and ‘Med3, min’ have the highest RMSE of almost 60%. This is due to the existence of dead pixels, which caused detected background levels of 0 (or relative -100%). This issue could be resolved after excluding a 10-pixel wide image border with ‘NB Med3, min’. The influence of noise and defective pixels could be further limited by choosing a bigger kernel size of 7x7 and 15x15 px for the median filter. Although the RMSE is slightly smaller for the latter kernel size, the processing time for median filtering rises with the kernel size and requires bigger areas, which only contain the background. Therefore, the ‘NB Med7, min’ is recommended to extract the background level from an EL image.

Green: Taking the mean of a Gaussian distribution, fitted to the first peak in an image intensity histogram, often estimated the background level as too high (Figure 3.7). Here, scattered EL light influenced most background areas. The few remaining areas, which were not influenced by EL, were too small to create a detectable peak in the smoothed image intensity histogram.

Purple: A kernel size of 11x11 px was chosen to calculate the spatial standard deviation. The background level was defined as its minimum. In all the evaluated images, this parameter indeed pointed to the image background. However, for five images this background level was increased due to scattered EL light. In these cases, this parameter overestimated the actual background level.

Blue: The motivation for taking the background level from a certain percentage of the relative cumulative distribution function is to remove non-representative pixel values. However, the percentage taken is arbitrary. If the percentage is too small (‘0.1%CDF’), dead pixel might still be included. For the parameter ‘0.5%CDF’ and the examined images, the RMSE was found to be minimal. A further improvement can be achieved if defective areas at the image border are excluded (‘NB’) and the influence of defective pixels is limited by first using a median filter. However, an

RMSE of over 10%, removed areas and arbitrary values for filter sizes and CDF percentages make a background level estimation from only the EL image less reliable.

The comparison of all parameters leads to the conclusion that the reliability of background level estimation is questionable and this method should only be considered if no background image exists (for example in receiving EL images from outside your own laboratory)

## 3.2 Signal-To-Noise Ratio (SNR)

The scope of this section is to obtain the signal-to-noise ratio (SNR) from only one or two EL images together with a background image or estimated background level (Section 3.1). Different approaches to measure signal and noise are presented. A method is proposed to measure a spatially averaged SNR (Equation 3.16) and a method to calculate an SNR map (Equation 3.17). A comparison of the proposed parameters to the existing  $SNR_{Hinken}$  (Equation 3.4) is shown in Subsection 3.2.5.

The SNR can be used to map the estimated intensity based uncertainty originating from the image itself and to match given image quality criteria. Determining the SNR can aid quantitative comparison and analysis of EL images and is useful to define the minimum requirements of an imaging setup. The draft IEC standard TS 60904-13 [46] requires an SNR greater than or equal to 45 for indoor measurements. This requirement and definition (Equation 3.16) are informed by this doctoral prospect.

### 3.2.1 INTRODUCTION

The SNR is an indicator of the quality of the captured signal (here EL) over a noise signal. Although this definition appears straight forward, recent literature on EL struggles to apply it: Often SNR is mentioned but not further explained [47–49]. SNR values are given as subjective descriptions

[50, 51] or numbers are assigned without equation or reference [52]. If equations are given, they are restricted to homogenous areas within an image [33, 51] or only applicable if further information about the imaging system is known [53]. The problem arises mainly from the largely varying approaches that are available to calculate the SNR of images.

This section focusses on the averaged SNR as an image quality parameter, but also spatially resolved SNR maps used for uncertainty analysis (Section 6.1). It starts with a definition of the SNR. Noise and signal are discussed separately. The influence of approximations, such as a simplified noise model, arithmetic averaging and the extraction of the SNR from only one or two images is analysed.

In this work, the SNR is defined as a combination of the measured signal  $S$ , its offset (or background)  $Bg$  and noise  $N$  as follows (Figure 3.9):

$$SNR = \frac{S - Bg}{N} \quad (3.2)$$

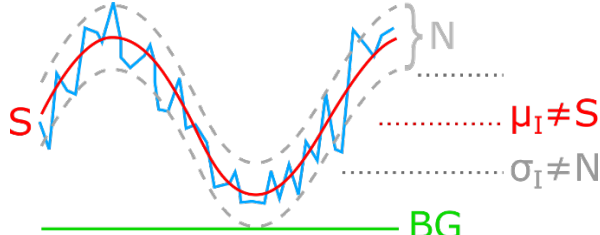


**Figure 3.9: Schematic of signal, noise and background**

### Spatial approach

In its simplest form the signal is approximated as the spatial average image intensity  $\mu_I$  and noise as its standard deviation [51, 54]:

$$SNR_0 = \frac{\mu_I}{\sigma_I} \quad (3.3)$$

This ratio strongly depends on the imaged scene because mean and standard deviation depend on the intensity distribution of the image.

Since EL images are not homogenous, a robust and generalised SNR requires a more appropriate definition.

### Temporal approach

Hinken et.al. [53] determine the SNR as a temporal average from multiple, background corrected, images ( $I_0 \dots I_n$ ), taken in series, as:

$$SNR_{Hinken} = \frac{\mu(I_0 \dots I_n)}{\sigma(I_0 \dots I_n)} \quad (3.4)$$

However, this method requires multiple EL images to be taken and does not define how to average the resulting SNR map.

## 3.2.2 WHAT IS ‘NOISE’?

Noise can be defined as a combination of shot (or photon)-, thermal (or dark)- and readout noise [45]. If Gaussian distributed, it can be calculated as the standard deviation of an unfiltered signal.

However, the pixel intensity across EL images is expected to vary, thus estimation of the signal noise from its standard deviation will cause a noise overestimation. This subsection presents and compares different noise parameters used to calculate the SNR using Equation 3.2.

### 3.2.2.1 NOISE FROM REPRESENTATIVE BACKGROUND AREA

If the background level can be assumed constant, part of the overall noise can be calculated from the standard deviation of a representative background area ( $N_{BG}$ ). This defined background area should be free of erroneous pixels such as hot pixels, single-time-effects, environmental and EL light in order to not artificially increase the standard deviation. The representative background area can be used for both, background level and noise estimation.

To include cameras without an overscan area, the noise level is taken from the standard deviation of a specified area  $[x_1:x_2, y_1:y_2]$  within a background image:

$$N_{BG} = std(I_{Bg}[x_1:x_2, y_1:y_2]) \quad (3.5)$$

### 3.2.2.2 SHOT NOISE

$N_{BG}$  neglects the influence of shot noise. Shot noise describes the statistical variations of detected photons due to their quantum nature. The different noise levels can be visualised if the magnitude difference (Figure 3.10) is taken between two EL images. Both images are taken with the same setup and with the same exposure time.

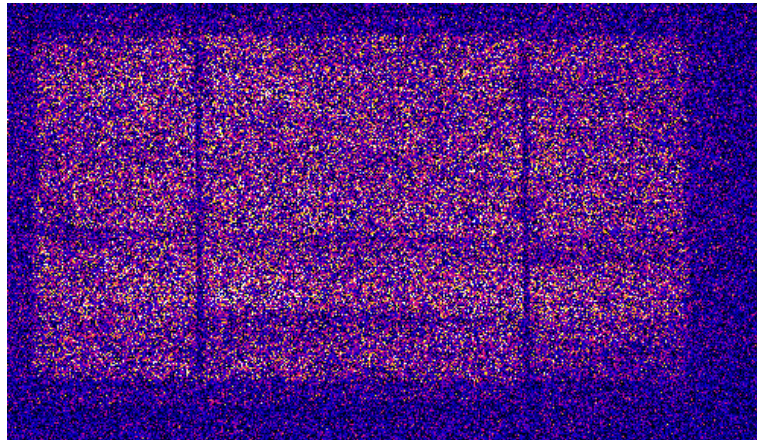


**Figure 3.10: Magnitude difference of the two EL images of the EFG mini-module, shown in Figure 3.6**

The DUT can be clearly differentiated from the background due to different noise levels. Using the square root dependence of shot noise to its signal ( $S$ ) [55],  $N_{BG}$  can be extended as follows:

$$N_{BGS} = N_{BG} + a\sqrt{S} \quad (3.6)$$

For simplification the scaling factor ( $a$ ) will be defined as 1 for the moment.

### 3.2.2.3 NOISE FROM A TWO IMAGE DIFFERENCE

As discussed in [56], noise can also be effectively determined as the difference between two images ( $I_1, I_2$ ) taken from the same setup and with the same exposure time. Noise can be calculated as follows using Equation 3.8:

$$N_{diff2} = \sqrt{0.5} \cdot \text{mean}(|I_1 - I_2|) \cdot f_{RA} \quad (3.7)$$

With `mean()` being the spatial average of all values.

Because the noise level is taken from two images, the factor  $\sqrt{0.5}$  scales this sum of variances. The root mean square error (RMSE) is a popular method to average deviations due to its statistical similarity to the standard deviation. However, the existence of outliers (such as hot pixels) can lead to an overestimation of the RMSE. A higher stability towards outliers is given with the average absolute deviation ( $AAD = \text{mean}(|I_1 - I_2|)$ ). If  $(I_1 - I_2)$  is Gaussian distributed, its AAD can be scaled to an RMSE average according to [57] using the factor:

$$f_{RA} = \frac{RMSE}{AAD} = \left(\frac{2}{\pi}\right)^{-0.5} \quad (3.8)$$

An example of the negative influence of outliers to RMSE averaging is shown in Figure 3.11.

### 3.2.2.4 NOISE FROM A ONE IMAGE DIFFERENCE

If no second image ( $I_2$ ) is available, noise can also be extracted from the difference between the unfiltered and noise filtered image. Here, the noise-filtered image ( $I_{med}$ ) is generated using a median filter with a kernel size of 3x3 px:

$$N_{diff1} = \text{mean}(|I_1 - I_{med}|) \cdot f_{RA} \quad (3.9)$$

### 3.2.2.5 NOISE-LEVEL-FUNCTION

The noise level as function of image intensity ( $k$ ) can be described with a noise-level-function (NLF, Figure 3.11). According to [58] the NLF can be calculated from the original or noisy image ( $I_1$ ) and a noise-free image average ( $I_{Av}$ ) with  $i$  being a specified intensity (-range) using:

$$NLF(\varphi) = \sqrt{\text{mean}[(I_1(k) - I_{Av}(k))^2]} \quad (3.10)$$

For this purpose, the difference image ( $I_{diff} = I_1 - I_{Av}$ ) has to be averaged for different intensity levels derived from the image histogram of  $I_{Av}$ . Instead of the RMSE, the AAD is chosen for averaging due to the better outlier stability. To determine the minimum number of images needed in order to calculate a sufficient NLF, three methods of calculating  $I_{diff}$  and two averaging methods are discussed and compared below.

$I_{Av}$  can be calculated from the average of multiple images ( $I_n$ ) of the same imaging setup (Multi):

$$I_{diff,multi} \approx I_1 - \text{mean}(I_1, \dots, I_n) \quad (3.11)$$

If only two equivalent images are available, the noise level can be also extracted from two noisy sources (Duo):

$$I_{diff,duo} \approx (I_1 - I_2) \cdot \sqrt{0.5} \quad (3.12)$$

If only one EL image is available  $I_{Av}$  can be estimated from the median filtered (kernel size=3) image ( $I_{med}$ ) (Single):

$$I_{diff,single} \approx (I_1 - I_{med}) \cdot f_{med} \quad (3.13)$$

Due to the small size of the median kernel of  $3 \cdot 3 = 9$  px the median still includes a certain noise fraction. During this work, it was found that  $f_{med} = 1 + \frac{1}{9}$  is a suitable factor to correct for noise which remains after median filtering. It is applied in both ‘Single’ plots in Figure 3.11. This figure compares the two different averaging methods (RMSE, AAD) and the three approaches to obtain  $I_{diff}$  used to calculate  $NLF(\varphi)$ . For both ‘Multi’ plots, a series of 10 EL images was averaged.

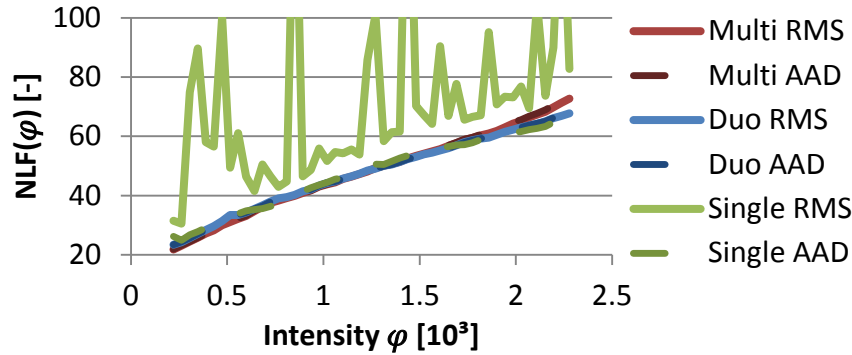
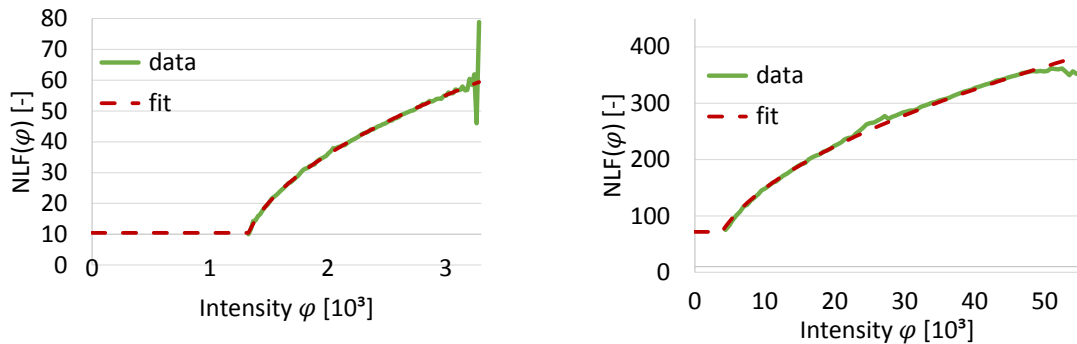


**Figure 3.11: Comparison of different approaches to estimate the noise-level-function  $NLF(\varphi)$  of the EL image shown in Figure 3.6**

With the exception of ‘Single RMSE’, it is apparent that all plots are almost identical. This indicates that  $NLF(\varphi)$  can be obtained from even one single image. In contrast, the ‘Single RMSE’ plot appears highly distorted. Here,  $I_{diff}$  contained many outliers created by subtracting a median filtered image.

As Figure 3.12 shows, the NLF can be fitted with the following equation:

$$NLF(\varphi) = \begin{cases} a \cdot \sqrt{\varphi - b} & \text{if } NLF(\varphi) < c \\ c & \text{otherwise} \end{cases} \quad (3.14)$$



a) Camera: Apogee Alfa F  
 Setup: Figure 3.6

b) Camera: Cool Samba 830HR  
 Setup: Figure 4.3

**Figure 3.12:** NLF (Duo AAD) calculated for two different camera systems; fit using Equation 3.14

### 3.2.2.6 COMPARISON OF DIFFERENT NOISE PARAMETERS

This subsection compares the proposed parameters for quantifying the noise level of an image. The AAD is used henceforth to calculate  $NLF(\varphi)$ . Figure 3.13 visualizes the trend of the following eight different parameters:

Blue:

- Bg1 - Noise from standard deviation of a 50x50 px area within an extra background image (Equation 3.5)
- Bg2 - Noise from the entire background image (Equation 3.5)
- BgS - Same as above but adding shot noise (Equation 3.6)

Orange:

- diff2 - Noise from the difference of two equivalent images (Equation 3.7)
- diff1 - Noise from the difference of a noisy and a noise-filtered image (Equation 3.9).

Green:

- NLF10 - noise-level-function from a fit generated with 10 equivalent images (Equation 3.11)
- NLF2 - The same, but using two equivalent images (Equation 3.12)
- NLF1 - The same, but using one image (Equation 3.13)

To highlight the influence of different EL-to-background ratios, images from three different imaging setups were used. The region of interest (ROI) was further decreased in 20 steps from the entire image to an excerpt within the device.

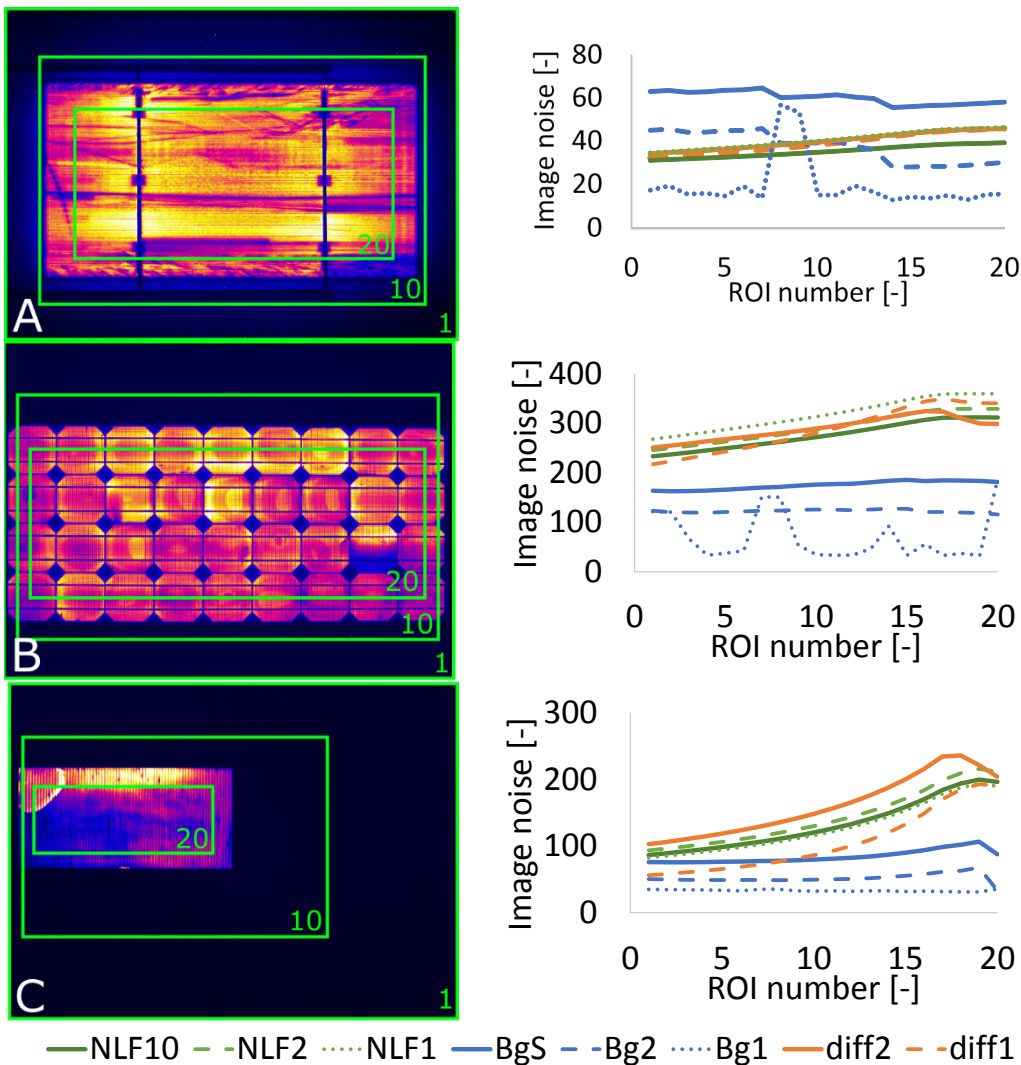


**Figure 3.13: Comparison of different noise parameters, calculated for different ROIs; A) EFG mini module; B) Monocrystalline Si module; C) CIGS module; Camera: Cool Samba 830HR**

Evaluating the three different subfigures in Figure 3.13, it is evident that the different noise parameters result in part in very different noise levels. The results vary up to factor six. In detail:

BG - Blue: The dotted Bg1 varies strongly for the setups (A) and (B). This is due to high intensity ('hot') pixels within the ROI, which artificially increase the standard deviation. The effect was not apparent in Bg2 when

the complete background image was averaged. Due to inhomogeneities within the background images used, Bg2 is on average larger than Bg1. BgS is larger than Bg2 by a constant value. Recognizing the high deviations within and relative to the other parameters, the examined background-based parameters should not be considered for noise level estimation.

NLF - Green: All green graphs are comparably close together and follow the same trend of an increase of noise for smaller ROIs. This is as expected since Figure 3.10 clearly shows that the noise level is higher over the device. For setup (A) and (B) the noise-level-function using 10 calibration images gives smaller results than those using two or only one image. It is assumed that by averaging multiple images the influence of outlier pixels was decreased which also decreased the NLF.

diff - Orange: Both orange graphs are close to the green ones of the NLF. This shows that if only one averaged value is required to describe noise, a difference image from two or one image is suitable. For (C) the trend of diff1 is much smaller than that of diff2. This can be explained with the comparable high background content in this setup. For these areas, a median filter with a kernel size of only 3x3 px is not suitable for filtering all noise. As soon as the ROI excludes the background area, diff2 and diff1 align.

The comparison of the different parameters generates the following conclusions: If only an averaged noise parameter is needed, the standard deviation from a difference image obtained from two or one images can be sufficient. If two equivalent images are available, diff2 should be used rather than diff1. However, a noise map can only be created if the NLF is measured. NLF parameters using multiple (more than 2) calibration images should be preferred in order to decrease the impact of outliers distorting the NLF.

### 3.2.3 WHAT IS ‘SIGNAL’?

To extract the signal level from an EL image, noise is not the only distortion to be removed. Erroneous ('hot') pixels from physical defects in a camera sensor as well as single-time-effects (STE) can lead to wrong conclusions especially for quantitative analysis. Detection and removal of STE and imaging artefacts is detailed in Section 4.1 and 4.4.

The outcome of denoising algorithms is extensively discussed in [59–61]. Therefore, the following discussion is kept brief.

#### 3.2.3.1 COMPARISON OF DIFFERENT DENOISING FILTERS

Figure 3.14 shows a comparison of different image filters on a 108x108 px ROI of the EL image in Figure 3.13(A).

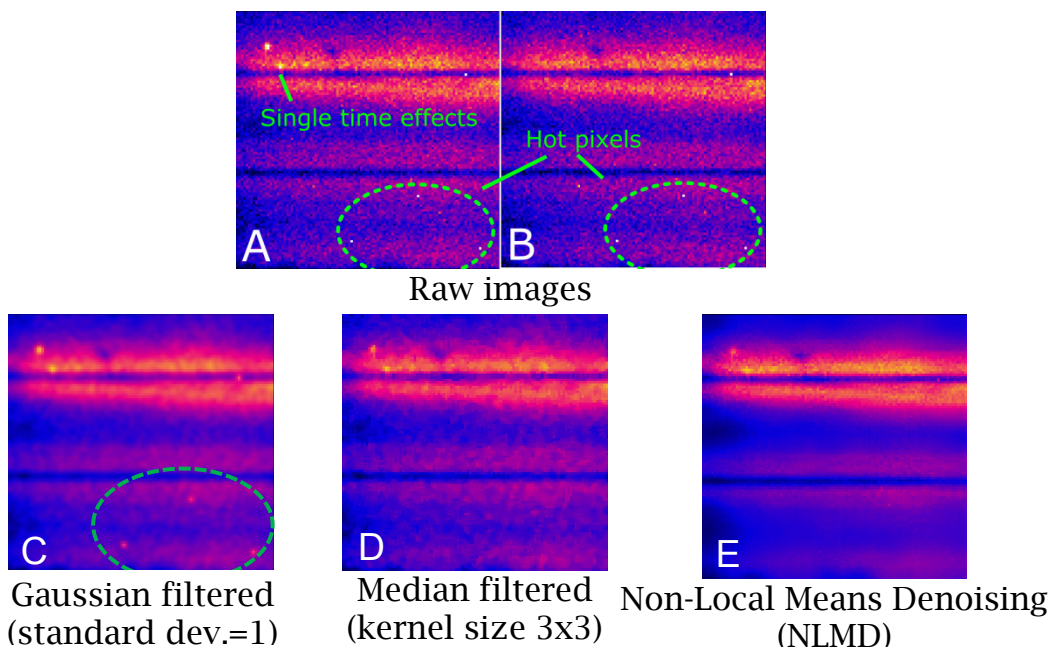


**Figure 3.14: ROI displaying two fingers of the EFG module shown in Figure 3.6**

The first row shows the two equivalent EL images taken. Single-time-effects are visible in (A) and hot pixels occur both in (A) and (B). Two simple and popular image filters are Gaussian and median filter. As visible in (C), the applied Gaussian filter was unable to remove hot pixels.

A higher standard deviation of the blur kernel would decrease their influence but conversely would blur out image details. A median filter however can successfully remove hot pixels without removing image details. More sophisticated algorithms, like the Non-Local Means Denoising (NLMD) can further decrease the influence of noise [62]. None of the three filters, applied on the RAW image (A) was able to remove the STE visible in the top left of the image.

Figure 3.15 shows image Figure 3.14(A) after STE removal (A), applied threshold median (B) and NLMD filter (C).

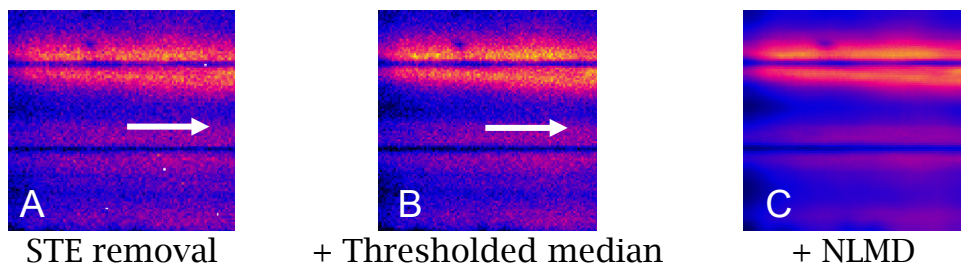


**Figure 3.15: Proposed filter algorithm applied on Figure 3.14A**

It can be summarised that the discussed filters are suitable to improve the optical representation of an EL image. If noise is defined as constant or function of signal, the precise determination of the signal is essential for the quality of an SNR map. The proposed filter, shown in Figure 3.15, includes STE removal (Section 4.1) and threshold median filter (Section 4.4).

For image quality analysis only an averaged SNR parameter is needed. In this case, none of the mentioned filters have to be applied because spatial averaging already removes the remaining distortions.

Figure 3.16 shows that for an average of an area of 10x10 px or greater the relative deviation between both raw images or between the filtered results is practically zero.

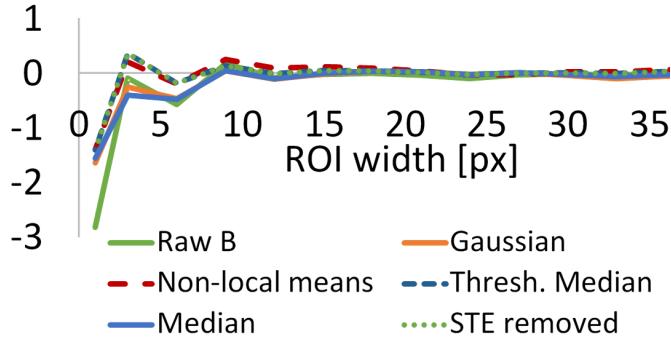


**Figure 3.16: Average deviation between both raw images ('Raw B') and filtered results over increasing ROI size within the images shown in Figure 3.14 from 1x1 px in the centre to 35x35 px**

### 3.2.4 SNR AVERAGING

In order to minimize the acceptable exposure time, one representative SNR parameter is often preferred to an SNR map. A simple average of an SNR map will include background areas around and within the PV device (busbars and inactive areas). This causes the averaged SNR to also depend on device type and size.

#### 3.2.4.1 BACKGROUND EXCLUSION

To remove these inactive (background) areas, the following algorithm is proposed:

Calculate an intensity histogram of the EL image (Figure 3.7)

1. Fit both dominant peaks with a Gaussian distribution ( $G_{EL}, G_{BG}$ ) defined by mean ( $\mu_{EL}, \mu_{BG}$ ) and standard deviation ( $\sigma_{EL}, \sigma_{BG}$ ) of the respective peaks.
2. Calculate the signal minimum ( $EL_{min}$ ) using:

$$EL_{min} = \begin{cases} \mu_{BG} + 3 \cdot \sigma_{BG} \\ \text{Intersection}(G_{EL}, G_{BG}) \quad \text{if } EL_{min} > \mu_{EL} - 3 \cdot \sigma_{EL} \end{cases} \quad (3.15)$$

3. Exclude all values smaller  $EL_{min}$  from the following averaging process.

Figure 3.17 displays two differently averaged SNR parameters with and without the above described background exclusion algorithm (xBG). Both parameters represent noise with the noise-level-function (NLF). For  $SNR_{NLF,50}$  all remaining values were arithmetically averaged.  $SNR_{NLF,75}$  on the other hand, describes the value that is exceeded by 75% of the EL signal. It can be obtained from the cumulative distribution function at 25%. To visualize the influence of different PV device-to-background ratios, the same 20 ROIs as shown in Figure 3.13 were chosen.

Background exclusion was applied on both solid lines. Consequently, their value is mostly constant for different ROIs. As soon as the ROI does not include any background areas around the device, the dashed lines (no background exclusion) reach the same level as the solid lines. For Figure 3.17B the parameters with background exclusion are even then slightly higher. This is due to the background exclusion method, which also removes inactive areas within the PV device.

The results indicate that the proposed background exclusion algorithm is suitable to calculate an averaged SNR parameter independent of the background area size.

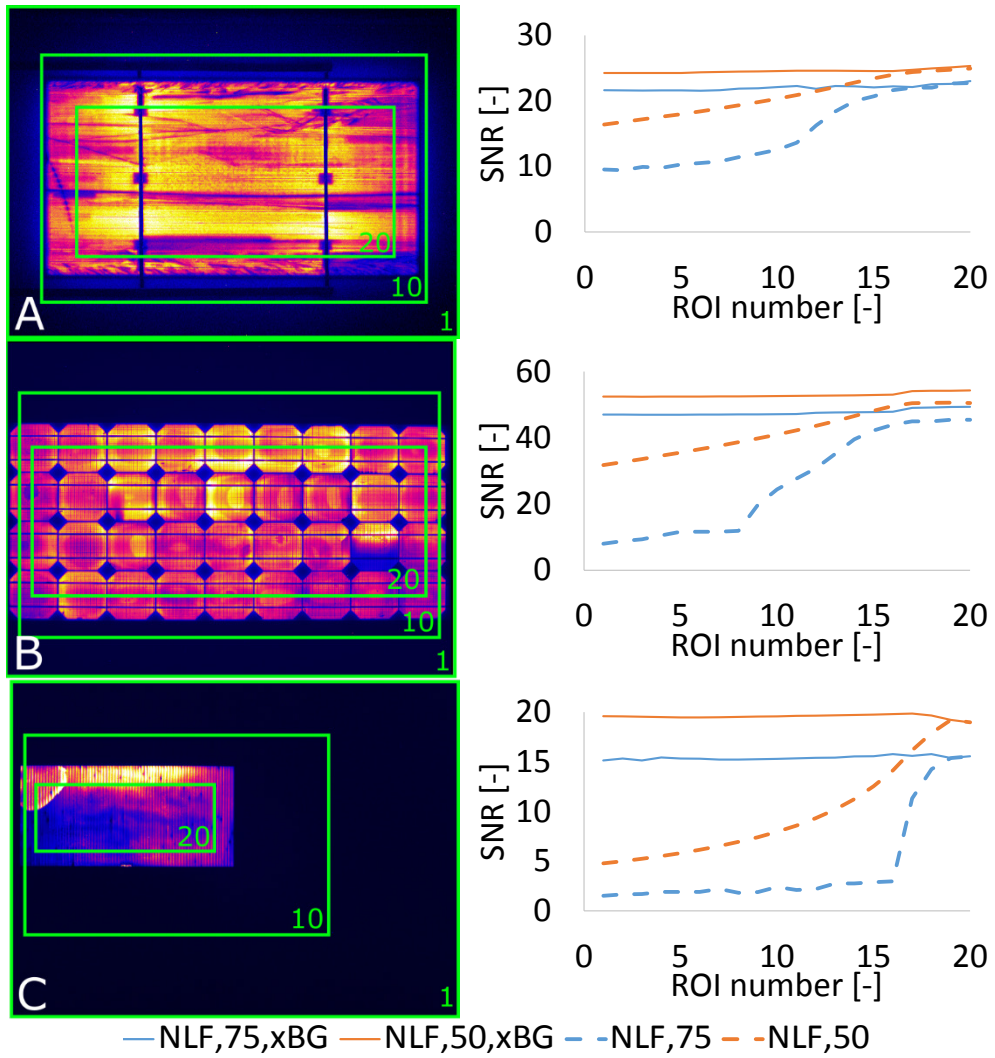


Figure 3.17: SNR map (left) and comparison of four differently averaged SNR for 20 different ROIs, illustrated as green boxes (left)

### 3.2.5 SNR COMPARISON

So far, different methods to estimate signal, noise and background (Section 3.1) as well as different averaging approaches were reviewed. This section discusses the expected error due to the use of simplifications and limited data sets.

### 3.2.5.1 EVALUATION OF NOISE-LEVEL-FUNCTION AND BACKGROUND EXCLUSION

Noise-level-function (NLF) and background exclusion for SNR averaging cannot be calculated by simple functions but requires extensively coded solutions. Hence, it may be desirable to replace the NLF with a constant noise level and to simply average the entire SNR map. To compare the individual deviation, the SNR of 10 different EL image sets was calculated using:

'NLF, xBG' (Blue): Noise as noise-level-function (Equation 3.12), background exclusion by Equation 3.15

'cN, xBG' (Orange): Like above, but using a constant noise level (Equation 3.7)

'NLF, avg' (Grey): Noise as noise-level-function (Equation 3.12), but averaging the entire SNR map by arithmetic mean

'cN, avg' (Green): Like above, but using a constant noise level as defined in Equation 3.7. By defining the noise level as an average absolute deviation of two equivalent EL images ( $I_1, I_2$ ) and averaging the full resulting image. This method of determining the SNR can be found in the current IEC standard draft [46] and can be described with the following equation:

$$SNR_{cN,avg} = \frac{\sum ((0.5 \cdot (I_1 + I_2)) - I_{BG})}{\sum (\sqrt{0.5} \cdot |I_1 - I_2| \cdot \left(\frac{2}{\pi}\right)^{-0.5})} \quad (3.16)$$

Each EL image set consisted of two EL images taken in series with the same exposure time and one background image. The image sets were taken with two different cameras. The PV devices were chosen to be a representative selection. Figure 3.18 displays the deviation of the averaged SNR of the last three parameters relative to 'NLF, xBG'.

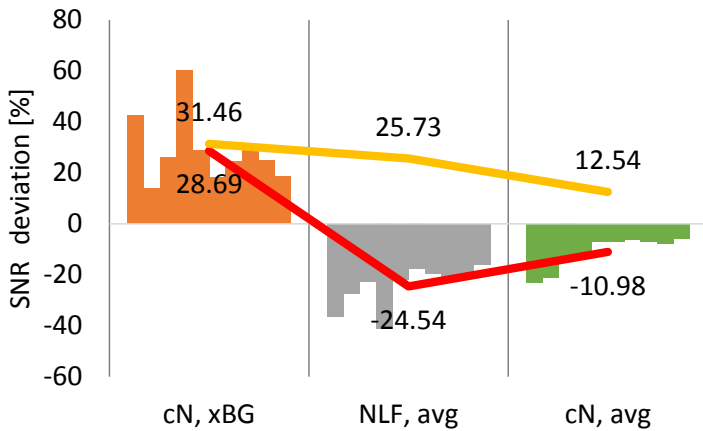


**Figure 3.18: SNR deviation due to the use of different methods relative to ‘NLF, xBG’ using the full image set ( $I_1$ ,  $I_2$ ,  $I_{BG}$ ); average (red) and RMSE (yellow)**

From Figure 3.18 it is apparent that the individual deviations for every parameter follow a similar trend:

**‘cN, xBG’ (Orange):** This method overestimates the SNR compared to ‘NLF, xBG’. This is due to the noise level being calculated from the entire image. This also included background areas with lower noise level. However, these background areas were excluded from averaging, resulting in higher SNR values.

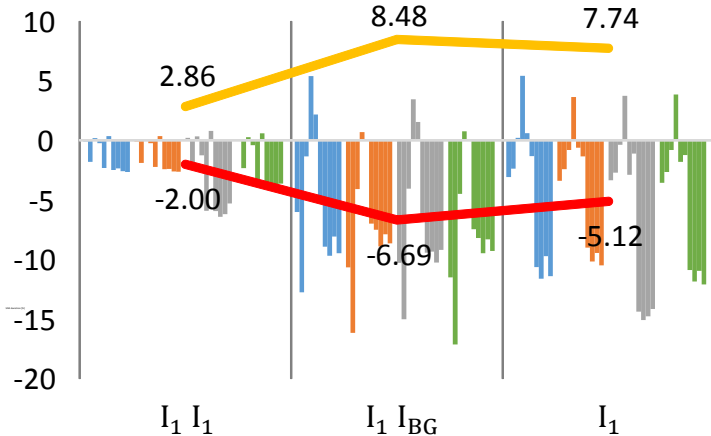
**‘NLF, avg’ (Grey):** If noise is calculated from a noise-level-function, but background areas are included in the averaging, the averaged SNR is underestimated because of low SNR values (around 1) in background areas.

**‘cN, avg’ (Green):** This method likewise underestimates the noise and the signal level. It is a fast and simple alternative that slightly underestimates the SNR (around 11%) compared to ‘NLF, xBG’.

### 3.2.5.2 DATA QUALITY

Two equivalent EL images ( $I_1$ ,  $I_2$ ) and a background image ( $I_{BG}$ ) are not always available for SNR measurement. The associated error relative to a full image set is shown in Figure 3.19 for the same 10 EL image sets as used for Figure 3.18. The bar colours correspond to the ones used in Figure 3.18 with blue representing ‘NLF, xBG’.

For ' $I_1 I_2$ ' only the background image was missing. For ' $I_1 I_{BG}$ ' the second EL image was missing and for ' $I_1$ ' only one EL image was used for SNR calculation.



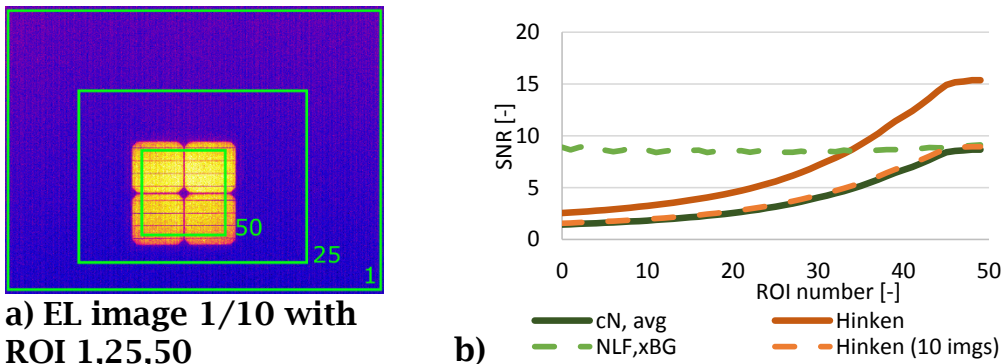
**Figure 3.19: SNR deviation due to the use of different image sets relative to the full image set ( $I_1, I_2, I_{BG}$ ); average (red) and RMSE (yellow)**

Figure 3.19 shows that the individual deviation between the different discussed noise and averaging methods within the same image set is very similar. The SNR deviation is therefore more dependent on the available image set than on the method of calculation. The SNR deviation is mostly negative. This is beneficial since it means that an SNR determined with less than the proposed three images is known to (on average) underestimate the actual result. The deviation is smallest for the image set ' $I_1 I_2$ '. This means that the error from noise estimation using only one image has a bigger influence than the error from background level estimation (method 'NB Med7, min', Subsection 3.1.3).

### 3.2.5.3 PERFORMANCE IN COMPARISON TO HINKENS SNR

Two SNR parameters from the previous Subsection 3.2.5.1 ('cN, avg' and 'NLF, xBG') were chosen for a comparison (Figure 3.20) to the SNR defined by Hinken et al. (Equation 3.4). Similar to Figure 3.17 the SNR was calculated for ROIs with decreasing background ratio. Two background

corrected EL images were used for all SNR parameters, excluding ‘Hinken 10 imgs’ in which were used 10 EL images, taken in series.



**Figure 3.20: Comparison of two SNR parameters proposed in this section with the SNR defined by Hinken et al. (Equation 3.4)**

SNR ‘NLF, xBG’ is the only parameter, which remains stable for different ROI sizes. All other parameters increase for decreasing ROI sizes, indicating a background sensitivity. For ROIs smaller than or equal to the size of the PV module (ROI 46-50) most SNR remain constant and are practically identical. Only Hinkens SNR executed on two EL images overestimates the SNR for all ROI. These results allow the following conclusion:

- SNR ‘cN, avg’ (Equation 3.16) returns the same values as Hinkens SNR (if executed on 10 images) but using only two EL images. A representative SNR should be calculated from an ROI without background areas.
- SNR ‘NLF, xBG’ leads to similar results but is not influenced by background area.

### 3.2.6 SECTION SUMMARY

This section discussed different methods to calculate signal and noise ratio (SNR) using one to three EL images. Methods to filter the signal from erroneous values were presented.

It was proposed to calculate the SNR from two EL images taken in series and one background image with the same exposure time. If only one EL

image and/or no background image are available, the SNR will be underestimated up to -7%. The proposed SNR algorithm includes background exclusion (xBG) and the determination of a noise-level-function (NLF). The NLF describes noise as standard deviation over image intensity.

However, the implementation of NLF and xBG is not trivial. A simplified SNR using a constant noise level and a spatial average (Equation 3.16) was found to underestimate the SNR by -11%. For this parameter, it is suggested to exclude background areas from the calculation. The current IEC 60904-13 draft suggests this method to measure image quality [46]. The SNR map represents a major part of the intensity uncertainty of raw EL images (Section 6.1). For the case of two available EL images ( $I_1, I_2$ ) and one background image ( $I_{BG}$ ), it is proposed to calculate an SNR map as follows:

$$SNR_{NLF} = \frac{S_{cor}}{NLF(S_{cor})} \quad (3.17)$$

$$S_{cor} = FILTER(0.5 \cdot (I_1 + I_2) - I_{BG}) \quad (3.18)$$

Herein the NLF should be fitted using Equation 3.14 and noise should be extracted from a difference image using Equation 3.12. *FILTER* describes a spatial noise filter. A simple, yet effective method using a median filter (kernel size = 3x3 px) and a more powerful combined filter (Figure 3.15) are proposed. Spatial resolved SNR (Equation 3.17) are further applied in Subsection 7.2.3.2 to map uncertainty. Its spatial average (using xBG) is used in Subsection 7.2.1.2 for image quality comparison.

### 3.3 Best Focus Determination

Many EL camera systems use a manually focused lens in which the best sharpness is estimated by subjective comparison of images at different focus levels. In order to find the optimum focus, a parameter quantifying

the focus level can be helpful. Pertuz et al. compare various focus parameters obtained from a single image to their robustness to noise, image contrast, saturation and window size [63]. He concludes that Laplacian-based operators have the best overall performance but also that the operator performance depends strongly on the imaging setup. A selection of four promising parameters was chosen from this source for application to EL images. Two different CCD cameras (A, B) and four different PV technologies were compared. The focus level was manually changed to obtain 9 to 13 focal points before and behind the image plane. A sharp image was expected to be at position 5-7. Lower or higher positions should increasingly blur the image. The comparison (Figure 3.21) shows that the gradient-magnitude-based ‘Tenengrad’ is the only parameter with the expected single maximum, indicating best focus. The Tenengrad of an image ( $I$ ) is defined as follows:

$$\text{Tenengrad}(I) = \text{mean}({G_x}^2 + {G_y}^2) \quad (3.19)$$

$$G_x = \begin{bmatrix} -1 & 0 & +1 \\ -2 & 0 & +2 \\ -1 & 0 & +1 \end{bmatrix} \otimes I \quad \text{and} \quad G_y = \begin{bmatrix} -1 & -2 & -1 \\ 0 & 0 & 0 \\ +1 & +2 & +1 \end{bmatrix} \otimes I \quad (3.20)$$

$G_x$  and  $G_y$  are the approximated horizontal and vertical image gradients obtained from convolution ( $\otimes$ ) of an image with a 3x3 kernel (Sobel operator [64]).

The trend of the absolute Tenengrad for all different focus levels (Figure 3.21a) is shown in Figure 3.22. The value range differs between the examined images. Therefore, Tenengrad cannot be used to calculate the absolute image sharpness. For this, different methods are detailed in Section 3.4.

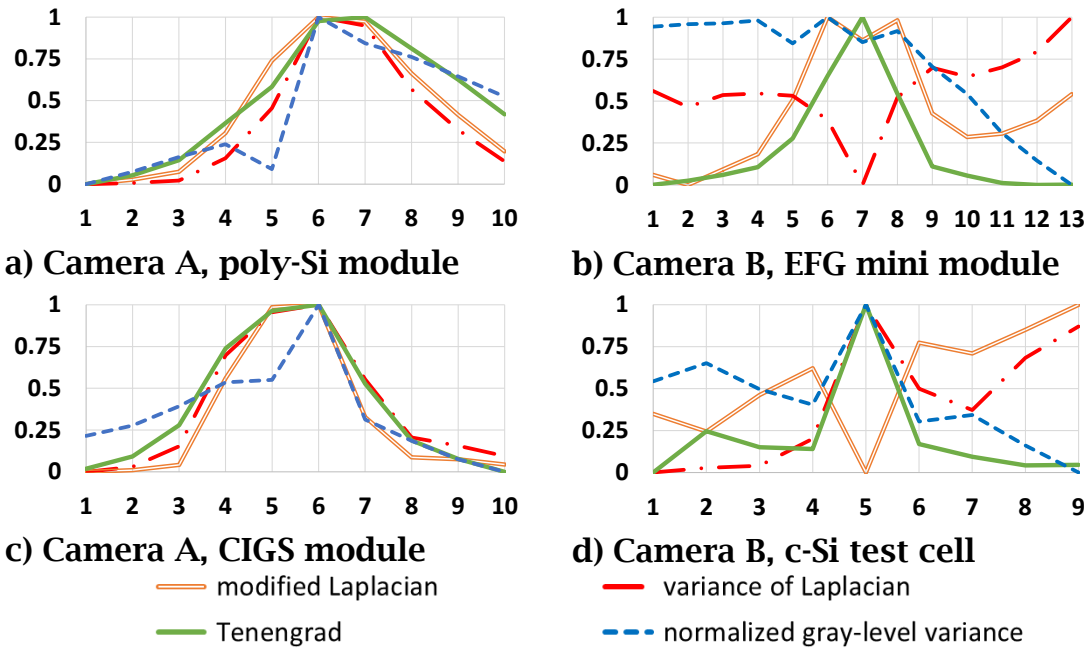


**Figure 3.21: Comparison of four focus parameters on two cameras and four PV technologies on 9 to 13 focus positions; all values normalised to their maximum**

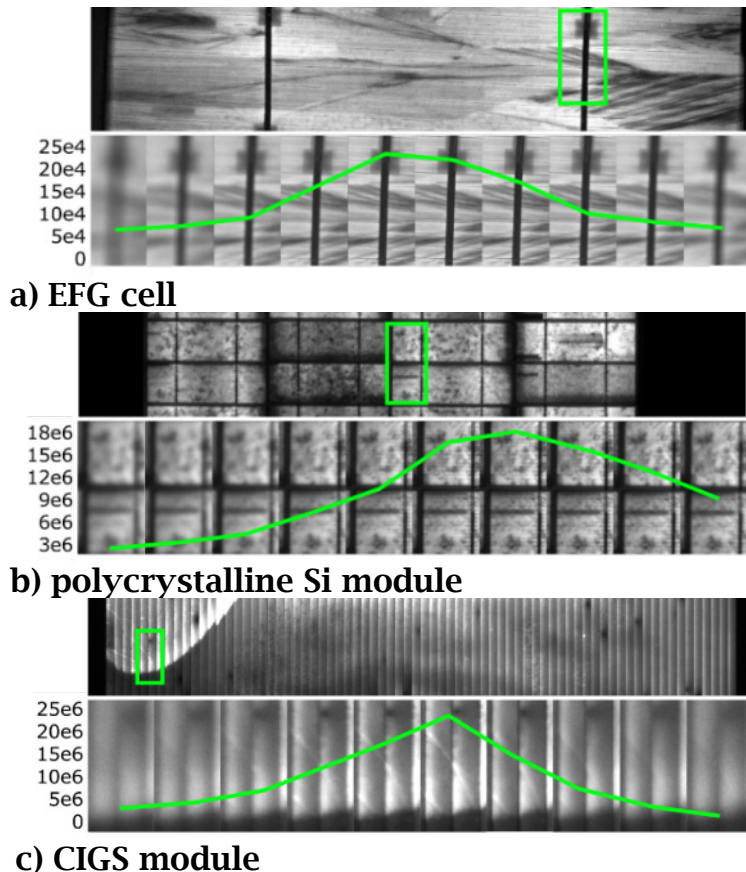


**Figure 3.22: EL image images at different focal positions; green box: area of image detail; green plot: absolute Tenengrad of the image detail**

## 3.4 Image Sharpness

Every camera based measurement system, including electroluminescence imaging, is prone to blur. The precise determination of sharpness can be used to define the resolvable object size, to measure position uncertainty, to sharpen images and to compare images. This section provides procedures for quantifying and measuring image sharpness without the need for specialised measurement equipment. Five different approaches to measure the modulation transfer function (MTF) and point spread function (PSF) on synthetic patterns and EL images are discussed. If the PSF is defined by its standard deviation, the measurement results differ less than  $\pm 5\%$  in the majority of cases. A parameter defining the smallest resolvable object size ( $s_{obj}$ ) is introduced. It enables direct scaling of the effective resolution of different imaging systems and thus opens the possibility to compare images with much higher precision. With this, detailed fault analysis of PV devices from different EL imaging systems becomes possible.

### 3.4.1 INTRODUCTION

Even taken in focus, luminescence images remain somewhat blurred due to the remaining focal mismatch, diffraction, chromatic aberration, photon scattering, light trapping and electrical smearing [65–67]. The Tenengrad parameter can be used as a scene dependent sharpness measure to determine the best camera focus (Section 3.3). In contrast to this, this section focusses on the measurement of scene independent sharpness parameters.

The absolute image sharpness is essential to:

- Classify the quality of a measurement system.
- Sharpen images using deconvolution.
- Calculate the position uncertainty of the EL signal.
- Quantitatively compare images acquired by different labs (Section 3.4.6).

- Determine whether features (cracks, disconnected fingers) can actually be resolved (Subsection 3.4.6.2).

The latter problem can be explained with the following example: If EL images of the same device but taken with different imaging systems are analysed, the image resolution or sharpness can differ. These differences can lead to artefacts in the difference image (Figure 3.23), making a comparison difficult or impractical.



**Figure 3.23: Explanatory line plots along the same edge in a sharp and a blurry image (A,B); Difference image (A-B)**

Figure 3.24 shows two EL images (A,B), taken at different times during an accelerated ageing test. Both images show the same cell, but have a different resolution ( $r$ ) and sharpness, defined by the standard deviation of a Gaussian blur kernel ( $\sigma_G$ ).

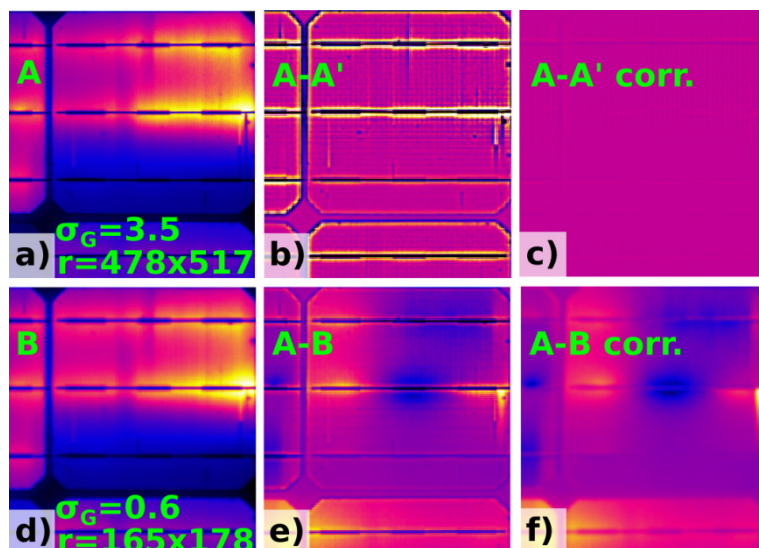


**Figure 3.24: EL images A,B (a,d) and their differences without (b,e) and with sharpness correction (c,f); colour scale is identical for (b,c) and (e,f)**

A difference of both images (e) or image (A) with different  $r$  and  $\sigma_G$  values (b) shows that high gradient variations such as cell edges, busbars or disconnected fingers distort the difference image. After both images are brought to the same (lower) sharpness level (Subsection 3.4.6.3), only signal changes remain (c,f).

This section gives an overview of relevant sharpness functions and parameters used to classify EL images. Thereafter, two sharpness novel measurement methods are introduced and compared with three (partly modified) methods from literature. Finally, an algorithm is introduced to equalize absolute sharpness of images even at different image resolutions and blur.

### 3.4.2 SHARPNESS FUNCTIONS

The sharpness measurement methods in Subsection 3.4.4 are based on different functional expressions of image sharpness. Description and conversion of these functions is content of this subsection.

#### 3.4.2.1 POINT SPREAD FUNCTION

The point spread function (PSF) describes the response of an imaging system to a point source (convolution, Figure 3.25). Its inverse, image deconvolution, can be used to increase the image contrast and quality.

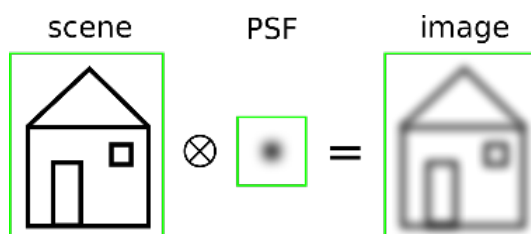


**Figure 3.25:** Image as convolution of an object or sharp image with a PSF

### 3.4.2.2 LINE SPREAD FUNCTION

The line spread function (LSF) is the 1D integral of the 2D PSF along a specified angle or edge orientation ( $\alpha$ ) with  $R$  being its rotation matrix:

$$LSF_\alpha = \int R \times PSF(x, y) dx \quad R = \begin{bmatrix} \cos(\alpha) & -\sin(\alpha) \\ \sin(\alpha) & \cos(\alpha) \end{bmatrix} \quad (3.21)$$

For a representative LSF, the result has to be averaged for multiple angles:

$$LSF = \text{mean}_{\alpha=0}^{\alpha=2\pi}(LSF_\alpha) \quad (3.22)$$

The inverse operation  $PSF = fn(LSF)$  is detailed in [68].

### 3.4.2.3 MODULATION TRANSFER FUNCTION

The performance of an imaging system is often evaluated using the modulation transfer function (MTF) [69]. It describes the change of contrast of a number of black and white lines (resp. cycles) per length or cycle frequency (cy). That frequency is often expressed relative to pixel size [ $\frac{cy}{mm}$ ] or picture height [ $\frac{cy}{PH}$ ]. In this section, the MTF is defined as the number of cycles per pixel [ $\frac{cy}{px}$ ] since the physical length [mm] is separated in Equation 3.31. The theoretical maximum frequency, according to the Nyquist sampling theorem is  $0.5 \frac{cy}{px}$  (one line every two pixels) [70].

The popular spoke pattern for sharpness measurement is shown in Figure 3.26. MTF measurements follow the principle of measuring maximum ( $I_{pmax}$ ) and minimum ( $I_{pmin}$ ) intensities on circles of different radii around the pattern centre and calculating the relative contrast as follows:

$$y_{MTF} = \frac{I_{pmax} - I_{pmin}}{I_{pmax} + I_{pmin}} \quad (3.23)$$

The MTF measurement procedure is further described in [71].

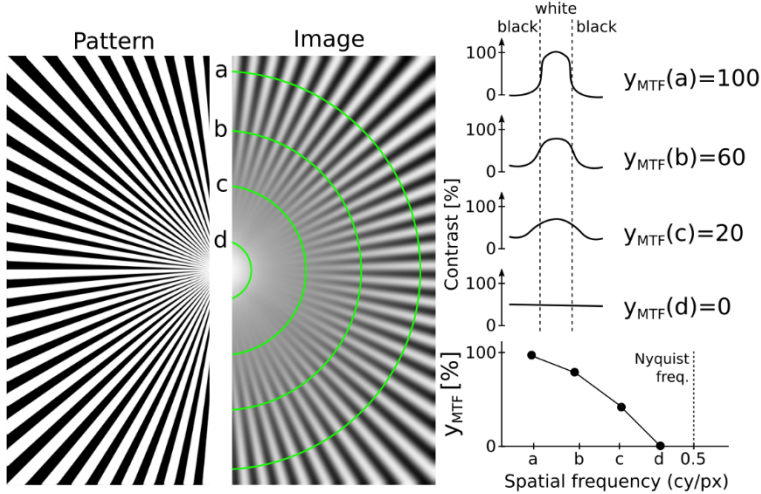


**Figure 3.26: Spoke target (left), its image (middle) and example line plots (top right) used to calculate the MTF (bottom right)**

The MTF can also be obtained from the absolute of the complex Discrete Fourier Transform (DFT) of the LSF [72]:

$$MTF = |\text{DFT}(LSF)| \quad (3.24)$$

In this conversion, information regarding the phase shift (phase transfer function, PhTF) from the LSF is lost. Together, phase shift and modulation build up the optical transfer function (OTF). Therefore, to obtain the LSF back from a MTF, the PhTF will be assumed to be coequally increasing for increasing spatial frequencies:

$$PhTF = \frac{\pi}{n} [0, i, -(i+1), (i+2), -(i+3), \dots]_{i=0}^{i=n} \quad (3.25)$$

$$OTF = MTF \cdot e^{\sqrt{-1} \cdot PhTF} \quad (3.26)$$

$$LSF = \text{DFT}^{-1}(OTF) \quad (3.27)$$

Where:

---

$n$	Number of MTF data points
-----	---------------------------

---

### 3.4.3 SHARPNESS PARAMETERS

#### 3.4.3.1 STANDARD DEVIATION OF A GAUSSIAN PSF ( $\sigma_G$ )

Often the PSF of cameras used for EL is assumed to be a radially-symmetric Gaussian distribution [67, 73]. In this case the PSF is fully defined by its standard deviation ( $\sigma_G$ ).

#### 3.4.3.2 LINE-WIDTH AT HALF CONTRAST ( $w_{50}$ )

$w_{50}$  is the width of a line within a line pattern that is still resolved with half its contrast (Figure 3.27). It can be obtained from the spatial frequency at which MTF is at 50% ( $MTF_{50}$ ):

$$w_{50} = \frac{1}{2 \cdot MTF_{50}} \quad (3.28)$$

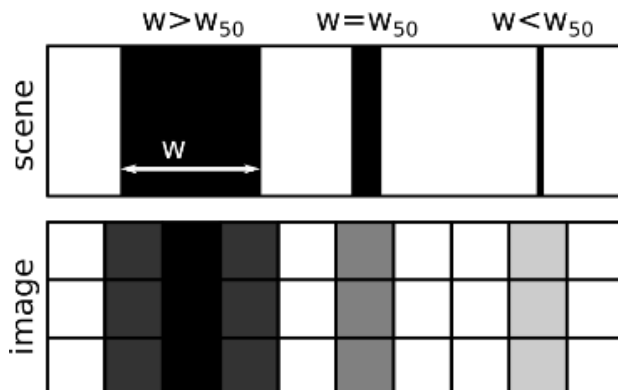


**Figure 3.27:** Different line widths ( $w$ ) of an imaged scene will be resolved with different contrast levels.

If the PSF is assumed to be Gaussian distributed,  $w_{50}$  can be obtained numerically from  $\sigma_G$ . For  $\sigma_G > 1.15$  px the relationship is directly proportional (Equation 3.29):

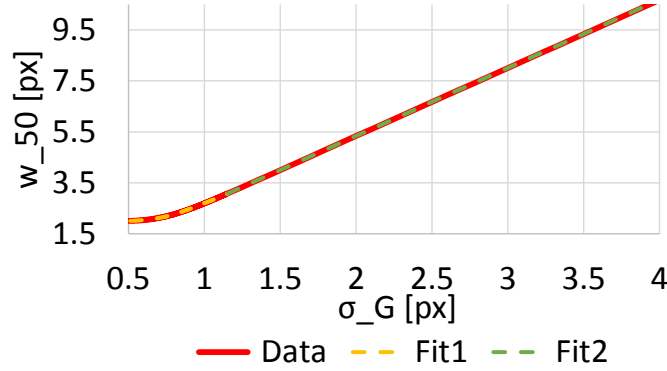


**Figure 3.28: Numerically calculated relationship between  $\sigma_G$  and  $w_{50}$ . Both fit equations described in Equation 3.29**

$$w_{50}(\sigma_G) = \begin{cases} 2, & \sigma_G < 0.5 \\ \sum c_j \cdot \sigma_G^j, & 0.5 \leq \sigma_G < 1.15 \\ \frac{\sigma_G}{0.3746}, & \sigma_G \geq 1.15 \end{cases} \quad (3.29)$$

Where:

$j$	4	3	2	1	0
$c_i$	-2.234	5.534	-2.206	-0.832	2.415

### 3.4.3.3 SMALLEST RESOLVABLE OBJECT SIZE ( $s_{obj}$ )

When referring to the number of resolvable features in an imaging system, the size of a pixel ( $s_{px}$ ) is a common metric. It can be obtained from the width of the imaged scene ( $w_I$ ) and the resolution in x-axis ( $r_x$ ).

$$s_{px} = \frac{w_I \text{ [mm]}}{r_x \text{ [px]}} \quad (3.30)$$

However, even when in focus, image digitalization and lens diffraction limit the sharpness of an imaging system. A more suitable parameter introduced in this work is the smallest resolvable object size ( $s_{obj}$ ). It is defined as pixel size of a perfectly sharp image that resolves the same information as the blurry image taken. It can be obtained from scaling  $s_{px}$  with the resolution factor ( $f_{res}$ ):

$$s_{obj} = f_{res} \cdot s_{px} \quad (3.31)$$

Images of the same  $s_{obj}$  resolve their image scene to the same quality (Figure 3.29). This is important when evaluating images of different resolution and sharpness.

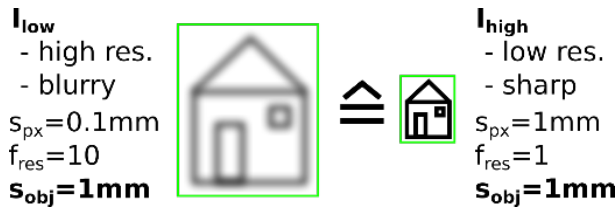


Figure 3.29: Schematic of the concept of smallest resolvable object size

### 3.4.4 SHARPNESS MEASUREMENT

#### 3.4.4.1 MASKING EL DEVICES

A major difference between conventional optical imaging and EL is the light source. In conventional images, the captured light is reflected from a light source (sun or artificial light); whereas EL measures the light source itself. Therefore, transmittance rather than reflection patterns must be measured for EL image quality assessment.

These patterns can be made by masking the measured device with a flat, opaque object or by putting a printed (paper) mask on top of the device.

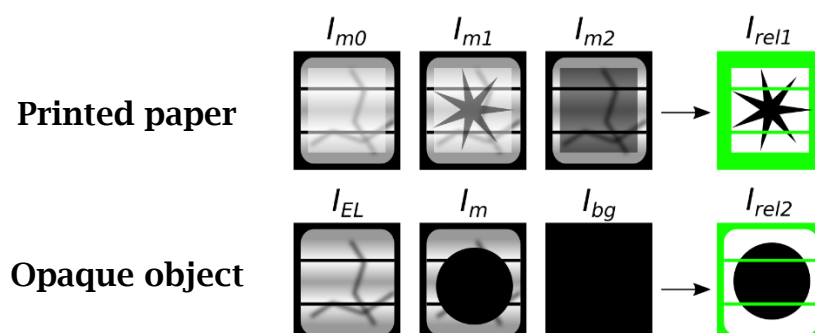


Figure 3.30: Schematic of the formation of a relative image from multiple (un-)masked EL images; the green areas are not suitable for sharpness measurement

A relative image, scaled from 0-1, can then be calculated as follows:

$$I_{rel1} = \frac{I_{m1} - I_{m2}}{I_{m0} - I_{m2}} \quad (3.32)$$

$$I_{rel2} = 1 - \frac{I_{EL} - I_m}{I_{EL} - I_{bg}} \quad (3.33)$$

#### 3.4.4.2 METHOD A: LSF MEASUREMENT USING EDGE SPREAD

Three papers, written by Walter, Teal, Breitenstein et al. determine the PSF as a transformation of a measured LSF, taken from a wafer edge or a masked area on top of a wafer [66, 68, 74]. This measurement neglects radial variation of the PSF but calculates the point spread even for larger distances (up to 500 px) from the edge. Since EL intensity deviations influence the measurement and a uniform emitter might not be available (for instance sharpness measurement on thin film devices), this method is applied to the relative image ( $I_{rel2}$ ) rather than the image itself.

#### 3.4.4.3 METHOD B: MTF MEASUREMENT USING V-CUT

A opaque material (such as two metal plates or metal tape) is placed on a PV device and forms two sharp, crossing edges (Figure 3.31a). The pixel intensity along the red line ( $L_2$ ) does not change abruptly from bright to dark towards the intersection of both edges ( $L_1, L_3$ ). Instead, the blurriness of the image mitigates this transition (Figure 3.31e).

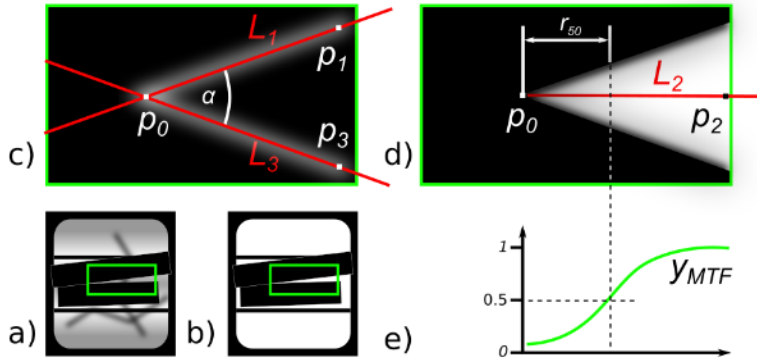


**Figure 3.31:** MTF measurement schematic for V-cut method; a) EL image; b) Relative image ( $I_{rel}$ ); c) Edge gradient image ( $G_{Edge}$ ) to detect edge lines ( $L_1, L_3$ ); d)  $I_{rel}$  detail; e) Image intensity along middle line ( $L_2$ )

The edge lines ( $L_1, L_3$ ) run through the local maxima of an edge gradient image (Figure 3.31c), calculated from the first derivate (Sobel filter, Section 3.3) in horizontal ( $G_x$ ) and vertical direction ( $G_y$ ):

$$G_{Edge} = \sqrt{G_x^2 + G_y^2} \quad (3.34)$$

The MTF can be expressed as the image intensity from the intersection point ( $P_0$ ) towards ( $P_2$ ) over the inverse cut radian, defined by the distance from intersection ( $r$ ) and its angle ( $\alpha$ ):

$$x_{MTF} = \frac{1}{2 \cdot r \cdot \alpha} \quad (3.35)$$

$$y_{MTF} = I_{rel2}[\overline{P_0 P_2}] \quad (3.36)$$

Multiple measurements at different positions and rotation angles should be averaged in order to average out individual deviations. It was found that a bi-directional moving average is suitable to smooth the slope of  $y_{MTF}$  (Figure 3.32).

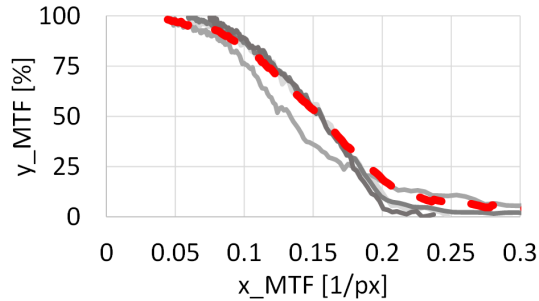


**Figure 3.32:** Example result of MTF obtained with 3 V-cut measurements; red: Averaged and smoothed result

In order to obtain a reliable measurement result, at least five measurements should be averaged. The opening angle ( $\alpha$ ) should be between three and five degrees. The optical conditions of this measurement deviate to a spoke-target-based measurement (method C). Therefore  $x_{MTF}$  has to be scaled accordingly. More information on measurement number, opening angle and  $x_{MTF}$  scaling can be found in Appendix 4.3.

#### 3.4.4.4 METHOD C: MTF MEASUREMENT USING SPOKE TARGET

In this method, the EL device is masked with a printed spoke target pattern (Figure 3.26). An additional glass plate, put on top of the paper, reduces the space between paper and PV device.

Since EL travels through the paper and glass, a contrast image using an unmasked and masked EL image results in an inhomogeneous and blurred relative image. Its MTF cannot be used. If however the relative image is created according to Equation 3.32, using a blank paper ( $I_{m0}$ ), the printed spoke pattern ( $I_{m1}$ ) and a fully black paper ( $I_{m2}$ ), its relative image ( $I_{rel1}$ ) is properly scaled between 0-1 and EL intensity deviations can be neglected (Figure 3.33).

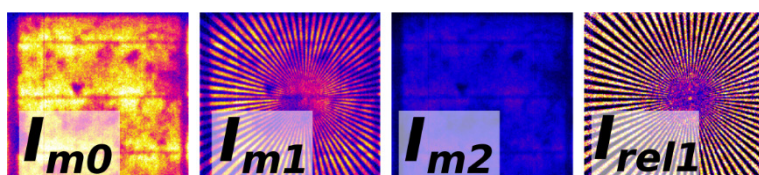


**Figure 3.33:** Different paper masks on top of a PV device and resulting relative image (right)

The spatial frequency ( $x_{MTF}$ ) is calculated by the ratio of cycles (number of bright and dark line pairs) around the circumference of a circle of a given radius ( $r$ ):

$$x_{MTF} = \frac{n_{cycles}}{2 \cdot \pi \cdot r} \left[ \frac{cy}{px} \right] \quad (3.37)$$

Since  $I_{rel1}$  is already scaled, Equation 3.23 simplifies to:

$$y_{MTF1} = I_{pmax} - I_{pmin} \quad (3.38)$$

However, the exclusive focus on maximum and minimum values causes an overestimation of the contrast if the peak value is not yet influenced by blur (Figure 3.34). In this case, contrast ( $y_{MTF}$ ) is better-defined using the mean of peak average (green/red areas), which improves extreme value behaviour of the MTF trend (see Section 3.4.4.2):

$$y_{MTF2} = \frac{I_{pmax} + \text{mean}(I_{high})}{2} - \frac{I_{pmin} + \text{mean}(I_{low})}{2} \quad (3.39)$$

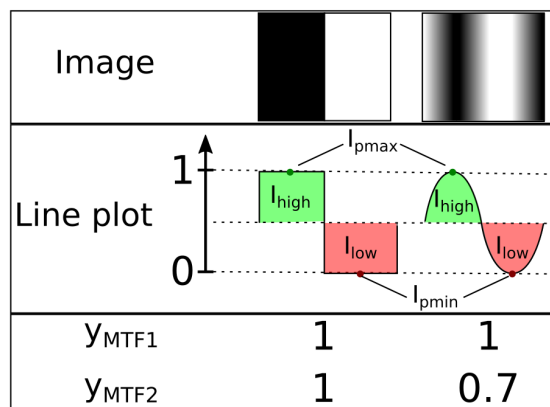


**Figure 3.34: Schematic of image contrast calculation using spoke target, referring to Equation 3.38 and 3.39**

Since  $y_{MTF2}$  is calculated from an average of every single pair of bright and dark lines, the resulting MTF has a higher accuracy and noise stability in comparison to the MTF obtained from the V-cut method B.

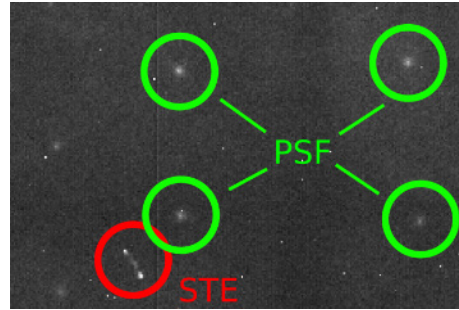
#### 3.4.4.5 METHOD D: PSF USING MULTIPLE PINHOLES

The PSF can be measured directly by imaging a point light source. This can be for instance a halogen lamp behind an aperture in a dark room [75]. However, its measurement should be within the luminescence wavelength range due to the wavelength dependency of the PSF.

A method for direct PSF measurement for module scale luminescence images was first suggested in [66]. It uses a single 100 µm pinhole to measure the PSF and a Lorenz fit to remove remaining noise. In this section, noise will be decreased by averaging up to 300 individual pinholes, each smaller than the pixel size. The pinholes were created with a needle piercing black flocked self-adhesive paper which was then taped onto a glass plate (Figure 3.35a). Figure 3.35b shows an EL image detail of the measurement at 200 s exposure time. The number of single-time-effects (STE) requires an image correction beyond simple background removal (Section 4.1). Hot pixels were removed as described in Section 4.4.



a) Light image of pinhole mask



b) EL image detail of PV device shining through pinholes, forming each a point spread function (green); red: single-time-effect (imaging artefact)

Figure 3.35: Example images Method D

After image correction, the local peaks were detected as values all higher than 20% of the image maximum above the background noise. A point-distance filter ensured that every pinhole-PSF was only detected once. To map all PSF on top of each other, the centre of gravity of each PSF was chosen as origin. Sub-pixel interpolation was performed using third order

spline interpolation. As Figure 3.36 shows, the averaging procedure is suitable to reduce residual noise, even at low SNR.

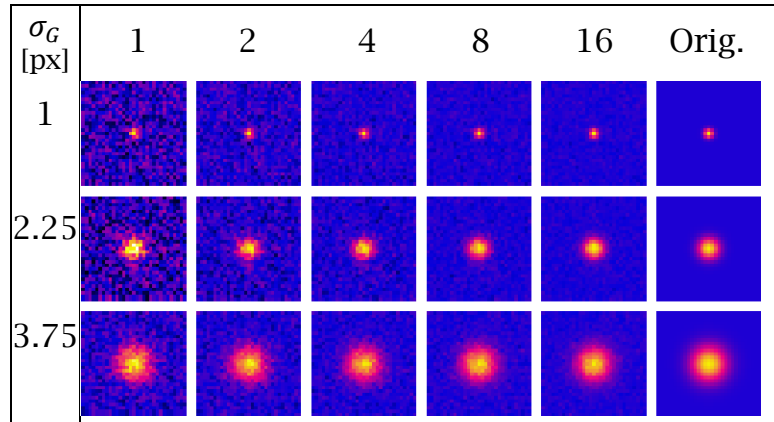


**Figure 3.36: Intermediate PSF from averaging 1 to 16 pinhole PSF at SNR=2; Last column: Gaussian input PSF**

The measurement error was determined for a synthetic pinhole pattern (Table 3.4D) which was blurred with a Gaussian PSF. The RMSE between input and measured PSF might not decrease for increasing numbers of averaged pinhole PSF (Figure 3.37) for low SNR and sharp images ( $\sigma_G \leq 1 \text{ px}$ ). For higher  $\sigma_G$  and/or higher SNR the error decreases by around one magnitude after 50 pinhole averages. After 300 averages, the error decreases by 1.5 magnitudes. This is in accordance to a  $\sqrt{n}$  decrease, as expected for averaging Gaussian distributions.

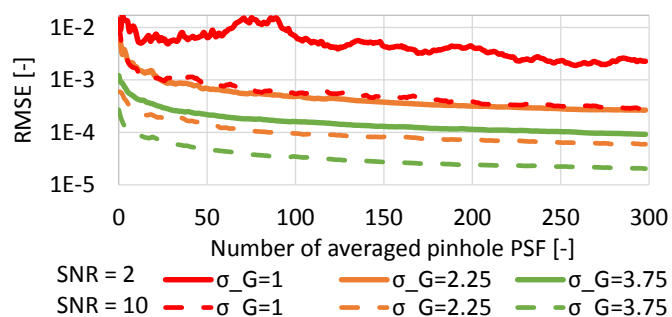


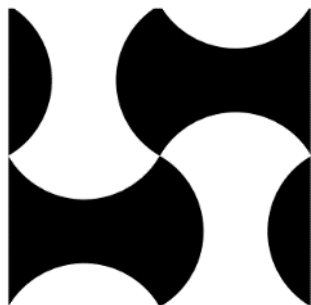
**Figure 3.37: Simulation of the measurement error (RMSE) for direct PSF measurement from averaging multiple pinhole PSF using a synthetic measurement pattern (Table 3.4, D)**

As the RMSE is always above zero it is clear that noise remains to a certain extent, despite averaging. It can be removed with different filter and

averaging algorithms, which are applied in the method comparison (Subsection 3.4.5). Their description however is beyond the scope of this section.

#### 3.4.4.6 METHOD E: PSF USING DISK MASK

As mentioned above, PSF recovery from a LSF assumes the PSF to be radially symmetric. This can lead to erroneous results (especially for image deconvolution). Instead of only measuring the LSF at a specified angle, Joshi et al. evaluate the LSF at all possible angles using a tiled calibration pattern (Figure 3.38a) [67]. For sharpness measurement on EL devices, the presented method E requires a flat, round, opaque object (such as a CD or disk shaped plate, Figure 3.38b).



a) As used by [67, 70]



b) Compact Disk, as used in this section

**Figure 3.38: Mask/pattern used to measure the LSF at different angles**

The following algorithm is used to recover the PSF from the edge spread around such an object:

Capture one EL image of a PV device without ( $I_{EL}$ ) and one or multiple images with added mask ( $I_m$ ) at different positions (Figure 3.39).

The mask should be flat, opaque and ideally unreflective. The mask can be either a round disk (Figure 3.39) or a round hole within a metal plate. Only the round disk method is discussed here. To calculate the PSF:

1. Calculate the relative image ( $I_{rel2}$ ) (Equation 3.33).
2. Remove lens distortion (Section 4.6).

3. Detect and cut out the area around circles.
4. Convert  $I_{rel2}$  to the polar coordinate system to obtain the edge spread function for variable angles ( $\alpha$ ) (Figure 3.40a). Set the origin to the circle centre.
5. Calculate the image gradient in the y-axis (Sobel filter) to obtain the line spread function ( $LSF$ ) (Figure 3.40b).
6. Normalize the  $LSF$ , so that  $\max(LSF, \alpha) = 1$
7. Create an initial  $PSF_{init}$  using an LSF average over  $\alpha$  using the method described in [68].
8. Obtain the desired  $PSF_{disk}$  by minimizing the following function:

$$\arg \min_{PSF_{disk}} \{ \text{sum}(PSF_{disk}, \alpha) - LSF(\alpha) \} \quad (3.40)$$

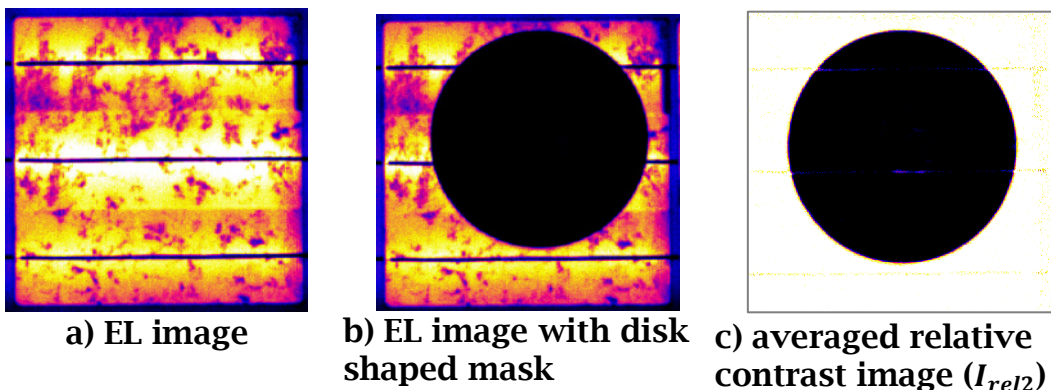


Figure 3.39: Masking a PV cell using a disk

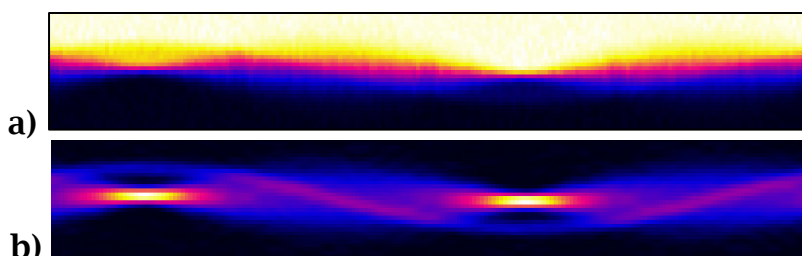
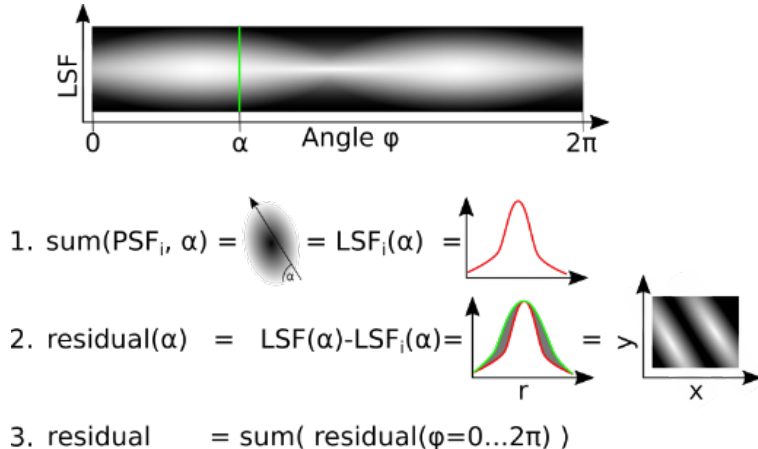


Figure 3.40: Example edge spread function (a) and its derivate, a line spread function (b) for variable angles (along x-axis) for PSF(B) shown in Figure 3.42

To further clarify Equation 3.40, the calculation of the residual (to be minimised in order to find  $PSF_{disk}$ ) is shown in Figure 3.41. Step 1 below shows the sum along an angle ( $\alpha$ ) of the PSF of the current iteration step

(i) to calculate the LSF. The difference between the calculated and measured LSF is then plotted along every angle used. The sum of all angle-residuals then gives the actual residual (step 3)



**Figure 3.41: Schematic calculation of the residual for one angle ( $\alpha$ ) and an intermediate  $\text{PSF}_i$**

The optimization problem is nonlinear. It is solved using the Jacobian-free Newton-Krylov method [76] and LGMRES as linear solver [77]. For all test cases, the solver converged after less than 5 iterations.

The proposed method is verified using different generated PSFs as follows:

1. Generate multiple  $\text{PSF}_{orig}$  (kernel size = 31 px)

For every PSF:

2. Draw a black circle into a white 500x500 px array.
3. Convolute that array using the generated  $\text{PSF}_{orig}$  (Figure 3.25).
4. Add Gaussian noise to the array, regarding SNR of 30.
5. Calculate  $\text{PSF}_{out}$  using the proposed method.
6. Compare the RMSE for  $\text{PSF}_{disk}$  and  $\text{PSF}_{init}$  to  $\text{PSF}_{orig}$  as:

$$C_{improv} = 100\% \cdot \frac{\text{RMSE}_{disk} - \text{RMSE}_{init}}{\text{RMSE}_{disk} + \text{RMSE}_{init}} \quad (3.41)$$

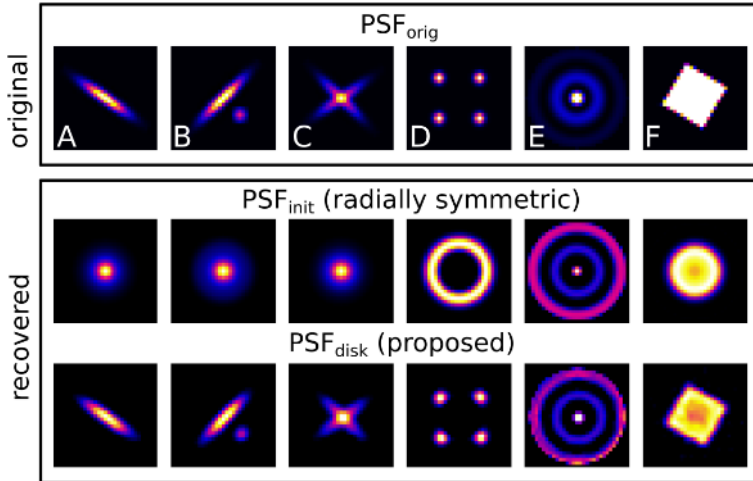


**Figure 3.42: Comparison of different original and recovered PSF**

As shown in Figure 3.42, the shapes of all PSF can be recovered using the proposed method. The more a PSF deviates from a radially symmetric shape the higher is the improvement from this method in comparison to that in [68] (Table 3.3).

**Table 3.3: RMSE of recovered to original PSF and improvement from the proposed method, relative to the radially symmetric  $PSF_{init}$  in [68]**

A	B	C	D	E	F
$RMS_{disk}$ [%]					
0.07	0.16	0.11	0.22	3.40	0.06
$C_{improv}$ (mask=disk) [%]					
57.6	21.2	16.1	29.3	0.2	15.2
$C_{improv}$ (mask=hole) [%]					
30.0	22.8	18.2	26.7	0.1	10.9

Both mask types (disk or round hole) improved the result relative to the radially symmetric approach in [68]. On average  $C_{improv}$  is higher if a disk shaped mask is used. It is assumed that a disk is advantageous to a hole due to the larger signal fraction leading to a higher SNR across the blurred edge.

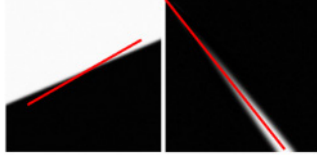
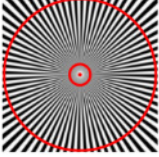
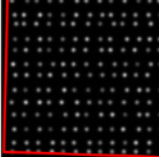
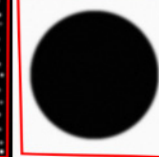
Excluding PSF(E), the RMSE of all recovered PSF is far below one percent. This indicates the successful recovery of the original PSF. However, the intensity distribution from PSF(E) centre to border does not decrease as should in both  $PSF_{disk}$  and  $PSF_{init}$ . This shows certain PSF shapes (in this case an airy disk) will not be fully recoverable. Further investigation regarding shape limitation would be necessary, but is outside of the scope of this work.

### 3.4.5 COMPARING SHARPNESS MEASUREMENT METHODS

#### 3.4.5.1 VALIDATION ON SYNTHETIC PATTERNS

In order to validate the ability to measure sharpness using the methods discussed in the previous section, the methods were executed on synthetic patterns of a defined noise level and blurriness (Table 3.4). All guide lines or distances given to the computer algorithm were approximate since the precise position of pattern features is calculated by the algorithm itself.

**Table 3.4: Example synthetic patterns and given guide lines (red) used for validation (SNR=30, pattern size=501x501 px)**

Method	A	B	C	D	E
Pattern					
Output	LSF	MTF	MTF	PSF	PSF

The synthetic patterns were blurred with a radially symmetric PSF of a standard deviation ( $\sigma_G$ ) between 0.5 and 4.5 px. The measured sharpness parameters were then transformed back to  $\sigma_G$  and plotted against each other for two different image noise levels (Figure 3.43).

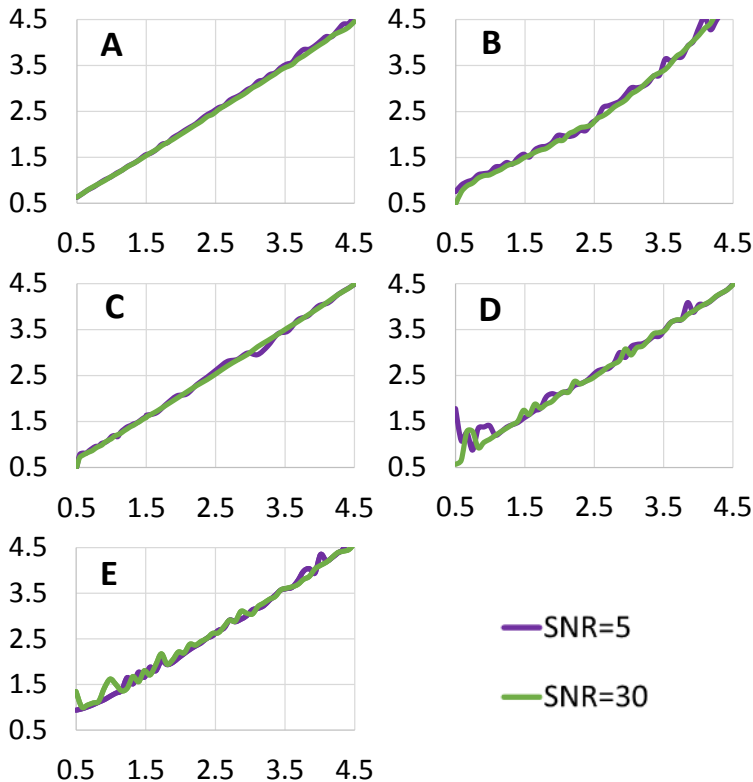


**Figure 3.43: Output vs input  $\sigma_G$  values for sharpness measurement method A-E applied to synthetic patterns shown in Table 3.4**

It was observed that all methods were able to recover the defined image sharpness to a certain extent. Methods A and C give the most accurate results. Method B slightly overestimates  $\sigma_G$  for values above 3.5 px. For  $\sigma_G < 1$  px method D can return values which are too high, especially for low SNR. This is due to noise affecting the detection of the pinhole centre of gravity in each individual PSF. This spatial variation results in erroneously larger averaged PSF.

A direct comparison of the performance of the individual sharpness methods for three different  $\sigma_G$  is given in Figure 3.44. Therein, the MTF measured with method A-E was plotted with the one directly obtained from the Fourier transform of an LSF defined by the input  $\sigma_G$  (Equation 3.24). For all three  $\sigma_G$ , method B underestimates the contrast below 50%. This is because in this method only one bright line blurs into the background instead of the successively decreasing line widths of white and black lines (method C). Again, the resulting MTF of method A and C are closest to the original and both direct PSF measurement methods D

and E underestimate the MTF and therefore underestimate the image sharpness. The relative deviation of method E is below 5% for  $\sigma_G$  at 2.25 px and above.

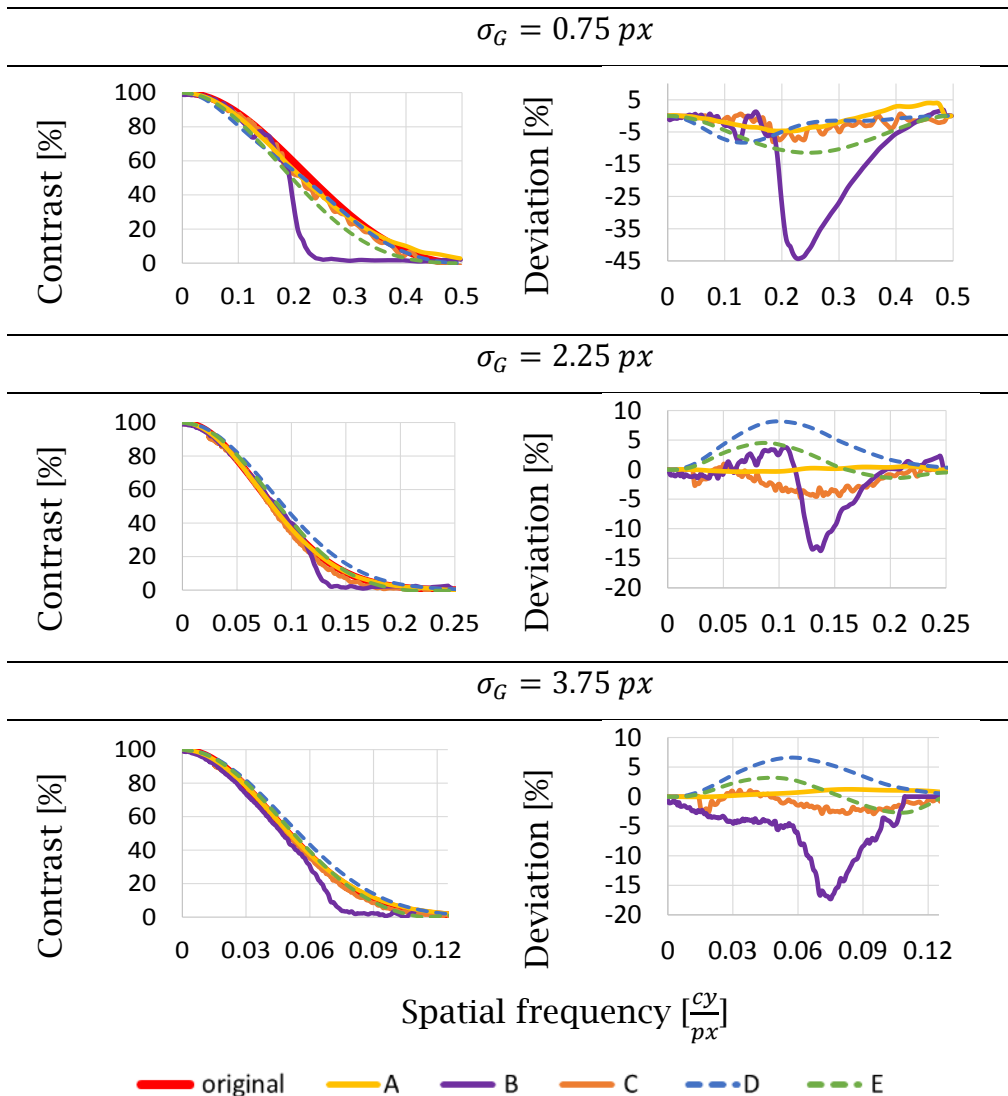


**Figure 3.44: Calculated modulation transfer functions (MTF, left) and their relative deviation (right) from the reference MTF (red)**

### 3.4.5.2 VALIDATION ON EL IMAGES

Method A-E were also evaluated on an EL imaging system for PV modules. The camera focus was set to three different focal points F1-F3 (Figure 3.45).

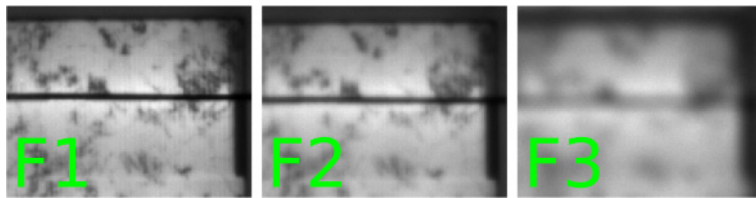


**Figure 3.45: Camera focus used for comparison of sharpness measurement methods A-E**

In addition to dark current and un-masked EL image, one to four images were taken with masks added on top of the poly-Si module. The PV module was masked with flat metal plates (method A, B), a blank and two printed papers (method C), black-flocked paper, punctured with a needle to create ca. 300 pinholes and adhered to a glass plate (method D) as well as with a CD which is opaque in the IR (method E).

**Table 3.5: Image setup to evaluate measurement method A-E**

Method	A	B	C	D	E
Masked EL image (excerpt: Method D)					
Number of images	1	4	1	2	1
Exposure time [s]	20	20	20	200/ 400	20
Patterns/image	10	2	1	1	1

The MTFs obtained from the imaging setups shown in Table 3.5 are detailed in Figure 3.46. In order to test under real life conditions, the exposure time of 20 s (excluding method D) was set short on purpose to get a comparatively low SNR of 30 for the EL images. The method to calculate the SNR used one EL and one background image. This method is described as 'NLF, xBG' in Section 3.1.

In contrast to the theoretical evaluation discussed before, in this measurement the actual image sharpness is not known. Therefore, the deviation (Figure 3.46, right) is relative to the average of all the methods. For F1 and F2, all methods return similar MTFs with deviations mostly

below 10%. Only method B produces an obviously incorrect result for the heavily blurred F3.

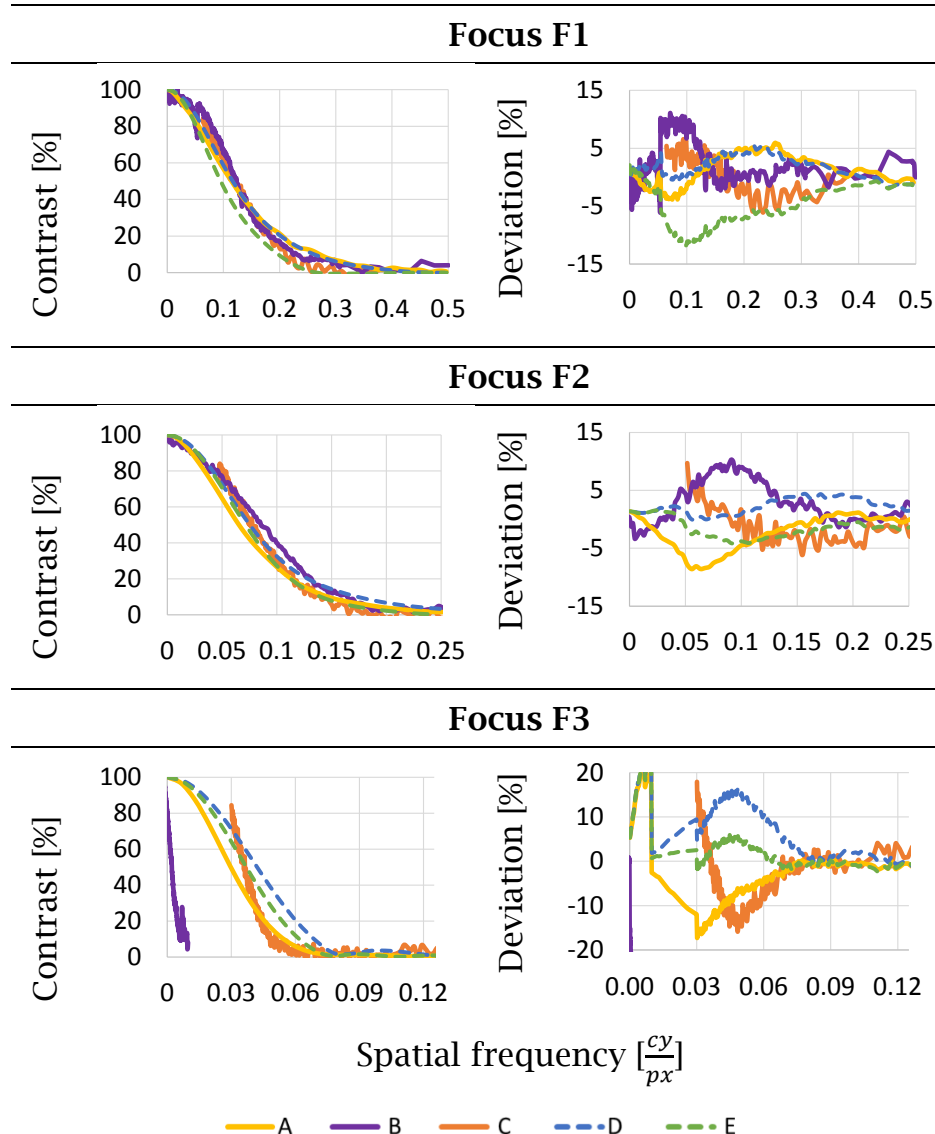


**Figure 3.46: Calculated modulation transfer functions (left) and their relative deviation (right) from the reference MTF (red)**

Method A and B have the highest deviations relative to the average, whilst deviations for method C and E are lowest. Image sharpness is underestimated for the sharpest focus F1 with method E. This might be caused by reflections between DUT and disk. Figure 3.43 however shows that this overestimation can be found in synthetic data as well.

A qualitative comparison of the resulting PSF is shown in Figure 3.47.

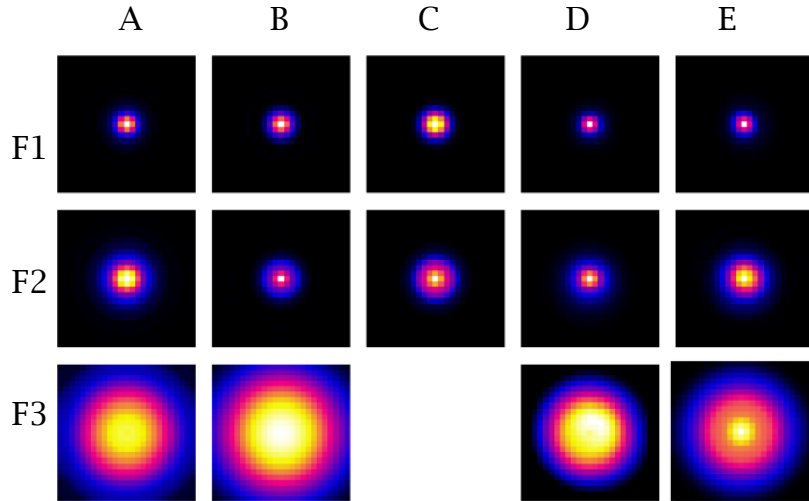


**Figure 3.47: Qualitative representation of directly measured or calculated PSF for focus F1-F3**

Since only method D and E measure the PSF, the PSF from the other methods was obtained from the transformations discussed in Subsection 3.4.2. All PSF were normalised relative to their maximum value. The general trend for increasing PSF for F1 to F3 can be seen for all methods. For method C, the spoke target was not big enough to capture the entire MTF at F3. Its slope had to be extrapolated because no contrast values existed above 85%. This resulted in the MTF increase being too steep. Therefore, the transformed PSF was much too small and excluded from comparison. A comparison of the three derived image sharpness parameters  $f_{res}$ ,  $\sigma_G$  and  $w_{50}$  is given in Table 3.6.

The application of PSF for image deconvolution is described in Section 4.5.

**Table 3.6: Comparison of image sharpness parameters for the imaging setup shown in Figure 3.45**

$f_{res}$	A	B	C	D	E
F1	3.1	2.9	2.9	2.8	3.2
F2	5.4	4.2	4.7	4.8	5.1
F3	12.2	(170)	9.9	8.6	9.8
$\sigma_G$					
F1	1.6	1.5	1.5	1.5	1.7
F2	2.9	2.2	2.4	2.5	2.6
F3	6.3	(87)	5.1	4.5	5.1
$w_{50}$					
F1	4.3	4.1	4.1	3.9	4.5
F2	7.6	5.8	6.4	6.6	7.0
F3	16.8	(233)	13.6	11.9	13.5
<b>Relative to average</b>					
F1	4.7%	-2.9%	-2.4%	-6.1%	6.9%
F2	13.9%	-12.9%	-4.0%	1.2%	4.1%
F3	20.5%	-	-2.5%	-14.8%	-3.2%

Within their individual limitations, all methods A-E can be used to measure image sharpness. In detail:

Method A: Introduced in [74], this method yielded results within the expected range. If the PSF is assumed radially variable, the measurement has to be repeated for different edge angles. Nevertheless, method A will only produce radially invariant PSF (Figure 3.42).

Method B: The simplicity of this method enables the measurement of the MTF without the need for specialised image processing software (Appendix 3). Only the image gradient and a plot of image intensities along a specified line are needed. However, this method requires multiple repetitions to reduce the error. An additional correction (Appendix 4.3.3) must be applied to acquire similar results to method C. In addition, the image contrast below 50% is mostly underestimated.

Method C: As the results indicate, this de facto standard for image sharpness measurement can be applied to EL imaging as well, using a relative image (Figure 3.30). With measuring peak minima, maxima and averages, this method cannot be executed easily by hand. The printed resolution of the pattern will additionally limit the application, especially

for high resolution EL (for instance on PV cells). Nevertheless, its noise stability and the small deviations relative to the other methods make this the preferred method for MTF measurement.

Method D: The results obtained with the only direct PSF measurement are within the expected range. However, 10-20 times longer exposure times were required to reach a sufficient SNR. Additionally, the need for the measured pinholes to be smaller than pixel size can cause problems when measuring small scale or high-resolution systems.

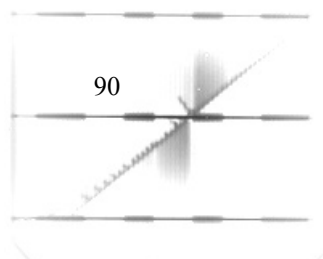
Method E: By evaluating the edge spread along the disk mask, this method can restore radially variable PSF without the need for long exposure times. The simple measurement setup and readily available round and flat objects (such as compact discs) make this method the preferred option for PSF measurement.

### 3.4.6 COMPARING IMAGES AT DIFFERENT SHARPNESS LEVELS

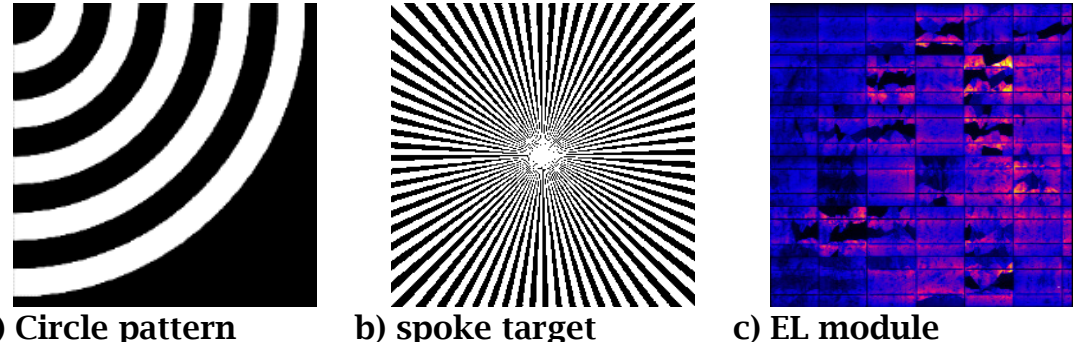
#### 3.4.6.1 RELATION BETWEEN RESOLUTION FACTOR AND IMAGE SHARPNESS

If it is assumed that a measured unsharp image can be described as a convolution of a sharp image with a Gaussian blur kernel (with  $\sigma_G$  as its standard deviation), the resolution factor  $f_{res}$  can be obtained as follows:

1. Generate a high resolution image ( $I_{high}$ , Figure 3.48) of resolution ( $r_{high}$ ).
2. Create  $I_{low}$  by down-sampling  $I_{high}$ , where  $r_{low} = \frac{r_{high}}{f_{res}}$ . Interpolate the pixel values of  $I_{low}$  using the pixel-area relation method [78].
3. Scale  $I_{low}$  back to  $r_{high}$  by up-sampling using bilinear interpolation. This creates a low quality image of the same size as  $I_{high}$ .
4. Find  $\sigma_G$  as the standard deviation of the Gaussian blur kernel, where the average absolute deviation (AAD) of a Gaussian filtered  $I_{high}$  to  $I_{low}$  is minimal. The AAD is used instead of the more common RMSE due to its higher stability towards outliers [57]:



$$\arg \min_{\sigma_G} \{AAD[\text{Gaussian}(I_{high}, \sigma_G) - I_{low}]\} \quad (3.42)$$



a) Circle pattern      b) spoke target      c) EL module

Figure 3.48: Patterns used for calculating  $\sigma_G$  for given  $f_{res}$

This linear optimization problem (Equation 3.42) was solved using the Brent method [79]. The results obtained from the three chosen patterns (synthetic and real images) follow the same trend (Figure 3.49). This validates the dashed fit where  $\sigma_G$  is directly proportional to  $f_{res}$  (for  $\sigma_G > 1$ ). For smaller  $\sigma_G$ ,  $f_{res}$  approaches 1 (i.e. no resolution change) in a combined logarithmic-linear relation (Equation 3.43).

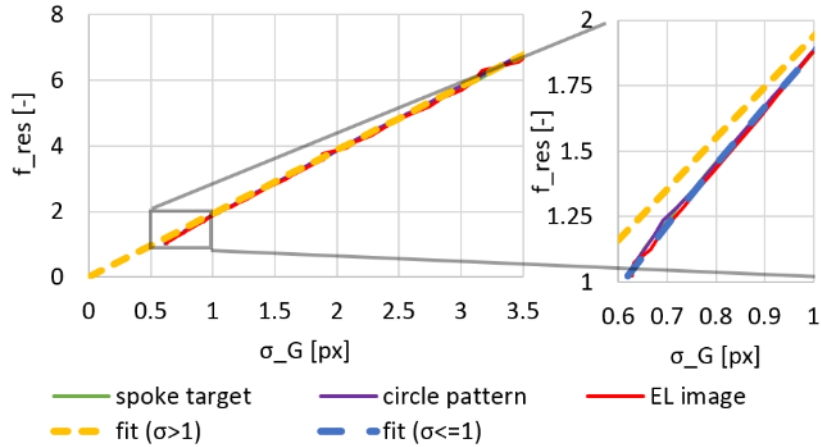


Figure 3.49:  $\sigma_G$  trend for different  $f_{res}$  using the patterns in Figure 3.48; yellow fit: Equation 3.43.

This allows the conclusion that for a known standard deviation of a Gaussian PSF ( $\sigma_G$ ) the equivalent resolution factor ( $f_{res}$ ) can be determined using:

$$f_{res}(\sigma_G) = \begin{cases} a \cdot \log_e(b \cdot \sigma_G) + c \cdot \sigma_G - d, & \sigma_G \leq 1 \\ e \cdot \sigma_G, & \sigma_G > 1 \end{cases} \approx 2\sigma_G \quad (3.43)$$

Where: **a**    **b**    **c**    **d**    **e**

0.591	10.482	1.494	1.005	1.937
-------	--------	-------	-------	-------

### 3.4.6.2 COMPARING BLURRED AND COEQUALLY SCALED IMAGES

To highlight the concept of object resolution, a PV cell (Figure 3.50) was either blurred with  $\sigma_G$  or coequally down-scaled using Equation 3.43 regarding equal  $s_{Obj}$  (Equation 3.31). It was observed that the quality of the displayed features is practically identical.

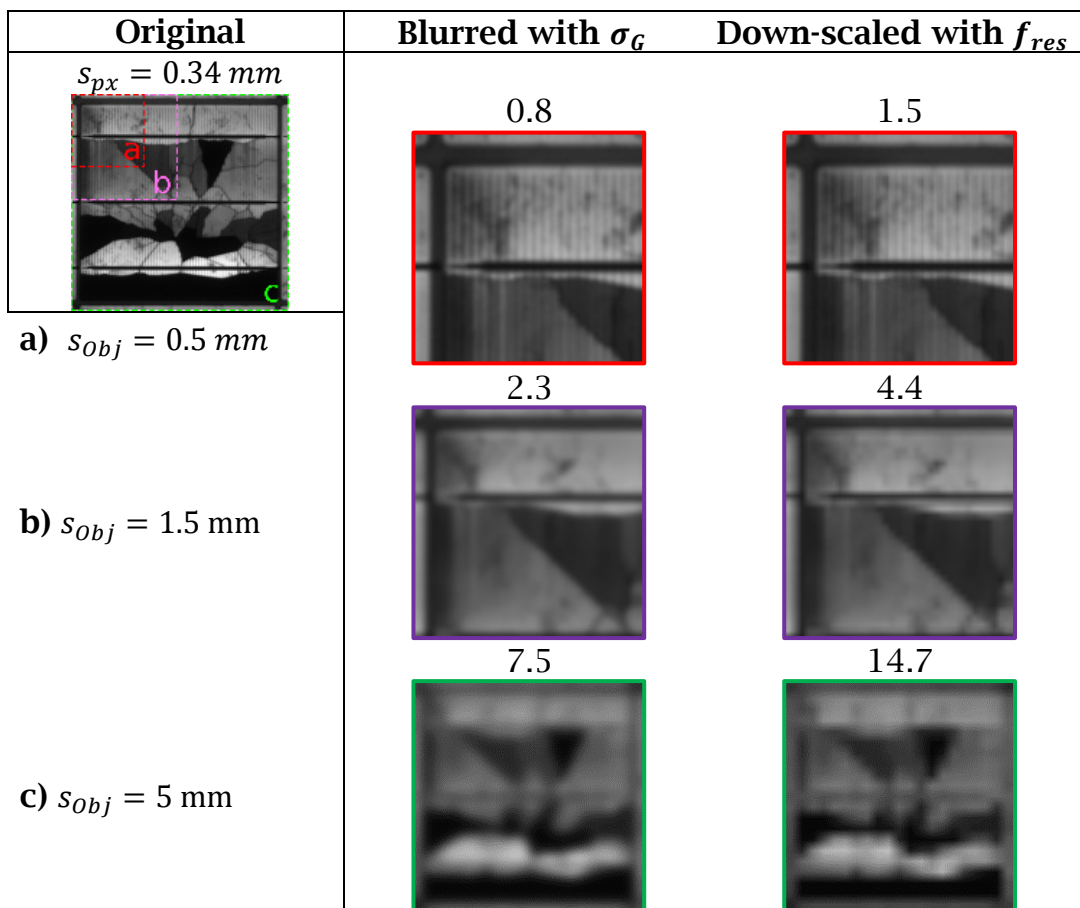


**Figure 3.50: Comparison of the resolved features of a PV device image which is either blurred (middle) or coequally down-scaled (right)**

Fingers are distinguishable for a calculated object size  $s_{Obj} = 0.5 \text{ mm}$ . A coarser resolution of  $s_{Obj} = 1.5 \text{ mm}$  only displays disconnected fingers

and partially cracks. At  $s_{Obj} = 5 \text{ mm}$  only busbars and electrically isolated areas can be distinguished.

### 3.4.6.3 EQUALIZING IMAGE SHARPNESS

When comparing two EL images, it is beneficial to have both at the same image sharpness level. Otherwise difference images contain artefacts (Figure 3.23). The sharpness adjustment (Figure 3.24c,f) is made as follows:

1. Calculate size ratio ( $f$ ) from resolution ( $r$ ) of the larger (A) and smaller (B) image:

$$f = \frac{r_A}{r_B} \quad (3.44)$$

2. Calculate blur due to the different resolutions using the inverse of Equation 3.43:

$$\sigma_f = f_{res}^{-1}(f) \quad (3.45)$$

3. Calculate the effective sharpness of image (B), if brought the same resolution as (A). If the PSF is assumed Gaussian distributed, its variances can be summed. The effective sharpness ( $\sigma_{eff,B}$ ), using the sharpness of the smaller image ( $\sigma_B$ ) becomes:

$$\sigma_{eff,B} = \sqrt{\sigma_f^2 + \sigma_B^2} \quad (3.46)$$

4. If  $\sigma_{eff,B} < \sigma_A$ , blur image (B) using the difference sharpness ( $\sigma_{diff,B}$ ):

$$\sigma_{diff,B} = \sqrt{\sigma_{eff,B}^2 - \sigma_A^2} \quad (3.47)$$

5. If  $\sigma_{eff,B} > \sigma_A$ , blur image (A) using the difference sharpness ( $\sigma_{diff,A}$ ):

$$\sigma_{diff,A} = \sqrt{\sigma_A^2 - \sigma_{eff,B}^2} \quad (3.48)$$

### 3.4.7 SHARPNESS ESTIMATION FROM IMAGE COMPARISON

Subsection 3.4.4 focused on measuring image sharpness using different calibration images. If a calibration image is not available but instead a set of images displaying the same scene, image sharpness can still be calculated. For this, the following conditions should be fulfilled:

1. The PSF is assumed to be Gaussian distributed and sharpness is defined by its standard deviation ( $\sigma$ ).
2. All images display the same scene at the same brightness and contrast.
3. The PSF's standard deviation of the sharpest image ( $\sigma_{ref,abs}$ ) is known.

In this case, for every image ( $I_i$ ), difference sharpness ( $\sigma_{i,diff}$ ) can be calculated from the minimum of the following condition:

$$\sigma_{i,diff} = \operatorname{argmin}(I_i - \text{Gaussian}(I_0, \sigma_{i,diff})) \quad (3.49)$$

This optimization problem can be solved using the Brent method [79]. From  $\sigma_{i,diff}$  and the known sharpness of the sharpest reference image ( $\sigma_{ref,abs}$ ) the sharpness of every image can be calculated using:

$$\sigma_{c,abs} = \sqrt{\sigma_{i,diff}^2 + \sigma_{ref,abs}^2} \quad (3.50)$$

Figure 3.51 shows given and calculated sharpness levels for a set of randomly blurred synthetic circle patterns. As Subfigure (b) shows, the values used to blur the patterns agree with those obtained from the presented method. However, if small and noisy patterns are used and the difference between  $\sigma_{ref,abs}$  and  $\sigma_{i,diff}$  is relatively small, the estimated sharpness levels can be erroneous. In Subfigure (c)  $\sigma_{ref,abs}$  was set to 1.5 px (from 1 px in (b)). This caused  $\sigma_{i,abs}$  closest to  $\sigma_{ref,abs}$  (position 7) to be underestimated.

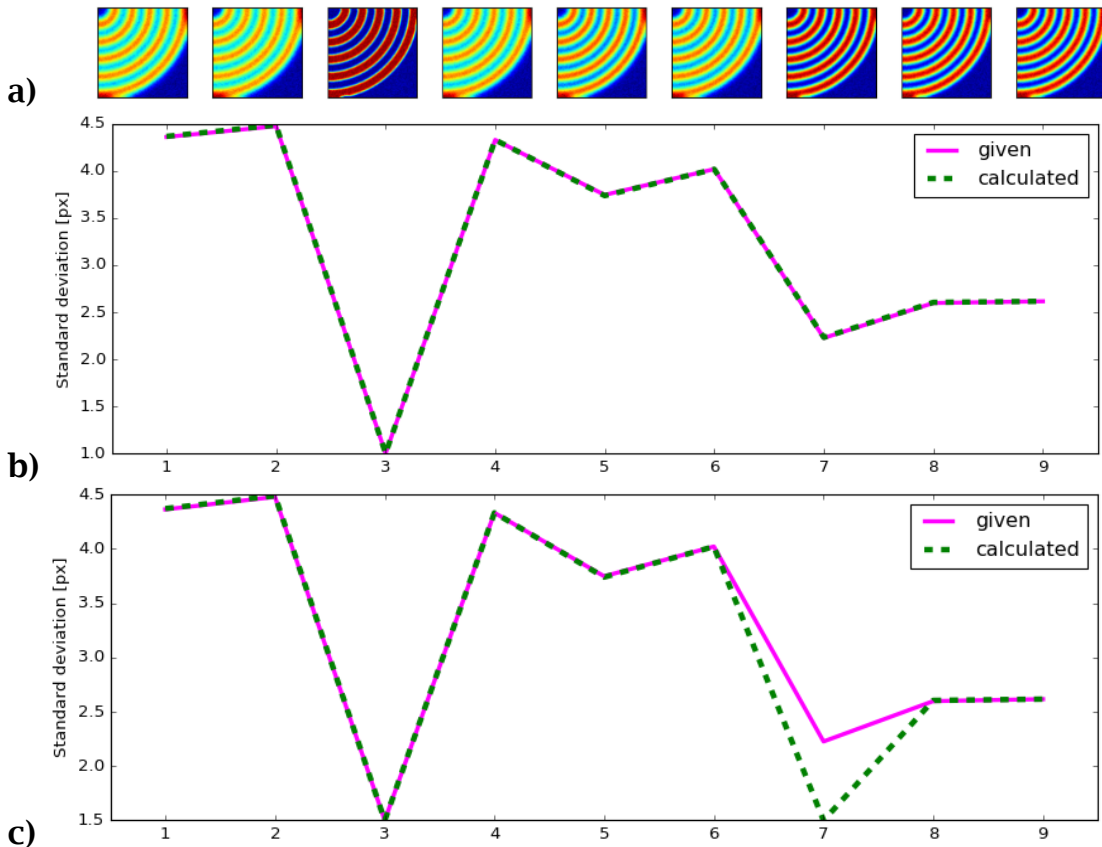


**Figure 3.51 Result of sharpness estimation from image comparison;**  
**a)** synthetic circle patterns (SNR=15, resolution=100x100 px), blurred with different randomly chosen  $\sigma$ ; **b)** comparison of given to obtained  $\sigma$ ; **c)** same as (b), but  $\sigma_{0,abs}=1.5$  px instead of 1 px (position  $i=3$ ); Note that values are discrete and lines are only to guide the eye

### 3.4.8 SECTION SUMMARY

This section gave an overview of different functions and parameters used to describe image sharpness as well as their transformation into each other.

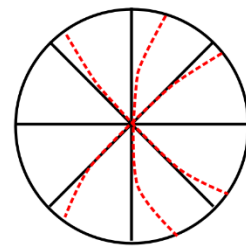
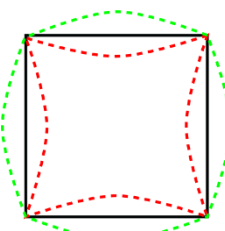
Five different sharpness measurement methods were presented and compared with synthetic patterns and EL images. The best method for measuring image sharpness depends on the parameter to be measured. To measure the modulation transfer function (i.e. image contrast over a spatial frequency) the best results were obtained using a printed spoke target on top of the PV device. To measure a radially variable point spread

function, masking a PV device with a flat disk (such as a CD) provides a simple measurement setup which returns precise results.

Furthermore, the smallest resolvable object size ( $s_{Obj}$ ) was introduced. It enables comparison of the effective resolution of different imaging systems. The section described how to equalize the sharpness of images taken with different cameras. These techniques reduce image artefacts in difference images, improving the precision of the image comparison. An additional method of extracting sharpness from a set of equivalent images was presented in the case that no calibration images to measure sharpness exist.

### 3.5 Lens distortion

The shape of the camera lens used and positioning errors during the assembly of the camera can result in radial and tangential distortion respectively (Figure 3.52).



**a) Radial distortion (green: positive, red: negative, black: no distortion)**    **b) tangential distortion (red: with, black: without distortion)**

Figure 3.52: Types on lens distortion

The spatial correction of the radial distortion can be described using [80]:

$$x_{corrected} = x \cdot (1 + k_1 r^2 + k_2 r^4 + k_3 r^6) \quad (3.51)$$

$$y_{corrected} = y \cdot (1 + k_1 r^2 + k_2 r^4 + k_3 r^6) \quad (3.52)$$

... and tangential distortion using:

$$x_{corrected} = x + [2p_1y + p_2(r^2 + 2x^2)] \quad (3.53)$$

$$y_{corrected} = y + [2p_2x + p_1(r^2 + 2y^2)] \quad (3.54)$$

Where:

---

$x, y$  Original position in the image

$x_{corrected}, y_{corrected}$  Position after correction

$k_1, k_2, k_3, p_1, p_2$  Distortion coefficients

---

These five distortion coefficients along with image centre and focal length can be identified by several camera calibration techniques. One technique uses multiple images of a chessboard (for example 7x8) or alternatively a ring calibration pattern [81] in various angles and positions. It is recommended to keep the pattern size within 25-75% relative to the size of the image plane. To reduce the influence of corner detection errors and pattern inhomogeneity at least 15 images should be captured.

In this work, images of an in-plane chessboard pattern (Figure 3.53) were captured. The Python interface of the C++ library OpenCV [64] was then used to detect inner chessboard corner points (`cv2.findChessboardCorners` and `cv2.cornerSubPix`). The camera matrix and distortion coefficients were obtained using `cv2.calibrateCamera`. [64]

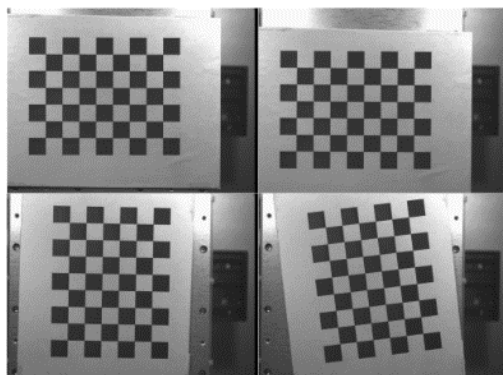


**Figure 3.53: Four example images of an in-plane chessboard pattern at different positions and rotations used to calculate lens distortion**

## 3.6 In-Plane Flat Field Measurement

### 3.6.1 INTRODUCTION

The image intensity of EL images is largely influenced by off-axis illumination and camera sensor imperfections. For quantitative EL imaging their correction is essential. If neglected, pixel intensities can vary significantly (>50%) across the image.

Intensity modulating distortions can be categorised into optical aberrations and other imperfections such as vignetting and flare. Optical aberrations cause light to reach the sensor at slightly shifted locations, resulting in a less sharp and more distorted image. Vignetting causes the light to only partially reach the sensor, resulting in erroneous quantitative results. Since the use of EL imaging is evolving to emphasise quantitative analysis, such imperfections must be corrected for. This section evaluates methods for measuring and correcting illuminance inhomogeneities in the specialised field of luminescence imaging of PV devices.

The inhomogeneities can be removed by dividing every (dark current corrected) EL image by a flat field image ( $I_{FF}$ ). The  $I_{FF}$  describes the spatial non-uniformity of light detection. It is mainly caused by:

1. Vignetting (natural, optical, mechanical): Inhomogeneous illumination of the sensor due to projection via the camera lens [72, 82], best described by the vignetting image ( $I_{Vig}$ ) and
2. Sensitivity: Pixel specific quantum efficiency of the camera sensor (and optical inhomogeneities, such as soiling), best described by the sensitivity image ( $I_S$ , Figure 3.54):

$$I_{FF} = I_{Vig} \cdot I_S \quad (3.55)$$

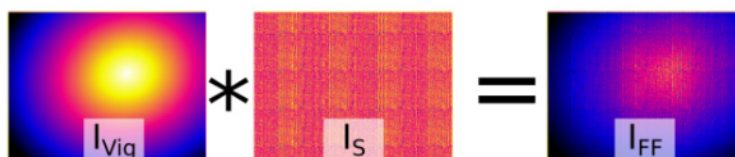


**Figure 3.54: Creation of a flat field image**

Figure 3.55 compares EL difference images of the same PV device taken under the same conditions, but at different positions within the image plane (row a). The images were background corrected [25, 33, 43], the lens distortion [64] was removed and the position of all images was unified [83]. An image with the most central position of the DUT was chosen as reference image. The absolute deviation between reference and other EL images is shown in row b. It reveals significant variations. The same deviation with additional flat field correction (before lens distortion removal) is shown in row c). Here, deviations are close to negligible. Row b and c have the same colour scale, which shows that flat field correction is essential for quantitative evaluation of EL images.

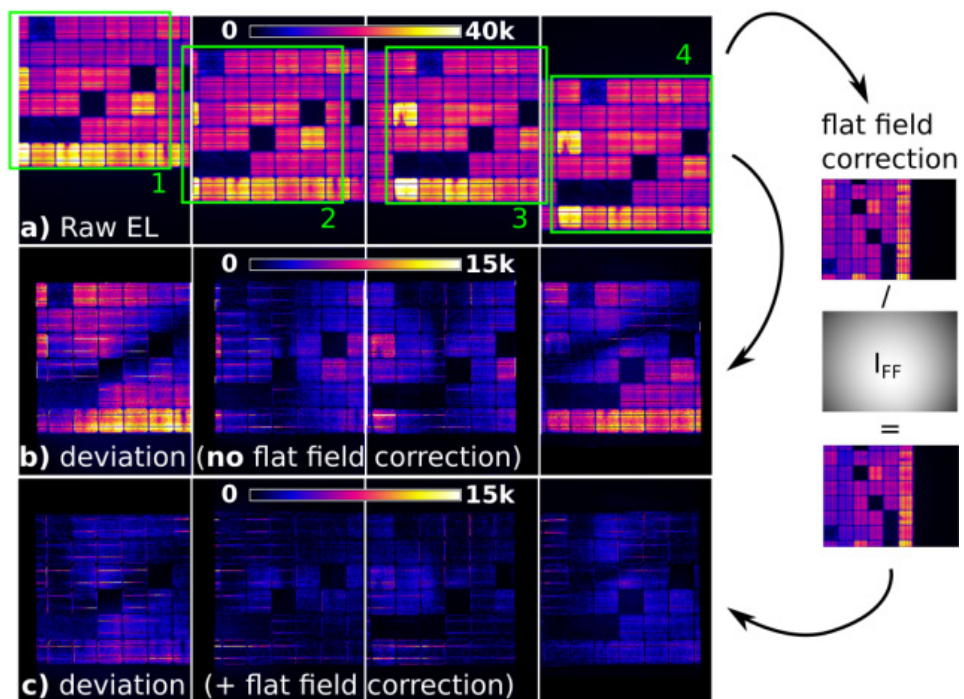


**Figure 3.55:** Intensity of the same PV module imaged at (a) different positions and corresponding absolute intensity deviations (b) without and (c) with vignetting correction relative to the reference image

The existing methods to obtain  $I_{Vig}$  and respective  $I_{FF}$  vary:

For astronomy based applications, Howell uses the inside of a telescope dome or the dawn or dusk sky as homogenous sources for obtaining  $I_{FF}$  [84]. Kang et al. extract  $I_{Vig}$  through imaging a sheet of white paper in the focal plane. There,  $I_{Vig}$  is calculated as function of off-axis illumination

(i.e. natural vignetting) and other vignetting [85]. This function is referred to as KW in Subsection 3.6.3.

Unlike many other imaging techniques, EL imaging captures the light source itself and not its reflection. Therefore, many common flat field calibration methods cannot be directly adopted.

A few papers have described flat field calibration for EL imaging so far: Flat field measurement with a ‘homogenous’ light source at short distance and out of focus of the camera was used in [8, 33]. It was reported that even a high resolution LCD flat panel, emitting red light at 612 nm, can be used as an approximation for measuring CdTe solar cells with a recombination peak at around 850 nm [86]. In this work, this method is referred to as X.

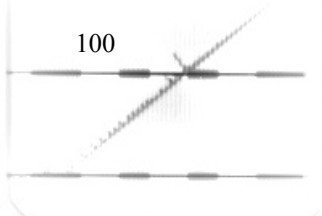
A similar measurement with a ‘homogenous’ light source (such as rear contact solar cell) and with a defocussed lens is proposed by Köntges et al. [25]. Herein optical paths differ due to changed focus and no specification regarding distance between lens and light source is given.

The same publication also proposes an ‘angle-of-view’ fit function. This function calculates the intensity decrease from a Lambertian surface for variable aperture angles. This method is used further on to fit measured image intensities. It is referred to as AoV in Subsection 3.6.3.

In this section, it is assumed that the influence of pixel sensitivity ( $I_s$ ) is minor. Therefore, the focus is on five vignetting measurement methods (A-E) in comparison to the aforementioned method X. To improve results, different post processing methods are discussed and applied to the measurement result. The quality of vignetting removal of these measurement-post-processing combinations is evaluated in Subsection 3.6.4. Finally, the acquisition of sensitivity images is described in Subsection 3.6.5.

### 3.6.2 VIGNETTING MEASUREMENT

Vignetting is measured on two module-scale EL imaging systems using different light sources. However, homogeneous sources of such size,



which emit similar spectra to PV DUTs, are rarely available. The following methods bypass this issue, through either correcting or averaging source inhomogeneity. All images taken were first corrected for dark current, by subtracting a background image ( $I_{BG}$ ) taken at the same exposure time, before processing (Subsection 3.1 and 4.2).

Camera aperture, exposure time, emitted waveband of the source as well as distance and orientation between source and camera influence the measured result. Their influence is analysed in Section 3.7. Here, it is assumed that the quality of vignetting characterisation depends on whether the optical properties of the imaged source are representative of a typical DUT's luminescence. Therefore, it is advisable to perform vignetting measurements in the usual measurement plane, with the same camera parameters and the same wavelength range as the DUT.

The imperfections causing vignetting and sensitivity inhomogeneities are temporally stable. Therefore, it is not required to repeatedly calibrate the system. However, temporal stability of the system components and reference conditions must be ensured during calibration. The camera is considered stable after it has reached a constant operating temperature. Time stable emission of the source must also be ensured for vignetting measurements. If a PV device is chosen as source, it should be kept in forward biased excitation until its temperature stabilizes. Especially in the case of metastable PV devices, the stability of emission must be checked after measurements.

### 3.6.2.1 METHOD A: DIRECT MEASUREMENT AT SHORT DISTANCE WITH SPATIAL INHOMOGENEITY CORRECTION

Similar to the aforementioned method X, this method images the source directly in front of the camera lens in order to blur out spatial inhomogeneities. However, even heavily defocussed, strong inhomogeneities in a PV module (such as wave-pattern from cell layout, see Figure 3.56a) remain. Therefore, a more uniform source (such as an LCD screen, see Figure 3.56b) is desirable. To the naked eye, these sources

may look uniform, however an intensity difference of up to 10% was found for the same LCD source, when imaged at slightly different positions in front of the lens. An unintentionally introduced gap between source and lens also alters the result due to off-axis illumination (Figure 3.56c).

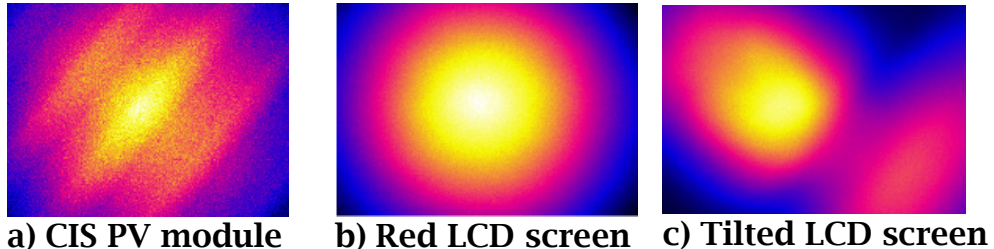


**Figure 3.56: Method A, example images**

Therefore, method A images the source directly in front of the lens, but differs from method X in that a minimum of 10 ( $i=0$  to 9) images of the source are taken, at different positions and rotation angles relative to the optical axis. It is assumed that spatial non-uniformity averages out. However, the angular dependency of the source will still affect the result, since the source is imaged out of the image plane. The vignetting calibration image ( $I_{Vig}$ ) is then obtained from the mean along these images as follows:

$$I_{Vig,A,sum} = \sum_{i=1}^n I_i$$

$$I_{Vig,A} = \frac{I_{Vig,A,sum}}{\max(I_{Vig,A,sum})} \quad (3.56)$$

The sum operator operates over all given images by the same pixel index and therefore returns an image. Finally, the image is normalised to obtain  $I_{Vig,A}$ .

### 3.6.2.2 METHOD B: DISCRETE SPOT AVERAGE

Method A measures vignetting directly in front of the camera. Hence, the direction of light rays differs to that in a standard measurement setup and can cause erroneous results. To measure vignetting in plane with the DUT, the calibration source is placed directly on a DUT mounted in the imaging plane. This aligns the optical axis between the camera and source as it will be for actual EL measurements. The source size should not exceed 10% of the image plane, to allow multiple images of it to be taken at different positions (Figure 3.57a). Using the following algorithm, a set of points  $(x_i, y_i, z_i)$  used to fit a vignetting function (Section 3.6.3) is obtained:

For every image ( $I_i$ ) taken:

1. Select foreground mask ( $M_i$ ) as all values higher than a threshold ( $T_{Otsu}$ ) determined using Otsu's method [87]:

$$M_i = I_i > T_{Otsu} \quad (3.57)$$

2. Filter small areas and select the largest masked/selected coherent pixel group ( $M_{i,max}$ ) of size ( $n$ ).
3. Extract the centre of gravity ( $x_i, y_i$ ) and average intensity ( $z_i$ ) in the selected area:

$$x_i, y_i = \frac{1}{n} \iint M_{i,max} dx dy \quad (3.58)$$

$$z_i = mean(I_i[M_{i,max}]) \quad (3.59)$$

The averaged intensities ( $z_i$ ) of all pixel groups are used to fit a vignetting equation [88]:

$$I_{Vig,B} = FIT(x_i, y_i, z_i) \quad (3.60)$$

An example fit is shown in Figure 3.57b.

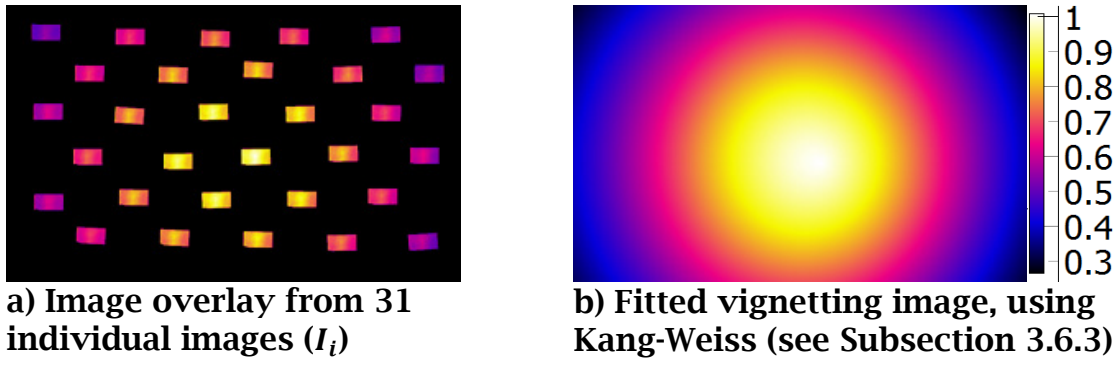


**Figure 3.57: Method B example result using a red mobile phone screen as light source**

This introduced method combines the simplicity of method A with in-plane imaging. In doing so, it trades uncertainty due to out-of-plane imaging for uncertainty of the light sources temporal stability. Similarly, errors due to wavelength and angular differences remain. Additionally, using only a small number of images/locations to fit the whole image adds to the measurement uncertainty.

### 3.6.2.3 METHOD C: LOCAL MAXIMUM OF MULTIPLE DUTS

Often, EL images are provided without any (flat field) calibration images. In this case, vignetting correction for the measurement system can be extracted using EL images of different devices. If it is assumed that the local intensity deviation averages out with a large number of devices, the following algorithm may be used to obtain  $I_{Vig,C}$ . For every image ( $I_i$ ):

1. Apply Gaussian blur (set kernel size to 10% of image height)
2. Scale  $I_i$  to values 0...1 in order to average images of different devices, taken at different exposure times and/or with different applied currents:

$$I_{i,norm} = \frac{I_i}{\max(I_i)} \quad (3.61)$$

3. Calculate  $I_{Vig,C}$  from moving maximum over all images ( $I_{i,norm}$ ):

$$I_{Vig,C}[M_i] = I_{i,norm}[M_i]; \quad M_i = I_{i,norm} > I_{Vig,C} \quad (3.62)$$

An example result of this method using post processing (POLY, Subsection 3.6.3) is shown in Figure 3.58.

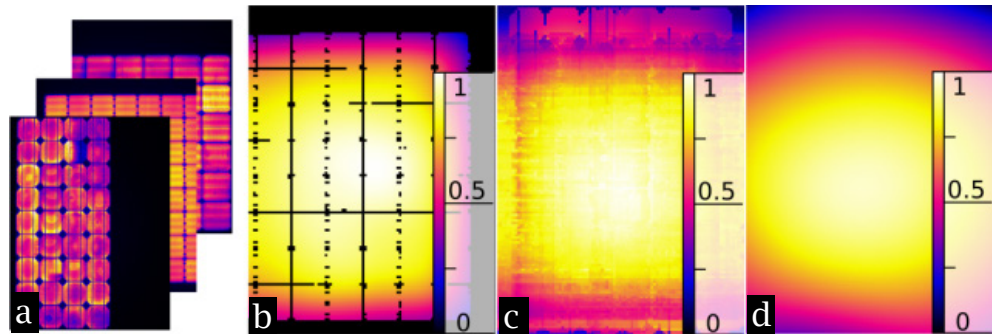


**Figure 3.58: Method C example results; a) EL image set of different DUTs; b)  $I_{Vig,C}$  for 1<sup>st</sup> EL image; c)  $I_{Vig,C}$  for 20 images; d)  $I_{Vig,C}$  after post processing**

### 3.6.2.4 METHOD D: VIGNETTING-OBJECT SEPARATION FROM DISCRETE STEPS

In contrast to Method C this method corrects for the DUT's inhomogeneity not through averaging different devices, but through measuring average intensities of the same device at different predefined positions.

This can be, for example, single cells of a c-Si based module. Multiple EL images of the DUT at different discrete locations within the image plane are taken (Figure 3.59a).

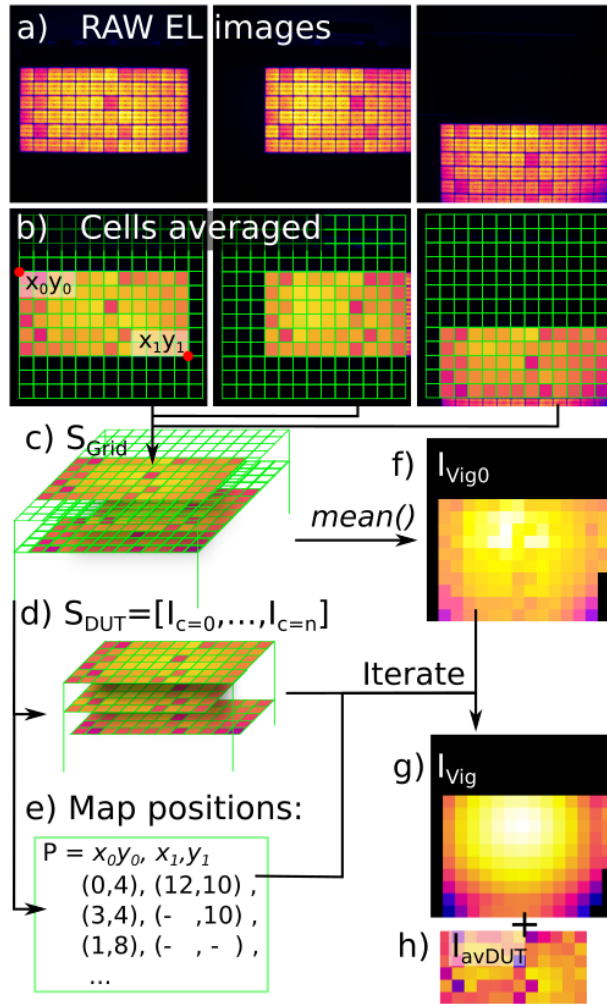


**Figure 3.59: Method D schematic to obtain vignetting image**

In the example shown, the image plane is divided into a 13x13 grid of 120x120 mm squares. The DUT is a 12x6 cell c-Si module. For each imaged position, the image intensity within each grid square is averaged. The result is assigned to a layer of the image stack ( $S_{Grid}$ ) incorporating the DUT and the image plane (Figure 3.59c). Areas imaging the background are excluded using a threshold condition (Subsection 3.2.4.1). In the example, 10 images ( $n=10$ ) were used (only three shown for clarity). From the average over all grid images, an initial vignetting image ( $I_{Vig0}$ ) is built (Figure 3.59f). From the same stack, a new stack containing only DUT cells ( $S_{DUT}$ ) is created and cell positions ( $P$ ), needed to index the same areas in  $S_{Grid}$  and  $S_{DUT}$ , are extracted (Figure 3.59c,d).

$I_{Vig,D}$  is then calculated iteratively with the iteration step ( $i$ ) and the image index ( $c$ ) as follows:

1. Extract the average DUT cell values:

$$I_{avDUT,i} = \frac{\sum_{c=0}^{c=n-1} \left( \frac{S_{DUT}[c]}{I_{vig,i}[P[c]]} \right)}{n} \quad (3.63)$$

2. Create next vignetting map from average ratio between the DUT stack and the average cell values:

$$I_{Vig,i+1}[P[c]] = \frac{\sum_{c=0}^{c=n-1} \left( \frac{S_{DUT}[c]}{I_{avDUT,i}} \right)}{n} \quad (3.64)$$

3. Check iteration criterion using given threshold value ( $t$ ):

If  $\sum(I_{Vig,i+1} - I_{Vig,i}) > t$  then go to step 1, else:

$$I_{Vig,D} = \frac{I_{Vig,i+1}}{\max(I_{Vig,i+1})} \quad (3.65)$$

This method measures vignetting in plane and allows use of the same DUT for calibration and measurement. However, its result is a low-resolution grid, which needs to be up-scaled to camera resolution. For this, bi-linear interpolation is used. Missing or incorrect areas within  $I_{Vig,D}$  are corrected through post processing (Subsection 3.6.3). This method can be adjusted easily for different grid cell (and physical PV cell) sizes, but needs precise placement of the DUT in order to not affect the measured averages.

#### 3.6.2.5 METHOD E: VIGNETTING-OBJECT SEPARATION USING PATTERN RECOGNITION

This method builds on method D. Instead of averaging DUT intensities within a predetermined grid, the translation and rotation of the DUT is detected within each EL image ( $I_i$ ) relative to a reference image ( $I_{ref}$ ) using pattern recognition (Subsection 4.7.2). This has two advantages:

- The DUT position within the image can be chosen randomly, provided that a good overall coverage of the measurement plane is achieved.
- The resulting vignetting image has the same resolution as the input images. (for instance 3000x4000 vs 13x13 via method D)

$I_{Vig,E}$  is obtained as follows (Figure 3.60):

1. The DUT is imaged at different positions and (if needed - not required) angles within the image plane.  
 $I_{ref}$  showing most of the DUT (preferably without rotation) is selected for later pattern recognition.
2. Similar to method C, an initial vignetting array is calculated from the moving maximum of each  $I_i$ . Reasonable improvements to image quality are achieved for image areas that are covered by at least three DUT images. The resulting array is smoothed to reduce inhomogeneities.
3. a) Each  $I_i$  is transformed to the same perspective as  $I_{ref}$  (Subsection 4.7.2.1).  
b) Overall vignetting is extracted from the individual vignetting image from each rectified DUT image via inverse perspective transformation.
4. Each rectified DUT image (a) is divided by each rectified vignetting array (b), respectively. The result is averaged to obtain the first vignetting corrected DUT image (c).
5. Each rectified DUT image (a) is divided by (c) to recover each individual vignetting array. All arrays are perspective transformed into the original position using the same process as in step 3.  
Steps 4 and 5 are repeated until the difference between the last two vignetting arrays falls below a given iteration threshold.
6. Empty areas are filled and inhomogeneities smoothed out in post processing (Subsection 3.6.3) to obtain  $I_{Vig,E}$ .

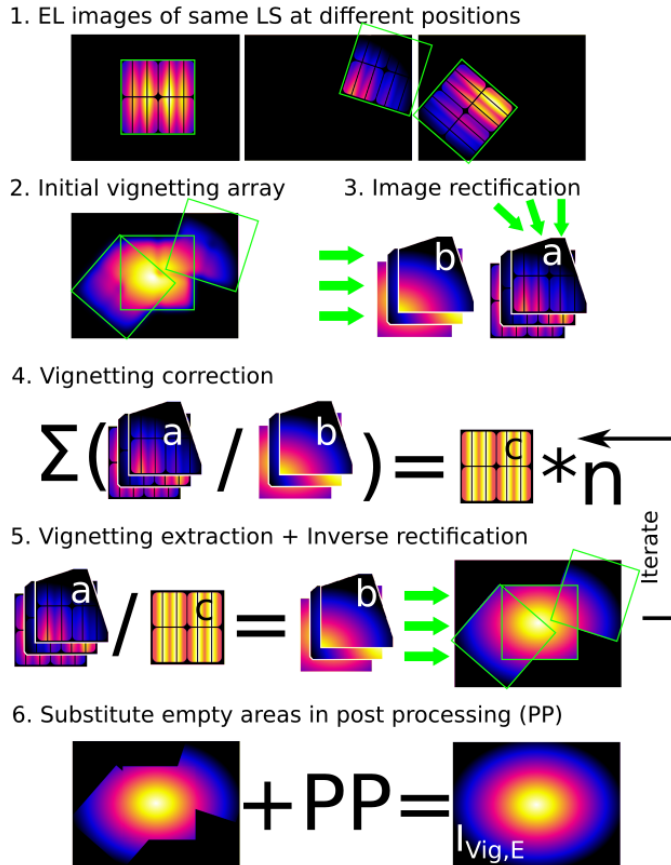


**Figure 3.60: Method E schematic to obtain vignetting image**

Figure 3.61 gives examples for images (a) and (c) from step 4, initial vignetting map from step 2 and final vignetting map from step 5 in Figure 3.60. The DUTs shown in row I have each different sizes, relative to the image plane: Whilst the large CIS module extends above the image height, the small CIGS module occupies only a fraction of it. To improve pattern recognition on the (comparatively uniform) left-hand side CIS module, three distinctive marks were taped on the device.

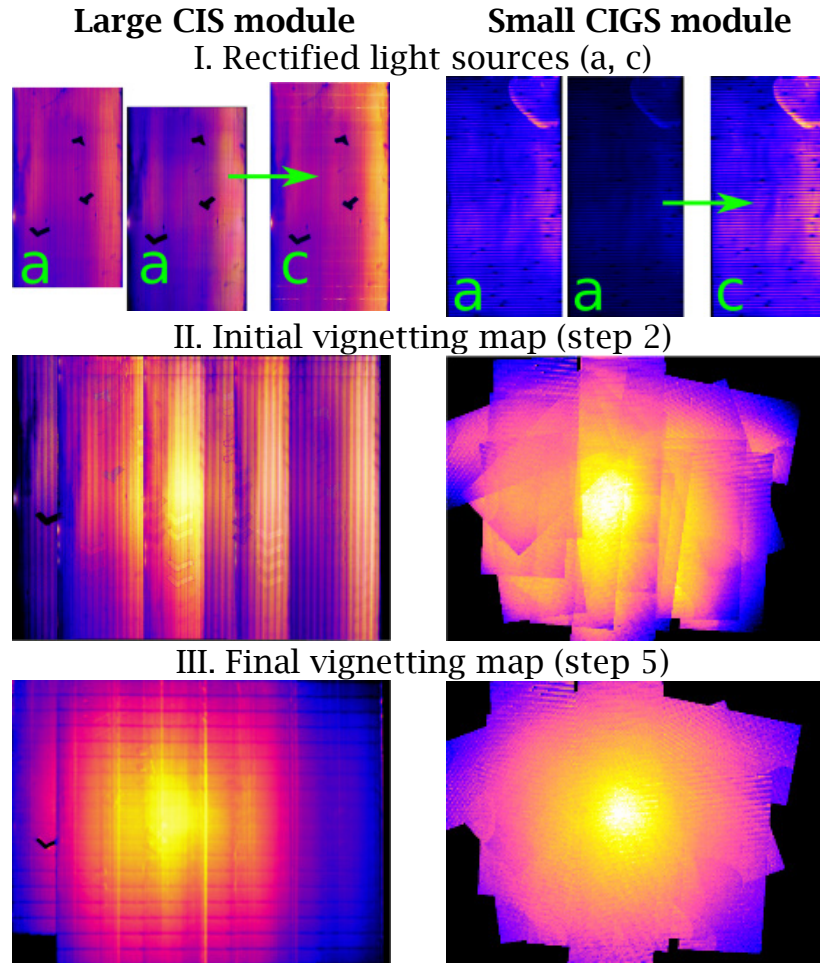
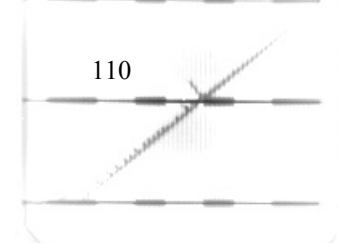


**Figure 3.61: Example results of method E**

### 3.6.3 POST PROCESSING

All vignetting measurement methods result in either a vignetting image or discrete points. The vignetting images (methods A, C, E) may include noise and artefacts and may not cover the whole imaging area. Conversely, the discrete points (methods B and D) provide only a sample of the overall imaging area. Thus, depending on the vignetting measurement method, a degree of post processing is often required to obtain a usable vignetting correction image. Since the effect of vignetting is continuous, smoothing algorithms (or filters) or functional approximation can be used to obtain a smooth vignetting correction image. The following methods are compared:

- **RAW:** resulting vignetting correction images from methods A-E without further processing



... with three functional approximations:

- **KW:** Simplified Kang-Weiss vignetting Equation 3.66 from [88]
- **AoV:** Angle-of-view equation from [25] and
- **POLY:** 2<sup>nd</sup> order 2D polynomial fit

... which are applied in two fashions:

- = (**replace**): Every image pixel is replaced with a fitted value.
- + (**repair**): Only empty areas are infilled with fitted values. For 'POLY repair' this also includes high gradient areas.

Finally, common filter algorithms are applied to 'KW Repair':

- **Gauss:** Convolution with Gaussian kernel and
- **Median:** Image pixels within same kernel are replaced with their local median

Both filters use kernel size of 5% image width. The simplified Kang-Weiss vignetting equation from [88] is:

$$I_{vign} = A \cdot (1 - \alpha \cdot d) \quad (3.66)$$

$$A = \frac{1}{\left(1 + \left(\frac{d}{f}\right)^2\right)^2} \quad (3.67)$$

$$d = \sqrt{(x - x_0)^2 + (y - y_0)^2} \quad (3.68)$$

Where:

---

$f$	Focal length [px]
$x_0, y_0$	Image centre [px]
$\alpha$	Geometric vignetting factor [-]

---

Figure 3.62 illustrates example results of the post processing methods applied to two similar samples obtained using method E in different imaging setups (Centre for Renewable Energy Systems Technology UK, [CREST], Laboratory of Photovoltaics and Optoelectronics, SL [LPVO]). The upper part of the RAW vignetting image (a) was not characterised and remains black due to spatial constraints of the LPVO setup. Similarly, a

vertical line remains black in the RAW vignetting image (b) of the CREST setup. All post processing methods filled the black areas. Additionally, both RAW images still show some remaining patterns seen as vertical and horizontal lines. These are caused by misalignment errors after perspective transformation in method E. When post processing is applied in ‘+’ (repair) fashion, these artefacts remain, but when the ‘=’ replace fashion is used they disappear. ‘+POLY’ also smoothens out these high gradient variations. ‘Gauss’ and ‘median’ filtering of ‘+KW’ additionally blurs or even removes these artefacts.

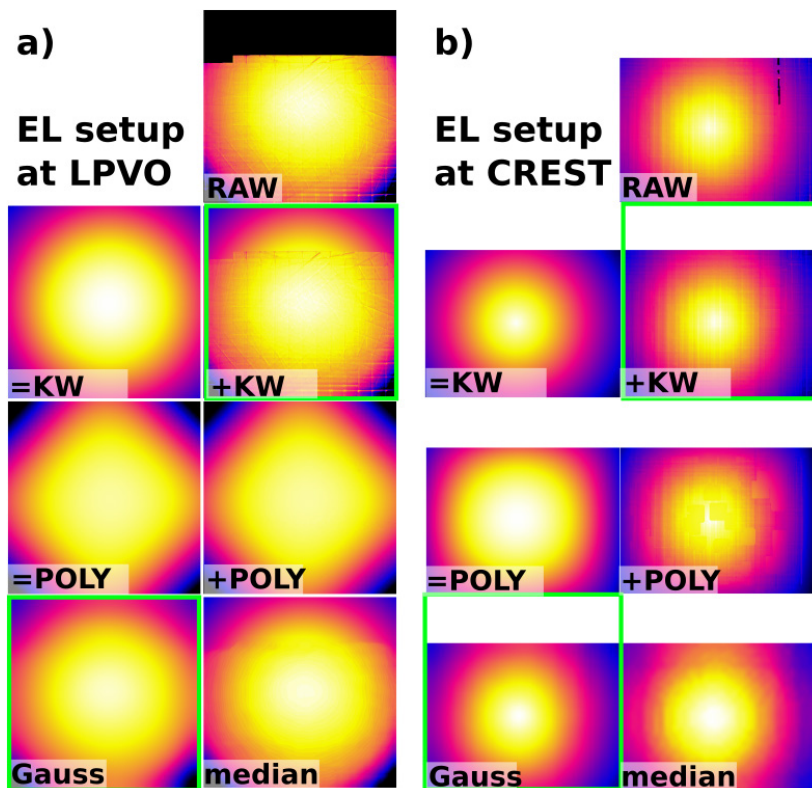


**Figure 3.62: Comparison of different post processing methods applied to two similar samples on two different EL setups; Raw image obtained from method E; values scaled 50-100%; proposed post processing methods highlighted green**

Depending on the measurement method and quality of the RAW image, different post processing methods are found to be superior (see Subsection 3.6.4). In general, ‘+KW’ together with a Gaussian filter is proposed for filling empty areas and smoothing out measurement artefacts.

### 3.6.4 VIGNETTING COMPARISON

The following algorithm to compare vignetting measurement methods and applicable post processing algorithms is similar to the presented method E. In the same way, multiple images of the DUT are taken at different (random) positions within the image plane (Figure 3.63a).

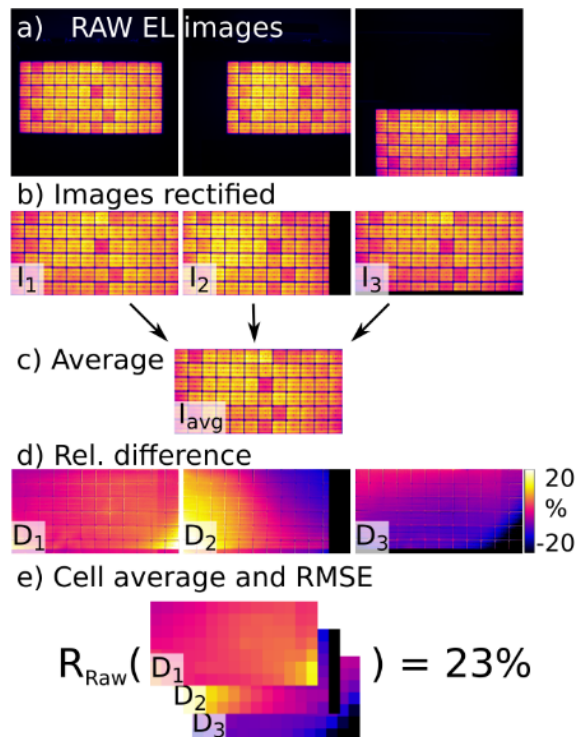


**Figure 3.63: Schematic of calculating error from residual vignetting**

Images are rectified using the same feature matching algorithm (b). From all rectified images ( $I_i$ ), an image average ( $I_{avg}$ ) is built (c). A relative difference image ( $D_i$ ) is then calculated for each  $I_i$  as follows:

$$D_i = \frac{I_i - I_{avg}}{I_{avg}} \quad (3.69)$$

Misalignment errors after perspective transformation can cause high magnitudes along high gradient variation, such as at cell edges and busbars. To remove this influence, a cell average is performed. It results in a lower resolution image (e) which should only contain vignetting effects. A root-mean-square error (RMSE) of all cell-averaged difference

images finally returns the relative error caused by residual vignetting ( $R$ ). In the following comparison, this algorithm is performed first on uncorrected EL images to obtain the inherent setup vignetting error ( $R_{raw}$ ), and then on all vignetting corrected images to obtain the residual vignetting error ( $R_{i,j}$ ). Vignetting correction was performed for all measurement methods ( $i$ ) and all post processing methods ( $j$ ). From all RMSE pairs ( $R_{raw}, R_{i,j}$ ) the vignetting correction quality ( $Q_{i,j}$ ) is determined as follows:

$$Q_{i,j} = \frac{R_{raw} - R_{i,j}}{R_{raw}} \quad (3.70)$$

A comparison of different vignetting and post processing method combinations is shown in Figure 3.64 for the two different setup-module combinations (a - CREST setup: Si module, b - LPVO setup: Si HIT module). Image setup parameters for both cases are shown in Table 3.7.

**Table 3.7: Image setup parameters of compared cases**

	CREST	LPVO
Camera name	Sensocam HR-830	FLI ML16803
Focal length	25 mm	50 mm
Aperture	f/2.8	f/2.8

The evaluated methods are shown as coloured plots. Along the x-axis different post processing methods are compared. The plots listed in the legend are:

- **X (LCD/PV):** average of three randomly chosen close distance images, as described in [8, 33].  
 Sources are either a red **LCD** screen or an equivalent **PV** device
- **A (LCD/PV):** method A using 10 images
- **B (LCD/small PV):** method B using average position and intensity of 10 images of a red LCD screen or 1 cell mini module imaged in imaging plane

- **C (diff PV):** method C using 30 randomly chosen EL images of c-Si modules
- **D (large PV):** method D using EL images of a c-Si PV module at discrete positions
- **E (large PV):** method E, using EL images of c-Si modules at random positions

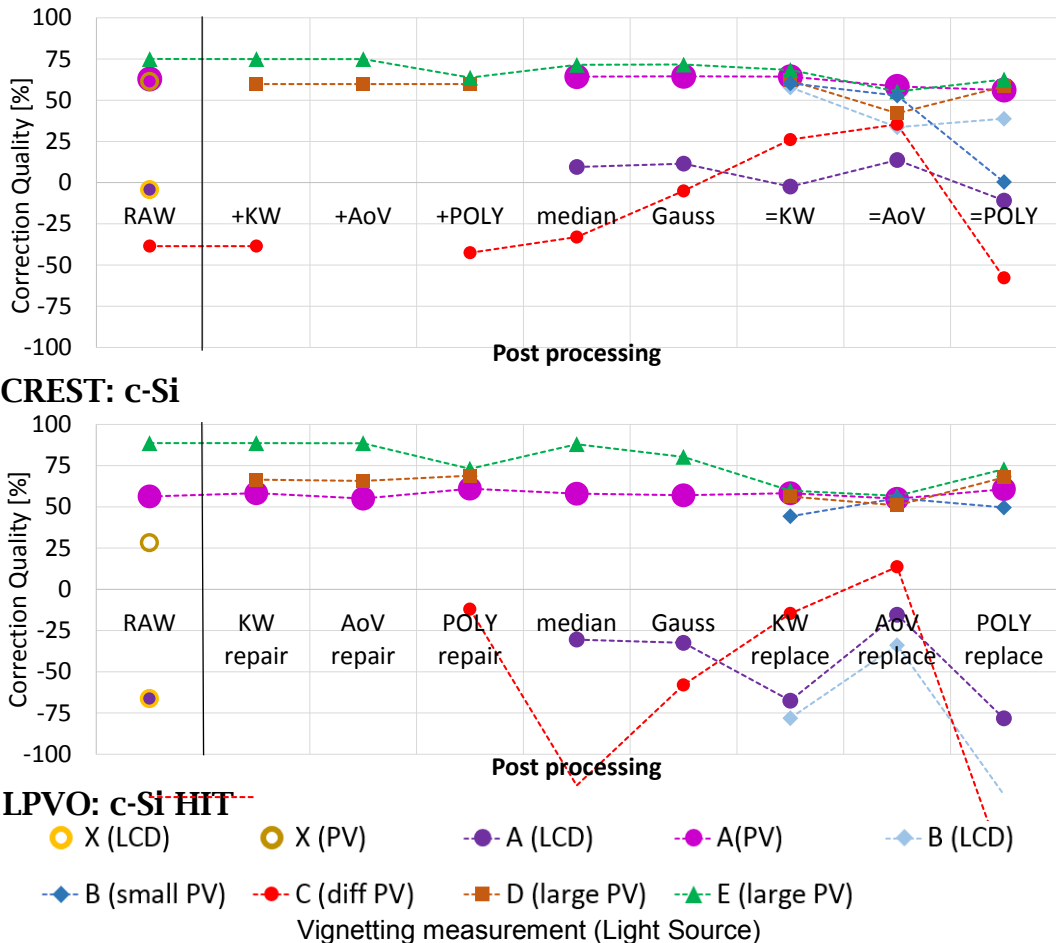


**Figure 3.64: Correction quality ( $Q_{i,j}$ , Equation 3.70) for two different EL setup-module combinations: a) CREST (Si module); b) LPVO (Si HIT module); Note that the values are discrete and the lines are only to guide the eye**

Vignetting correction quality ranges from below -120% to 90%. This means that some methods even decreased the image quality. In order to find the best suitable vignetting correction method, boxplots based on data shown in Figure 3.64 were generated (Figure 3.65). Method E corrected vignetting to the best extent. It is followed by methods D, A(PV), and B(PV) which

still provide good correction. On the other side, method C, X(LCD), A(LCD) and B(LCD) often even decreased image quality due to vignetting overcorrection.

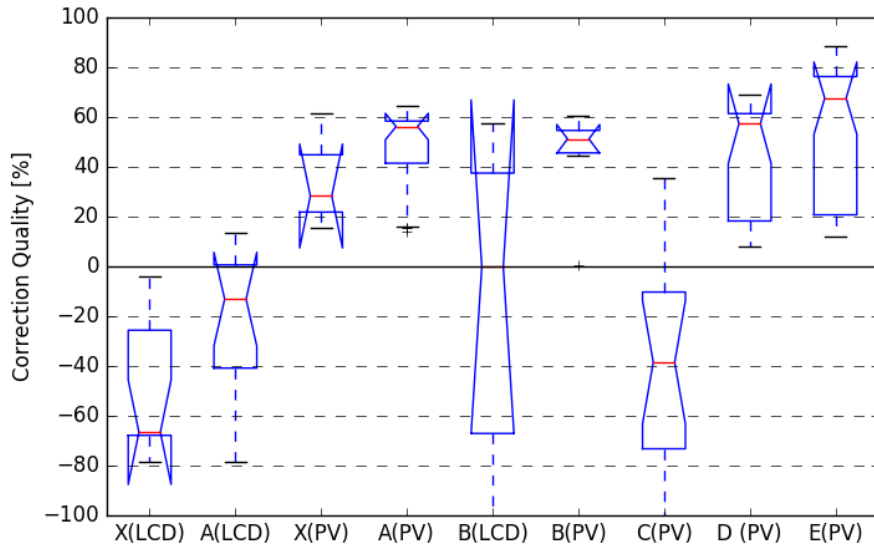


**Figure 3.65: Vignetting method comparison from values shown in Figure 3.64**

Methods of highest correction quality still had an absolute intensity deviation ( $R_{i,j}$ ) of 1 to 2%. Below, results are evaluated by method.

Methods X(LCD, PV) (light/dark yellow) and A (light/dark purple): Consistently lowest improvements and even degradations are gained by using an LCD display as a light source. Its angular dependence, and wavelength range differs too much from the actual imaging circumstances resulting in erroneous vignetting maps. In contrast, using a PV device (similar to expected DUTs) rather than a red LCD screen provided better vignetting correction. Using a weighted average of multiples of these images (method A) improved the correction and brought the method in-par with the others. The use of post processing techniques is not essential. The results show that the effect of post processing is small, not always beneficial and very specific to each case.

Method B (dark/light blue): This rather simple method allows in-plane vignetting measurement. If measured with a light source equal or similar to the DUT, it also measures at the correct wavelength range and angular distribution. The result has to be fitted with a polynomial or a vignetting

function. For this, in all cases around 25 spots, evenly distributed within the image plane, were measured. It is important that the spot images do not introduce additional inhomogeneities. Therefore, they should be small relative to the image plane and they should be averaged. In case [b] the correction quality is around minus 50% (Figure 3.64b). Figure 3.66 shows why:

Subfigure (a) shows residual vignetting after correction by the vignetting map, measured with a PV panel. It reveals significant overestimation of the vignetting by imaging the LCD screen. If however the result is divided by a vignetting map measured with the same device, no visible vignetting remains. Instead, a horizontal gradient in the image (Figure 3.66b) becomes visible. The erroneous vignetting estimation stems from high angular dependence of the LCD screen, which was only observed after a careful examination of the measurement procedure. This example shows how important the selection of a suitable source is, and how much can it affect the otherwise good method B.

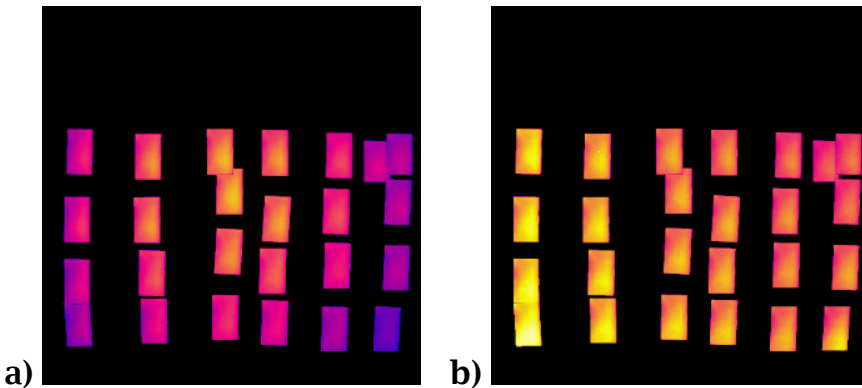


**Figure 3.66: Sum of all images used to measure method B of case [b] after vignetting correction using a) method A(PV) and b) A(LCD). Both images scaled identically**

Method C (red): Only in a few cases, this method increased the image quality. Using a random selection of EL images in the hope that their weighted average might return something close enough to an actual vignetting measurement is only advisable if vignetting correction is needed but no calibration is available. For the applied post processing methods, POLY gives the worst results but a functional fit such as AoV or

KW can deliver something positive. The reason why the simple AoV gives better results than KW is shown in Figure 3.67. The RAW measurement result shows that the vignetting centre appears to be on the left of the image centre. This is however wrong because the source in the EL image set is more on the left side. Here for AoV vignetting measurement the centre of the fit was equal to the image centre, therefore the AoV fit corrects for the erroneous central position, whereas the KW fit also finds the wrong central position. POLY gives the result closest to the RAW image, which obviously resembles the module position and shape. For method C, AoV with its fixed central position provides the best post processing option.

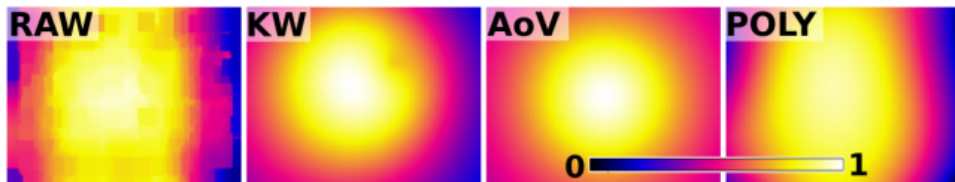


**Figure 3.67: Comparison of resulting vignetting maps for method C in case [a]**

Method D (dark brown): This method demands the positions of the imaged DUT to be within a precise grid. Although the resolution of the returned RAW image is limited by the number of columns and rows in the grid, the image quality improvement is amongst the highest. The first reason is that the light source is the actual DUT with no spectral, angular or distance mismatch and the second is that vignetting is a continuous effect and thus the undefined areas are well fitted between the grid points, which cover the whole imaging plane. Because the majority of the image plane is measured, the selection of the post processing option does not strongly influence the result. However, it can be observed that AoV (especially with '=' (replace) post processing) yields the worst results, POLY the best and KW is between the two. The reason is that when the grid is dense enough, the irregular vignetting (different central point, effect of optical and mechanical vignetting) is better defined by the measurements than by the functions that define only natural vignetting.

Method E (green): Although the code to extract  $I_{Vig,E}$  is rather complex, creating the input images is straightforward because the DUT does not have to be imaged at fixed positions. When the device in the input image covers most of the image plane and different image intensities can be averaged out over all images, the RAW result leads already to very good results (Figure 3.64).

Post processing methods (x-axis): The results do not show a clearly or consistently superior method. Even more they often show the negative influence of post processing. In general, only the ‘REPAIR’ based methods maintained quality, while other post processing methods caused a quality decrease. As the two blue line plots in Figure 3.68 show, both AoV and KW replacements caused a vignetting overcorrection in the image centre. A median filter has a better outlier stability and gives results closer to the RAW image. However, it often caused steps in the vignetting image. Although a Gaussian filter can blur information, it produced smooth and in comparison quantitatively good results.

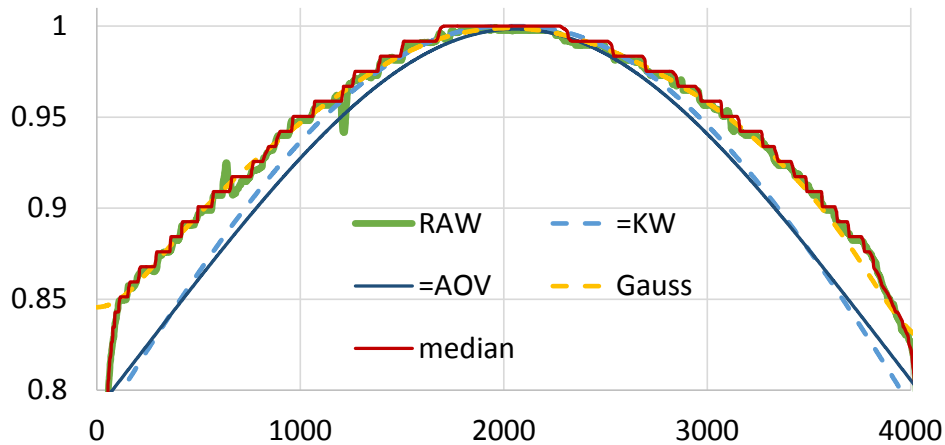


**Figure 3.68: Horizontal line plots through image centre of LPVO results from method E (Figure 3.62a)**

Comparing the influence of all post processing methods on the correction quality it can be seen that ‘+KW’ and ‘Gauss’ produced best results (Figure 3.69). Although the decision of the most suitable post processing method strongly depends on the quality of the RAW image and the shape of measured vignetting, a combination of ‘+KW’ and ‘Gauss’ is proposed.

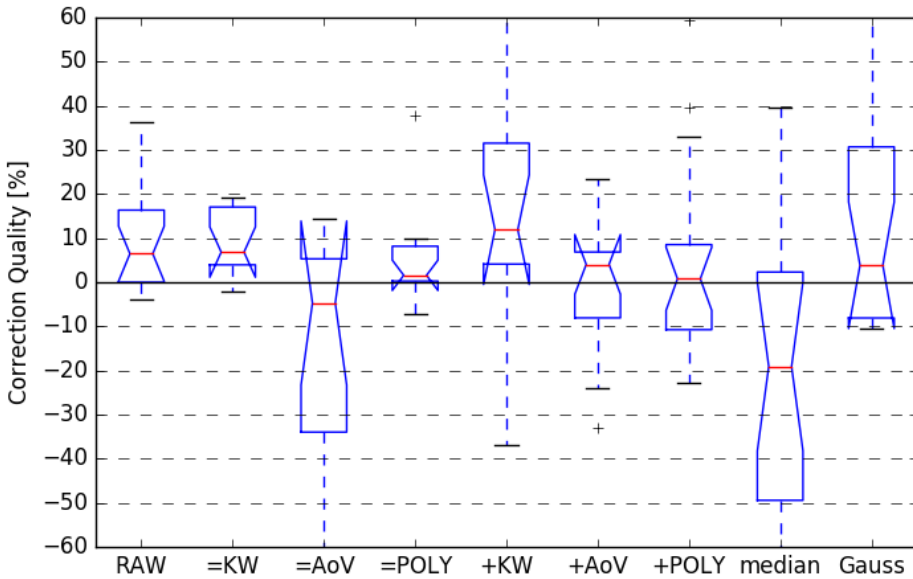


**Figure 3.69: Relative influence  $(Q_{i,j} - Q_i)/Q_i$  of different post processing methods on the correction quality from values shown in Figure 3.64**

### 3.6.5 SENSITIVITY MEASUREMENT

Every image pixel is affected by a different sensitivity in the camera sensor array, due to either inhomogeneity or damage for example from high-energy radiation. Because these effects manifest as high gradient variations, the sensor array sensitivity can be easily obtained from homogeneously illuminated images (such as method A, Subsection 3.6.2.1). The extraction of a sensitivity image ( $I_S$ ) is detailed in Figure 3.70. Herein a set of raw images ( $I_{RAW,i}$ ) is (after removal of the background image ( $I_{BG}$ )) divided by a respective smoothed image ( $I_{smoothed,i}$ ). It was found that a combination of median (kernel size = 3 px) and Gaussian filter (kernel size = 10% of image width) is sufficient to remove deviations from noise and sensitivity. The averaged result image ( $\text{mean}(I_{S,i})$ ) yields the sensitivity image ( $I_S$ ). In order to reduce noise in  $I_{BG}$  either multiple dark current images can be averaged or a linear regression of multiple dark current images at different exposure times can be applied (Section 3.1).

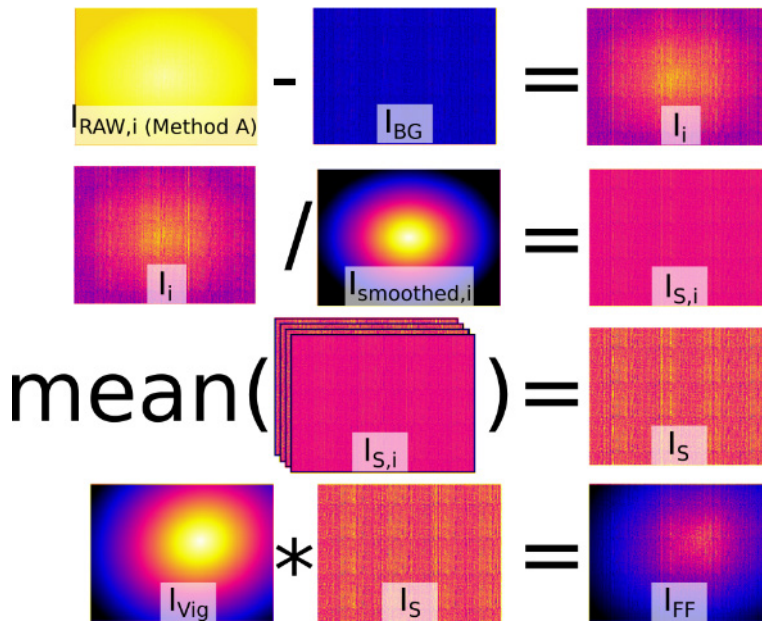


**Figure 3.70: Extraction of pixel sensitivity from raw EL images**

An example of a sensitivity map and the impact of sensitivity correction is shown in Figure 3.71 for an InGaAs camera. Sensitivity inhomogeneity in InGaAs sensor arrays is much more pronounced compared to silicon CCDs, due to differences in the device architecture. Although the deviation appears random, vertical lines and a darker area in the bottom-left part (Figure 3.71a) can be distinguished.

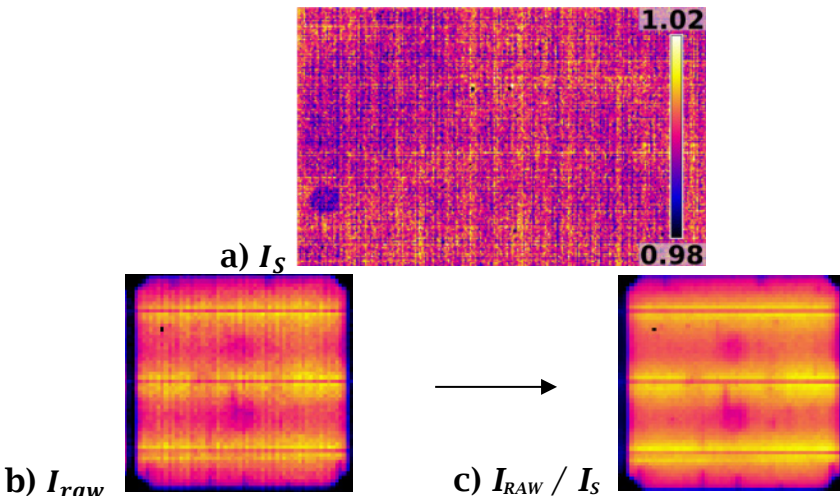


**Figure 3.71: a) Excerpt of resulting sensitivity map for an InGaAs camera; EL image taken with an InGaAs camera before (b) and after (c) sensitivity correction**

Despite the sensitivity inhomogeneity being more pronounced in InGaAs sensor arrays and silicon CMOS sensor arrays, it is also present in silicon CCDs. There, the difficulty in obtaining  $I_S$  is that dividing  $I_{Smoothed,i}$  from  $I_{RAW,i}$  likewise extracts pixel sensitivity, but also image noise. If too few images are averaged and the noise level in  $I_{BG}$  is too high, sensitivity correction can increase image noise. For both CCD cameras tested in this work (CREST, LPVO) over 10  $I_{RAW,i}$  with a signal-to-noise ratio SNR>110 were needed to increase the SNR by about 0.05, respectively 0.1%.

Considering the small increase it may be more advisable to omit sensitivity correction in CCDs and rather filter erroneous pixels with, for example, a threshold median, as detailed in Section 4.4.

### 3.6.6 SECTION SUMMARY

The flat field significantly influences pixel intensity of photovoltaic luminescence images. The main contributors to the flat field are vignetting and pixel sensitivity. The latter was shown to have a minor influence on the flat field corrected image. Therefore, this section focused on several measurement and post processing methods suitable for vignetting removal in EL images.

The most prevalently used vignetting measurement method images a “homogeneous” light source in close proximity to the camera lens. The simplest presented method herein, the method A (direct measurement at short distance with spatial inhomogeneity correction) upgrades this method by acquiring further images of the same source in different orientations to cancel out its inhomogeneity. The produced vignetting correction quality is close to the best methods when a light source, similar to the DUT is used. Due to simplicity and applicability, method A(PV) is proposed for general vignetting characterization.

Method E (vignetting-object separation using pattern recognition) is technically the most advanced method. It images the actual DUT in image plane at random positions, which ensures unchanging imaging

conditions. Amongst all tested methods, it produced the best results. Therefore, method E is proposed for precise luminescence characterisation. It is proposed to fill empty areas within the measured vignetting image with a Kang-Weiss functional fit. To smooth out erroneous pixels, a Gaussian filter can be used.

Other methods, B (discrete spot average), C (local maximum of multiple DUTs), and D (vignetting-object separation from discrete steps) use different approaches and while they may be suitable for specific cases, their performance is usually inferior.

## 3.7 Setup Dependency of the Effective Flat Field

The flat field image ( $I_{FF}$ ) describes the effective spatial non-uniformity of the EL image relative to the emitted EL signal. Its measurement on a planar setup is described in Section 3.6.  $I_{FF}$  may vary depending on the spectrum of the calibration source, lens aperture and exposure time of the camera as well as perspective (rotation and tilt) of the DUT. This section highlights the importance of measuring  $I_{FF}$  of a DUT with a source of a similar waveband. It is shown that  $I_{FF}$  deviates up to 20% if a red screen is used for calibration instead of a PV device (Subsection 3.7.1).

$I_{FF}$  is usually measured for a specific exposure time and aperture. Subsection 3.7.2 visualizes the influence of different exposure times and presents a correction of the influence from a manual camera shutter.

Due to the inverse-square law, EL emission is clearly distance dependent. Subsection 3.7.3.1 will however show that this law does not apply to the pixel-specific- but only the per-area integrated EL signal. Perspective distortion (tilt and rotation) cannot be avoided with on-field imaging (for example obtained by drones). The final Subsection 3.7.3.2 calculates the emission dependence on the emission angle, demonstrates an intensity correction and defines valid image positions as function of DUT tilt and rotation.

### 3.7.1 EMISSION WAVEBAND

Figure 3.72 shows the results of a flat field measurement (method A, Subsection 3.6.2.1) for three different light sources: (a) LCD screen displaying red image, (b) thin film module and (c) silicon module taken at two laboratories (CREST, LPVO). The wavelength ranges of these sources are approximately evenly distributed (600-800-1000 nm). As the difference images (Figure 3.72 right) show, vignetting differs more strongly for shorter wavelengths ( $b - a > c - b$ ). Whether this is caused by the non-linear chromatic aberration of the camera lens or different angular distribution functions between the examined sources is an open question.

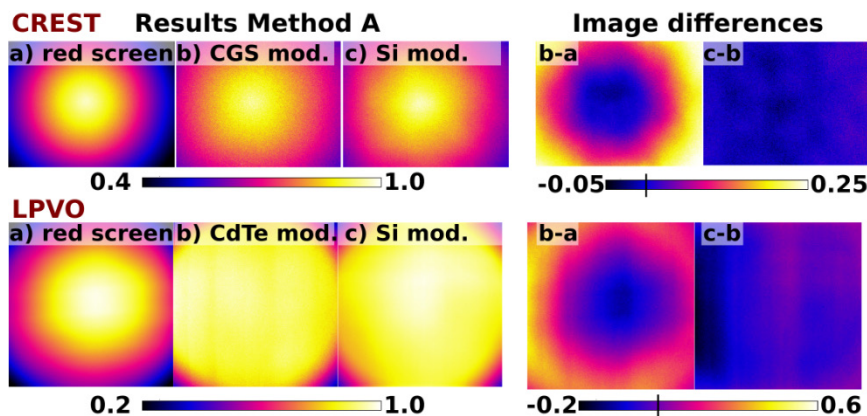


**Figure 3.72: Left: results of vignetting method A for three different LS (a-c); right: their differences**

Figure 3.73 shows radially averaged results, where the differences increase from image centre to corner. Between the red screen and the thin film module, vignetting factor differences can make up to 25% (CREST) or 60% (LPVO) for pixel values (Figure 3.72 right) or 25% for radial averages. Imaging the right waveband is therefore the most important factor for vignetting measurement.

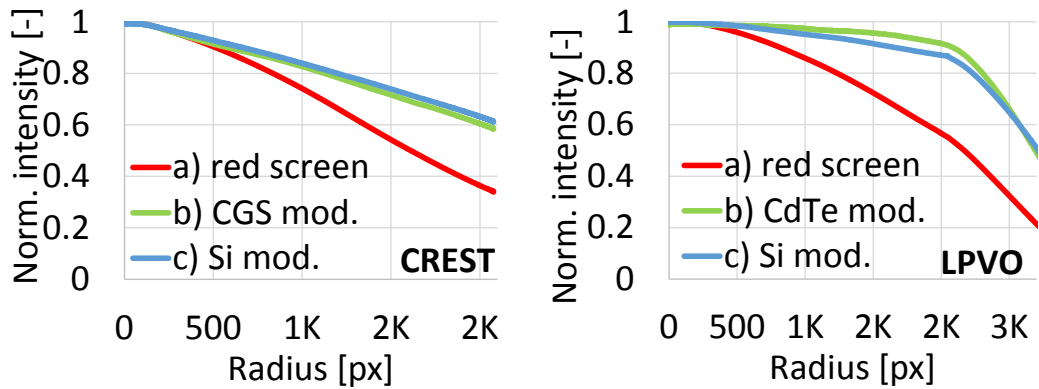


Figure 3.73: Radial averages for image (a) to (c), shown in Figure 3.72

### 3.7.2 CAMERA SETUP

#### 3.7.2.1 EXPOSURE TIME

If the imaging camera uses a mechanical shutter, its finite opening and closing time can cause an additional vignetting effect. Its significance is demonstrated in the following example: For an assumed shutter opening/closing time of 30  $\mu\text{s}$  and a dwell time (fully open) of 20  $\mu\text{s}$ , the central point is exposed for 80  $\mu\text{s}$ . This is four times longer than the corner areas. For an exposure time of 1 s the maximum difference, caused by the shutter would be still 6%. This time-dependent shutter vignetting ( $V_S(t)$ ) can be separated from EL images ( $I_{EL}$ ) as the ratio with a reference EL image ( $I_{EL,ref}$ ) taken at significantly higher exposure time ( $t_{ref}$ ):

$$V_S(t) = \frac{I_{EL}}{I_{EL,ref}} \frac{t_{ref}}{t} \quad (3.71)$$

The result is prone to noise especially for low  $\frac{t_{ref}}{t}$ , above background- or over low luminescence areas. A median filter can be used for noise reduction. The effective vignetting can then be calculated by multiplying shutter dependent- ( $V_S(t)$ ) and base vignetting ( $V_0$ ) (preferably measured at  $t_{ref}$ ):

$$V(t) = V_s(t) \cdot V_0(t_{ref}) \quad (3.72)$$

The time dependence of shutter vignetting is visualised in Figure 3.74, where the two shortest exposure times even caused a partial shutter opening.  $V_s(t)$  was taken from the displayed raw EL images, relative to one taken at  $t_{ref} = 750$  ms. The homogenous light intensity of the corrected EL images (3<sup>rd</sup> row) indicates the applicability of this method.

However, Equation 3.72 requires shutter vignetting maps to be available for multiple exposure times and only enables calculation of the effective vignetting within the range of available measurements. Vignetting maps for exposure times in-between available measurements are obtained using linear interpolation.

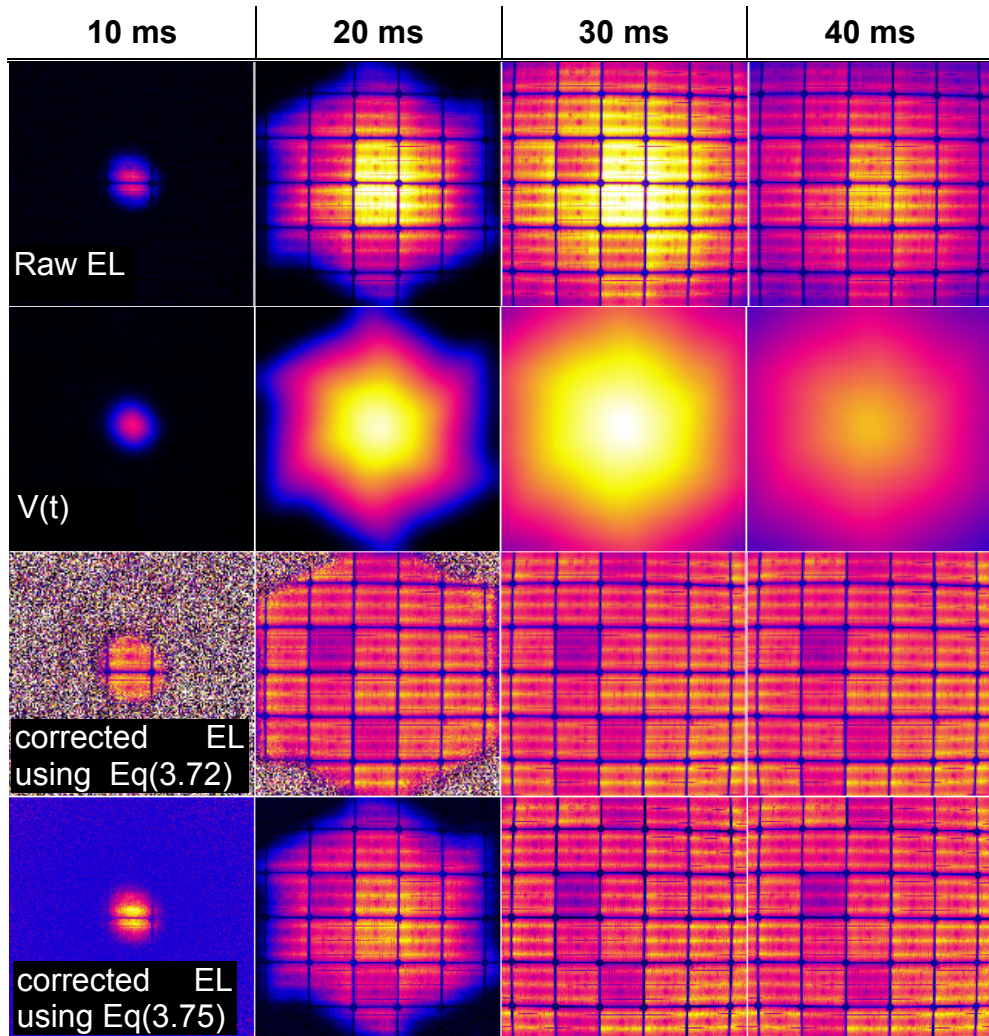


**Figure 3.74: EL images at different exposure times: uncorrected (raw) images (1st row); extracted vignetting map (2nd row); vignetting corrected Images (3-4th row); Camera: FLI ML16803, f/4**

$V_0(t_{ref})$  contains a certain amount of shutter vignetting ( $V_S$ ). Therefore, extrapolating towards higher exposure times underestimates  $V_S$ .

Figure 3.75b shows that the trend of  $V_S(t)$  is inversely proportional to the exposure time. Only the shortest exposure times (10, 20 ms) do not follow that trend. Figure 3.74 shows that at these times the shutter only opened partially.

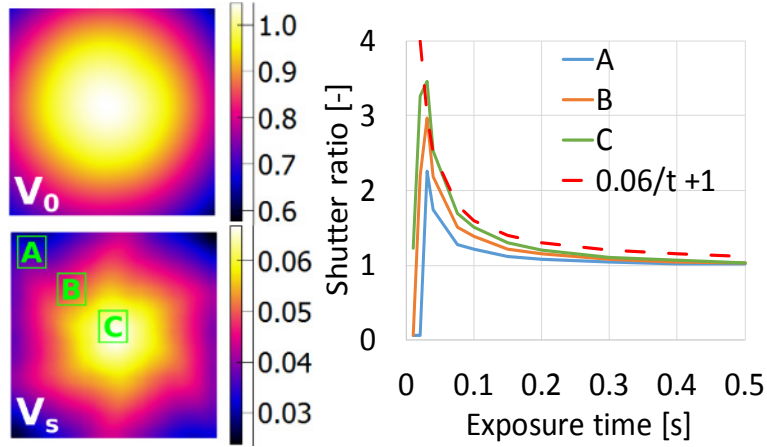


**Figure 3.75: Resulting base and shutter vignetting maps  $V_0, V_s$  (left) and shutter ratio ( $V_s(t)$ ) for different exposure times for three different regions A-C, shown left; Red dotted: example shutter ratio equivalent to region C; Camera FLI ML16803, f-number: f/4**

Noting the relationship  $V_s(t)$ ,  $V_s$  can be calculated as  $f(t^{-1})$  as the ascent of a linear equation through the origin (calculated using the temporal average mean()) as follows:

$$V_s = \text{mean}\left(\frac{V_s(t) - 1}{t^{-1}}\right) \quad (3.73)$$

To obtain a shutter independent (base) vignetting map ( $V_0$ ), the shutter ratio, relative to the shutter reference time ( $t_{ref}$ ) and vignetting time ( $t_0$ ) has to be removed as follows:

$$V_0 = \frac{V_0(t_0)}{1 - \left(\frac{V_s}{t_0} - \frac{V_s}{t_{ref}}\right)} \quad (3.74)$$

Both resulting, time independent maps  $V_0$  and  $V_s$  are shown in Figure 3.75 for the setup, displayed in Figure 3.74. The effective vignetting ( $V(t)$ ) can now be calculated as:

$$V(t) = \left(1 + \frac{V_s}{t}\right) \cdot V_0 \quad (3.75)$$

As shown in the last row of Figure 3.74, this model only works for exposure times, where  $V_s(t) \propto \frac{1}{t}$ . Therefore, EL images acquired in less than 30  $\mu$ s are not corrected sufficiently. Correcting for shutter vignetting is omitted in the vignetting method comparison (Subsection 3.6.4) because the in-plane flat field methods B-E (Subsection 3.6.2) have exposure times similar to the actual EL measurements.

### 3.7.2.2 LENS APERTURE

The camera aperture not only influences incoming light intensity but also its spatial distribution. As Figure 3.76 shows, both shutter and base vignetting change for different apertures. Increasing f-numbers emphasize the aperture visibility in  $V_s$ .

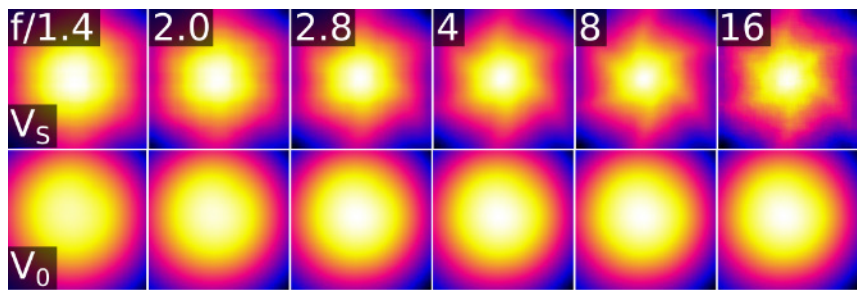


**Figure 3.76:** Normalised shutter ( $V_s$ ) and base ( $V_0$ ) vignetting maps for different f-numbers; Camera FLI ML16803.

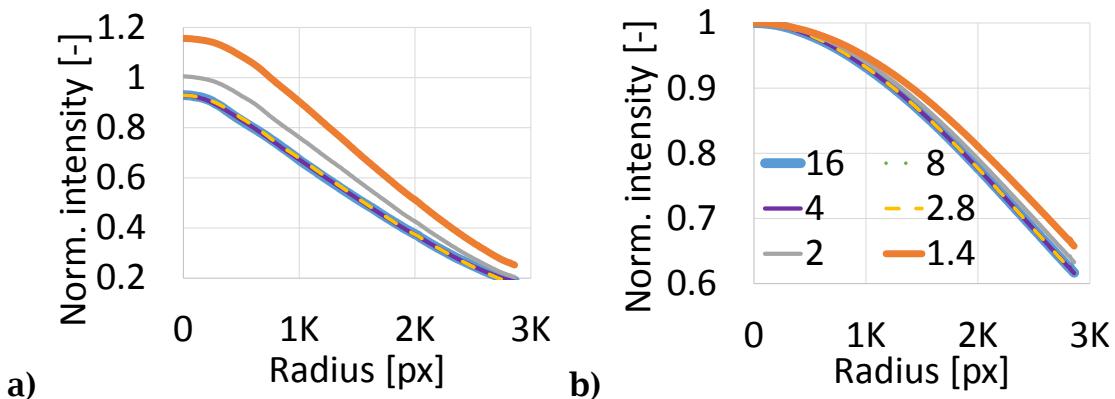


**Figure 3.77:** Radially averaged (a) shutter and (b) base vignetting over pixel radius for vignetting maps, shown in Figure 3.76

To quantitatively compare the results in Figure 3.76, the shutter and base vignetting maps were both scaled according to  $\max(V(t = 0.05s)) = 1$ .

Figure 3.77 shows that base vignetting increases towards the image corner especially for f-numbers 1.4 – 8. It also shows that the influence of shutter vignetting decreases for increasing f-numbers. This is as expected since light only passes through the central part of the shutter when the aperture is small (and therefore the f-number is high). Therefore, the period during which the shutter influences vignetting is reduced. When the aperture is large (small f-number) light passes through the majority of the shutter area. This increases the influence of the shutter (Figure 3.78).

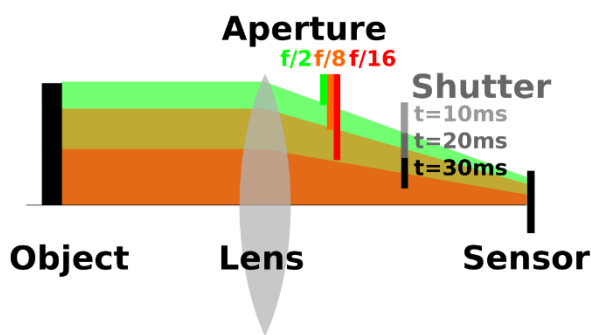


**Figure 3.78: Influence of different apertures on shutter vignetting;**  
**Whilst light through an open aperture (green) is influenced by all shutter positions, light through a closed aperture only ‘sees’ part of the shutter**

For cameras with a limited number of aperture positions, it is recommended to measure the flat field for all aperture positions used, rather than to correct the aperture influence in a similar fashion as described by Equation 3.75.

### 3.7.3 PERSPECTIVE

#### 3.7.3.1 DEVICE DISTANCE

Measuring the flat field in close distance (method A, Subsection 3.6.2.1) is based on the assumption that the EL intensity change with device distance is negligible. However, the inverse square law states that intensity  $\propto \frac{1}{\text{distance}^2}$ . To analyse this dependency, four EL images ( $I_{ref}, I_{1-3}$ )

of the same c-Si module at different distances to the camera were taken (Figure 3.79a). To extract the relative intensity differences ( $R_{i,j}$ ), the following steps were applied:

For both examined flat field images ( $I_{FF,1}, I_{FF,2}$ ) with index ( $i$ ):

For all EL images ( $I_{ref}, I_{1-3}$ ):

1. Subtract the background image.
2. Divide the result by the flat field image ( $I_{FF,i}$ ).
3. Remove the lens distortion.

For image  $I_{1-3}$  with index ( $j$ ):

4. Obtain perspective transformation (homography) matrix ( $H_{ref \rightarrow j}$ ) from a comparison of detected patterns in  $I_j$  and  $I_{ref}$  and fit the perspective of  $I_{ref}$  to the one of  $I_j$ :  
 $I_{ref \rightarrow j} = f(I_{ref}, H_{ref \rightarrow j})$  (Subsection 4.7.2.1).
5. Calculate ratio  $R_{i,j} = \frac{I_j}{I_{ref \rightarrow j}}$ .
6. Remove the edges, created by fitting errors of both images ( $I_{ref \rightarrow j}, I_j$ ) by setting all areas where the edge gradient is higher than a given threshold ( $T$ ) to NaN (not a number).

$$R_{i,j} \left[ \left( \frac{dR_{i,j}}{dx} \right)^2 + \left( \frac{dR_{i,j}}{dy} \right)^2 > T \right] = \text{NaN} \quad (3.76)$$

7. Apply a median filter (kernel size = 200 px) on  $R_{i,j}$ , ignoring all NaN.

As Figure 3.79c,d shows, the resulting ratios range between  $\pm 10\%$  and appear to be mostly influenced by the chosen flat field image (Subfigure b).

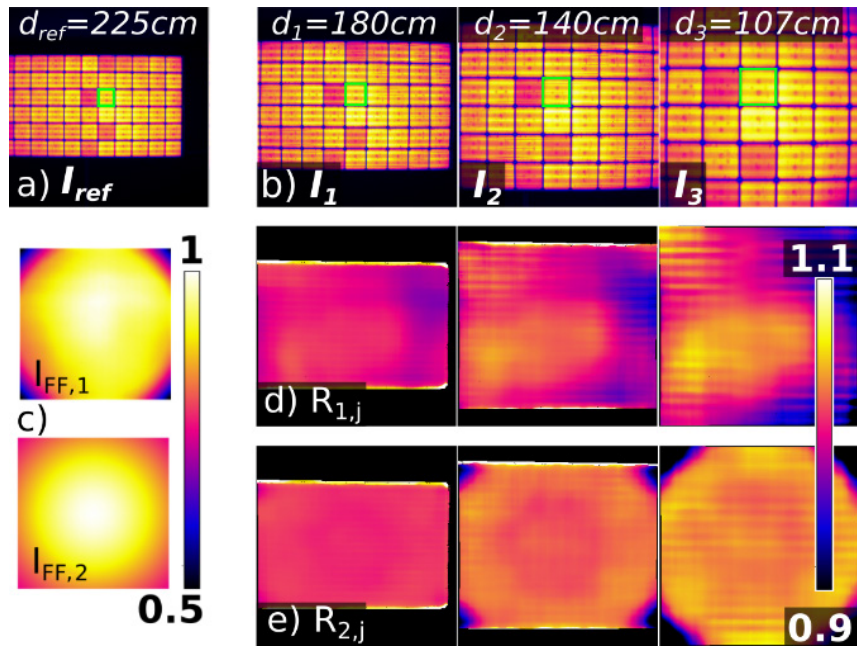


**Figure 3.79:** a-b) EL images of a Si module at different distances (LPVO);  
 c) Examined flat field images; d) Intensity ratio ( $R_{i,j}$ ) from  $d_{1-3}$  to reference  $d_0$  using  $I_{FF-1}$ ; e) same, using  $I_{FF-2}$

The measured intensity values within the green ROI (Figure 3.79a) are shown in Figure 3.80. If the sum of all four ROIs is plotted relative to the biggest ROI at  $d_3$  the trend follows the inverse square law. However, if the ROI averages are compared then the result remains constant. Therefore, it is concluded that the distance between camera and DUT has no influence on the specific pixel intensity.

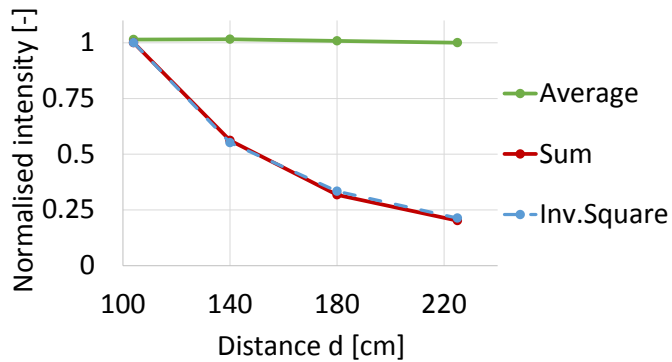


**Figure 3.80:** Normalised average and sum values of ROIs, shown in Figure 3.79a,b for different LS distances.

### 3.7.3.2 DEVICE TILT AND ROTATION

Maintaining an orthogonal angle between camera axis and DUT is often hard to achieve - especially in outdoor or on-field imaging.

The radiation exchange between two surfaces (camera and DUT), whereby surface1 << surface2, can be weighted using a view factor ( $\varphi_{12}$ ) [89].  $\varphi_{12}$  is a derivate of the inverse square law:

$$\varphi_{12} = \frac{1}{\pi} \int \frac{\cos(\beta_1) \cdot \cos(\beta_2)}{d^2} dA_2 \quad (3.77)$$

$$\sum_{i,j} \varphi_{12} = 1 \quad (3.78)$$

The parameters introduced in this section are shown diagrammatically in Figure 3.81.

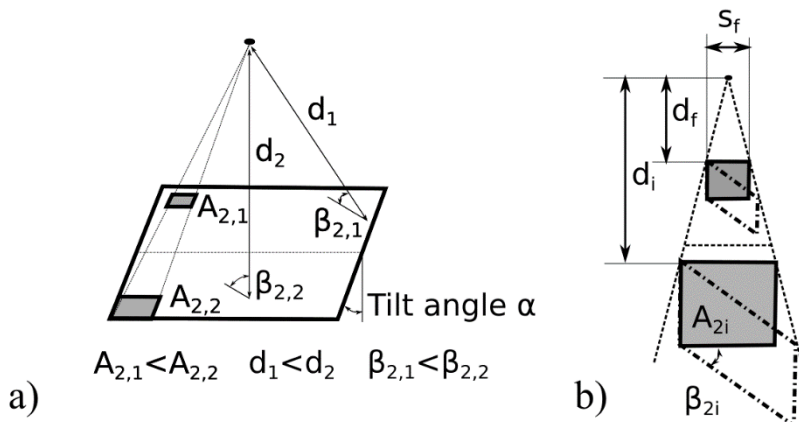


**Figure 3.81:** a) Perspective schematic of the view factor model; b) Calculation of the differential plane area ( $A_{2i}$ ) from distance and view angle

For EL imaging the Equation 3.77 can be simplified using the following assumptions:

- All light rays enter the camera lens at a normal angle, therefore  $\beta_1 = 0$ . This is valid, if vignetting (i.e. decreased light intensity for increasing  $\beta_1$ ) has already been corrected.
- The physical area ( $dA_2$ ) is discretised for every image pixel ( $i$ ) and becomes  $A_{2i}$ . Using the theorem of intersecting lines (Figure 3.81b)

and noting that the effective area increases with increasing view angle,  $A_{2,i}$  can be described using:

$$A_{2i} = \frac{\left(s_f \cdot \frac{d_i}{d_f}\right)^2}{\cos(\beta_{2i})} \quad (3.79)$$

Where  $d_f$  is the focal length respective distance to plane centre [mm] and  $s_f$  is the size of one pixel in focal plane in x,y [mm]. Within the range of one pixel,  $\beta_2$  and  $s$  are considered constant. This enables discretizing Equation 3.77 for every pixel ( $i$ ):

$$\varphi_{12} = \frac{\cos(\beta_{2i}) \cdot A_{2i}}{d_i^2} \quad (3.80)$$

If  $A_{2,i}$  is substituted by Equation 3.79 then the only two variable parameters  $d_i$  and  $\cos(\beta_{2i})$  cancel each other out. Noting Equation 3.78, the constants also cancel out. With this model and assuming a perfect Lambertian surface,  $\varphi_{12}$  does not change at all for different angles! However, at angles  $>60^\circ$  light intensity of a PV module decreases noticeably (Figure 3.84a, b). In this experiment, the angular dependence of EL light intensity, relative to  $0^\circ$  was calculated (Figure 3.82).

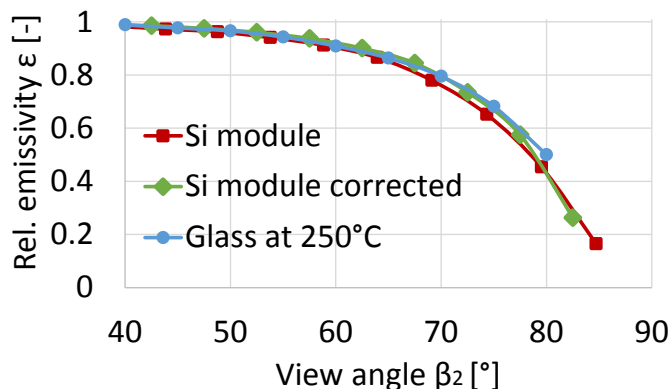


**Figure 3.82: Comparison of angular dependency of emissivity, relative to  $\beta_2 = 0^\circ$ ; Values for glass taken from [90]**

As expected, the calculated result is almost identical to the emissivity values ( $\varepsilon$ ) for glass, which are commonly used for thermography measurements.  $\varepsilon$  is obtained from the average EL signal of the angled module relative to the one of the module at  $0^\circ$  after correcting both images for vignetting, dark current and perspective. The red plot shows  $\varepsilon$  over DUT tilt angle ( $\alpha$ ). In this setup, the distance between camera and device midpoint ( $d_f$ ) is 1500 mm.

This, in comparison to the device dimension, relatively short distance causes the effective view angle ( $\beta_2$ ) to vary (Figure 3.83). Since this variation is not symmetrical, the red plot in Figure 3.82 does not represent the actual situation. To correct for these variable  $\beta_2$ , the median of all relative images was calculated for  $\beta_2$  bins of  $5^\circ$ . The distance of the resulting green plot even decreased relative to the emissivity of the glass.

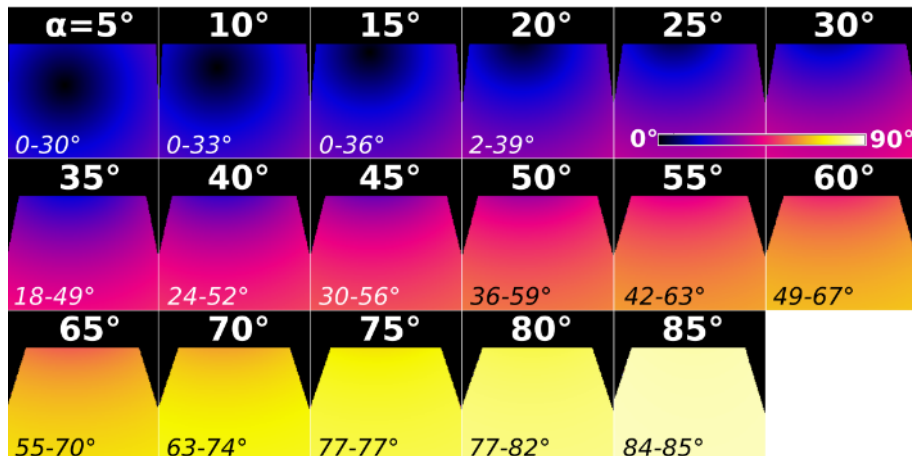


**Figure 3.83: Comparison of calculated effective view angles ( $\beta_2$ ) [ $^\circ$ ] for different DUT tilt angles ( $\alpha$ ) in Figure 3.84a**

To correct for intensity deviation from perspective distortion, all images (Figure 3.84a) were divided by their angular dependent relative emissivity values (Figure 3.84e). The result is shown in Figure 3.84d.

In comparison to Figure 3.84b it is apparent that the intensity decrease for angles  $>60^\circ$  is corrected. Subfigure (c) shows images (b) after division by their respective average (normalisation). For  $75^\circ$  and  $80^\circ$  light intensity slightly increases from image bottom to top. This trend is also corrected in (d). Only the last image ( $85^\circ$ ) shows inhomogeneous intensities.

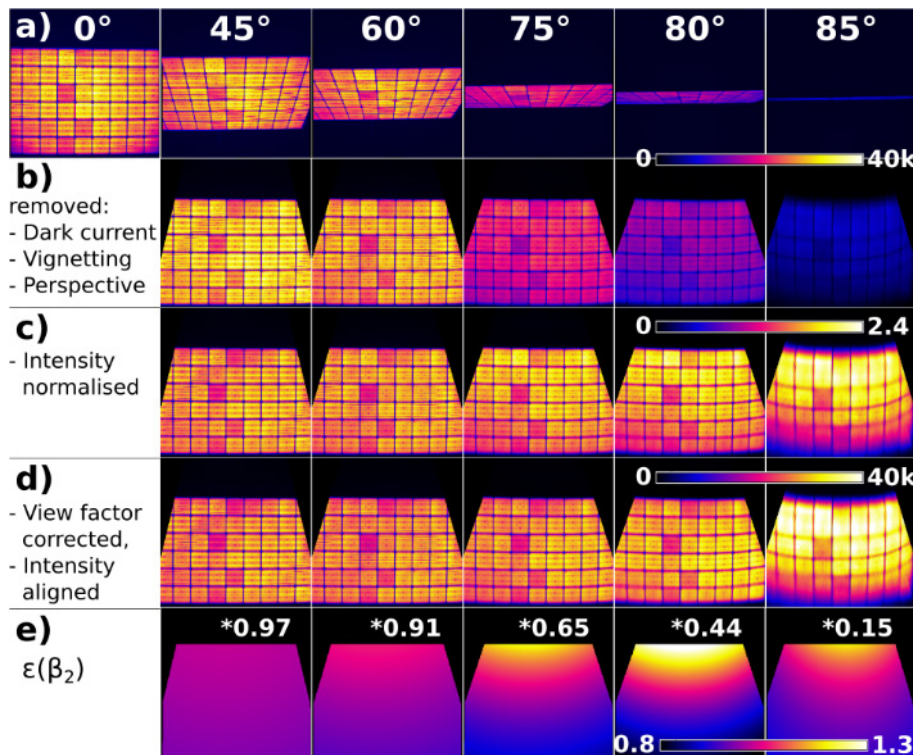


**Figure 3.84: a) EL images of a Si module imaged at variable tilt angles; b-d) different corrections from (a); e) relative emissivity**

As the original image in (a) shows, this is because the module edge points required for pose estimation could not be tracked precisely in this highly distorted and defocussed image.

To show their individual trends, the emission factor maps in (e) were scaled to a value, displayed on the image top. Without that scaling, a gradient within these maps would by hardly visible.

Taking this into account, as well as the fact that emissivity below 60° is almost constant, one could say intensity correction for tilted PV devices is not an issue for EL images. Depending on the imaging setup, this statement can be acceptable.

However, especially in outdoor imaging of larger areas (such as PV arrays) and under certain conditions, these deviations can become critical. In Figure 3.85, a 100x100 m PV array, as seen by a drone was simulated. The emissivity factor, shown in Figure 3.85c,d decreases in this example down to 75% at the corners of the drone's field of view - excluding vignetting.

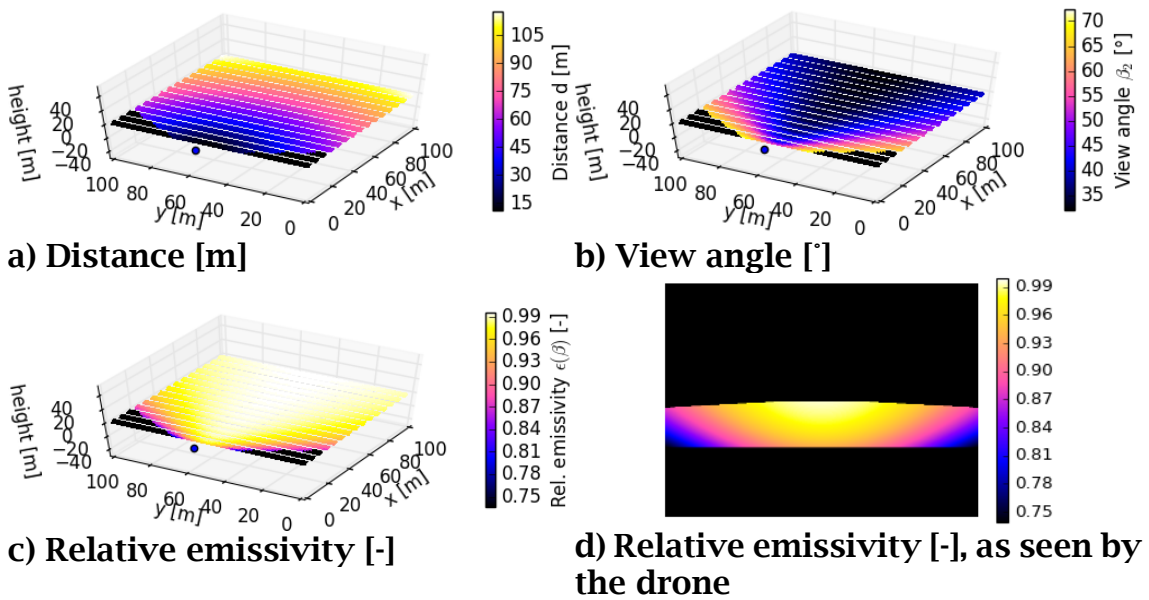


**Figure 3.85: Simulated optical parameters of a PV array from a drone's perspective; Drone position xyz: -10m,50m,5m (blue dot in (c)); Camera field-of-view: 60°**

An indication whether an intensity correction should be considered is given in Figure 3.86. If a maximum intensity decrease of 5% is accepted, view angles up to 50° are acceptable (Figure 3.82). As Figure 3.83 shows, the effective view angles not only depend on the objects orientation, but also its position within the image. Figure 3.86 therefore indicates areas to avoid, depending on the DUT's rotation and tilt. For a camera field-of-view (FOV) of 30° and a DUT rotation and tilt of 40° (red line), only image areas in the top left of the image would be acceptable. For a rotation of 15° and no tilt most areas in the image will have view angles <50° and only a small area in the image (x:0-2,y:8-10) would be problematic for FOV  $\geq 45^\circ$ .

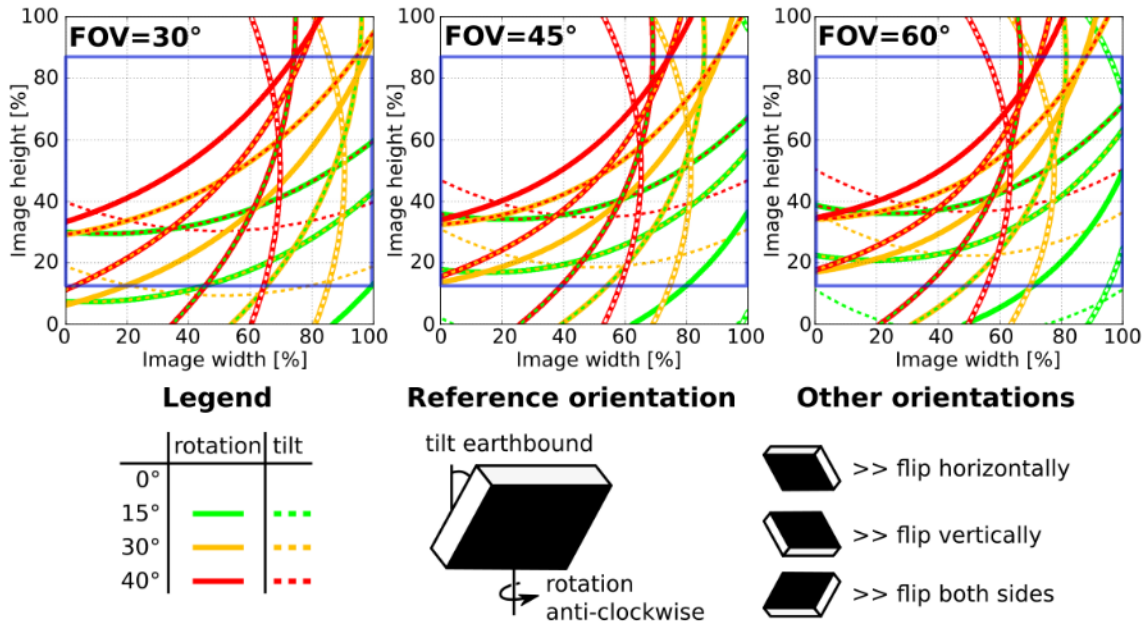


**Figure 3.86:** Image positions, where view angle  $\beta_2 \leq 50^\circ$  for a combination of different tilt and rotation angles of the measured PV device; a PV device imaged behind convex curves will have an intensity decrease of  $>5\%$  and therefore should be avoided or corrected for; blue box: image area, if camera aspect ratio is  $\frac{3}{4}$

### 3.7.4 SECTION SUMMARY

Flat field correction is essential for quantitative EL measurements to remove intensity distributions within EL images but also to allow inter-comparison across different imaging systems. Measured flat field images depend on the camera setup as well as orientation of the imaged DUT. These influences are analysed in this section.

It is shown that the flat field ( $I_{FF}$ ) depends on the emitted waveband of the imaged DUT. In the examined case,  $I_{FF}$  differed up to 20% towards the image corners between an imaged red LCD screen and a PV module. A comparison of different aperture adjustments shows an up to 5% higher flat field at the image corner between f1.4 and f16. Therefore, it is proposed to measure  $I_{FF}$  for each applied aperture and waveband rather than to correct for its influence. Other influences, namely exposure time and perspective, can be corrected for.

In the examined case for exposure times shorter than 100 ms the intensity varied 200-300% due to a mechanical shutter. However, this additional

shutter vignetting decrease is inversely proportional to exposure time. Therefore, it is proposed to only calculate the effective vignetting from base- and shutter vignetting maps for exposure times close to the opening/closing time of the shutter.

The imaged PV devices are not perfect Lambertian (diffuse) light sources. For view angles higher than  $50^\circ$  their relative emissivity decreases. Therefore, especially highly titled devices will appear darker. Depending on the imaging setup, this decrease can be corrected for by dividing the image by an emissivity factor map obtained from the DUT orientation.

## 3.8 Chapter Summary

When establishing an EL imaging setup, multiple calibration images should be taken in advance to reduce later measurement time and to enable image correction (Chapter 4):

If the light conditions within the imaging setup are immutable, dark current can be calculated as a function of exposure time. For this, multiple images under open circuit should be taken at a range of different exposure times. The subsequent fitting process was detailed in Subsection 3.1.2.

The current IEC draft 60904-13 in electroluminescence measurement suggests a minimum signal-to-noise ratio (SNR) of 15 for industrial and process control and a SNR of 45 for lab measurements. In order to minimise exposure time, it is suggested to calculate the SNR from two EL images and one background image (Equation 3.16). It was further shown that the noise level of an image is not constant, but rather a noise-level-function (NLF) of the EL signal intensity. A spatially resolved SNR map can be used to calculate part of the intensity-based uncertainty (Section 6.1). This chapter presented the simple, yet effective Tenengrad parameter to measure relative image sharpness (Equation 3.3). This can be used to find best focus level. The expression of absolute image sharpness as standard deviation of a Gaussian blur kernel or as factor on the image resolution

was presented in Subsection 3.4.3. The latter parameter can be directly used to determine the minimum resolvable object size. This knowledge enables determination of the ability to resolve features (such as cracks and fingers) in EL images.

A novel way to measure the point spread function (blur) using a commercially available compact disc (CD) is presented in Subsection 3.4.4.6. A programmatically simpler method to obtain a radially invariant PSF using a V-shaped mask or a printed spoke pattern was shown in Subsection 3.4.4.3 and 3.4.4.4.

Several methods are discussed in literature to measure the image flat field ( $I_{FF}$ ). The methods often rely on the assumption that the calibration device is spatially homogenous. As was shown, this can cause erroneous results. Section 3.6 therefore proposed different methods to measure and functionally fit  $I_{FF}$ . Even without any calibration  $I_{FF}$  can be estimated to a certain extent. A method imaging a PV device in the image plane at multiple random positions (Subsection 3.6.2.5) was found to give best results in a quantitative comparison.

The last Section 3.7 further described  $I_{FF}$  as function of exposure time, aperture, wave band and perspective orientation. Correction for exposure time and perspective were discussed in Subsection 3.7.2 and 3.7.3. It was shown that a PV device can be described as a diffuse Lambertian surface up to an angle of 50°. This reduces effort when rectifying perspective in EL images.

The source code, used to calculate the signal-to-noise ratio, to measure and validate sharpness, flat field, lens- and perspective distortion is made publicly available and is embedded in the image processing software dataArtist (Appendix 3).

# 4 IMAGE CORRECTION

To correct EL images, related distortions must be removed. This chapter covers the implemented image correction routine (Figure 4.1) using two EL images as well as a dedicated camera calibration file. The routine sequence is chosen for distortions to not impair subsequent steps.

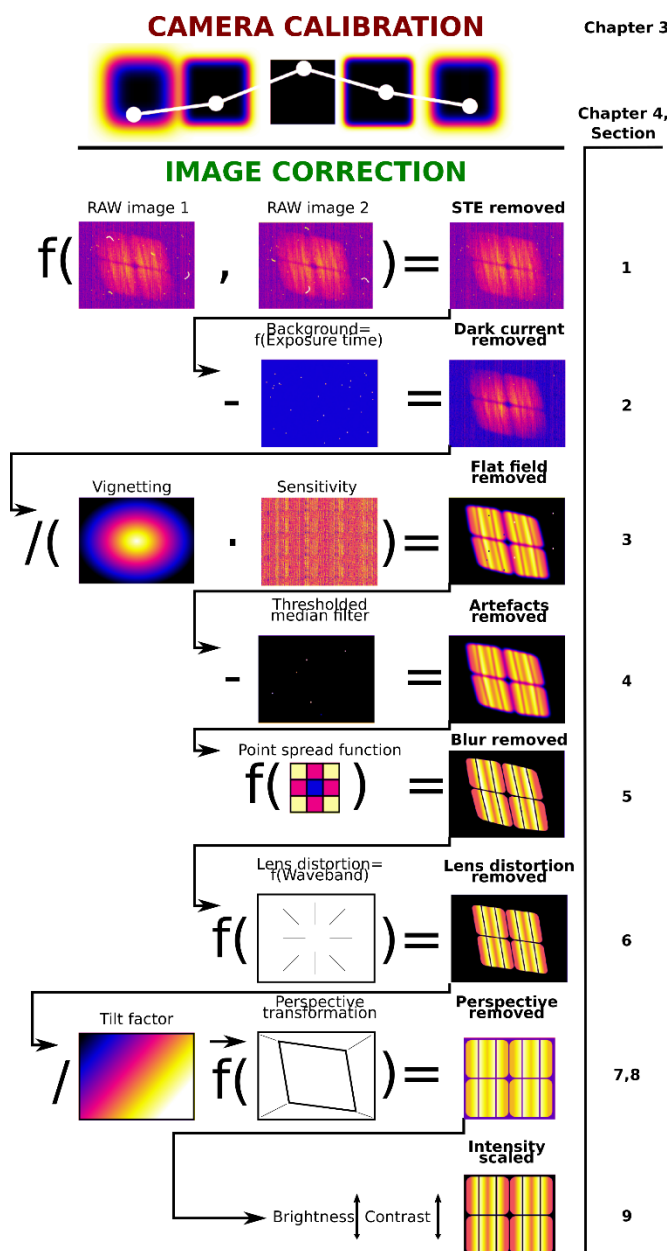


Figure 4.1: Overview of Chapter 4

First, temporal imaging artefacts (single-time-effects) are removed through evaluating changes in two EL images (Section 4.1). Using results from camera calibration (Chapter 3), the dark current which offsets the EL signal is removed (Section 4.2). Spatial image distribution is corrected for in the following Section 4.3. The removal of remaining artefacts is described in Section 4.4. Methods to sharpen images and to remove lens distortion are detailed in Section 4.5 and 4.6. Position and orientation of PV devices in EL images is detected and corrected for in Section 4.7. Precise alignment of two EL images is described in Section 4.8. Finally, intensity normalization (Section 4.9) ensures equal image contrast and brightness.

## 4.1 Single-time-effects

This section discusses the statistics and removal of specific EL image artefacts, called single-time-effects (STE). STE are caused by cosmic particles such as heavy ions, along with neutrons and protons with energies above 10 MeV [91]. When these mainly space-born particles cross the sensitive region of the CCD matrix, they cause effects of ionisation and lead to spots, which are only visible once after signal readout.

STE increase the intensity of affected pixels. Depending on whether STE occur in the EL image or in the background image, they are visible in the background-corrected EL image as bright or dark spots. In the latter case, the small spots or straight to curvy lines caused by STE can be conceivably confused with cell defects. In this section the intensity offset due to STE as well as their occurrence over time is evaluated. For the examined setup, it is shown that the disruptive influence of STE is visible for cell voltages under 0.65 V. For this case, a robust STE removal method is proposed using an additional EL image taken in series.

STE can be distinguished from hot pixels [92] by comparing two images taken in series with the same exposure time (Figure 4.2). Whilst hot pixels will remain constant in place and intensity, the probability of STE to occur

twice at the same time is negligible. STE saturate CCDs bit by bit. For space-borne CCDs Hill et al. reported that an exposure time of 1000 s would affect already 2.5% of the image [93].

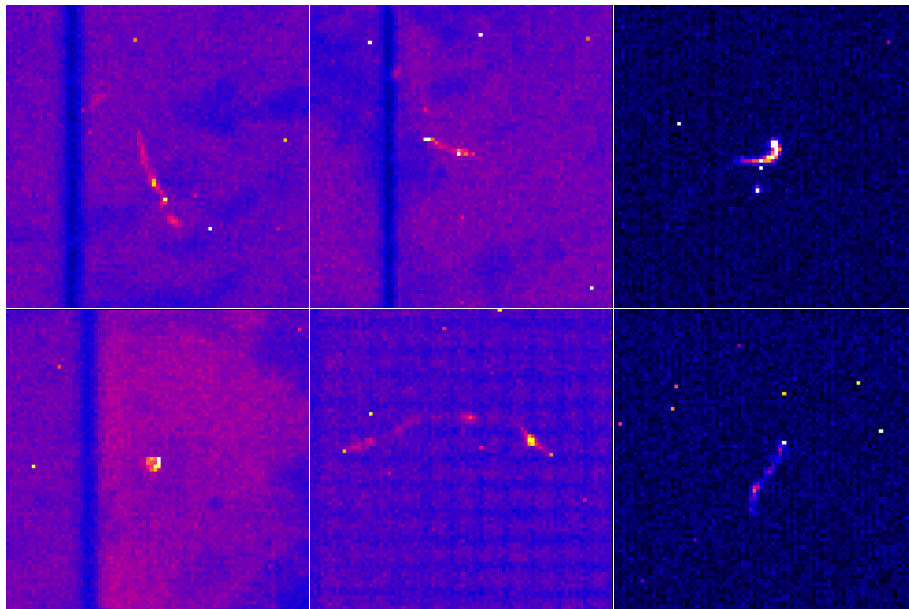


**Figure 4.2:** Selection of STE with different size and intensity; hot pixels are visible as single bright pixels

#### 4.1.1 STE MEASUREMENT AND STATISTICS

The following analysis describes the visibility of STE as detected in one cell of a 9x4 c-Si PV module (Figure 4.3).

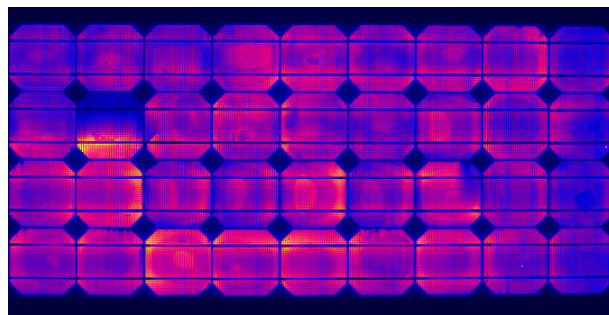


**Figure 4.3:** EL setup, used for statistical analysis on STE in this section

The results depends on the camera, the PV device and the EL imaging setup. For the examined setup, 116 background images were used. The images were taken with a SensoCam HR-830 camera between 14/04/2015

and 08/05/2015. An image mask ( $M_{STE}$ ), marking the position of STE, was created as follows:

1. Select an image pair of two images ( $I_1, I_2$ ) taken in series at the same exposure time.
2. Determine the noise-level-function ( $NLF$ , standard deviation over pixel intensity) as described in Subsection 3.2.2.5.
3. Calculate the difference image ( $I_{diff} = I_1 - I_2$ ).
4. Create a STE free template image from the local minimum:

$$I_{min} = \min(I_1, I_2) \quad (4.1)$$

5. Mask STE ( $M_{STE}$ ) as all pixel indices where the difference of both images exceeds the local  $NLF$  as:

$$M_{STE} = I_{diff} > 4 \cdot NLF(I_{min}) \quad (4.2)$$

6. In order to remove the image noise from  $M_{STE}$ , remove all positive elements that have no positive neighbours. This method can also remove STE consisting of only one pixel. However, the number of these pixels is small relative to otherwise remaining noise.

The number of STE was calculated as the number of spatially connected clusters within  $M_{STE}$  and can be seen in Figure 4.4a for different exposure times. As expected, the number of STE increases linearly with time. The average STE size was determined as the number of positive elements in  $M_{STE}$  divided by the number of STE identified. The result is shown in Figure 4.4b. The distribution of different STE sizes reduces with increasing exposure time because of the similarly increasing number of STE averaging the result.

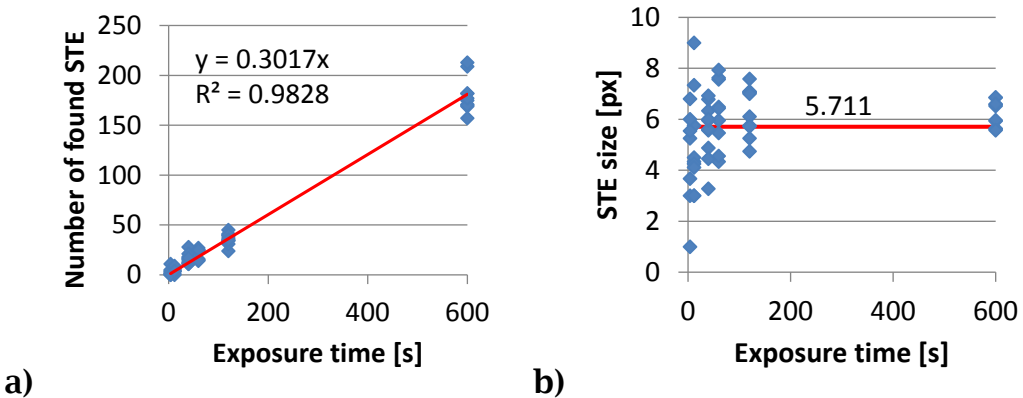


**Figure 4.4: STE development over exposure time**

A probability density function (PDF) of the STE pixel intensity was extracted from the difference image ( $I_{diff}$ ) at all STE positions ( $M_{STE}$ ) and averaged for all image pairs. The result (Figure 4.5) shows that the PDF can be approximated by an unbounded Johnson SU distribution (JSU) [94]. The JSU is a transformation of the normal distribution. JSU was chosen as best fit amongst 82 continuous distributions within Pythons `scipy.stats` package [95].

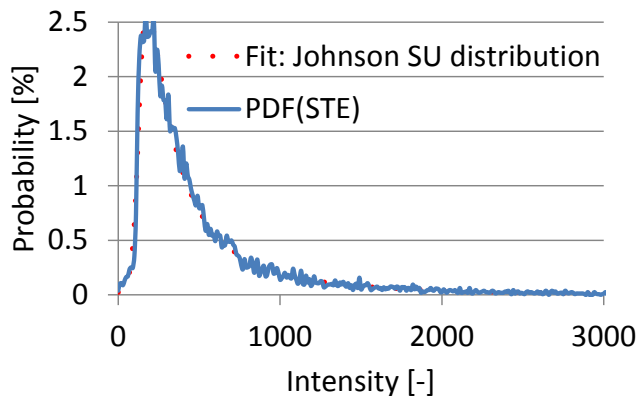


**Figure 4.5: Blue: Probability density function (PDF) of STE over pixel intensity; Red dots: PDF fit using a Johnson SU distribution**

Using the ascent and average STE size (Figure 4.4) as well as the ratio of PV cell size to image size, the probability of one STE being found in a specific cell of the DUT can be quantified (Figure 4.6). The plotted blue line indicates that on average every cell will have one STE at exposure times longer than 200 s. Given that many EL images are taken with longer

exposure times, this would mean that many defects identified from single images might actually be STE.

The visibility of features, such as STE, depends on the relative intensity difference. According to Webers law [96], the visibility threshold was found to be independent from image intensity under well-lit (photopic) conditions:

$$\frac{\Delta I}{I} = \text{constant} \approx 10\% \quad (4.3)$$

The visibility of STE in Figure 4.6 (red lines) is quantified for three different probabilities which can be explained as follows: The ‘50x50%’ case marks the probability of an STE with average intensity higher than the average EL signal. In contrast to this, the ‘1x1%’ case compares the effect on an STE within the highest one percent of the PDF (Figure 4.5) to the darkest 1% of a Gaussian distributed EL signal. This case is considered as the worst-case scenario. The resulting ratios are indirectly proportional because STE intensity remains constant whilst EL signal increases linearly with time.

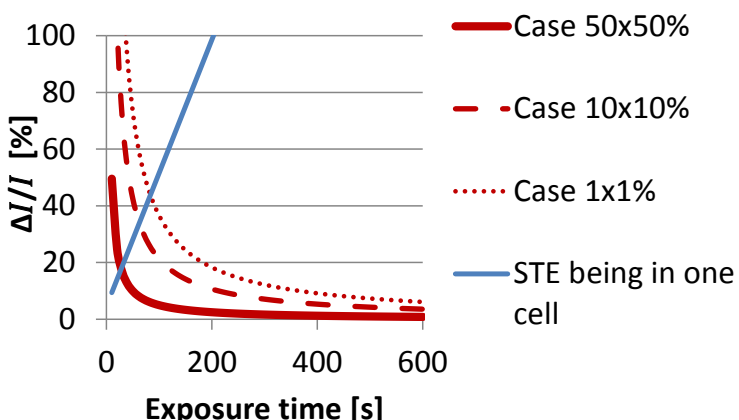


**Figure 4.6: Red: Intensity ratio (STE/EL) for three different cases; blue: Probability of one STE to be found in one cell in the module**

Figure 4.6 can be interpreted as follows: After 200 s, every cell will have on average one STE (blue line at 100%). At this time for the ‘10x10%’ case, the intensity ratio between STE and EL signal will be 10% or higher. This can be enough to misinterpret the STE as a shunt or micro-crack.

However, STE will often be too small to lead to these conclusions due to their small average size of about six pixels (Figure 4.4b).

Although the probability of STE occurrence increases linearly with exposure time, their intensity distribution remains constant. In consequence, Figure 4.7 shows the minimum EL intensity increase, at which 50%, 90%, 99% of STEs will not be noticed as artefacts.

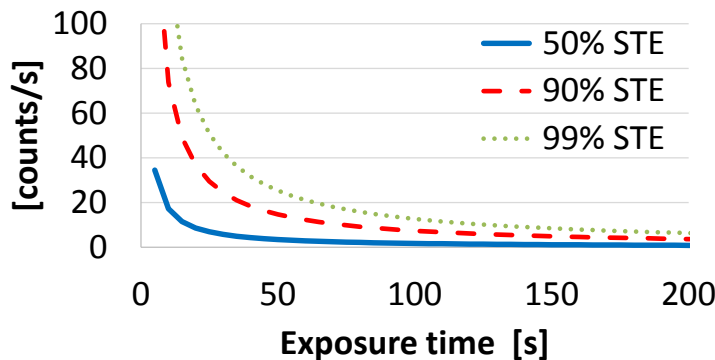


**Figure 4.7: Minimum intensity increase per second of a pixel in an EL image causing STE to be invisible, according to Equation 4.3**

For the available EL setup, the median intensity increase was measured for multiple modules at 10% and/or 100%  $I_{sc}$ . The injected power at 100%  $I_{sc}$  was in the range 4 to 450 W. In order to display these different devices in one figure, a simplified cell voltage ( $V_{cell}$ ) was calculated as the ratio of operation voltage ( $V_{mod}$ ) and number of cells ( $n_{cells}$ ):

$$V_{cell} = \frac{V_{mod}}{n_{cells}} \quad (4.4)$$

The resulting intensity increase vs cell voltage (Figure 4.8) follows an exponential relationship. This is as expected since the luminescence emission is proportional to  $\exp(V_{local})$  (Equation 2.2). Figure 4.7 suggests that an intensity increase above 100 counts/s would be suitable to make STE unnoticeable for exposure times over 20 s. For the devices examined, this intensity increase is on average exceeded for assumed cell voltages above 0.65 V (Figure 4.8).

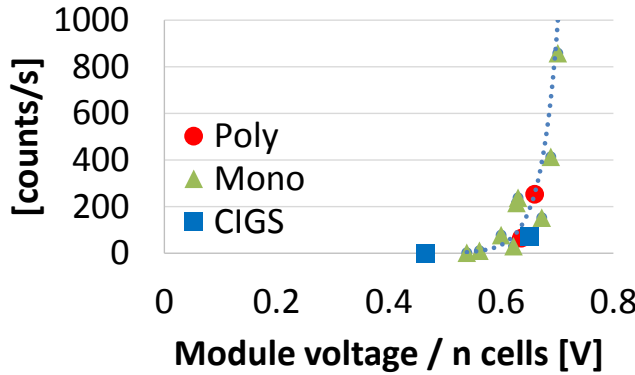


**Figure 4.8: Measured median intensity increase for 11 different modules at either 10%  $I_{sc}$  and/or 100%  $I_{sc}$**

It is suggested to carry out an STE removal routine for the following cases:

- Devices below the mentioned voltage of 0.65 V,
- Images with long exposure times and low SNR,
- Images to be used for calibration (such as flat field or background images).

#### 4.1.2 STE REMOVAL

Two EL images ( $I_1, I_2$ ) taken in series and at the same exposure time are needed. An STE mask is calculated using Equation 4.2. An average image ( $I_{avg}$ ) is built. All places identified with STE will be set to the STE free template image ( $I_{min}$ , Equation 4.1):

$$I_{avg} = 0.5 \cdot (I_1 + I_2) \quad (4.5)$$

$$I_{avg}[M_{STE}] = I_{min}[M_{STE}] \quad (4.6)$$

The averaging procedure (Equation 4.5) will also increase the signal-to-noise ratio (SNR) for every pixel, not affected by STE. The SNR will be increased by the following factor when averaging two images with Gaussian distributed noise:

$$f_{avg} = \frac{1}{\sqrt{0.5}} \approx 1.41 \quad (4.7)$$

As seen in Figure 4.9, the proposed STE removal routine not only removes the influence of STE but also increases the SNR.

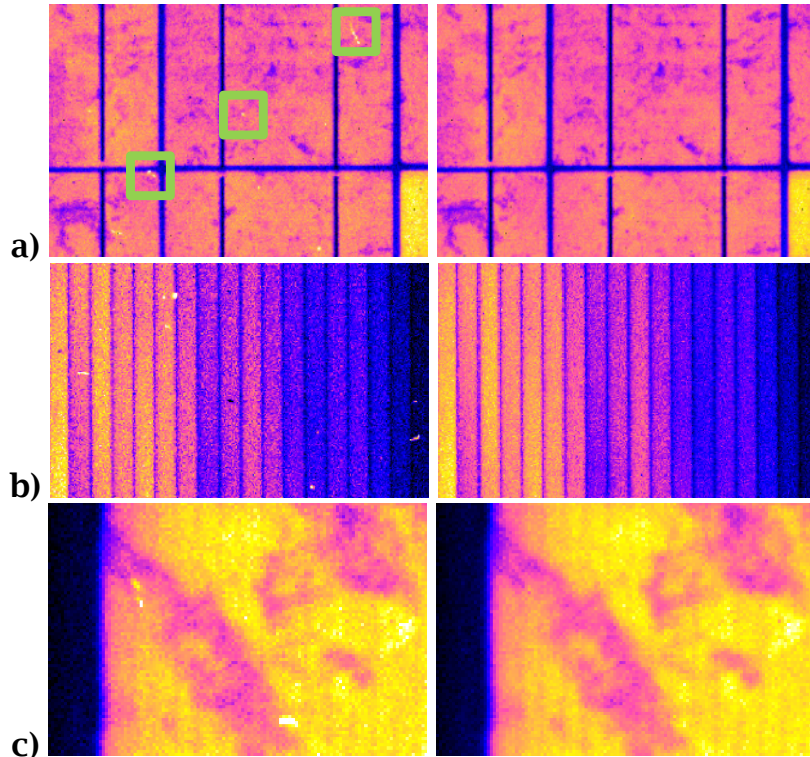


**Figure 4.9: Excerpt of three different EL images, affected by STE before (left) and after (right) STE removal**

#### 4.1.3 SECTION SUMMARY

This section described statistics and removal of single-time-effects (STE) caused by cosmic high-energy radiation interacting with the camera sensor. STE are imaging artefacts, which can be confused with cell defects. For the examined EL imaging setup, an average STE size of six pixels and intensity of 300 counts was observed. With on average one new STE every three seconds, every cell of the PV module, as for the case in Figure 4.3, would be affected with these image artefacts after an exposure time of 200 s.

However, STE remain invisible if the relative intensity difference is sufficiently small. If the DUT's EL signal increases over 100 counts/s, STE

will not be noticed for exposure times higher than 20 s. For the observed devices, a minimum cell voltage (neglecting series resistance) of 0.65 V was found to be enough to deliver the required photon flux. For devices with lower voltage, STE removal using an additional EL image is proposed. To remain at the same signal-to-noise ratio this method increases the absolute exposure time (ignoring time required for image capture and processing) by approximately 41%.

## 4.2 Background Removal

Removal of environmental stray light and dark current (thermal noise and defective pixels) is generally done by subtracting an EL image from an image of the same setup and exposure time under open circuit [8, 25, 33, 42, 43].

$$I_{EL,corr1} = I_{EL} - I_{BG} \quad (4.8)$$

These background images are prone to noise and STE. These artefacts decrease the quality of EL images after subtraction. Therefore, Section 3.1 proposed to either use an average of multiple background images or to calculate background from two calibration maps using the exposure time ( $\tau_{exp}$ ) as  $I_{BG}(\tau_{exp}) = a \cdot \tau_{exp} + b$ .

## 4.3 Flat field Removal

Impact and measurement of the flat field image ( $I_{FF}$ ) is detailed in Section 3.6. The background corrected EL image if divided by  $I_{FF}$  to correct for flat field.

$$I_{EL,corr2} = \frac{I_{EL,corr1}}{I_{FF}} \quad (4.9)$$

A carelessly created  $I_{FF}$  can cause residual flat field distortion after removal. These effects can become visible, when difference images are created (Subsection 7.2.2.2). In order to ensure a sufficient correction,  $I_{FF}$  should be tested beforehand as described in Subsection 3.6.4.

## 4.4 Image Artefacts

Dark current and flat field removal corrects most defective pixels. Since the camera sensor degrades over time, pixel defects occurring after camera calibration may remain. Their removal using a spatial standard deviation is described in [25, 42]. Depending on the kernel size, artefacts influence this Gaussian-based method to a certain extent. A higher stability towards these outliers can be achieved using a threshold median [43]. For this purpose, a median filtered image ( $I_{median}$ ) is created. All pixels with a relative deviation to the given image ( $I$ ) higher than a threshold ( $T$ ) are set to the median filtered value:

$$I \left[ T < \frac{I - I_{median}}{I_{median}} \right] = I_{median} \quad (4.10)$$

A pure median filter is sensitive to image features. However, for high  $T$  the threshold median only filters high gradient deviations without reducing the image quality. An example result is shown in Figure 4.10.

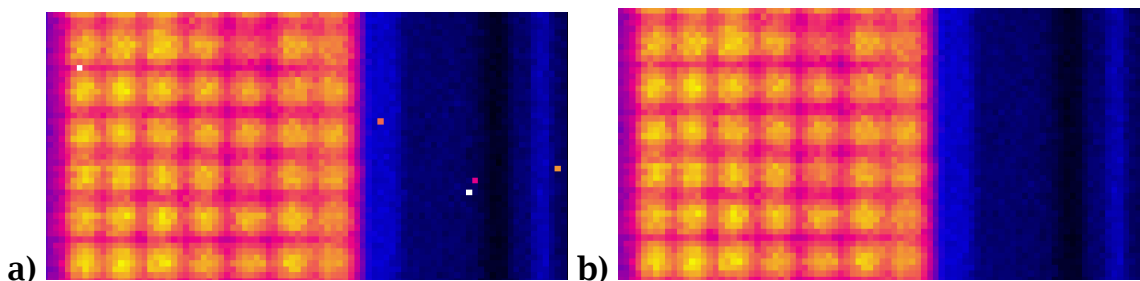


**Figure 4.10: EL image detail of a c-Si module before (a) and after artefact removal (b); Median kernel-size = 3 px;  $T = 0.2$**

## 4.5 Image Restoration

Image restoration can be separated into denoising and deconvolution (i.e. sharpening or deblurring) methods. Denoising is already discussed in Subsection 3.2.3.1. This section focusses on non-blind deconvolution routines. For non-blind deconvolution the point spread function (*PSF*) of an image ( $I_{bl}$ ) is needed. Its measurement is described in Section 3.4.4.

Image deconvolution is the inverse of image convolution ( $I_{bl} = I_{orig} \otimes PSF$ ). In general, deconvoluted images ( $I_{dec}$ ) do not fully recover the original (sharp) image ( $I_{orig}$ ). Rather they build a compromise between contrast increase and introduced noise/artefacts. This section presents and compares four different image deconvolution routines. The first one (unsharp masking) is chosen due to its simplicity, the following two are both commonly applied in luminescence imaging and the last method is the only one, which can be applied without an extra parameter ( $n$ ). This parameter either defines number of iterations or weights deconvolution intensity.

### 4.5.1 UNSHARP MASKING

This filter amplifies high gradient areas in images, causing a higher local contrast using [61]:

$$I_{dec} = I_{bl} + n(I_{bl} - (I_{bl} \otimes PSF)) \quad (4.11)$$

### 4.5.2 RICHARDSON-LUCY DEVONVOLUTION

This expectation-maximization algorithm is a common tool used in astronomy and luminescence based literature [66, 74, 97]. Although it copes with Poisson distributed shot noise in images (Subsection 3.2.2.2), the noise level can be artificially amplified in the result. Starting at  $I_{dec,0} =$

$\begin{bmatrix} 0.5 & \dots & 0.5 \\ \vdots & \ddots & 0.5 \\ 0.5 & \dots & 0.5 \end{bmatrix}$  the deconvoluted image  $I_{dec,n+1}$  is obtained iteratively [98]:

$$R_n = \frac{I_{bl}}{I_{dec,n} \otimes PSF} \quad (4.12)$$

$$I_{dec,n+1} = I_{dec,n} \cdot (R_n \otimes PSF) \quad (4.13)$$

### 4.5.3 WIENER DECONVOLUTION

In contrast to Richardson-Lucy, this filter works in the frequency domain. It penalizes frequencies using local noise minimization. It is applied in luminescence imaging in [68, 74].

### 4.5.4 UNSUPERVISED WIENER DECONVOLUTION

This filter extends the Wiener method with an automated regularization estimation using a Gibbs sampler. Therefore, it requires only a blurred image and a PSF. [99]

### 4.5.5 COMPARISON

The deconvolution methods were evaluated on a synthetic (1) and an EL image (2). The images were blurred with a radial symmetric (a) and an elliptic (b) 2D Gaussian PSF (Figure 4.11).

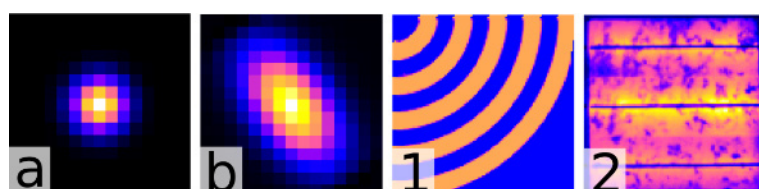


**Figure 4.11:** a,b) PSF used to blur  $I_{orig}$  of a synthetic pattern (1) and an EL image (2)

A comparison of the resulting (sharpened) images is shown in Figure 4.12 (synthetic pattern) and Figure 4.13 (EL image). An improvement ratio ( $Q$ ) is shown below every image. This ratio is calculated from a relative RMSE as follows:

$$Q = \frac{RMSE(I_{orig} - I_{bl}) - RMSE(I_{orig} - I_{dec})}{RMSE(I_{orig} - I_{bl})} \cdot 100\% \quad (4.14)$$

The smaller numbers in brackets (Figure 4.12, 4.13) show the deconvolution control parameter ( $n$ ). This parameter was determined by maximizing Equation 4.14 using the Brent method [79]. To evaluate noise stability, a mix of 70% Gaussian and 30% shot noise was added to  $I_{bl}$  in the bottom two rows causing a signal-to-noise ratio SNR of 10. The deconvoluted output from Richardson-Lucy was especially prone to few, but high magnitude artefacts. Therefore,  $I_{dec}$  was clipped to  $-100\%$  to  $200\%$  relative to the input intensity range.

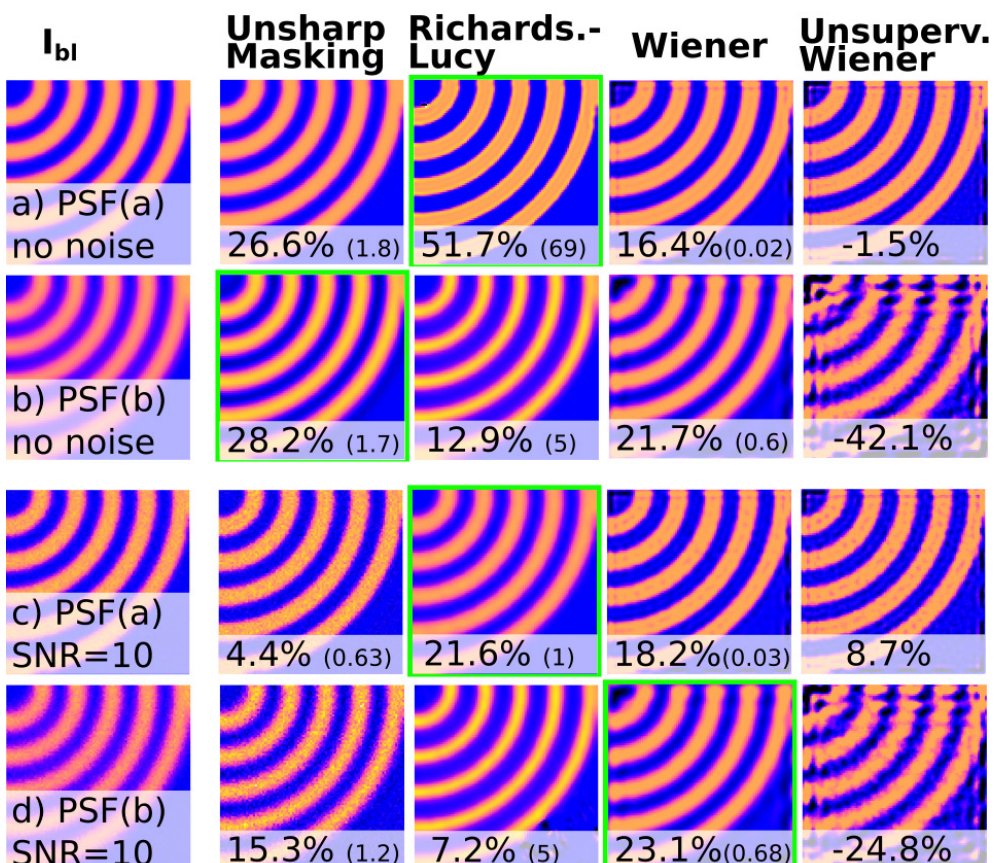


**Figure 4.12: Result of image deconvolution of the synthetic pattern (Figure 4.11(1)); first column: Input image ( $I_{bl}$ ) used for image deconvolution; 2<sup>nd</sup>-5<sup>th</sup> column: deconvolution output; large numbers: improvement ratio ( $Q$ , Equation 4.14); small number in brackets: control parameter ( $n$ ); green box: result with highest improvement ratio**

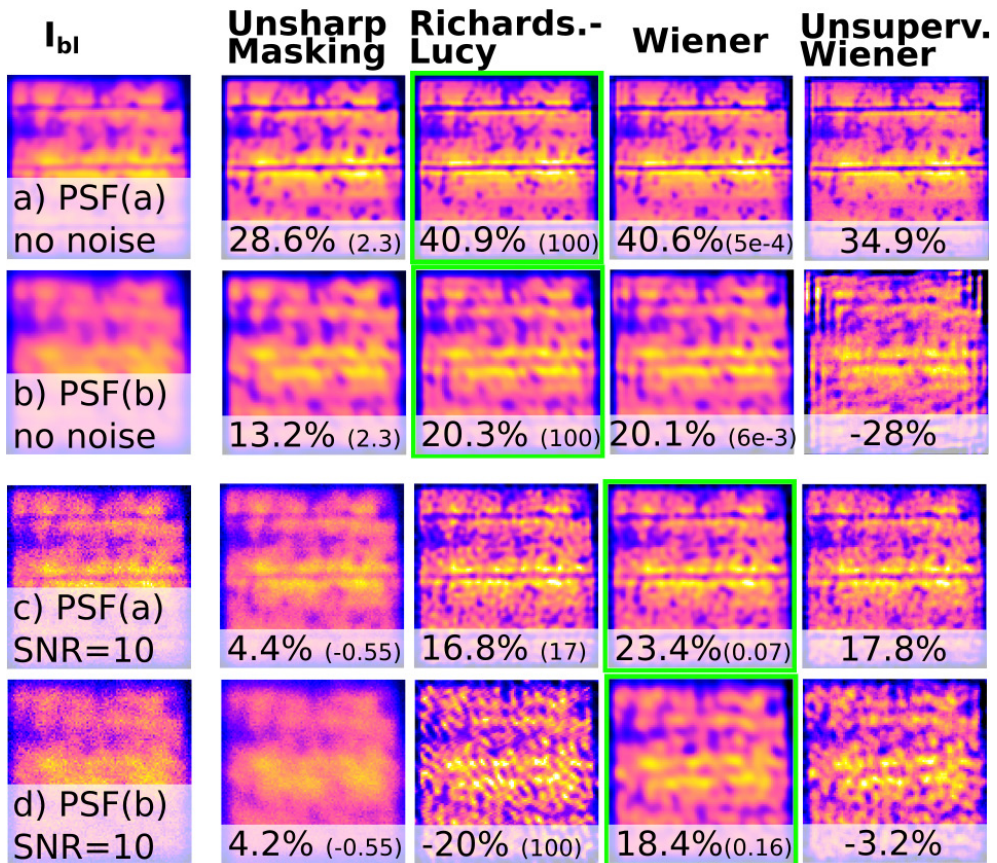


Figure 4.13: Same as Figure 4.12 for EL image (Figure 4.11(2))

Both Figure 4.12 and 4.13 show the common problems of image deconvolution: introduced noise, exaggerated gradients and artefacts.

Noise: Both Unsharp masking and Richardson-Lucy amplified existing image noise (Figure 4.13c,d). Therefore, noise removal with methods such as total variation regularization can be additionally applied [97].

Exaggerated gradients: On top and below both busbars (Figure 4.13a) image intensity increased to a higher value than in the original image. Although this can improve qualitative feature visibility, it can cause problematic distortions when evaluating difference images.

Artifacts: Results from Unsupervised Wiener generated a wave-shaped pattern along the image borders. Here the input image size is 100x100 pixels. It can be assumed that the extent of this artefacts decreases with larger images or smaller PSF. These wave-shaped patterns caused negative improvement ratios ( $Q$ ). Therefore, in the following comparison a border area of 20 pixels was excluded from the RMSE calculation in Equation

4.14. Figure 4.14 compares  $Q$  for the synthetic pattern (1) and the EL image (2) together with the PSF (a), shown in Figure 4.11 for three common problems (a-c). For Unsharp masking, Richardson-Lucy and Wiener the control parameter ( $n$ ) was determined once on the base of the average value of the varied problem parameter.

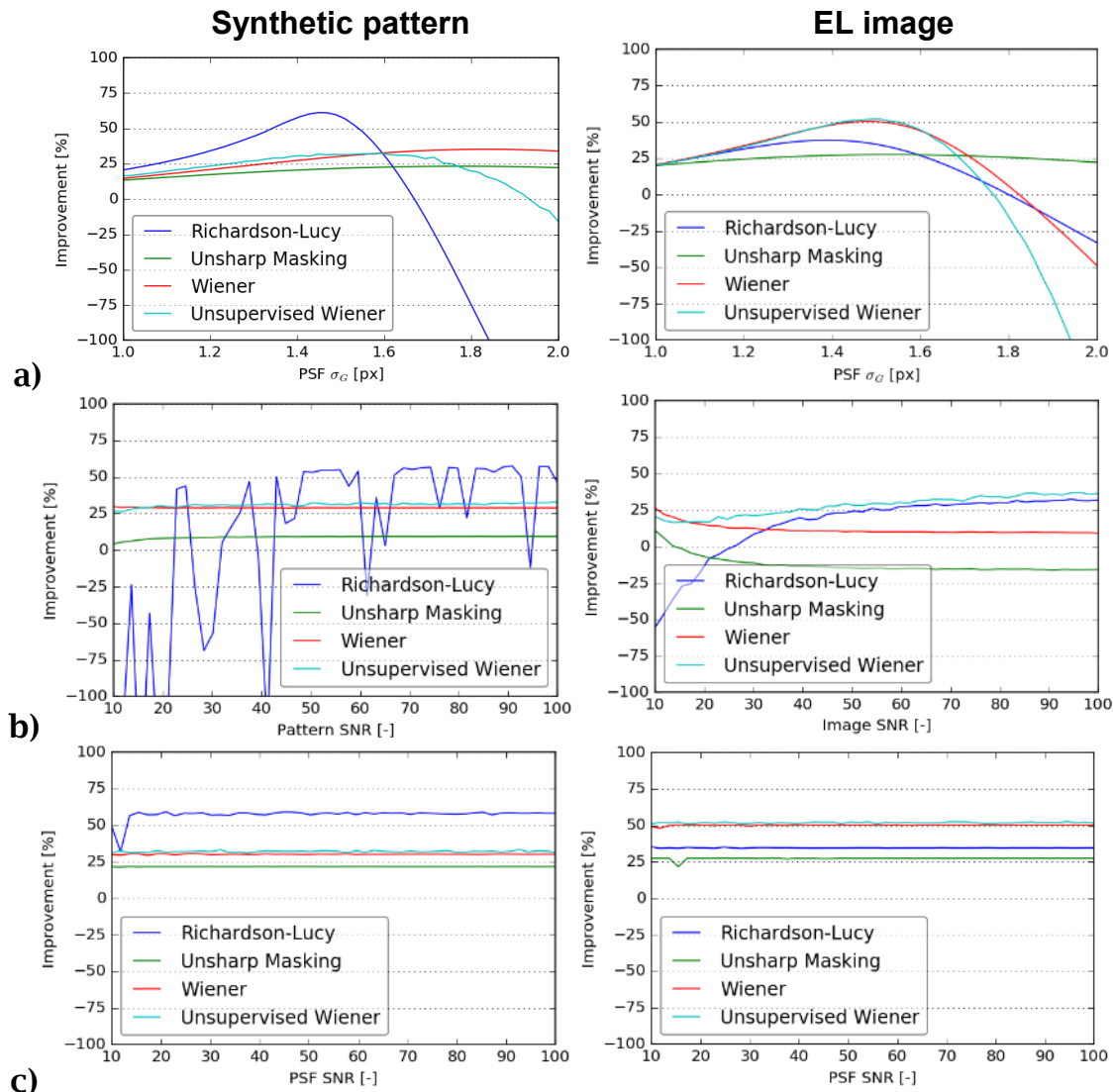


**Figure 4.14: Improvement ratio ( $Q$ ) for three varied problem parameters (a,b,c); left: results of synthetic pattern (1); right: results for EL image (2); both images were blurred with PSF (a) (Figure 4.11)**

Problem a: The standard deviation of the PSF ( $\sigma_G$ ) is not measured precisely. Whilst the actual  $\sigma_G$ , used to blur the synthetic pattern and EL image, is 1.5 px, the PSF used to sharpen the blurred images varied between 1 and 2 px. Whilst Richardson-Lucy gives the best improvements

for the synthetic pattern, it also shows highest sensitivity towards deviating  $\sigma_G$ . In general, smaller  $\sigma_G$  will cause a smaller improvement decrease than  $\sigma_G$  which are measured too large.

Problem b: Noisy input image. The SNR of the blurry input image varied from 10 to 100. Whilst noise is practically invisible at SNR=100, images with SNR=10 can be considered noisy (Figure 4.13c,d). For the synthetic pattern, the improvement generated with Richardson-Lucy varies strongly. This is due to introduced noise and artefacts. It can be assumed that an added noise filter would reduce these variations. Only for the EL image both Wiener and unsupervised Wiener showed slightly higher improvements for lower SNR values.

Problem c: Noisy PSF. The PSF can include a certain noise level, depending on the measurement method. If this noise is not removed with for instance a functional fit, PSF noise can be tolerated to a large extent as Figure 4.14c shows. For SNR greater than 20, improvement remains unchanged.

#### 4.5.6 SECTION SUMMARY

This section evaluated non-blind image deconvolution with a known point spread function (PSF). All the discussed deconvolution methods were able to partly restore image detail. Image deconvolution (sharpening) can introduce noise and artefacts and can overemphasize image gradients. Therefore, image deconvolution cannot substitute best focus determination (Section 3.3). For successful image deconvolution, the PSF must be determined precisely and the blurred image should have a high signal-to-noise ratio (SNR). For the evaluated EL images, both Wiener and unsupervised Wiener generated highest improvement ratios.

## 4.6 Lens Distortion Removal

Section 3.5 describes the measurement of lens distortion coefficients, focal length and image centre. These parameters are used to remove lens distortion using the Python interface of the C++ OpenCV framework as follows [64]:

1. Calculate size of the new image and adapt image centre and focal length to the image size (`cv2.getOptimalCameraMatrix`).
2. Generate a pixel indices array ( $M_{x,y}$ ) mapping the uncorrected to the corrected positions (`cv2.initUndistortRectifyMap`).
3. Remap the image using  $M_{x,y}$  (`cv2.remap`).

Figure 4.15 shows an example of lens distortion removal.

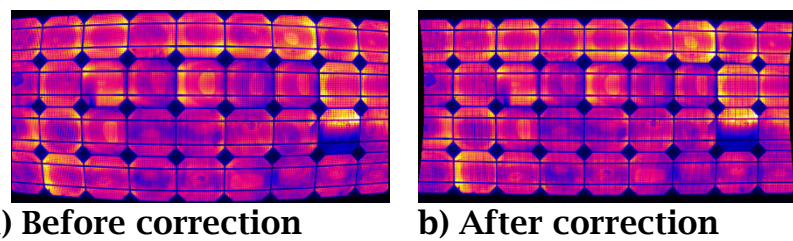
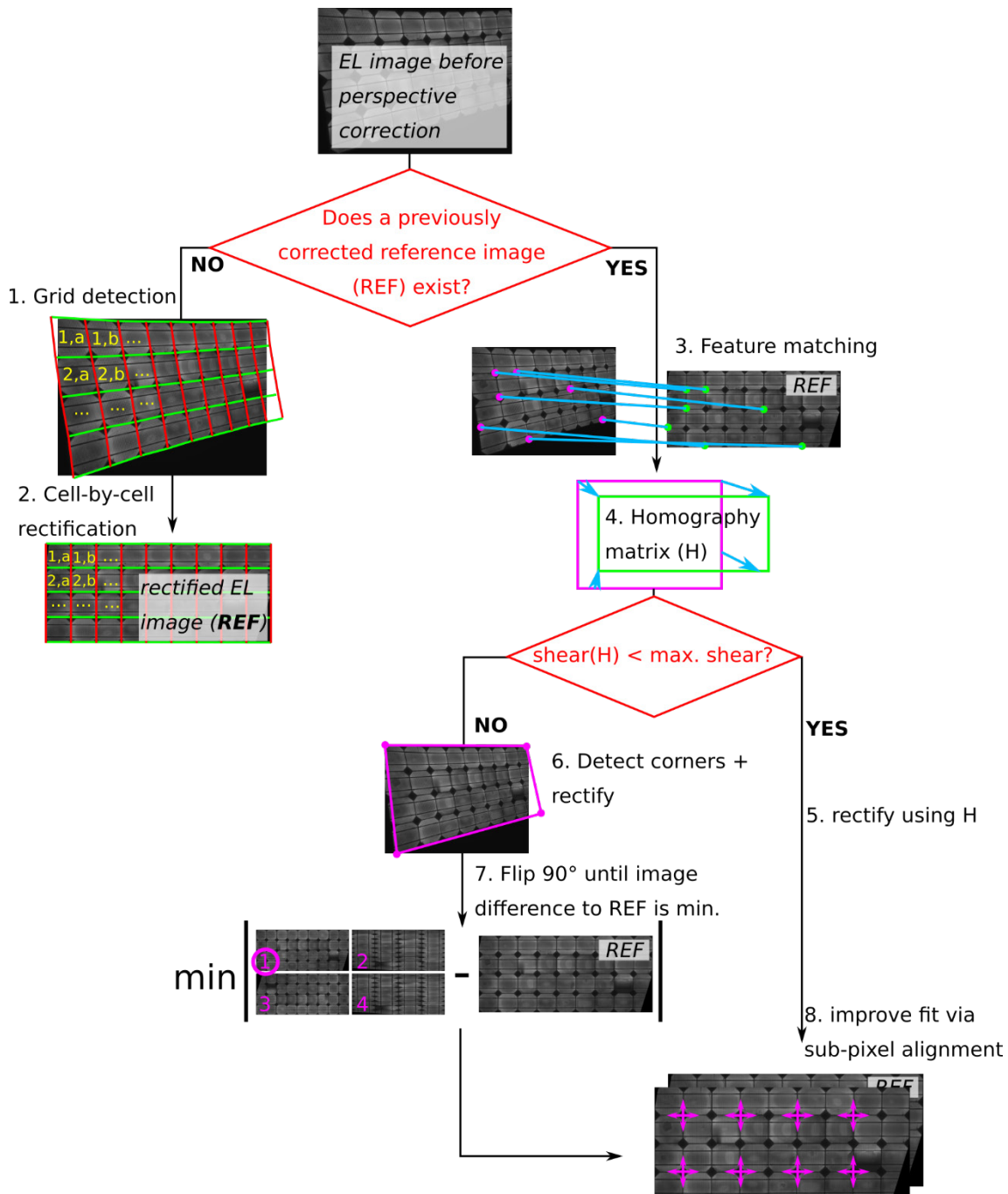


Figure 4.15: EL image of a PV module before (a) and after removal of lens distortion (b); Distortions have been exaggerated for clarification

## 4.7 Perspective Correction

The alignment of a PV device within an image is essential for image comparison within and across different measurement setups. The required perspective transformation or homography matrix ( $H$ ) can be obtained either from a reference image using pattern recognition, or without reference from detected features within the image. The routine implemented in this work is shown in Figure 4.16.



**Figure 4.16: Schematic for correcting perspective of an EL image with and without reference image**

The correction routine varies depending whether a reference image is available. A reference image is an EL image of the same device after perspective correction. If no reference image is available, a grid consisting of cell edges and busbars is detected in the image (step 1). The grid is then used to rectify the image by transforming every cell sequentially (step 2). Both steps are described in detail in Subsection 4.7.1. The

resulting image can be used as a reference to correct further images. In this case, distinctive features in both images are matched (step 3) in order to calculate the homography (step 4). The applicability of this method depends on the homography quality. In case of a low quality homography matrix, image rectification is done using the four detected DUT corners (step 6). The right DUT orientation is then determined from the minimum of the magnitude difference between rectified and reference image (step 7). Perspective correction with reference image is further described in Subsection 4.7.2. Finally, remaining spatial deviation between the rectified image and its reference is minimised by using sub-pixel alignment (Section 4.8).

#### 4.7.1 RECTIFICATION WITHOUT REFERENCE IMAGE

This section describes algorithms to detect DUT corners, cell edges, busbars and distances between cells. This information can be used to equalize image cell sizes and to create an image mask to exclude background areas. The DUT used as example is shown in Figure 4.17.

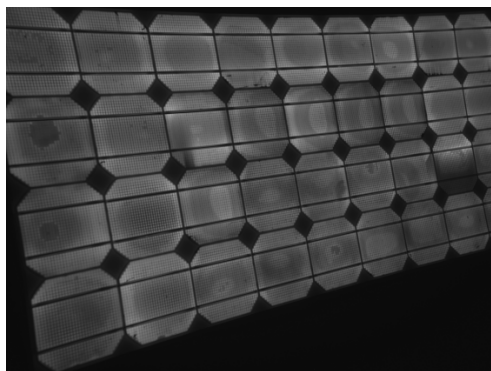


**Figure 4.17:** EL image of a c-Si module used as example in this section

##### 4.7.1.1 DEVICE CORNERS

For automated DUT corner detection the following approach was found to be reliable (Figure 4.18):

1. Create a binary image  $I_{bn} = I_{EL} > EL_{min}$  using the statistical EL signal minimum  $EL_{min}$  (intersection of EL and background signal, Equation 3.15).
2. Filter small features by applying a 2D minimum and maximum filter successively (kernel size = 5 px).
3. Move from each image edge towards the image centre and mark the edge position from the first detected non-zero pixel (coloured dots in Figure 4.18).
4. Fit a line through edge positions to obtain device edges. This can be done with a linear regression or the more robust maximum-line sum approach (Equation 4.15), explained below.
5. Obtain DUT corners ( $C_0 \dots C_3$ ) from intersection points of the fitted lines.

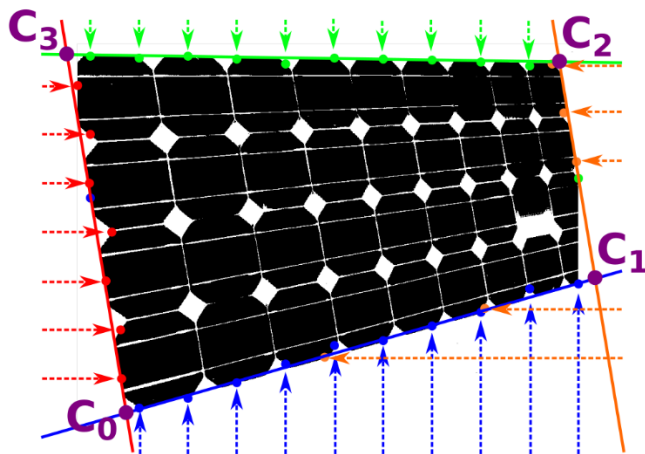


**Figure 4.18: Schematic of device corner detection**

#### 4.7.1.2 GRID CONSTRUCTION AND REFINEMENT

An initial grid (defined by its intersection points ( $P$ ), Figure 4.19a) can be created from detected DUT corners ( $C_0 \dots C_3$ ) and number of cells ( $n_x, n_y$ ) as follows:

Create an initial, regular mesh grid ( $P_0$ ) and use obtained homography matrix ( $H$ ) to transform  $P$ :

$$P_0 = \begin{bmatrix} 0 & \dots & n_x + 1 \\ \vdots & \dots & n_x + 1 \\ 0 & \dots & n_x + 1 \end{bmatrix}, \begin{bmatrix} 0 & \dots & 0 \\ \vdots & \vdots & \vdots \\ n_y + 1 & n_y + 1 & n_y + 1 \end{bmatrix}$$

For this, two functions, from the Python interface of the C++ framework OpenCV are used:

```
H = cv2.getPerspectiveTransform(
    [ [0,0], [nx,0], [nx,ny], [0,ny] ], [C0,C1,C2,C3] )
P = cv2.perspectiveTransform(P0, H)
```

In order to align  $P$  with the cell edges, a vertical and horizontal gradient image ( $G_y, G_x$ ) is created using the Sobel operator [64] (Figure 4.19b,c). The background is removed by setting  $G_{x,y}[I_{EL} < EL_{min}]$  to zero.

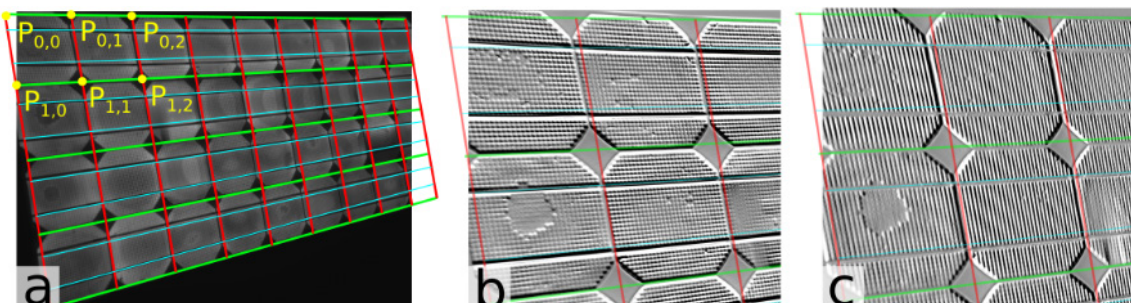


**Figure 4.19:** a) Initial grid ( $P$ ) adapted to DUT; Sobel filter in vertical (b) and horizontal (c) direction of top-left area in (a); filter kernel size=5 px

To refine the grid positions, lines ( $l_k$ ) are built from every point ( $P_{i,j}$ ) to the respective horizontal and vertical neighbour (green and red lines in Figure 4.19). An aligned sub-image around every line is created (Figure 4.20a).

On the assumption that a cell edge causes comparably high/low values in  $G_y, G_x$ , its position can be determined from the maximum/minimum of the summed values along all possible lines from the left ( $u$ ) to the right ( $v$ ) image border. In an  $(u \times v)$  array, the border position of the edge line (relative to the sub-image) can therefore be determined by listing all line sums as shown:

$$P_{u,v} = \arg \max (\text{sum}(G_{x,y}[line])) \quad (4.15)$$

The areas between the cells are enclosed by local minima and maxima in the respective gradient image. The cell edge line is defined as the average of both positions, obtained with Equation 4.15. An example is shown in Figure 4.20.

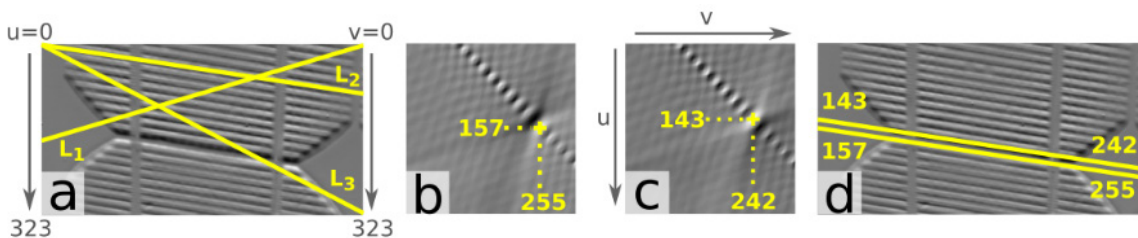


**Figure 4.20:** a) Vertical image gradient around an inter cell gap; three example lines ( $L_{1-3}$ ) from the left to the right image border; b) Line sum array ( $u \times v$ ) for all possible line combinations; c) Same, multiplied by (-1); Positions shown in (b,c) indicate position of array maximum used to define both edge lines (d)

The image grid after local refinement is shown in Figure 4.21. In certain circumstances the edges might not be fitted well with Equation 4.15. To correct these misfits, all positions that deviate more than 5% from a position obtained by a 2D polynomial fit will be set to that polynomial fit.

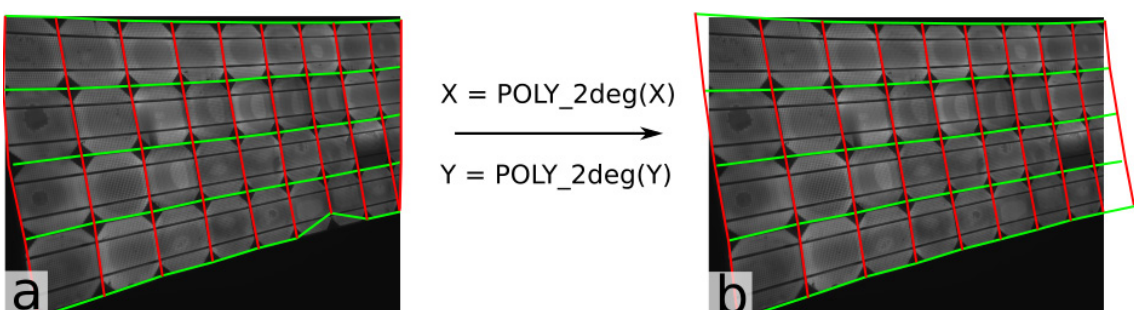


**Figure 4.21:** a) Image grid after refinement; b) Same after replacing all erroneous points with a 2<sup>nd</sup> order 2D-polynomial fit

The EL image can now be rectified by perspective transformation of every individual cell in the DUT (Figure 4.22a,b). The functions

`cv2.getPerspectiveTransform` and `cv2.warpPerspective` are used for this [64].

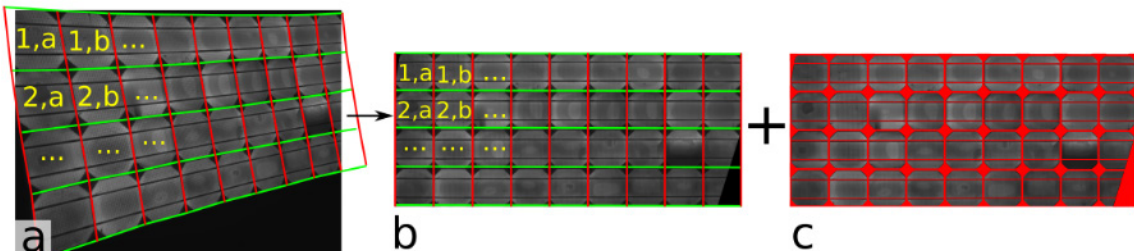


Figure 4.22: EL image with refined grid before (a) and after (b) rectification; c) Image mask to exclude inter cell areas and busbars

#### 4.7.1.3 MASKING THE RECTIFIED DUT IMAGE

To exclude inter cell areas and busbars from the device, the gap width between cells or across busbars must be determined. Line plots along multiple areas in the corrected EL image (Figure 4.23) are created. In every line plot, the gap width is defined as the number of pixels from local minima towards a given intensity threshold. It was found that  $y_{thresh} = y_{mn} + 0.35(y_{mx} - y_{mn})$  gives sufficient results. Within the created mask, the width of busbars, horizontal, vertical and diagonal cell gaps is set to the respective median value from all individual  $y_{thresh}$ .

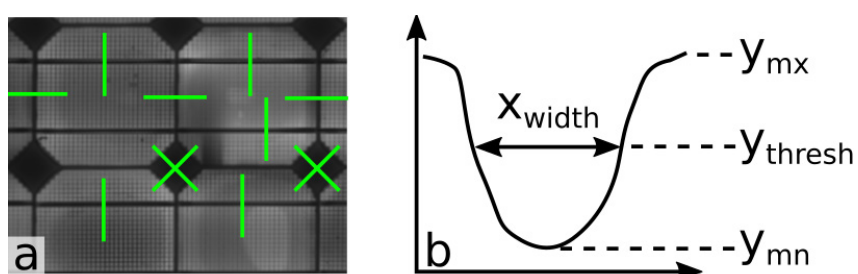


Figure 4.23: a) Example positions of line plots, used to determine gap widths; b) Schematic to measure gap width

## 4.7.2 RECTIFICATION WITH REFERENCE IMAGE

### 4.7.2.1 FEATURE MATCHING

If a reference image ( $I_{ref}$ ) is available, key points are detected and matched between both images ( $I, I_{ref}$ ) using the ‘ORB’ descriptor [100] and a brute force matcher (Figure 4.24). From the set of matched key points detected in both images ( $p_1, p_2$ ) the homography matrix ( $H$ ) is calculated using the Python bindings of the OpenCV framework:

```
H = cv2.findHomography(p1, p2) [0]
Icorr = cv2.warpPerspective(I, H, Iref.shape)
```

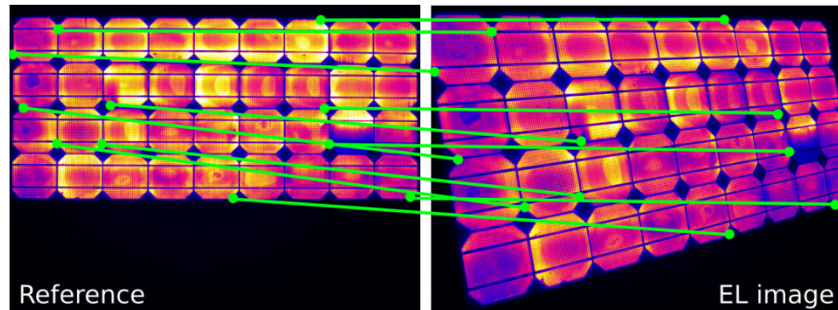


**Figure 4.24: Matched key points ( $p_1, p_2$ ) in rectified reference ( $I_{ref}$ ) and EL image ( $I$ )**

### 4.7.2.2 QUAD DETECTION AND DIRECT COMPARISON

The homography matrix ( $H$ ) includes information for horizontal and vertical translation, scale, rotation and shear. The latter parameter will be used to evaluate the homography quality. If the shear exceeds 0.05 then feature matching failed and the following fallback method is executed for perspective correction:

1. Detect DUT corner points (Subsection 4.7.1.1).
2. Execute perspective transformation into size of reference image ( $I_{ref}$ ).
3. Flip the transformed image ( $I_{corr}$ ) four times ( $0^\circ, 90^\circ, 180^\circ, 270^\circ$ ) and stop at rotation where  $\text{mean}|I_{corr} - I_{ref}|$  is minimal.

### 4.7.3 CORRECTION EXAMPLE

The proposed image correction routine is evaluated using a c-Si PV module imaged at four different positions:

- a) No tilt, position 1
- b) No tilt, position 2
- c) 15 ° tilt angle, position 1
- d) 35 ° tilt angle, position1, rotated

All images were captured in the large-scale EL chamber ‘HuLC’ (Appendix 2) using a SensoCam HR-830 camera with an image resolution of 3324x2504 px. For the sake of repeatability, all correction methods were executed automatically. If it is assumed that the EL signal does not change during imaging, a successful image correction should lead to practically identical results.

Figure 4.25 shows EL images with an identical colour map and scale of all four positions before (left) and after image correction (right). Looking at particularly cells {1,5} or {2,3} (row, column) it is clear that the intensity differs. This is due to the different influence of vignetting. However, after image correction differences in position and intensity are not visible. For position (c) and (d) corners of the image are missing because they were not imaged in the first place.

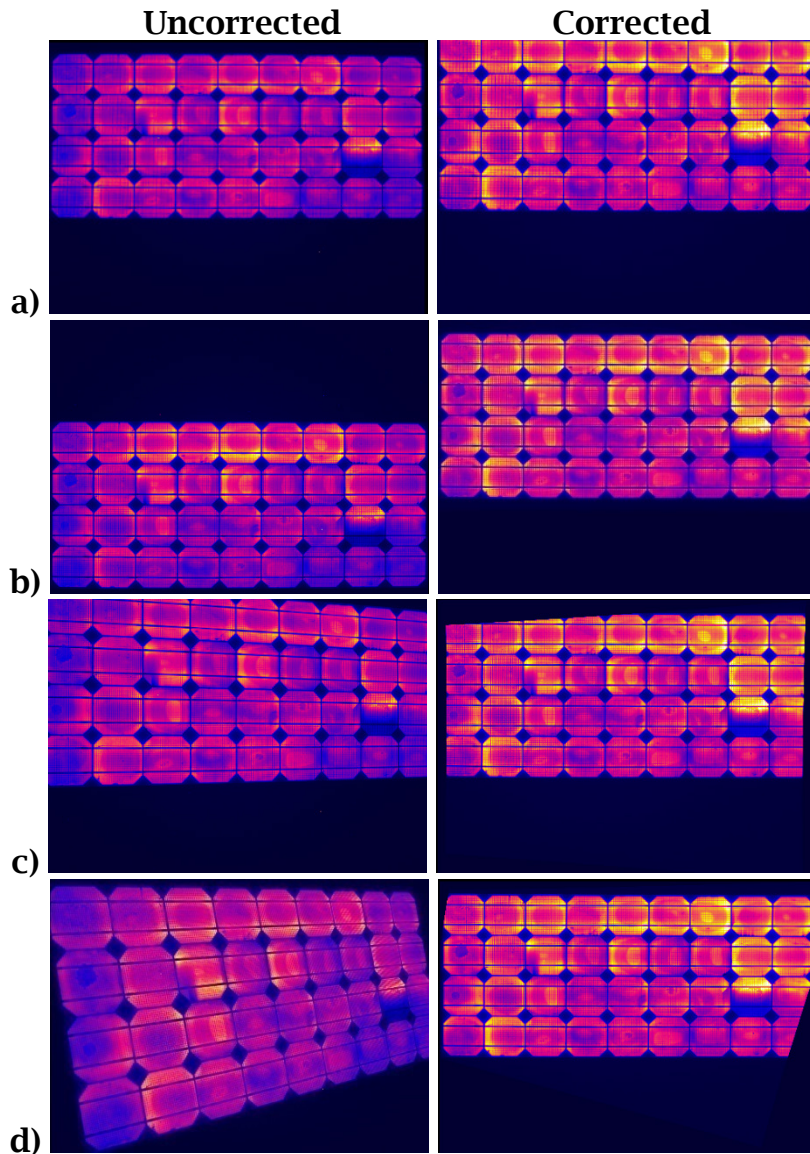


**Figure 4.25: Comparison of EL images before (left) and after image correction (right); scale and colour map are identical for all images**

Figure 4.26 shows the individual differences from corrected positions (b-d) to (a) as a colour layer on top of a grey-scaled image (a). The red box within the overview marks the position of the image detail. The majority of the image remains grey-scaled. This indicates low and homogenous difference images. A red arrow points to a reddish region below a crack in the detailed image. The reddish region indicates that even transient EL instabilities can be recovered even though the imaged position was different. The blue colouring around some cells indicates a positional error of about two pixel for position (d). This error can be due to a slight bend of the module, imperfect lens calibration or homography matrix.

Removal of this residual position error is detailed in the following Section 4.8.

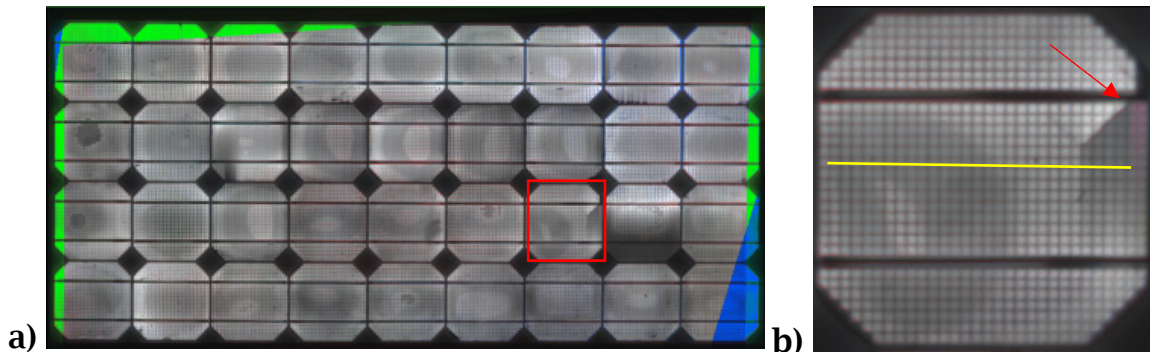


**Figure 4.26: EL comparison: overview (a) and detail (b); Differences to (Figure 4.25a) visualised as colour layer: b(red) c(green) d(blue); transparency scaled between 0-50% relative difference**

The yellow line in Figure 4.26b indicates the position of a line plot shown in Figure 4.27 (yellow line). The cell intensity and location of all corrected positions (a-d) is practically identical with a coefficient of variation of about 1%.

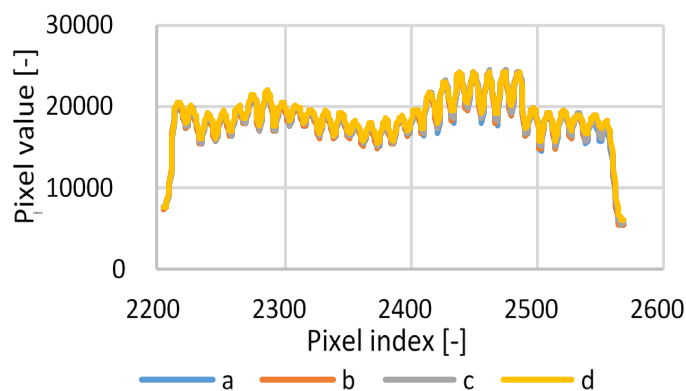


**Figure 4.27: EL line plot of yellow line in Figure 4.25**

## 4.8 Sub-pixel Alignment

Even after successful perspective correction, a positional error of one to five pixels can remain. This deviation causes difference images to overemphasize high gradient variations, like cell borders or busbars

(Figure 4.28c). This subsection presents a fast and comparably simple method to reduce spatial deviation to less than one pixel (Figure 4.28d).

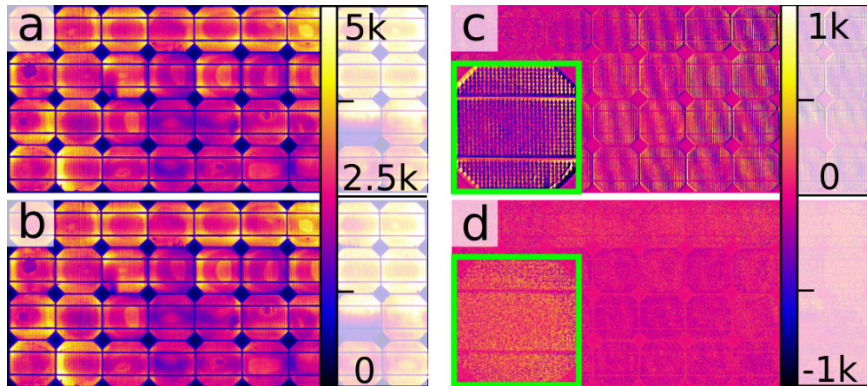


**Figure 4.28:** a-b) EL images of the same DUT measured at different days, background, lens and perspective corrected; c) difference image a-b; d) same, after sub-pixel alignment; green box: same cell magnified

Sub-pixel alignment calculates the spatial deviation ( $x, y$ ) from the phase shift of two superimposed patterns ( $P_1, P_2$ ). This method requires both EL images ( $I_1, I_2$ ) to display the same EL device under similar conditions and after perspective fit. Hereinafter, an  $(m \times n)$  array ( $O$ ), containing the spatial deviation ( $x, y$ ) will be created. In the presented example, the array has  $11 \times 5$  cells. For every cell in  $O$ , patterns from both EL images will be compared. The pattern, responsible for the deviation in  $x$  direction ( $P_x$ ) in one cell ( $i$ ) is a line plot ranging  $m_i \dots m_{i+1}$  and averaging all values in  $y$  direction ranging  $n_i \dots n_{i+1}$ . For this, both images of shape  $(s \times t)$  are rescaled to shape  $(m \times t)$  and  $(s \times n)$  (Figure 4.29a,b). Pixel averaging is done by pixel-area relation [78].

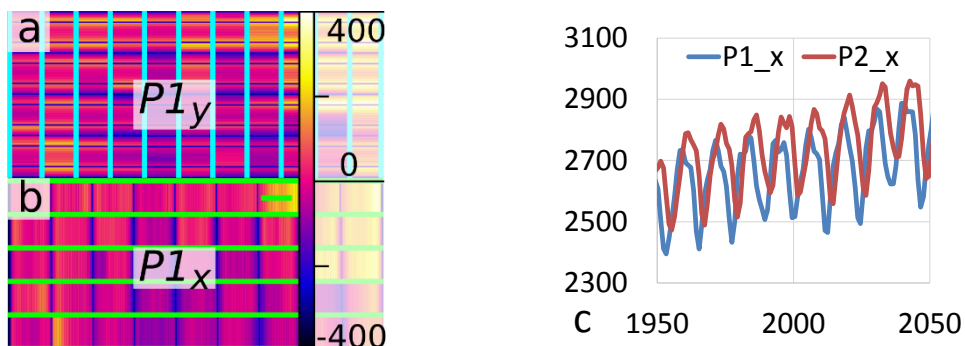


**Figure 4.29:** a-b) EL image (Figure 4.28a) after rescaling to  $11 \times 1463$  px (a) and  $3280 \times 5$  px (b); c) Line plot of both patterns in  $x$  direction in part of one top right cell (short green line in (b))

For every cell ( $i$ ) in  $O$ , spatial deviation is found by minimizing the following condition using the Brent method [79]:

$$O(i, x) = \min \left( P1_{x,i} - fn(P2_{x,i}, phase) \right) \quad (4.16)$$

$$O(i, y) = \min \left( P1_{y,i} - fn(P2_{y,i}, phase) \right)$$

$fn(\dots, phase)$ , shown in Equation 4.16, shifts given values using piece-wise linear interpolation. The resulting phase shift map in x and y direction is shown in Figure 4.30a,c. To filter single erroneous results, pixel deviations higher than a given threshold ( $\pm 30$  pixels) and 100% higher than their median filtered value (kernel size=3) were substituted with a 2D polynomial fit (degree=5, Figure 4.30b,d).

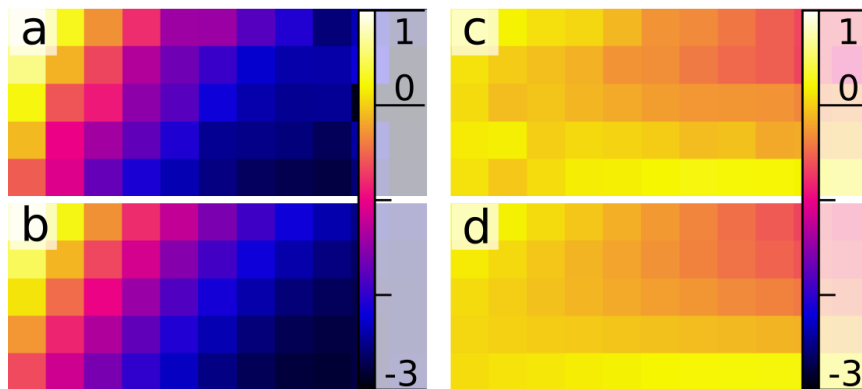


**Figure 4.30: a,c) Phase shift map ( $O$ ) between EL images (Figure 4.28a,b) in x (a) and y (c) direction; b,d) Same, after polynomial fit**

Finally,  $O$  is rescaled to the resolution of both EL images ( $s \times t$ ) (Figure 4.31a,b) and increased by the pixel index maps in x and y (Figure 4.31c,d). The resulting maps are then used to remap all pixels of EL image ( $I_1$ ).

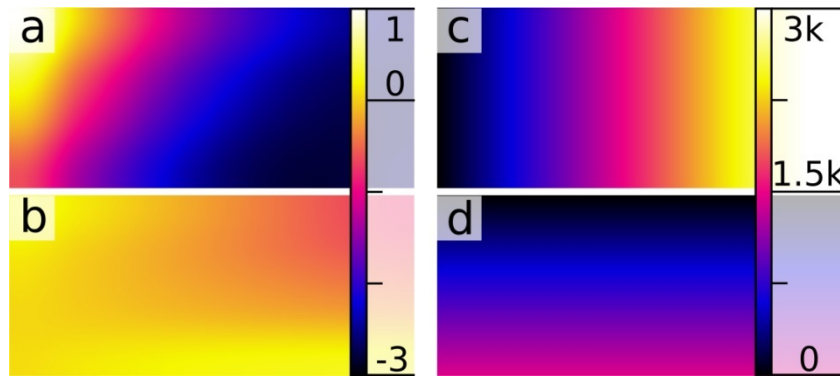


**Figure 4.31: a-b) Phase shift map (Figure 4.30b,d) after rescaling to EL image resolution; c,d) Pixel indices of all pixels in EL image ranging 0...3280 in x and 0...1463 in y direction**

The impact of sub-pixel alignment can be seen in Figure 4.32 which shows cell {5,5} of the c-Si module 'M2' from the NREL case study (Subsection 7.1). From top left to bottom right, the module was stressed both mechanically and thermally. Subfigure (a) shows the same cell imaged by eight separate EL measurements. The images were corrected for intensity and perspective, as described in this Chapter. The applied stress first created a micro-crack (green box), which later developed into a full Y-shaped crack. Subfigure (b) shows EL difference images ( $I_i - I_{i+1}$ ) without sub-pixel alignment. The micro-crack can be identified multiple times due to a small positional mismatch of the individual images. However, after sub-pixel alignment (c) this crack occurs only once in the difference images.

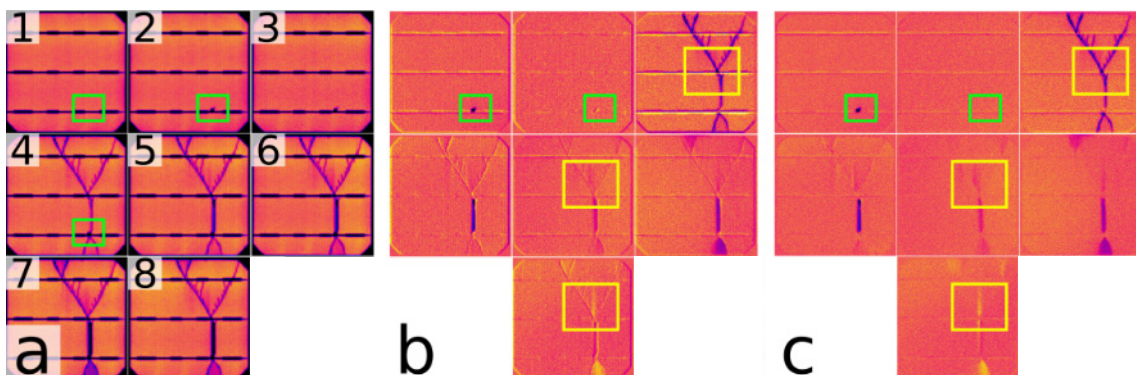


**Figure 4.32: Cell {5,5} of module 'M2' from NREL case study (Section 7.1); a) EL image of treatment step 1-8; b) EL difference image after perspective correction; c) same after sub-pixel alignment**

In the same way, the centre of the Y-crack (yellow box) is visible in all the difference images in Subfigure (b). Subfigure (c) however, only shows the intensity deviations along the crack and not the crack itself.

The improvement due to sub-pixel alignment is quantified in Table 4.1. Improvement was calculated as an absolute average deviation between every two consecutive EL images, relative to the mean pixel intensity of the respective first image. The detailed sub-pixel alignment procedure was repeated six times to improve the result. For every EL difference image, the relative deviation decreased after single and 6 step sub-pixel alignment.

**Table 4.1: Rel. average intensity deviation of EL difference images [%]**

Image	1	2	3	4	5	6	7	8
no sub-pixel alignment	4.16	6.98	12.15	5.94	6.33	6.89	7.16	35.10
single step alignment	2.89	5.61	10.55	3.13	3.41	3.73	3.71	33.68
6-step alignment	2.29	5.15	10.21	2.32	2.33	2.48	2.25	32.40

## 4.9 Intensity Normalisation

Different camera sensitivities, dark current levels and exposure times cause different brightness and contrast levels in EL images. These images need to be scaled accordingly in order to quantitatively compare EL differences. In both case studies in Chapter 7, image intensities are normalised as follows:

1. Calculate the cumulative distribution function (CDF) of all image intensities in the corrected EL image ( $I$ ).
2. Select minimum and maximum intensity ( $x_{min}, x_{max}$ ) from the CDF as those positions where CDF=2% and CDF=98%
3. Scale every image using:

$$I_{0 \dots 1} = \frac{I - x_{min}}{x_{max} - x_{min}} \quad (4.17)$$

If every image contains the same DUT in the same perspective, after intensity scaling intensity deviations are only due to EL signal changes (Figure 4.33, 4.34).

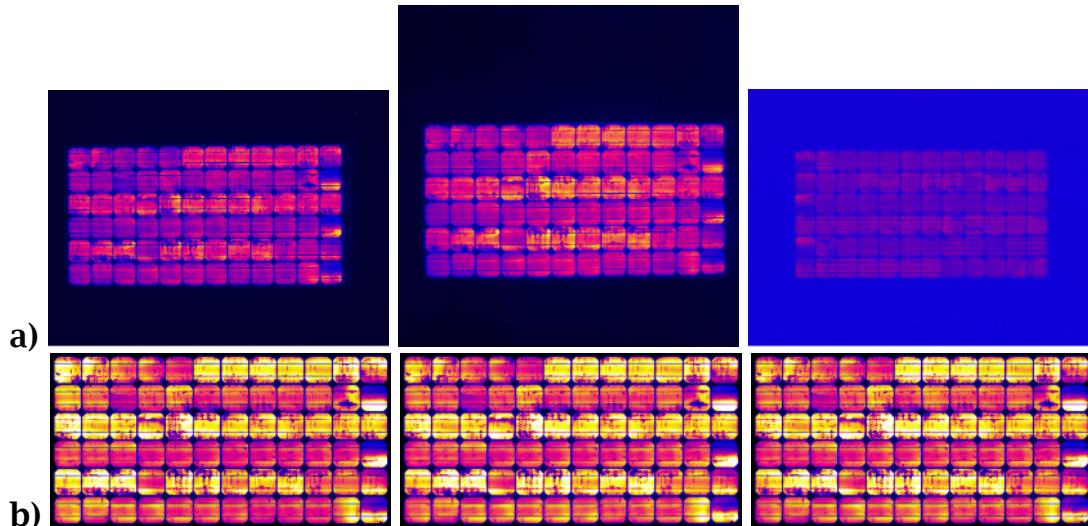


**Figure 4.33: Effect of intensity scaling; a) EL images of the same DUT from different laboratories scaled to their individual minimum and maximum intensity; b) same images after perspective correction and intensity normalisation**

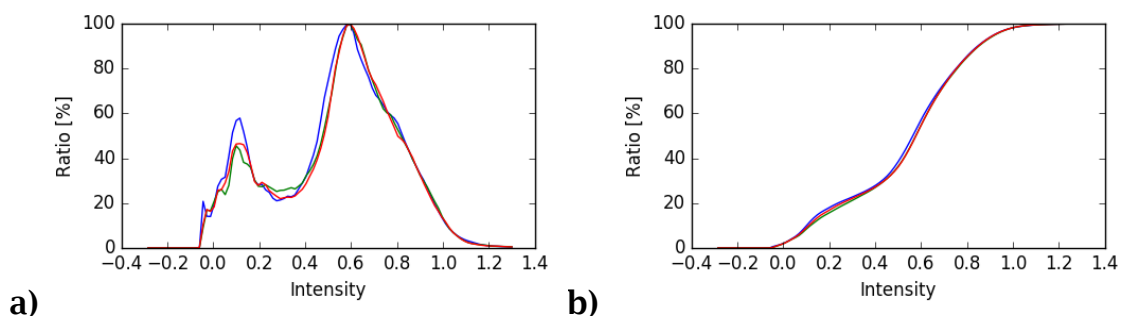


**Figure 4.34: a) Intensity distribution histogram; b) CDF of the images shown in (Figure 4.33b)**

## 4.10 Chapter Summary

To date EL image analysis is often restricted to manual comparison of visible features. The EL signal, captured by the imaging system, is superimposed by distortions and artefacts. In consequence, EL images become setup dependent and EL difference images taken at different measurements or laboratories are difficult to analyse.

This chapter provided an integral and automatable image correction routine. For the first time EL imaging artefacts, intensity differences and spatial distortions caused by the imaging system and the DUT perspective were removed together.

EL images taken from the same DUT and corrected with this routine differ mostly due to EL signal differences. EL images, analysed in both case studies in Chapter 7, were corrected according to this routine. The routine is embedded in the developed image processing software (Appendix 3).

# 5 EXTRACTING FEATURES FROM DIFFERENCE IMAGES

This chapter covers algorithms for detecting inactive areas (Section 5.2) and cracks (Section 5.3) in EL images that were corrected as described in Chapter 4. Parameters, derived from detected cracks, are introduced in Subsection 5.3.2. The impact of cracks in module performance is estimated in Subsection 5.3.3.

## 5.1 Introduction

In contrast to examples in literature [101, 102], in this work extrinsic defects (such as cracks and inactive areas) are extracted from the relative difference to two EL images ( $I_1, I_2$ ). EL images are corrected as discussed in Chapter 4. Two examples of corrected EL images (before and after a mechanical load test) are shown in Figure 5.1a,b. Intrinsic features superimpose extrinsic defects, especially for polycrystalline Si devices. This often impedes the differentiation between for example cracks and grain boundaries. In this work, relative difference images ( $dI_{rel}$ ) are used to correct luminescence inhomogeneities:

$$dI_{rel} = \frac{I_1 - I_2}{I_1} \quad (5.1)$$

As Figure 5.2 shows, in the relative difference image device intrinsics (such as grain boundaries) cancel out extrinsic features (such as cracks) dominate. The following subsections describe the extraction of cracks and inactive areas, shown as red lines and green areas in Figure 5.1d,f.

Inactive areas are separated into partly and fully inactive areas (light and dark green). If cracks are identified adjacent to darker (inactive) areas, they will set to be ‘disconnecting’ cracks (dark red). Otherwise, they will be labelled as ‘non-disconnecting’ cracks (light red).

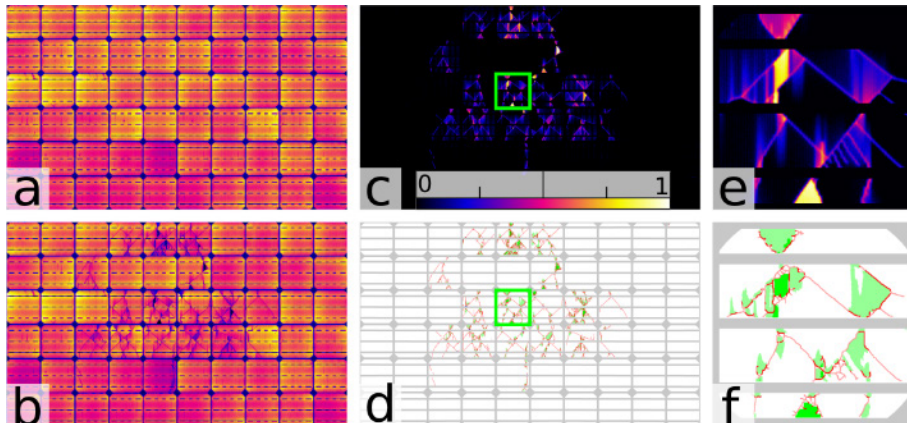


**Figure 5.1:** Monocrystalline Si module ‘M1’ from NREL case study in Section 7.1 before (a) and after mechanical load experiment (b); c) EL intensity difference; d) extracted feature map; e,f) EL intensity difference and feature map of cell {5,3}; red: cracks; green: inactive area

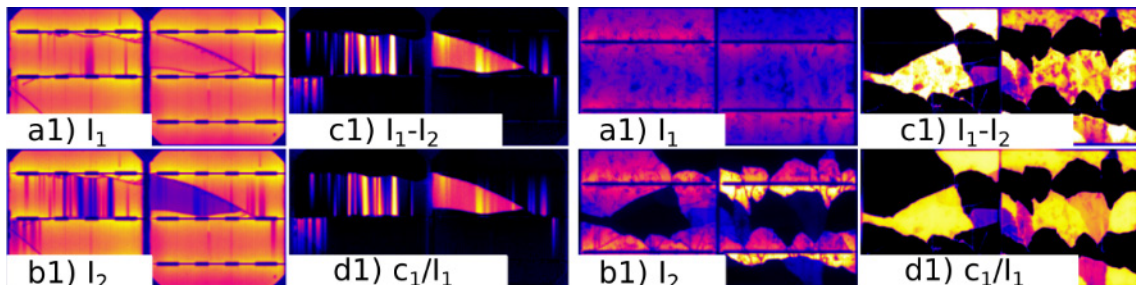


**Figure 5.2:** Comparison of an absolute difference image (c) to a relative one (d) for a monocrystalline (1) and a polycrystalline device (2)

## 5.2 Partly and Fully Inactive Areas

Partly inactive areas are defined as cell areas that are still electrically connected, but appear darker due to a higher series resistance [103] or shunts. In this work areas with a signal reduction higher than 30% are marked as partly inactive (light green). Areas with a signal reduction of more than 60% are set to be fully inactive. However, as discussed in

Subsection 7.1.2.3 it is controversial to what extent these areas are electrically isolated.

In order to filter signal noise, the relative difference image is median filtered (kernel size = 3 px). In a set of multiple difference images of the same device after different treatments, areas that were detected as inactive before will not be detected as inactive again, if the EL intensity did not continue to change after the first decrease. Therefore, if an area is detected twice as (partly) inactive, it is assumed fully inactive.

Since every crack also decreases signal intensity, inactive areas can also be detected along cracks (Figure 5.3a). This can be corrected using a combination of two-dimensional maximum filter (kernel size = 30x30 px) and ‘logical and’ ( $\wedge$ ). The filter sequence is shown in following Python-based pseudo-code and the filter result is shown in Figure 5.3c.

```
# STEP a: make copy of inactive area
disc2 = disc.copy()

# STEP b: remove areas around crack,
disc2[logical_and(maximum_filter(cracks, 30),disc)]=False

# STEP c: restore areas that still exist:
disc = logical_and(maximum_filter(disc2,30),disc)
```

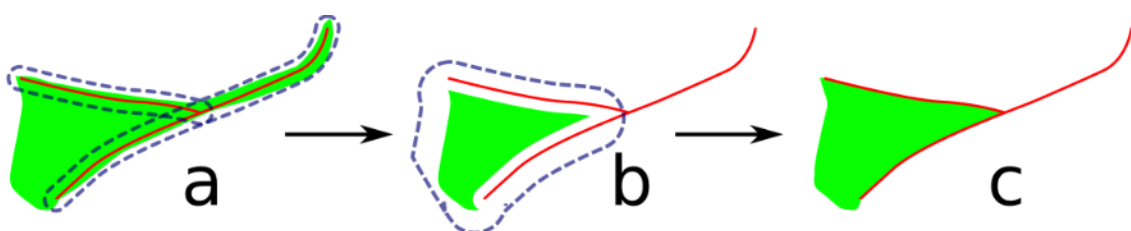


**Figure 5.3: Removal of falsely detected inactive areas along cracks; dashed area gives result for 2D maximum filter**

## 5.3 Cracks Detection

The detection of cracks is a more challenging task since they often cannot be successfully detected with a simple threshold condition as described in [101]. Anwar et al. detect cracks by applying a shape analysis on binary

EL images. The algorithm is trained with known crack shapes from a large EL image dataset [104, 105].

In this work, a crack is defined as a combination of high gradient variation together with a mono-directional propagation. This means that cracks are considered as lines, which are dark and more or less straight. The first criterion is fulfilled, if the edge magnitude of the difference image is higher than a given threshold. To calculate the edge magnitude (Figure 5.4b), the Laplace operator ( $L(I)$ ) [106] was used:

$$L(I) = \frac{1}{6} \begin{bmatrix} 0 & -1 & 0 \\ -1 & 4 & -1 \\ 0 & -1 & 0 \end{bmatrix} \otimes I \quad (5.2)$$

For the second condition the Histogram of Oriented Gradients (HOG) [107] is calculated. For this, depending on the number of measured propagation directions (in this case eight directions, Figure 5.4f) the difference image is convoluted with a line-shaped convolution kernel (also named ‘2-D matched filter’ in [102]). Hereinafter, a ‘line-likeness’ is measured from the maximum value of all directions within the HOG (Figure 5.4a).

This method works as follows: For each pixel and each propagation direction in the image, the pixel sum along this direction is calculated. The direction resulting in the highest sum marks the crack direction. In contrast to the otherwise similar anisotropic diffusion filter technique [104] this method calculates a result after a single convolution routine for each orientation.

A crack is detected if both described criteria exceed given thresholds (Figure 5.4c). In this work, the threshold for edge magnitude is 0.02 and for line-likeness is 0.045. To convert the identified areas into single-pixel lines, a skeleton (Figure 5.4d) of the binary result is created [108]. The propagation direction can be obtained as a by-product from crack detection using HOG (Figure 5.4e).

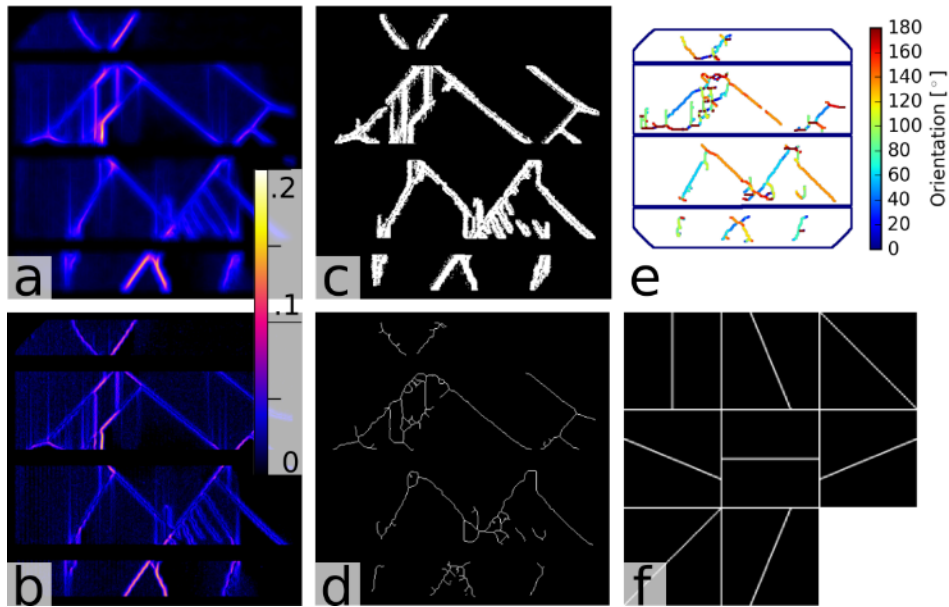


**Figure 5.4: Interim results for the highlighted cell {5, 3} in the relative EL difference image of Figure 5.1b;** a) Line-likeness from HOG maximum; b) Edge magnitude; c) Result of (a)  $> 0.045 \wedge$  (b)  $> 0.02$ ; d) (c) after skeletonisation; e) crack orientation map; f) convolution kernels, used to calculate HOG for eight different orientations using kernel size ( $k_{cr}$ ) = 41x41 pixels

### 5.3.1 LIMITATIONS

The described crack detection algorithm is prone to false positive or false negative detection. As Figure 5.5a shows, vertical image gradients caused by inactive fingers may be misinterpreted as cracks. Sub-pixel alignment is essential when difference images are analysed. However, if the EL signal differences between images are too great, the alignment error between both images can be up to a few pixels. This can cause cell edges or busbars to be detected as defective areas (Figure 5.5b). Spatial deviations can be falsely detected as cracks, especially for polycrystalline DUT (Figure 5.5c). Conversely, cracks at dark or along inactive areas can remain undetected if their image gradient is too small. In order to improve the success rate and quality of this feature detection algorithm, further evaluation is needed. The success rate of the algorithm can be evaluated by viewing at the corrected EL images and their extracted features in Appendix 4.1.

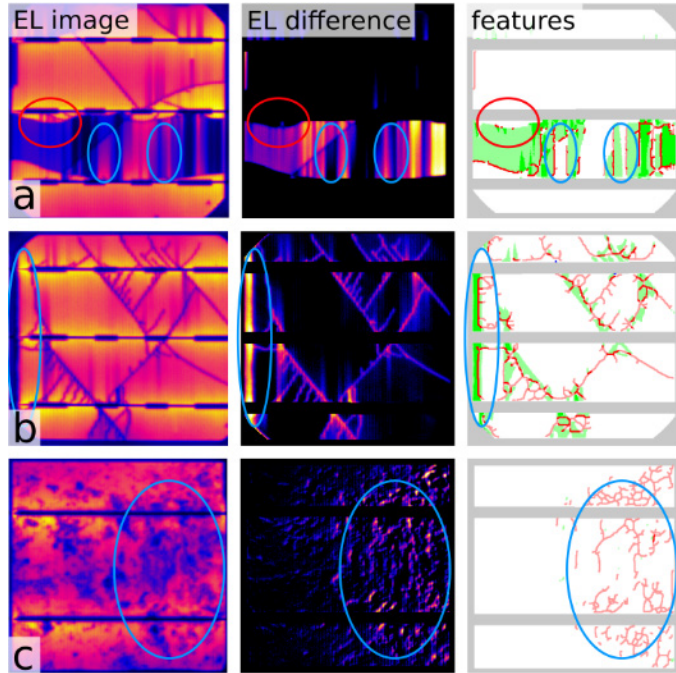


**Figure 5.5: EL image, EL difference image and thereof extracted features of three PV cells; False positive (blue) or false negative (red) detected cracks**

### 5.3.2 DERIVING QUANTITATIVE PARAMETERS

Qualitative crack classification has so far distinguishes either by crack number [103], appearance [109] or severity [103]. The resulting crack types include ‘dendritic’, ‘parallel to busbars’ and ‘45° angled’ as well as cracks rated as type A-C (non-disconnecting, disconnecting, isolating). In contrast to these approaches, this thesis focusses on a cell-by-cell parameterization of crack orientation maps (Figure 5.4e).

The crack length ( $l_{cr}$ ) is calculated from the sum of detected crack pixels ( $n_{cr}$ ) relative to cell width ( $s_{cell}$  [px]). The main crack direction ( $d_{cr}$ ) is extracted from the crack orientation map ( $d_i$ ):

$$l_{cr} = 100\% \cdot \frac{n_{cr}}{s_{cell}} \quad (5.3)$$

$$d_{cr} = \text{median}(d_i) \quad (5.4)$$

Crack fragmentation ( $f_{cr}$ ) represents the spread of different crack orientations. Values of  $f_{cr}$  below 30% indicate clearly orientated and straight cracks, whereas values above 60% suggest a broad distribution of different crack orientations and/or arched cracks.

To calculate ( $f_{cr}$ ) the numbers of pixels of each orientation ( $n_{px}(d_i)$ ) is counted and sorted by decreasing pixel number. An example based on the cell and convolutions kernels shown in Figure 5.4e,f is shown in Figure 5.6.

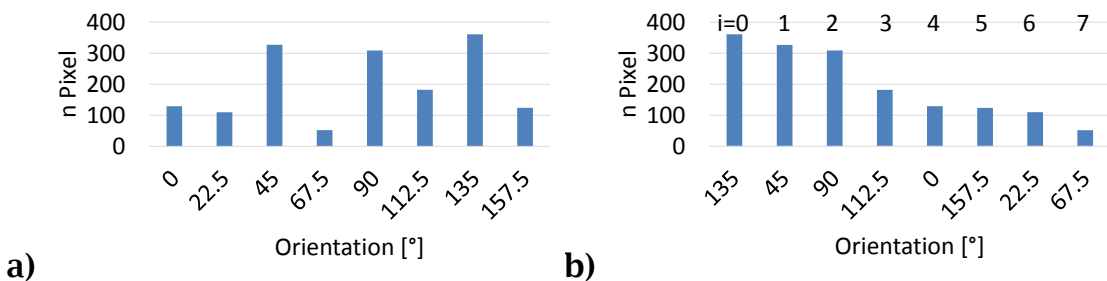


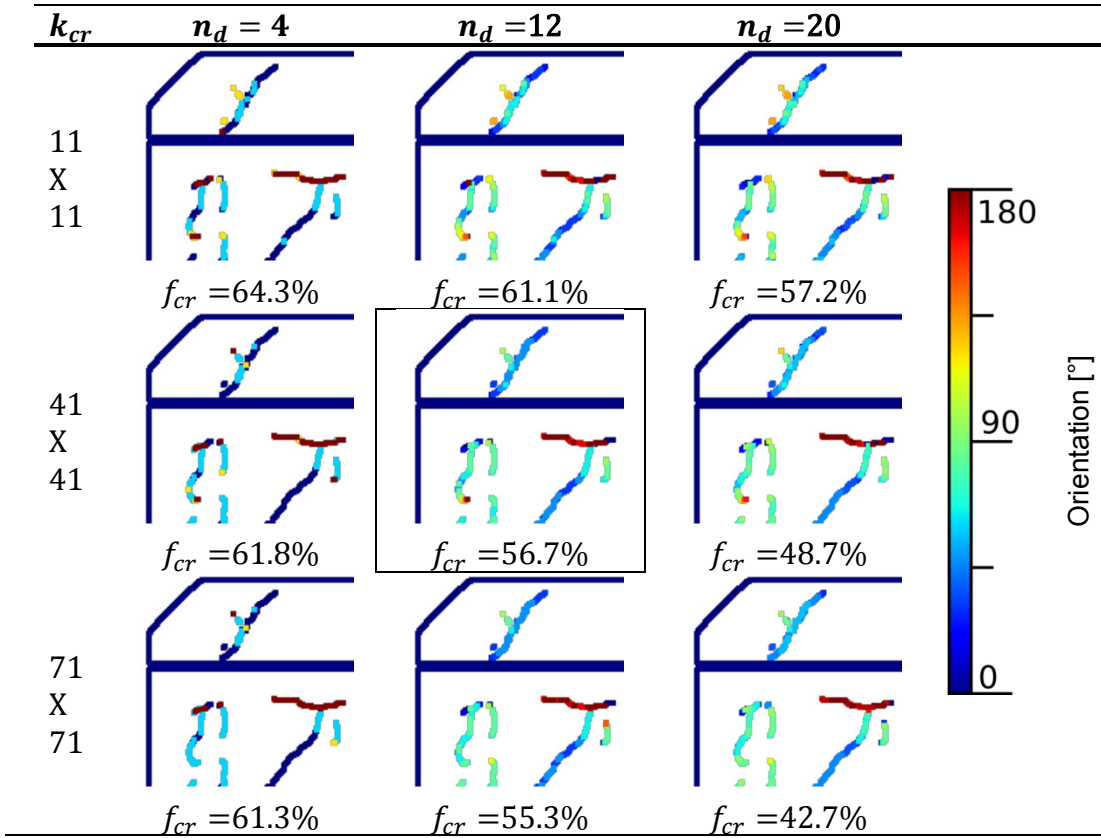
**Figure 5.6: Number of pixels at the same orientation, arranged by orientation (a) and by decreasing pixel number (b)**

From the orientation index ( $i$ ) and the number of directions ( $n_d$ ), the crack fragmentation can now be calculated as:

$$f_{cr} = 100\% \cdot \frac{\sum(n_{px}(d_i) \cdot i)}{(\sum(n_{px}) - 1) \cdot \frac{1}{2} \cdot n_d} \quad (5.5)$$

$f_{cr}$  depends on the number of evaluated discrete orientations ( $n_d$ ) as well as the size of the convolution kernel ( $k_{cr}$ ) (Table 5.1). The deviation between actual and assigned crack orientation decreases with increasing  $n_d$ . An increasing  $k_{cr}$  decreases the number of crack orientations identified, favouring longer cracks. In this work,  $n_d$  is set to 12 and  $k_{cr}$  to 41x41 (respective 10% cell width) as compromise between precision and computation speed (Table 5.1 middle).

**Table 5.1: Comparison of crack fragmentation ( $f_{cr}$ ) at different convolution kernel sizes and number ( $n_d$ ) of evaluated orientations**



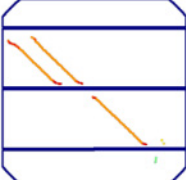
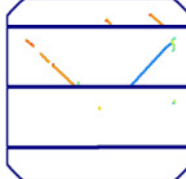
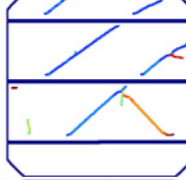
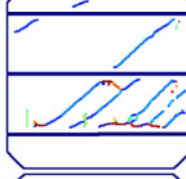
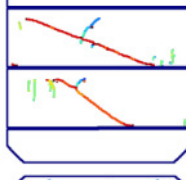
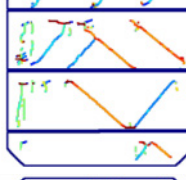
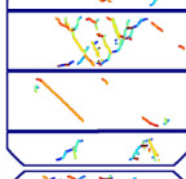
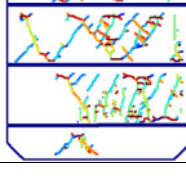
Whether crack orientations are more evenly distributed or more segregated into two peaks (X-shaped cracks) can be evaluated with the bimodality ( $b_{cr}$ ) of the crack orientation. It can be calculated from the skewness ( $g_{d_i}$ ) and excess kurtosis ( $k_{d_i}$ ) of the crack orientation distribution ( $d_i$ ) as follows [110]:

$$b_{cr} = 100\% \cdot \frac{g_{d_i}^2 + 1}{k + \frac{3(l_{cr} - 1)^2}{(l_{cr} - 2)(l_{cr} - 3)}} \quad (5.6)$$

However,  $b_{cr}$  does not distinguish, whether the main crack orientations are  $90^\circ$  apart and does not distinguish, whether the two major crack directions consist of many short cracks or a few long ones.

Table 5.2 compares the four described parameters on eight crack orientation maps.

**Table 5.2: Crack parameters calculated from example crack orientation maps**

ID	Crack orientation	$f_{cr}$	$l_{cr}$	$d_{cr}$	$b_{cr}$
1		<b>9.3%</b>	97.5%	135°	9.3%
2		<b>26.5%</b>	75.5%	135°	88.2
3		<b>27.7%</b>	181%	30°	70.3%
4		<b>30.6%</b>	277%	45°	29.3%
5		<b>38.4%</b>	205%	165°	81.3%
6		<b>56.7%</b>	398%	45°	47.2%
7		<b>67.5%</b>	338%	120°	55.7%
8		<b>70.9%</b>	873%	60°	61.9%

### 5.3.3 DERIVING ELECTRICAL CHARACTERISTICS FROM DETECTED CRACKS

Demant et al. conducted wafer breakage experiments and measured the wafer fracture strength as a function of crack length and orientation [105]. Since this thesis focusses on PV modules and the only measurement methods available are EL, LIV and DIV, a direct relationship between individual cracks and mechanical or electrical PV performance cannot be established. The case study in Section 7.1 analyses the influence of parameters, such as crack length and changed EL intensity on the device performance.

This subsection describes a fast and simple method to additionally estimate the increase in series resistance due to cracks using an example monocrystalline PV cell with three busbars (Figure 5.7a).

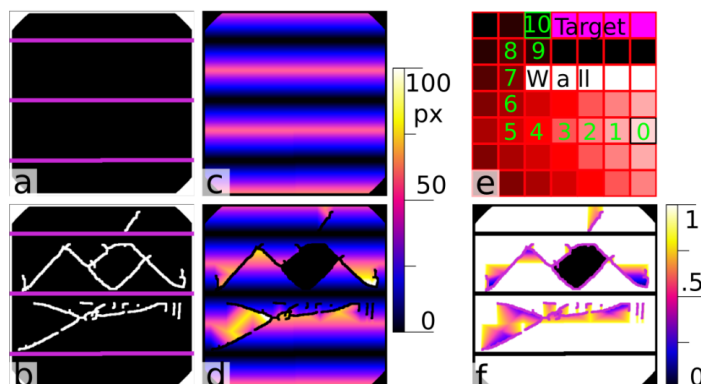


**Figure 5.7: Schematic for calculating series resistance increase maps; a,b) input busbar (target) and wall maps; c,d) resulting distance maps; e) Conditional region growth method; f) resulting series resistance factor map**

The minimum distance [px] to the closest connecting busbar (magenta lines) is calculated for every image pixel (black area). This is done with the following conditional region-growth algorithm (Figure 5.7e) using an array in which every pixel is labelled either ‘empty’, ‘wall’ (crack) or ‘target’ (busbar):

1. From the current position: Propagate towards direct neighbour pixels. Set every pixel which is not labelled ‘empty’ or ‘wall’ to the current iteration number.

2. Repeat with (1) for every new position.
3. Stop when new position is marked as ‘target’.

The resulting distance maps are calculated for both, the intact ( $D_0$ ) and cracked cell ( $D_{cr}$ ) (Figure 5.7c,d). Finally, the series resistance ratio ( $r_{Rs}$ ) from the ratio of both maps (Figure 5.7f) is calculated using:

$$r_{Rs} = \frac{D_0}{D_{cr}} \quad (5.7)$$

This method enables identification of isolated or high series resistance areas using only the detected crack positions. The  $r_{Rs}$  map average ( $f_{Rs}$ ) can be related to the actual power decrease. Four example results are compared to their origin EL images in Table 5.3.

**Table 5.3: Comparison of calculated series resistance increase maps and their respective EL image**

ID	EL image	$r_{Rs}$	$f_{Rs}$
1			82.1%
2			81.3%
3			91.9%
4			86.7%

In direct comparison between EL images and  $r_{Rs}$  maps, the deficiencies of this model become clear:

1. The model assumes that every crack is electrically isolating. However, for the majority of cracks in Table 5.3, fingers remain intact. Therefore, in cell 1 the two quadrilateral areas in the middle still emit light although they are surrounded by cracks.
2. When a crack is isolating (such as bottom right in cell 4) its influence extends not just to the closest, but also the opposite busbar. This crack only causes decreased  $r_{Rs}$  values to the central region between two busbars. Using the region-growth method described, the bottom half is unaffected - in contrast to the behaviour in the EL image.
3. The validity of  $r_{Rs}$  strongly depends on the accuracy of the crack detection. As the  $r_{Rs}$  map of cell 4 (bottom left) shows, even a small undetected cracked area can be decisive, as to whether an area is isolated or not.
4. Broken busbars are not considered.

Despite these deficiencies, this method can be useful for rating the ability of individual cracks to cause disconnections or inactive areas, similar to the crack criteria defined in [111].

## 5.4 Chapter Summary

Usually, features (like cracks) are extracted from single EL images and not from before/after differences. In particular for polycrystalline DUT, extrinsic features are superimposed with DUT intrinsics, like grain boundaries. The differentiation between both requires rather complicated algorithms. In contrast to this, this chapter presented algorithms to extract inactive areas and cracks from relative EL difference images. Therein, extrinsic features dominate.

After detailing feature extraction, four parameters to quantify detected cracks were introduced. These parameters allow a more sophisticated

statistical EL analysis than the rather loose crack counting method [103]. One of these parameters (crack length) will be correlated to module power decrease in Subsection 7.1.2.

Instead of manually subdividing cracks into their putative severity, their negative influence on DUT performance is calculated with a ‘series resistance factor’ map.

# 6 UNCERTAINTY ANALYSIS

How much can the intensity of a pixel or pixel group in an EL image be trusted to be representative for the actual EL signal? This section investigates different sources to the overall EL image uncertainty. It is separated into sources affecting uncertainty of signal intensity and uncertainty of signal position. Three different sub-uncertainty maps (noise, position, signal and correction) will be generated in order to calculate the overall uncertainty map due to the different rules of averaging uncertainty. This map assigns an uncertainty value to every pixel in an EL image (Figure 6.1).

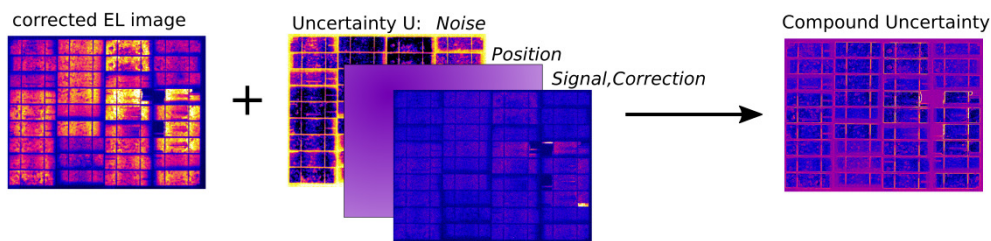


**Figure 6.1: Example uncertainty map for a corrected EL image of a c-Si module at 10%  $I_{sc}$**

## 6.1 Intensity Uncertainty

### 6.1.1 SIGNAL QUANTISATION

The quantization error of an analogous signal digitised between two discrete states namely 0 and 1 is its mean:  $\pm 0.5$  [112]. If the signal range is much bigger than the discretization states, a uniform distribution of all values within the range can be assumed. In this case the standard deviation within the step becomes  $\frac{1}{\sqrt{12}} \approx 0.298$  [113]. An increasing value range decreases the relative distance between discrete states. For the dark

current corrected measured pixel intensity ( $\Phi_{EL}$ ) the standard quantization or round-off uncertainty ( $U_{\Delta\Phi_{EL}}$ ) can then be expressed using:

$$U_{\Delta\Phi_{EL}} = \frac{1}{\sqrt{12} \cdot \Delta\Phi_{EL}} \quad (6.1)$$

In order to evaluate the importance of the quantization uncertainty,  $U_{\Delta\Phi_{EL}}$  is calculated for three common camera sensor depths ( $D = 8, 14, 16$  bit) and relative image intensities ( $r$ ). A homogenous dark current level of 5% is assumed.  $\Delta\Phi_{EL}$  is calculated as follows:

$$\Delta\Phi_{EL} = n \cdot r - 5\% \cdot n; \quad n = 2^D - 1; \quad r = \frac{\text{mean}(\Phi_{EL})}{n} \quad (6.2)$$

The resulting values for  $U_{\Delta\Phi_{EL}}$  are shown in Table 6.1.

**Table 6.1: Quantization uncertainty for different camera sensor depths and relative signal ranges**

$r$	8 bit (0...255)	14 bit (0...16383)	16 bit (0...65535)
10%	2.26%	0.04%	0.009%
30%	0.45%	0.007%	0.002%
50%	0.25%	0.004%	0.001%

An error above 2% occurred only with an 8 bit camera and a low signal intensity of 10% ( $\Phi_{EL} = 26$ ). In the EL Round Robin evaluation (Subsection 7.2.1) the majority of laboratories used a 16 bit camera and image intensities were distributed around 20% relative to the maximum possible value. This causes quantization uncertainty to be far below one percent. Therefore  $U_{\Delta\Phi_{EL}}$  is not considered any further.

## 6.1.2 IMAGE NOISE

The calculation of the signal-to-noise ratio (SNR) is described in detail in Section 3.1. Since signal quantization was found to be neglectable, the uncertainty due to image noise ( $U_{Noise}$ ) can be directly calculated from the inverse of the SNR:

$$U_{Noise} \equiv \frac{1}{SNR} \quad (6.3)$$

## 6.1.3 IMAGE CORRECTION

Background-, perspective- and flat field correction modify image intensity. Their correction residuals are discussed as follows.

### 6.1.3.1 BACKGROUND

In Section 3.1 it was shown that a background calibration is suitable to remove dark current, hot pixels and stray light, if light conditions are immutable. For variable light conditions however, an additional image taken at open-circuit voltage and otherwise identical settings should be taken instead.

Light conditions during outdoor EL measurements are generally variable. To decrease the influence of stray light, measurements are done with a mobile dark chamber, at night or with a lock-in technology. It is assumed that the influence of changing light conditions in a mobile chamber, during the night or during one lock-in cycle can be neglected. However as discussed, background correction can also increase image noise. This noise adds to the general image noise level. It will be recognised by the signal-to-noise ratio and does not need extra consideration.

### 6.1.3.2 PERSPECTIVE

The EL emission of PV devices changes less than 5% within a  $\pm 50^\circ$  tilt angle (Figure 3.82). For higher angles, the intensity decrease can be corrected. The success of this method relies on the precision of DUT corner detection. An intensity deviation from faulty perspective correction becomes visible above a tilt angle of  $80^\circ$  (Figure 3.84). EL images taken with such high perspective distortions are expected to be exceptional. Therefore, this source of uncertainty will not be considered.

### 6.1.3.3 FLAT FIELD

The evaluation of averaged cell intensities of corrected EL images of the same devices within the conducted EL Round Robin (Subsection 7.2.3.1) showed intensity deviations from 5 to 15%. It was found that these deviations were mostly caused by residual flat field distortion. As Section 3.6.4 concludes, the method applied within the Round Robin was found to be unsuitable for flat field measurement. If flat field is measured with other, more promising methods (like Method E, Subsection 3.6.2.5) the standard deviation of cell averages decreased in some cases to 1-2 %. This standard deviation is a valid estimation of uncertainty due to imperfect flat field correction. If it can be assumed that flat field calibration is done with a similarly precise method, uncertainty from image correction ( $U_{corr}$ ) is approximately 2%.

### 6.1.4 EL SIGNAL STABILITY

The emitted EL signal is not steady over time. Random variations ( $U_{EL-r}$ ), warm-up behaviour ( $U_{EL-w}$ ) as well as the dependency of calibration- to measurement exposure time ( $U_{EL} \left( \frac{t}{t_0} \right)$ ) are analysed in the following subsections.

#### 6.1.4.1 DUT WARM-UP

Transient EL changes during operation are mainly caused by different temperatures during the warm-up of the device. To evaluate the influence of these changes, a silicon and a thin-film DUT were imaged in steps of 30(60) s for 60(90) min. Initial, last and difference image are shown in Figure 6.2. For this evaluation, all images were corrected for dark current, flat field, lens, perspective and intensity as described in Chapter 4. Both DUT were operated at 100 %  $I_{sc}$ . It is assumed that transient EL signal variations are smaller for smaller  $I_{sc}$  due to reduced injected power and therefore reduced operating temperatures.

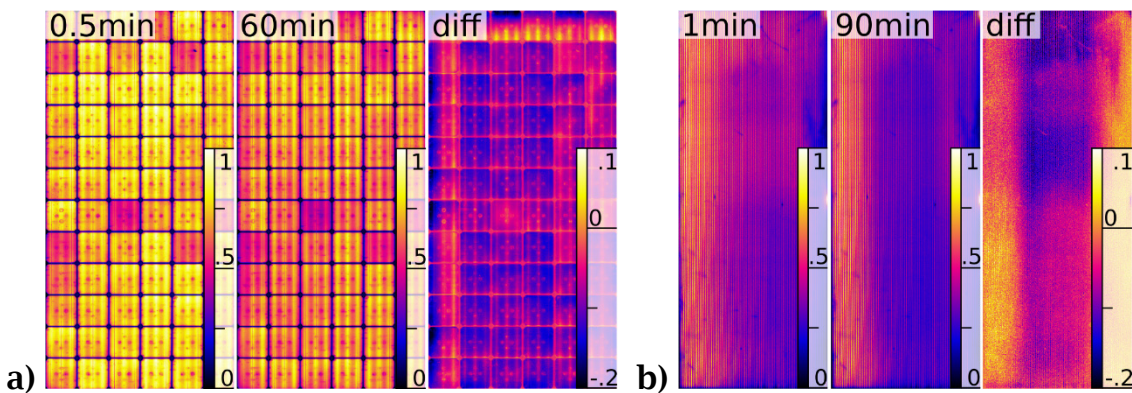


**Figure 6.2: Initial, final and (final-initial) difference EL images for a (a) c-Si and (b) CIS DUT**

In particular Figure 6.2a shows a decreased EL signal after 60 min of operation. The module was mounted on an L-shaped metallic structure. This structure becomes visible in the difference image ‘diff’. Along the busbars, image intensity decreased least during operation.

A less homogenous EL intensity change is shown in Figure 6.2b. Therein, intensity remains constant or even increases along the long edges whilst the centre area shows decreased values.

The change of the by-cell-averaged intensities (6x12 for the c-Si-module and 80x1 for the CIS-module) over measurement time, operation voltage and DUT temperature shows Figure 6.3 and 6.4. In this experiment, operation voltage was taken from a two-wire measurement. The DUT

temperature was measured with one temperature sensor, attached at the back of the DUT.

It is stated that the values obtained with a single or two sensors are not sufficient to capture the extent of DUT temperature differences. Deriving a physical model from these measurements would require a spatially resolved temperature map. This map would have to be measured with a thermography camera, which was not available and is therefore omitted.

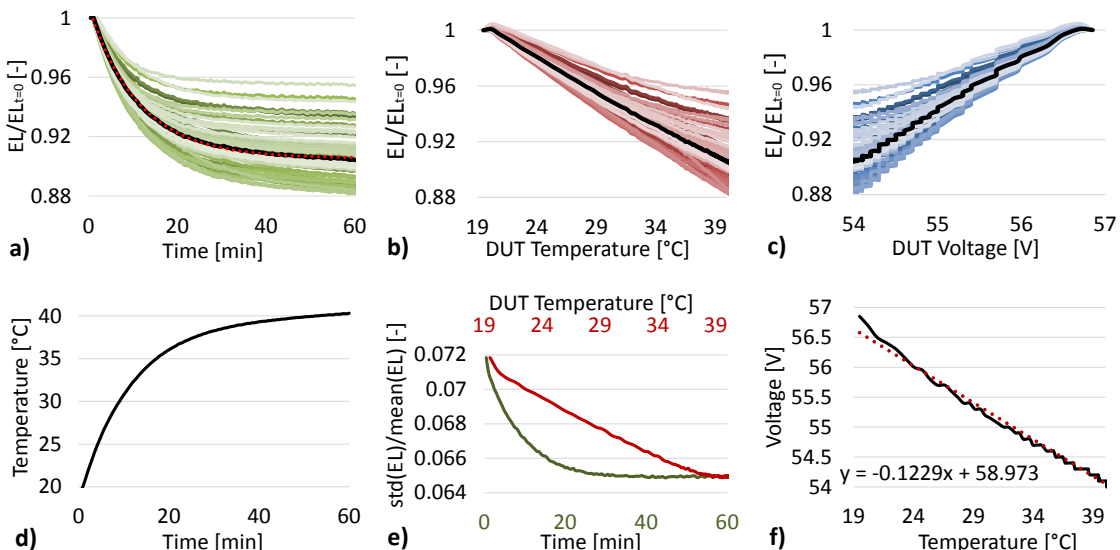


**Figure 6.3: Measurement results of a c-Si-module, shown in Figure 6.2a;**  
 a-c) Average cell values relative to first measurement;  
 a) Value ratio over measurement time;  
 b) Value ratio over average DUT temperature;  
 c) Value ratio over operation voltage; Black: Module average. Red: Fit using Equation 6.4;  
 d) Average DUT temperature over time;  
 e) standard deviation of all cells relative to DUT mean over measurement time [green] and DUT temperature [red];  
 f) Operation voltage over DUT temperature; red: linear fit

The trend in Figure 6.3a-c leads to the following conclusions: The module average (black) and also the cell averages decrease over time. After 60 min of operation, the intensity ranges from 88% to 96% of the initial intensity. The intensity decrease follows a linear trend, if compared to DUT temperature or operation voltage. As Subfigure (f) shows, the operation voltage decreased with temperature at roughly  $-120 \text{ mV/C}^{\circ}$ . Although the module temperature did not stabilize during

measurement time (d) it can be assumed that the maximum temperature is below 45°C. The relative standard deviation from all cell intensities (e) decreases over measurement time. This means that the cell intensities equalize slightly during operation. The same trend, plotted over DUT temperature (red line in (e)) again is linear within a wide range. Figure 6.4 shows the same plots for the CIS-module shown Figure 6.2b.

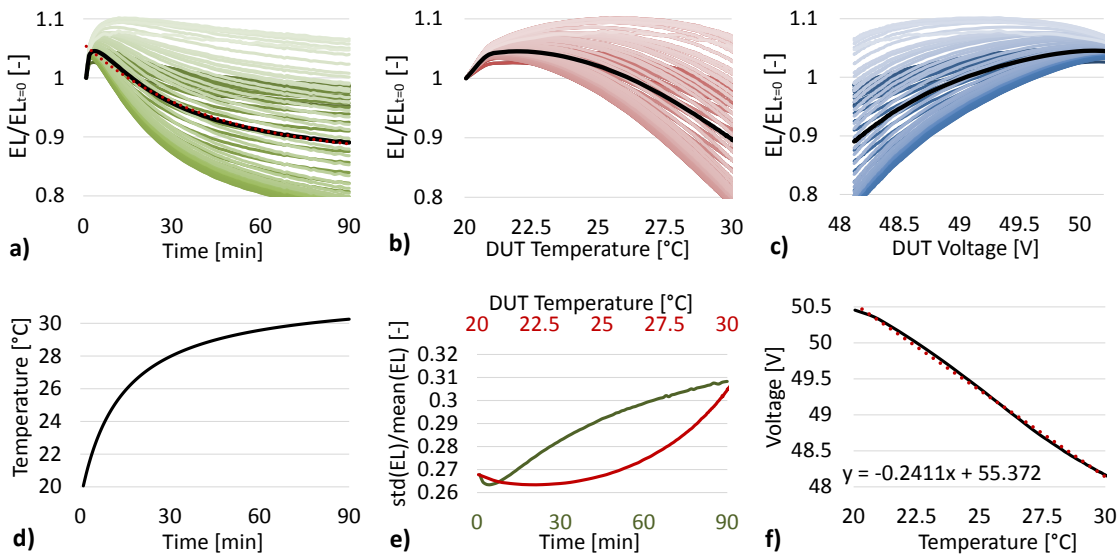


**Figure 6.4: Measurement results of CIS-module, shown in Figure 6.2b; for description of subfigures, see Figure 6.3**

The values in Figure 6.4 do not appear to settle homogenously. EL intensities rather increase over the first 20 min and then stabilise (Figure 6.4a). Also cell intensities do not change linearly with DUT temperature or operation voltage (b,c). Although the DUT temperature does not stabilize within the 90 min of measurement (d) it is assumed that the maximum temperature is lower than 32  $^{\circ}$ C. With -241 mV/ $^{\circ}$ C the thermal effect of operation voltage appears to be twice as high as for the c-Si-module (f). Metastabilities causing an EL increase of a similar CIGS device were also observed in [114] and therein ascribed to bulk series resistance reduction during bias soaking.

For both evaluated DUTs the average cell intensity over time follows the general decay function:

$$\varphi(t) = (\varphi_0 - \varphi_\infty) \cdot e^{-a \cdot t} + \varphi_\infty \quad (6.4)$$

Where:

---

$\varphi(t)$	EL signal at time t
$\varphi_0$	EL signal at t = 0 min
$\varphi_\infty$	EL signal at t = infinite
a	Diffusivity constant $[\frac{1}{min}]$

---

The intensity change over time for different diffusivities ( $a$ ) and an example EL intensity change from one to zero is shown in Figure 6.5.

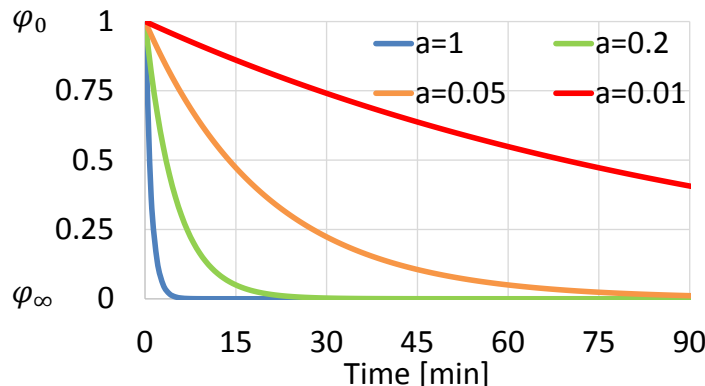


**Figure 6.5: Impact of different diffusivities ( $a$ ) on the EL intensity change over time**

The exponential function (Equation 6.4) was used to fit the 120(90) images taken of both DUT. For the CIS-module, EL images at measurement times smaller 20 min were excluded since the EL signal did not follow Equation 6.4 (Figure 6.4a). The resulting maps for the EL signal at  $t=0$ ,  $t=infinite$  and their difference are shown in Figure 6.6.

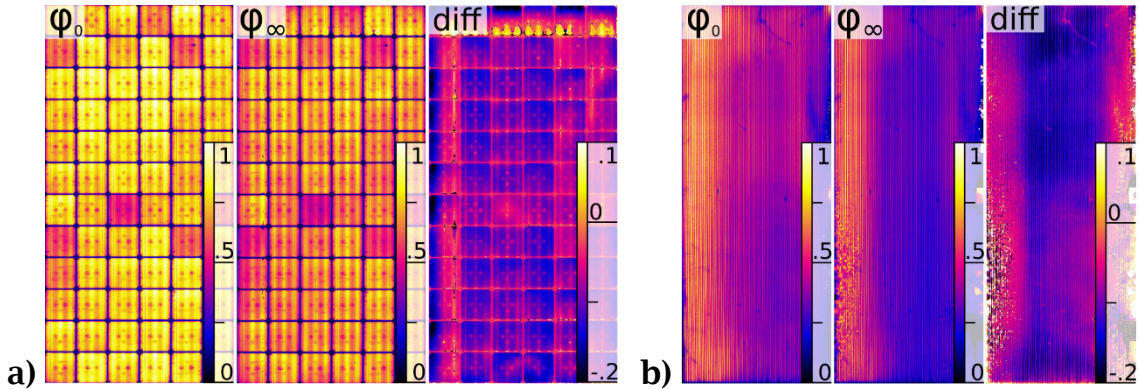


**Figure 6.6: Resulting maps from fitting every image pixel along measurement time using Equation 6.4 for (a) c-Si and (b) CIS DUT; intensities scaled in same range as Figure 6.2**

With  $\varphi_\infty$  an extrapolated EL image at  $t=\text{infinite}$  was calculated and with it, the steady-state EL signal. The strong similarities in comparison to Figure 6.2 are as expected. Differences can be seen in Subfigure (a) along the busbars in the left row and top column where in particular the difference image shows higher values. The difference image in Subfigure (b) also shows a stronger separation between intensities along the long edges and the DUT centre. To allow an undisturbed view in both ‘diff’ images, pixels that could not be fitted with Equation 6.4 were substituted with interpolated values obtained from a k-nearest neighbour approach.

If the EL signal is defined to be stabilised if the relative difference to its  $\varphi_\infty$  value is below 5% ( $m = 0.05$ ), then the time required to stabilize the signal ( $t_{st}$ ) can be calculated as follows:

$$t_{st} = \frac{\ln\left(\frac{m \cdot \varphi_0 + (1 - m)\varphi_\infty - \varphi_\infty}{\varphi_0 - \varphi_\infty}\right)}{-a} \quad (6.5)$$

The resulting maps together with diffusivity ( $a$ ) are shown in Figure 6.7.

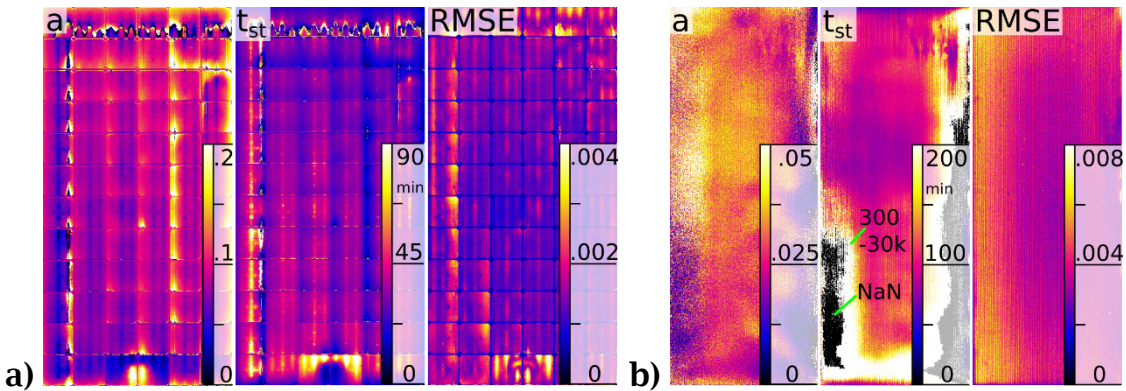


**Figure 6.7: Diffusivity (a), stabilisation time ( $t_{st}$ ) and RMSE of the fitted DUT maps in Figure 6.6**

The resulting maps are independent of the initial and final EL signal. Diffusivity and stabilisation time are inversely proportional. The diffusivity map in Figure 6.7a shows the impact of the junction box at the bottom of the DUT. Directly over the junction box the EL signal stabilises comparatively quickly. On both sides of the junction box however, it takes more than 90 min to stabilise. The small circular prints on every cell of the c-Si module are caused from cell handling during manufacturing. It can be seen that their stabilisation time is comparatively long.

The results shown in Subfigure (b) are less revealing. However, it is shown that low diffusivity values at the bottom left and right cause erroneously long or wrong stabilisation times. It can be assumed that more EL images at measurement times higher than 90 min would have improved the fit quality. A histogram of the  $t_{st}$  maps shows the area ratio [%] which stabilises at which measurement time (Figure 6.8).

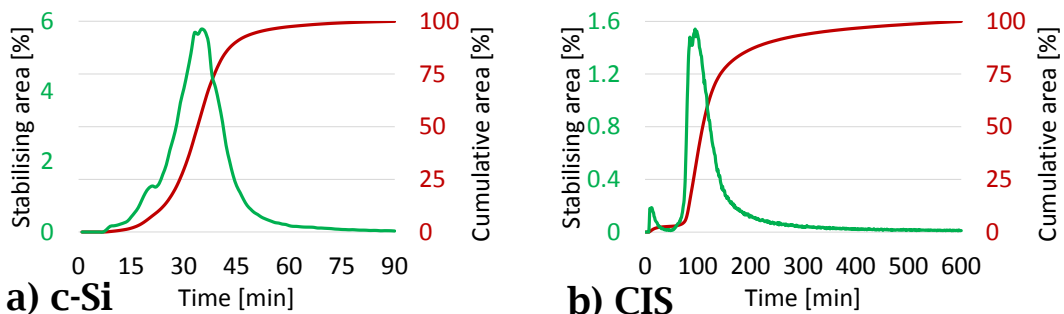


**Figure 6.8: Stabilising DUT area (green) from histogram of  $t_{st}$  maps, shown in Figure 6.7; red: cumulative sum of green plot**

The stabilisation area of the c-Si module follows a Gaussian distribution with a mean time of 43 min. For the CIS module the majority of areas stabilised after 100 min and after the last measured time (90 min).

The EL signal deviation ( $d(t)$ ) relative to the final measurement is shown in Figure 6.9.

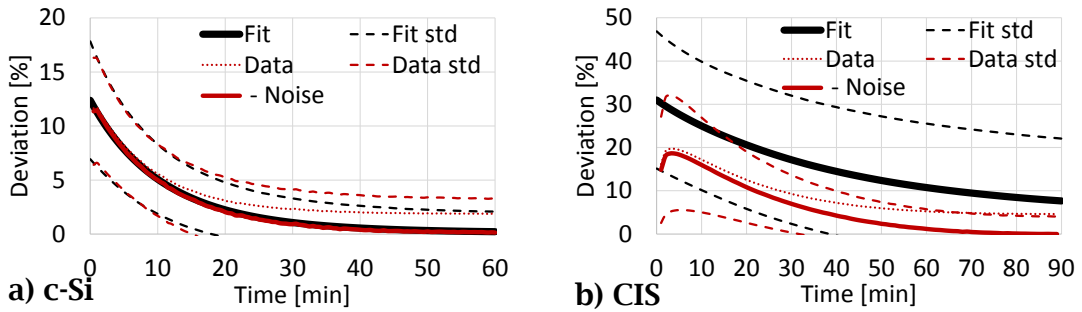


**Figure 6.9: EL signal deviation, relative to  $\varphi_\infty$  or relative to last measurement; red: deviation from measured EL images; black: deviation from fit using Equation 6.4**

Therein, black lines show the deviation calculated from the fitted maps:

$$d_{fit}(t) = \frac{|\varphi_\infty - \varphi(t)|}{\varphi_\infty} \quad (6.6)$$

Full lines show the mean of the resulting deviation map and dashed lines show its standard deviation. In comparison to this, red lines show mean and deviation obtained from all measured EL images, relative to the last image ( $\varphi_{last}$ ):

$$d_{meas}(t) = \frac{|\varphi_{last} - \varphi_t|}{\varphi_{last}} \quad (6.7)$$

As the red dotted lines show, deviation stabilizes at a certain level above zero. This is due to remaining image noise. The influence of image noise is already evaluated in Subsection 6.1.2. Therefore, in this discussion noise is removed by subtracting every  $d_{meas}(t)$  using:

$$d_{meas,2}(t) = d_{meas}(t) - \frac{d_{meas}(t_{last})^2}{d_{meas}(t)} \quad (6.8)$$

This assumption only holds true, if the EL change between the last two measurements is negligible and the last difference is mostly caused by image noise. Figure 6.9a shows a good agreement between the deviation from fitted and measured data. The average deviation falls to 5% after the first 10 minutes of measurement. This discovery lead to the creation of the requirement for a 10 minute warm-up time before measuring EL in the conducted EL Round Robin (Section 7.2).

In comparison to (a), Subfigure (b) is again less conclusive. The EL signal deviation, calculated from fitted maps (black) indicates a remaining deviation of 10% at the last measurement time of 90 min. Looking at the measured results (red), the deviations fall to 5% after 40 min. Since the measured results use the last EL image as a reference, the last deviation is zero at 90 min. Therefore an offset of 10% between measured and fitted data is almost constant for the duration of measurements. The deviation increases only within the first five minutes. As Figure 6.4 shows this is due to the globally increasing EL signal at that time.

#### 6.1.4.1.1 QUANTIFYING WARM-UP UNCERTAINTY

EL signal deviation in the warm-up phase is mainly caused by temperature changes. For DUTs with known warm-up behaviour ( $\varphi(t, \varphi_0, \varphi_\infty, a)$ ), the related uncertainty ( $U_{EL-w}$ ) can be described by the root-mean-square fit error. For the two analysed cases, this error is below one percent and can be neglected. For the analysed CIS module, the decay Equation 6.4 is only applicable for measurements after 20 min warm-up.

The calculated fit depends on the measurement environment which includes ambient temperature, applied current (in this case 100%  $I_{sc}$ ) as well as conduction of the DUT mounting frame and air convection in the measurement chamber. Forced convection by ventilation can reduce temperature differences and cause a faster stabilisation. In addition, a

thermally conductive (particularly metal) mounting frame can visibly influence the EL signal.

However, these conditions are normally unknown or not measured. Therefore, the following two models (Table 6.2) are introduced to quantify EL warm-up uncertainty ( $U_{EL-w}$ ).

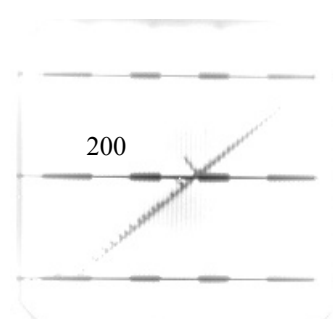
**Table 6.2: Models used to quantify  $U_{EL-w}$  derived from Figure 6.9**

Model A	Model B		
Ambient temperature $20 \pm 5^\circ\text{C}$	No information		
Closed measurement chamber	No information		
Forced warm-up phase of $10 \pm 2$ min at the same current as measured	Measurement taken at some point between 0...15 min within warm-up phase		
Exposure time within 2 min			
Crystalline	Thin-film	Crystalline	Thin-film
$U_{EL-w} = 0.6\%$	$=0.8\%$	$U_{EL-w} = 2.8\%$	$=2.8\%$

Whilst model A is limited to indoor measurements, model B can be applied in every case. Model B includes the probability that measurements in prior (including those to set up exposure time) could have heated up the DUT to a certain extent. To calculate  $U_{EL-w}$ , the standard deviation of the average EL deviation (Figure 6.9, red line) is calculated for values from 8 to 12 min (model A  $\rightarrow 0.6\%, 0.8\%$ ) and from 0 to 15 min (model B  $\rightarrow 2.6\%$ ).

In model B it is additionally assumed that the conductivity of the DUT mounting frame influences the EL signal. To estimate its influence Figure 6.10 shows a line plot in x-axis of the first two cell columns.

A maximum deviation of  $\pm 4\%$  within the two cells can be seen. If it is assumed that this deviation is zero at  $t=0$  and its increase follows the same exponential function as the deviation in Figure 6.9a, its standard deviation becomes 1.1%. The effective uncertainty for model B therefore becomes  $U_{EL-w} = \sqrt{(2.6\%)^2 + (1.1\%)^2} = 2.8\%$ .



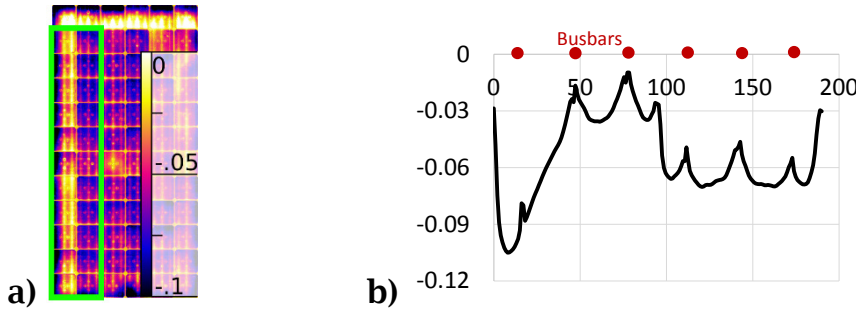


**Figure 6.10: a) EL difference image of c-Si module between 1 min and 15 min; b) Line plot in x-axis from green box in (a); busbar positions indicated with red circles**

#### 6.1.4.2 RANDOM VARIATIONS

Between 20/04/2015 and 03/06/2015, 15 individual EL measurements were conducted on a c-Si and a CIGS module. The setup (module mounting frame, cable connection, power supply control and camera) was kept identical for every individual measurement.

In every image set, two EL and two dark current images were taken at same current and exposure time. Every set resulted in one EL image, corrected for dark current, single-time-effects, lens, vignetting, and perspective (Chapter 4). Fifteen corrected EL images from the two DUT are shown in Figure 6.11-6.13. Therein, Subfigure (b, c) shows the individual difference to a measurement average for the entire device (b) and a region of interest (c).

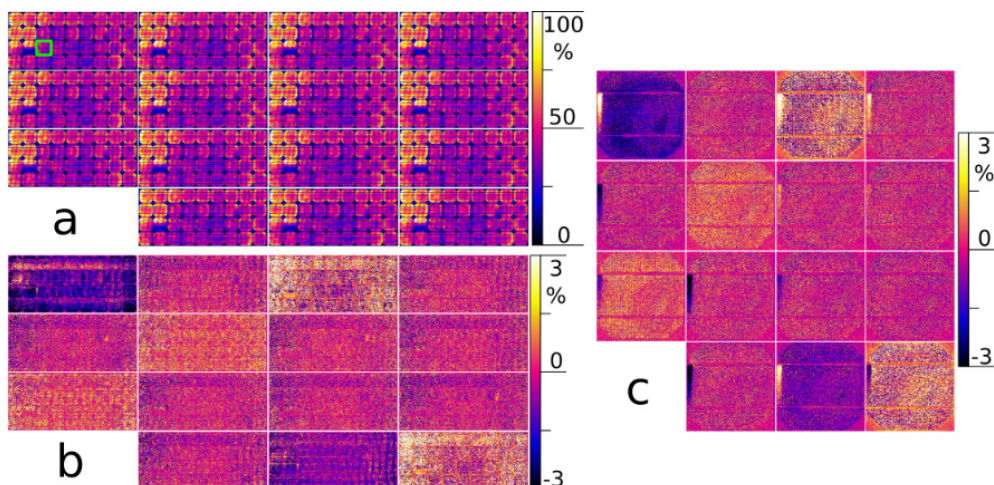


**Figure 6.11: a) corrected EL images of a c-Si module at 100%  $I_{sc}$ ; b) difference image relative to average of all EL images; c) same for ROI (green box) shown in (a)**

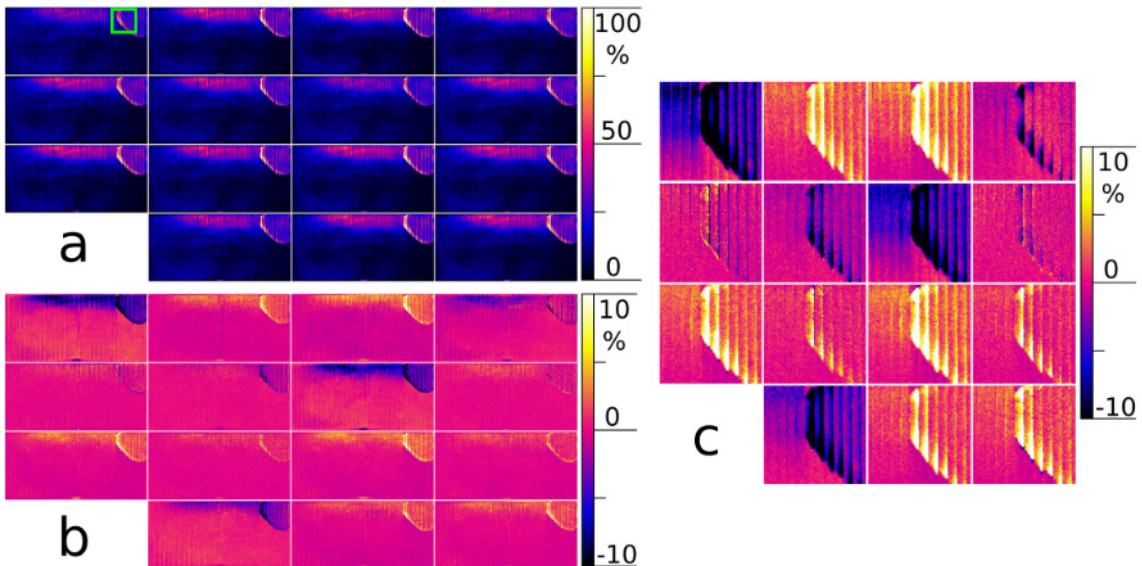


Figure 6.12: Same as Figure 6.11 for a CIGS module at 100%  $I_{sc}$

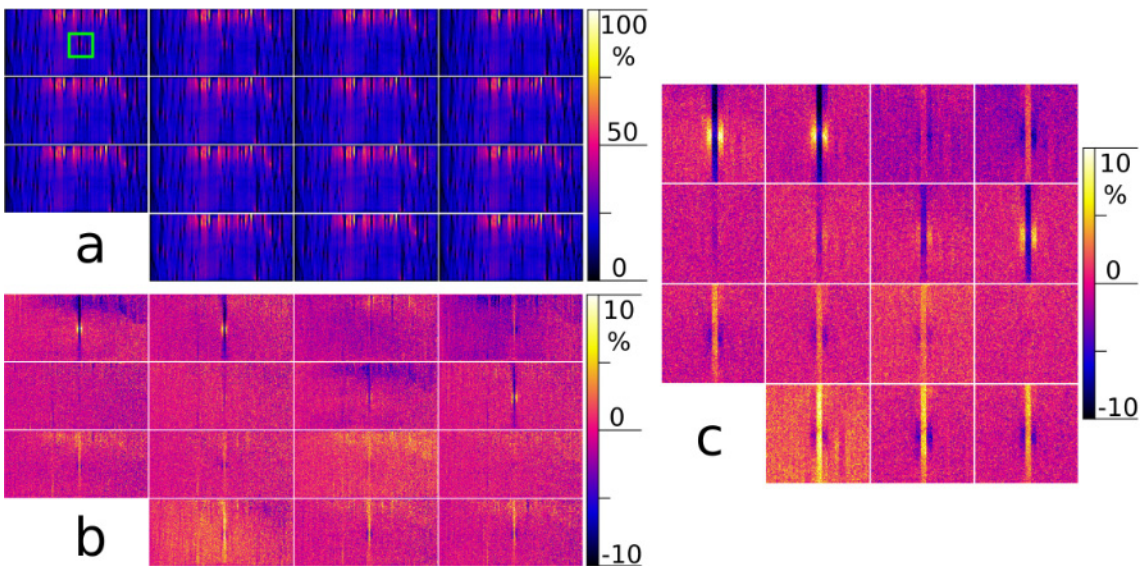
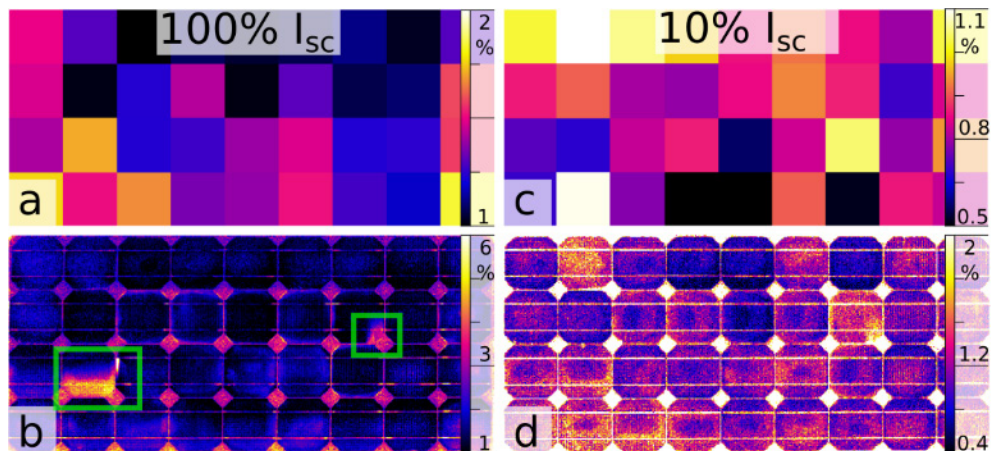


Figure 6.13: Same as Figure 6.12 at 10%  $I_{sc}$

Although the imaging setup was kept identical, the EL signal can be influenced by module handling, variations in connection resistance, electrical disturbances, ambient temperatures as well as signal fluctuations (Subsection 6.1.4.3). For the tested c-Si module, Figure 6.11b shows homogenous variations across the entire module. Subfigure (c) shows a fluctuating signal due to electrical reconnection next to a crack. In contrast to this, Figure 6.12b shows more localised variations mostly around high series resistance areas. In the 10%  $I_{sc}$  EL image (Figure 6.13)

the influence of series resistance is comparably lower. Due to the lower voltage, cell connection issues dominate EL deviations (Subfigure c).

From the EL images shown, the temporal RMSE was calculated and evaluated at module, cell and pixel scale. For cell and module averages, the respective area was spatially averaged before the RMSE was calculated. Results on two different area sizes are shown in Figure 6.14 and 6.15.



**Figure 6.14:** RMSE maps calculated from EL images of c-Si module (Figure 6.11) at 100%  $I_{sc}$  (a,b) and 10%  $I_{sc}$  (c,d); a,c) cell average; b,d) 7x7 pixel average

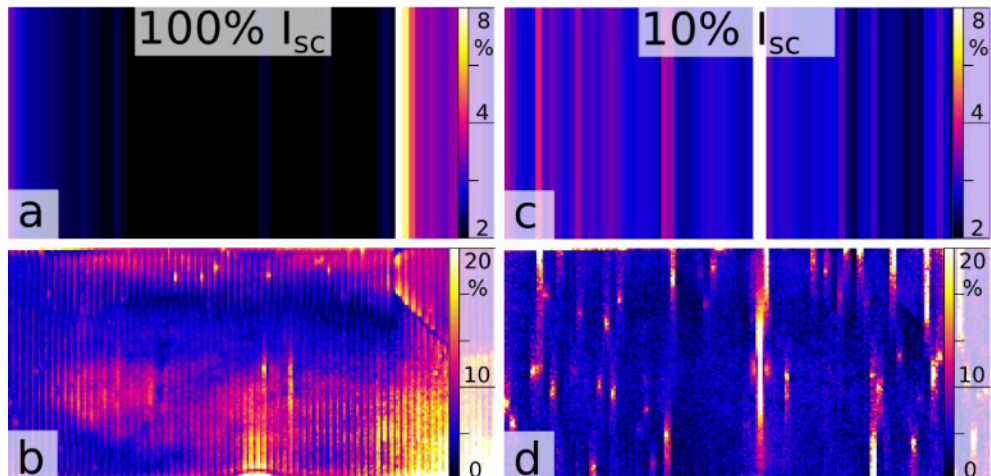


**Figure 6.15:** Same as Figure 6.14 for CIGS module (Figure 6.12)

The RMSE is relatively small and evenly distributed across the evaluated c-Si module (Figure 6.14). At 100 %  $I_{sc}$ , only one cell shows a larger area of higher deviation due to busbar connection issues. In addition, two smaller areas deviate due to cracks (green boxes).

Looking at the CIGS module (Figure 6.15) deviations are more spacious at 100%  $I_{sc}$  and more localised at 10%  $I_{sc}$ . Bright spots in Figure 6.15d can be caused by shunts. They are also visible but less pronounced in Figure 6.15b.

Since EL signal deviations are mostly smaller than 10% relative to their mean signal, image noise influences the result, especially if the averaged area is small. The following equation thereby calculates relative pixel noise ( $N_{px}$ ) for a difference image ( $\sqrt{2}$ , due to sum of variances) and an averaged area of width ( $w$ ) and height ( $h$ ):

$$N_{px} = \frac{1}{SNR} \sqrt{2} \frac{1}{\sqrt{w \cdot h}} \quad (6.9)$$

For both modules and both currents, the signal-to-noise ratio (SNR) was calculated using two EL images (taken in series) and one background image (taken at the same exposure time). Background areas were excluded from the SNR average. SNR calculation is further described in Subsection 3.1. Table 6.3 lists the calculated SNR and well as the pixel noise ( $N_{px}$ ) for different area sizes.

**Table 6.3: Top: calculated SNR for both devices at 10% and 100%  $I_{sc}$ ; bottom: area and area specific pixel noise ( $N_{px}$ )**

	c-Si		CIGS	
	10% $I_{sc}$	100% $I_{sc}$	10% $I_{sc}$	100% $I_{sc}$
SNR [-]	19.19	19.73	6.11	10.95

	Area [px]	$N_{px}$ [%]		Area [px]	$N_{px}$ [%]	
Module	3242x1453	2.55e-3	2.48e-3	1650x1000	0.018	0.01
Cell	355x355	0.02	0.02	22x1000	0.15	0.09
7 px	7x7	1.05	1.02	7x7	3.31	1.84
1 px	7x7	7.37	7.17	1x1	23.15	12.92

The influence of  $N_{px}$  is negligibly small for module and cell averages. If only few pixels are averaged however, noise can impact the calculated

RMSE. Table 6.4 lists the average and standard deviation for the calculated RMSE maps at module, cell and pixel level.

The table shows that the EL intensity variation increases temporally and spatially (by standard deviation of the RMSE map) with decreasing averaged area.

**Table 6.4: Average and standard deviation of calculated temporal RMSE maps shown in Figure 6.14 and 6.15**

[%]	c-Si				CIGS			
	<b>10% <math>I_{sc}</math></b>		<b>100% <math>I_{sc}</math></b>		<b>10% <math>I_{sc}</math></b>		<b>100% <math>I_{sc}</math></b>	
Area	Mean	St.dev.	Mean	St.dev.	Mean	St.dev.	Mean	St.dev.
Module	0.78	-	1.21	-	3.14	-	1.91	-
Cell	0.8	0.16	1.33	0.23	3.51	1.06	2.64	1.23
7 px	1.26	0.8	1.8	0.86	5.83	3.72	7.53	4.46
1 px	3.23	1.56	3.18	1.00	11.27	9.81	9.6	5.87

If pixel noise and EL signal are taken as independent coefficients, influencing the measured deviation, the influence of the EL signal can be extracted as follows:

$$U_{EL-r} = \sqrt{\text{RMSE}(I_i)^2 - N_{px}^2} \quad (6.10)$$

Table 6.5 lists the random EL variation ( $U_{EL-r}$ ) for the same areas, calculated from ‘Mean’ values, shown in Table 6.4 and  $N_{px}$ , shown in Table 6.3.

**Table 6.5: Resulting uncertainty due to random signal variations for two devices and two currents**

$U_{EL-r}$ [%]	c-Si		CIGS	
	<b>10% <math>I_{sc}</math></b>	<b>100% <math>I_{sc}</math></b>	<b>10% <math>I_{sc}</math></b>	<b>100% <math>I_{sc}</math></b>
Module	0.78	1.21	3.14	1.91
Cell	0.79	1.33	3.51	2.64
7 px	0.69	1.48	4.8	7.30
1 px	-	-	-	-

With  $U_{EL-r}$  values around 0.7 to 0.8% (10%  $I_{sc}$ ) respective 1.2 to 1.4% (10%  $I_{sc}$ ), no clear dependency on the averaged area can be identified for the c-Si module.  $U_{EL-r}$  decreases with increasing averaged area for the CIGS module. The last row in Table 6.5 remains empty because in this case the assumed pixel noise is higher than the calculated intensity deviation, resulting in a negative value within the square root (Equation 6.10).

#### 6.1.4.3 EXPOSURE TIME DEPENDENCY

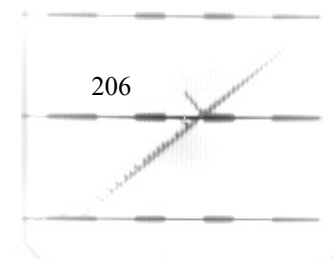
Uncertainty from signal variations is specific to the exposure time ( $t_0$ ) of the EL image set, used to measure it. For EL images taken at exposure times ( $t$ ) longer than  $t_0$ , the resulting uncertainty will be less, since variations average out during exposure. On the other hand,  $U_{EL}$  increases for exposure times shorter than  $t_0$ .  $U_{EL}$  can be adapted to exposure times ( $t$ ), different from  $t_0$  as follows:

$$U_{EL} \left( \frac{t}{t_0} \right) = \frac{U_{EL}}{\sqrt{\frac{t}{t_0}}} \quad (6.11)$$

This equation originates from the assumption that EL variations are Gaussian distributed. When summed, its variances ( $\sigma^2$ ) also sum [115]:

$$\sigma_{sum} = \sqrt{\sum \sigma_t^2} \quad (6.12)$$

However, the EL signal can vary over time due to positional drifts of cells or performance parameters changed with temperature, especially near extrinsic defects [116]. Figure 6.16 shows a polycrystalline Si module with several broken and inactive areas in the middle of the first two columns. In a set of 20 successively taken EL images at  $t_0 = 12$  s, multiple areas change their intensity. For every image taken, the average intensity within



the green ROIs in Subfigure (a) was plotted in (b). Areas disconnected over time, or reconnected once or twice. Due to the short absolute measurement time (4 min) and the high noise level in every image, a linear regression was used (instead of an exponential decay, Equation 6.4), to obtain a better fit the EL signal over time. The RMSE was then calculated from the differences between fitted and actual images (c).

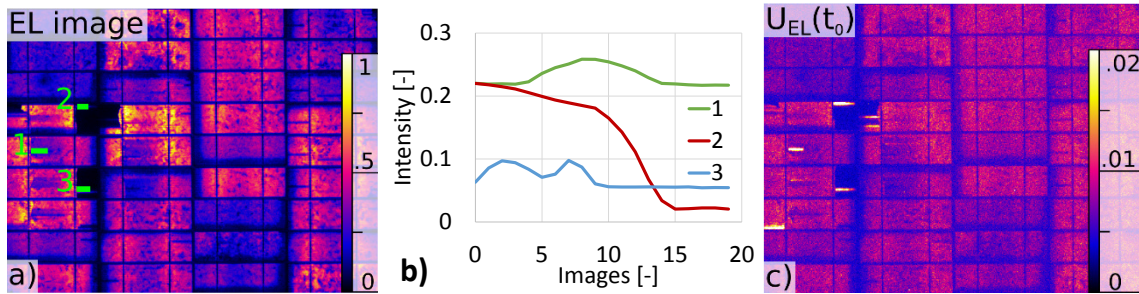


**Figure 6.16: Polycrystalline Si module;** a) EL image average (1-20); b) Average pixel intensity over measurement time for three ROIs, shown in (a); c) RMSE, calculated from the 20 taken EL images

The influence of signal fluctuations (named ‘events’) on uncertainty for exposure times different to  $t_0$  was evaluated numerically. For this, the signal was defined by its average (in this case zero) and standard deviation as well as event frequency ( $f$ ) and duration ( $d$ ). Three example synthetic signals with the same standard deviation of one are shown in Figure 6.17. Event position and amplitude follow a uniform, respective normal distribution.

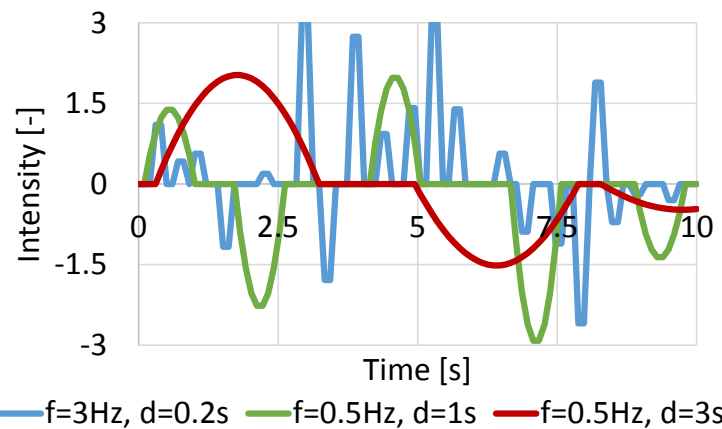


**Figure 6.17: Three example synthetic signals with  $\mu = 0$ ,  $\sigma = 1$**

Every signal was integrated (i.e. captured) at different exposure times. The standard deviation of multiple integrations (in this case 300) was then calculated. The result becomes dependent only on exposure time and event frequency. Event duration does not influence the result, since it determines the signal standard deviation, which cancels out due to the normalisation. The results are made dimensionless by substituting exposure time ( $t[s]$ ) with an exposure time ratio ( $\frac{t}{t_0}$ ) and event duration ( $d[s]$ ) with a duration ratio ( $\frac{d}{t_0}$ ). The resulting standard deviation scaling factor ( $f_\sigma$ ) can be seen in Figure 6.18. Therein, multiple duration ratios (coloured lines) are plotted for exposure time ratios from 1/16 to 16. Additionally the signal uncertainty (Equation 6.11) was added to both Subfigures (black line). In delimitation, this plot is named ‘var’, since its standard deviation is made up of random oscillations.

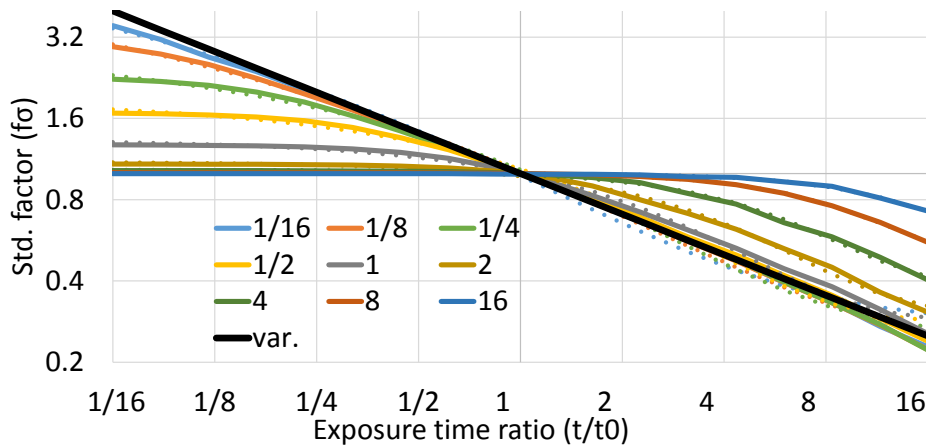


**Figure 6.18: Standard deviation scaling factor ( $f_\sigma$ ) where the series represent different event durations ( $\frac{d}{t_0}$ )**

The black plot ‘var’ increases earlier for  $\frac{t}{t_0} < 1$  and decreases earlier for  $\frac{t}{t_0} > 1$  than the coloured plots. Whilst plots with duration ratios  $\frac{d}{t_0} < 1$  spread towards  $\frac{t}{t_0} < 1$ , plots with an event duration longer than exposure time ( $\frac{d}{t_0} > 1$ ) spread towards  $\frac{t}{t_0} > 1$ . These trends can be explained as follows:

The effective standard deviation of a signal which changes slowly over multiple EL images ( $\frac{d}{t_0} > 1$ ) decreases with decreasing exposure time since the events responsible for that standard deviation will vary less. High frequent events (such as light blue in Figure 6.18) however, will still vary enough at shorter exposure times. In contrast, low frequent events become higher frequent for increasing exposure times, weakening the standard deviation decrease.

The dotted plots adjacent every line in Figure 6.18 show a fit using an extended decay function, similar to Equation 6.5:

$$f_t\left(\frac{t}{t_0}\right) = (f_0 - f_\infty) \cdot e^{-a \cdot (t/t_0)^b} + f_\infty \quad (6.13)$$

The four parameters ( $a, f_0, b, f_\infty$ ), required to build this equation are plotted for different relative event durations ( $\frac{d}{t_0}$ ) in Figure 6.19.

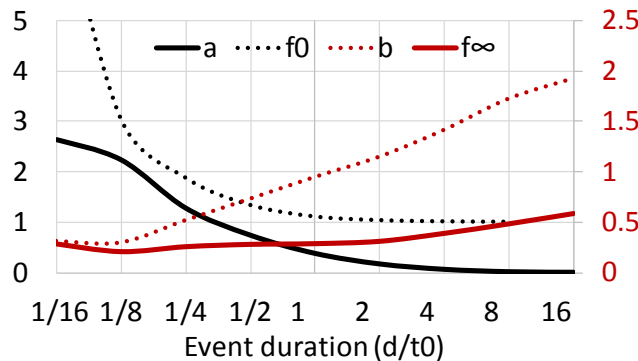
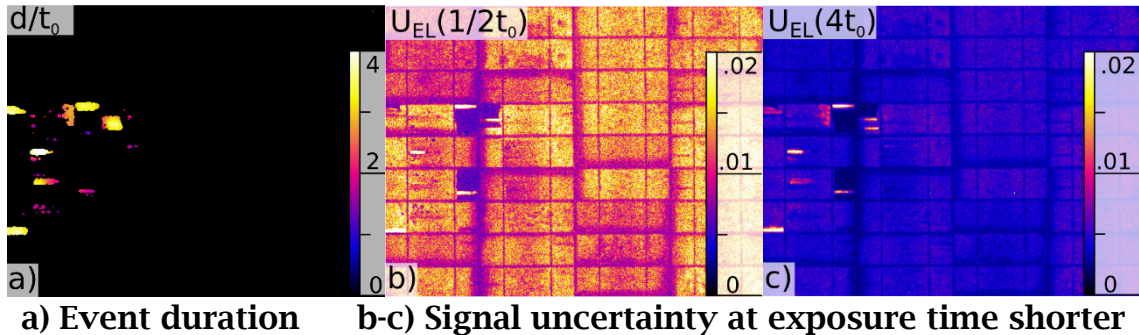


**Figure 6.19: Fit parameter for Equation 6.13**

The relative event duration ( $\frac{d}{t_0}$ ) for the c-Si module (Figure 6.16a) is shown in Figure 6.20a.



a) Event duration for EL images (Figure 6.16a)  
 b-c) Signal uncertainty at exposure time shorter (b) and longer (c) than reference time ( $t_0$ )  
**Figure 6.20: Example result of exposure time dependent uncertainty**

$\frac{d}{t_0}$  is calculated as follows for every EL image:

1. Calculate the difference between all images and image fit ( $dEL$ ) from linear regression and the standard error of the fit ( $U_0$ ).
2. Select events ( $E$ ) using:

$$E = dEL > \frac{U_0}{2} \quad (6.14)$$

3. Calculate  $\frac{d}{t_0}$  as the average length of positive elements along the time dimension in  $E$ .

For all positive elements in Figure 6.20a, the exposure-time-dependent uncertainty was calculated using:

$$U_{EL}\left(\frac{t}{t_0}\right) = f_t\left(\frac{t}{t_0}\right) \cdot U_{EL} \quad (6.15)$$

For all remaining elements  $U_{EL}\left(\frac{t}{t_0}\right)$  was calculated using Equation 6.11.

Figure 6.20b-c show the resulting signal uncertainty for two example exposure times  $\frac{1}{2}t_0$  and  $4t_0$ .

In comparison with Figure 6.20a it is shown that the uncertainty of areas with fluctuating events (middle left) does not increase as much for shorter exposure times but also does not decrease as clearly for increasing exposure times. Event durations shorter than exposure time ( $t_0$ ) cannot

be measured with the above-described method. Therefore event durations shorter or close to  $t_0$  should be calculated using Equation 6.11.

### 6.1.5 INTENSITY UNCERTAINTY AVERAGING

If a pixel area ( $|x_w, y_h|$ ) with width ( $w$ ) and height ( $h$ ) rather than a single pixel is evaluated, different averaging methods are suitable depending on the uncertainty type:

Noise based uncertainty ( $U_{Noise}$ ): Gaussian distributed image noise decreases when averaged. In the same way  $U_{Noise}$  decreases with the square root of the number of values:

$$U_{Noise} = \frac{\text{mean}(U_{Noise}|x_w, y_h|)}{\sqrt{w \cdot h}} \quad (6.16)$$

EL signal and image correction uncertainty ( $U_{EL,corr}$ ): The uncertainty associated with EL signal variations of image correction is not affected by averaging, therefore:

$$U_{EL,corr} = \text{mean}(U_{EL,corr}|x_w, y_h|) \quad (6.17)$$

### 6.1.6 SECTION SUMMARY

EL emission of a DUT decreases exponentially with increasing time under forward bias. This warm-up behaviour ( $U_{EL-w}$ ) can be in part corrected for if the DUT diffusivity can be estimated and measurement conditions are controlled. Additional EL signal variations have many reasons. Amongst others are device handling, changed contact resistances to the connectors, electrical disturbances and temperature variations.

In this section, warm-up behaviour was measured on one crystalline and one thin-film device in one measurement set. Exposure time dependency was measured on two similar devices with multiple individual

measurements. Deriving a general signal uncertainty from these few measurements would not be reliable. However, acknowledging the need for comprehensive values and recognizing that an uncertainty analysis of this extent would not be feasible for non-academic applications, signal uncertainty ( $U_{EL}$ ) can be set to  $\sqrt{(U_{EL})2.8\%^2 + (U_{corr})2\%^2} \approx 3.4\%$  if the following conditions are fulfilled:

- Exposure times are similar to exposure time ( $t_0$ ) used to measure  $U_{EL-w}$  and  $U_{EL-r}$ . In this case, no exposure time correction is needed.
- No information about DUT warm-up is given (Table 6.2, model B)
- DUT type differences are not considered. Uncertainty values are taken from the measured thin-film device.
- Only cell averages of measured random signal variations are evaluated.

## 6.2 Position Uncertainty

This section focuses on position uncertainty due to perspective and lens distortion (Figure 6.21). Firstly, position uncertainty will be defined as 2D vector array ( $\overrightarrow{\sigma_{pos}} = \begin{pmatrix} \sigma_x \\ \sigma_y \end{pmatrix}$ ) mapping the spatial standard deviation of every pixel in an image. This array will then be transformed onto the actual pixel-intensity dependent scalar uncertainty map ( $U_{pos}$ ).

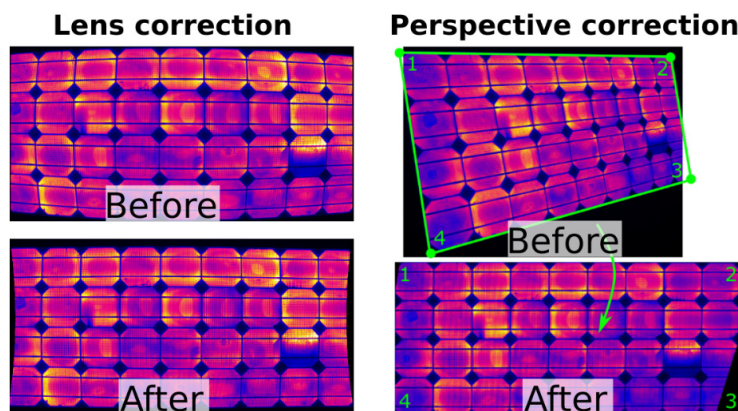


**Figure 6.21: Example for lens and perspective correction; distortion exaggerated for clarity**

### 6.2.1 IMAGE SHARPNESS

This parameter ( $\sigma_G$ ) equals the standard deviation of a point-spread-function (blur) which is assumed to be Gaussian distributed (Subsection 3.4.3.1).

### 6.2.2 RE-PROJECTION ERROR

The re-projection error ( $\sigma_{rep}$ ) estimates the uncertainty of a pixel position after correction of lens distortion. It originates from the RMSE of the difference between detected features within the camera calibration pattern and re-projected points [64]. In this work, it is assumed that the individual RMSE at each feature point does not follow a functional relationship and therefore the re-projection error is assumed spatially uniform. In contrast to other contributors to position uncertainty,  $\sigma_{rep}$  only measures the uncertainty of alignment. Misalignments caused by the re-projection error can be partly corrected with and without reference image (Section 4.7).

### 6.2.3 DEPTH-OF-FIELD BLUR

If the angle between optical axis and image plane is not perpendicular, certain areas of the PV device will be out of focus.

The depth-of-field (DOF) sensitivity is mostly dependent on the camera lens' f-number ( $A$ ) and focal length ( $f$ ). Pertuz et al. [63] describes the derived defocus ( $\sigma_{DOF}$ ) as a function of the distance ( $d$ ) between lens and image plane as:

$$\sigma_{DOF}(d) = \frac{k}{A} \cdot \frac{f^2 \cdot |d - d_f|}{d \cdot (d_f - f)} \quad (6.18)$$

Where  $d_f$  is the in-focus distance.  $k$  is a camera dependent parameter relating the blur circle to an actual point spread function (PSF). In this

work, the PSF is assumed to be Gaussian distributed and therefore  $k$  is set to 2.335. This number describes the ratio of the full width at half maximum (FWHM) over standard distribution.

A depth map of the image plane ( $d(x, y)$ ) could be measured with a depth sensitive camera but can also be estimated from the four corner points of the PV device. The Python interface of the C++ library OpenCV provides the function `cv2.solvePnP` which returns a translation vector ( $t$ ) and rotation vector ( $r$ ). Together with `cv2.Rodrigues` (which transforms  $r$  to a rotation matrix ( $R$ )) and the camera matrix ( $C$ ),  $d(x, y)$  can be calculated as follows [64]:

$$d(x, y) = R^{-1} \cdot \left( s \cdot (C^{-1} \cdot \begin{bmatrix} x \\ y \\ 1 \end{bmatrix}) - t \right); \quad s = \frac{(R^{-1} \cdot t)[2]}{(R^{-1} \cdot C^{-1} \cdot \begin{bmatrix} x \\ y \\ 1 \end{bmatrix})[2]} \quad (6.19)$$

In order to evaluate the influence of DOF, the following test case (Figure 6.22) is simulated: A 1.2 m PV module is imaged at different distances (0.6-1.5 m) and different angles ( $0^\circ$ - $90^\circ$ , respective orthogonal to parallel to camera axis). The DUT centre is focussed.

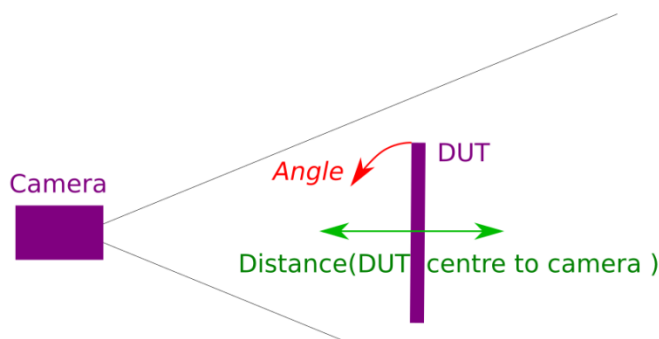


**Figure 6.22: Schematic of simulated test case**

Two different camera lenses with two common focal lengths of 25(50) mm at three different apertures (defined by f-number) are used for imaging.  $\sigma_{DOF}$  is then calculated using Equation 6.18. The results are shown in Figure 6.23.

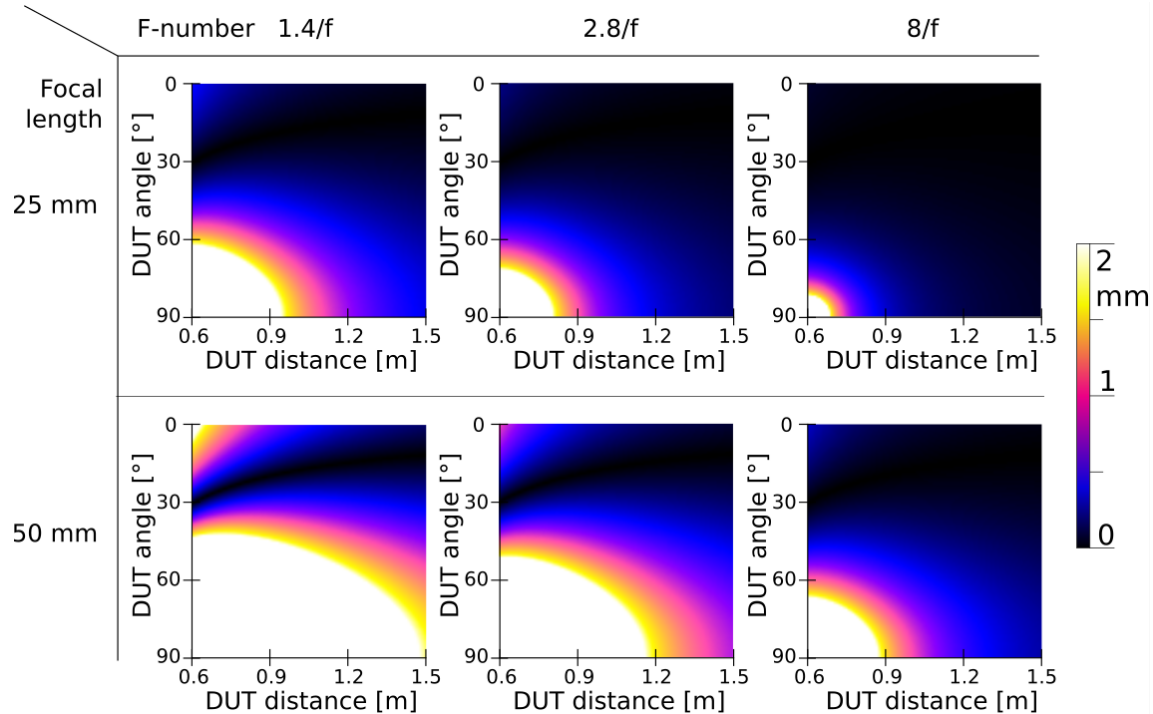


**Figure 6.23: Resulting  $\sigma_{DOF}$  for different f-numbers (columns) and focal lengths (rows)**

$\sigma_{DOF}$  is highest at high DUT angles and small distances. If it can be assumed that angles in outdoor measurements are below  $60^\circ$ , a minimum distance of 1 m is already sufficient for a focal length of 25 mm to obtain  $\sigma_{DOF}$  below one mm. To fit the entire DUT into the image plane at such a small distance a wide-angle camera lens with a field-of-view of  $60^\circ$  or higher would be necessary ( $\frac{0.5 \cdot 1.2 \text{ m}}{\tan(0.5 \cdot 60^\circ)} = 1.04 \text{ m}$ ). Therefore, DOF can be neglected for comparably short focal lengths around 24 mm. If however a longer focal length (50 mm) and a wide aperture (f/1.4) is chosen, this minimum distance increases to over 2 m. Additionally, if the distance between camera and DUT is below 1 m, DOF blur can become visible, even if the DUT is not tilted (Figure 6.23, 2<sup>nd</sup> column top-left). Therefore, when measuring image sharpness, point spread functions of variable sizes need to be taken into account.

#### 6.2.4 PIXEL DEFLECTION

The correction of both lens and perspective distortion can cause image areas to shrink and expand. Intermediate pixels interpolate between relocated pixels and increase the deflection uncertainty. Figure 6.24 gives a simplified example for the x-axis. Therein, the green area indicates an area to be expanded due to deflection. Its size doubles during the remap (a-b). Likewise, the pixel indices map ( $m_{x,y}$ ) changes.

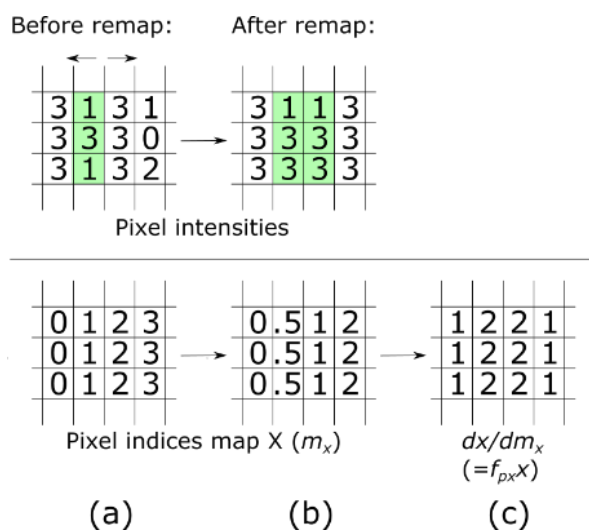


**Figure 6.24: Schematic of deflection uncertainty of the x-axis due to image remapping**

The increase in pixel size ( $\overrightarrow{f_{px,\#}}$ ) can be obtained from the magnitude map-index gradient ( $d\#/dm_\#$ ) using:

$$\overrightarrow{f_{px,\#}} = \begin{pmatrix} \left| \frac{dx}{dm_x} \right| \\ \left| \frac{dy}{dm_y} \right| \end{pmatrix} \quad (6.20)$$

$\overrightarrow{f_{px,\#}}$  measures the expansion of the original pixel size. Its average is equal to the area ratio of a DUT after vs before remapping. # acts as placeholder for pixel deflection caused by lens distortion ( $\overrightarrow{f_{px,l}}$ ) and perspective correction ( $\overrightarrow{f_{px,p}}$ ). For calculating  $\overrightarrow{\sigma_{pos}}$  both factors need to be applied

individually, since lens based uncertainties are based on the raw EL image but  $\overrightarrow{\sigma_{pos}}$  is based on the corrected image:

$$\overrightarrow{\sigma_{lens}} = \overrightarrow{f_{px,l}} \sqrt{{\sigma_G}^2 + {\sigma_{rep}}^2} \quad (6.21)$$

To be based on the corrected EL image, both lens and DOF based uncertainty arrays ( $\sigma_{lens}$ ,  $\sigma_{DOF}$ ) need to be perspective transformed ( $T$ , Section 4.7) before they can be scaled with  $\overrightarrow{f_{px,p}}$ :

$$\overrightarrow{\sigma_{pos}} = \overrightarrow{f_{px,p}} \sqrt{T({\overrightarrow{\sigma_{lens}}}^2) + T({\overrightarrow{\sigma_{DOF}}}^2)} \quad (6.22)$$

## 6.2.5 NEGLECTED POSITION UNCERTAINTY FACTORS

### Positional error from object corner detection

The position uncertainty of corrected EL images depends on the method used to detect the DUT corners (Subsection 4.7.1.1). In the following comparison, it is assumed that device corners were detected precisely.

### Interpolation error

Non-integer values within the pixel index map ( $m_{x,y}$ ) result in interpolated pixel intensities using the neighbouring pixels. Interpolation methods can be distinguished by the number and weights of included neighbours. Every method (nearest neighbour, bi-linear, cubic et cetera) is a trade-off between introduced blur and precision. In this thesis, it is assumed that uncertainty due to interpolation is fully covered by pixel deflection  $\overrightarrow{f_{px}}$  and is independent from the interpolation method used.

## 6.2.6 CALCULATING UNCERTAINTY $U_{pos}$ FROM $\overrightarrow{\sigma_{pos}}$

So far the uncertainty is given as the standard deviation ( $\overrightarrow{\sigma_{pos}} = (\frac{\sigma_x}{\sigma_y})$ ) of all the pixels in x and y-axis. To transform these values into the pixel

intensity uncertainty, the following steps are conducted on every image pixel ( $I[x, y]$ ):

1. Calculate a local point spread function (PSF) as a Gaussian distribution with standard deviation ( $\sigma_x, \sigma_y$ ).
2. Calculate the local PSF-weighted standard deviation (indices  $i, j$ ) by multiplying the difference to all neighbouring pixels within the PSF (size=2s+1) with the respective PSF value.
3. The sum of all the differences gives the local intensity uncertainty:

$$U_{pos}[x, y] = \sqrt{\sum_{i=-s}^{s+1} \sum_{j=-s}^{s+1} (I[x, y] - I[x + i, y + j])^2 \cdot \text{PSF}(\sigma_x, \sigma_y)[i, j]} \quad (6.23)$$

The resulting map ( $U_{pos}$ ) is sensitive to high gradient variations of pixel intensity. This is obvious, because blur affects high gradient changes like at cell borders or busbars more than low gradient changes, like at the image background.

### 6.2.7 EXAMPLE POSITION UNCERTAINTY OF A PERSPECTIVE AND LENS-CORRECTED EL IMAGE

Several contributors and the resulting position uncertainty map of a perspective and lens corrected PV module are shown in Figure 6.25. In this example, an image sharpness ( $\sigma_G$ ) of 0.5 px was assumed. As results from re-projection error and pixel deflection from lens distortion removal, a rather homogenous  $\sigma_{Lens}$  ranging between 0.77 – 0.79 px can be seen (Subfigure b). The corrected EL image and its position uncertainty ( $U_{pos}$ ) is shown in (c,e). In this example,  $U_{pos}$  varies up to 15% at cell borders and busbars.  $U_{pos}$  also increases slightly from left to right. This is due to image pixels doubling their size due to deflection ( $f_{px,p} = 2$ , Subfigure f). Due to its small values, the influence of depth-of-field blur ( $\sigma_{DOF}$ , Subfigure d) can be neglected.

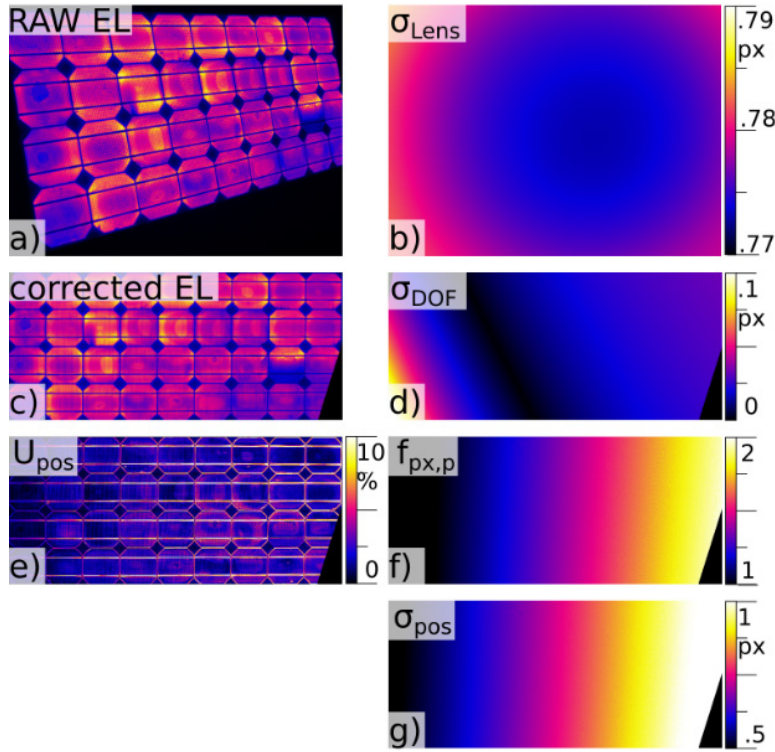


**Figure 6.25: RAW EL, corrected EL and related position uncertainty  $U_{pos}$  (left); contributors to  $U_{pos}$  (right);  $\overrightarrow{\sigma_{Lens}}$ ,  $\overrightarrow{\sigma_{pos}}$ ,  $\overrightarrow{f_{px,p}}$  shown as magnitude**

The influence of perspective distortion is shown in Figure 6.26. Therein the top-right cell is shown after image correction. It can be seen that image sharpness decreases (Subfigure b) and equally position uncertainty (Subfigure c) increases.

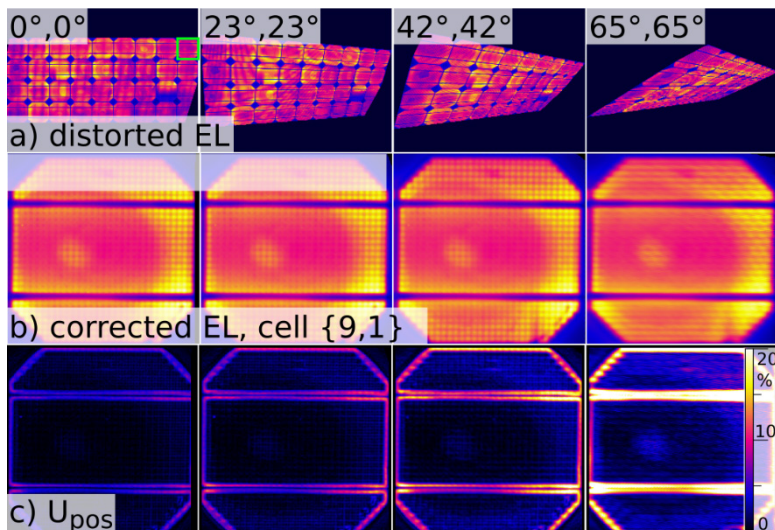


**Figure 6.26: a) Artificially distorted EL image of a c-Si module, rotated in x and y-axis respectively 0 to 65°; b) subsection of one cell (green box in (a)); c) position uncertainty of same area**

### 6.2.8 POSITION UNCERTAINTY AVERAGING AND VALIDATION

The quantification of uncertainty due to the imaging system blur or perspective distortion is part of the dilemma of estimating a signal error without knowing the actual signal. To validate Equation 6.23, three synthetic patterns ( $P_0$ ) were generated (Figure 6.27-6.29, first column). Every pattern was Gaussian blurred ( $P_{blurred}$ ) with a known standard deviation. In this case, the actual intensity deviation due to blur is known (Subfigures a, last column). This can be used to evaluate the quality to calculated uncertainty maps (Subfigures a, 3<sup>rd</sup> column). Comparing both error and uncertainty maps it is clear that all uncertainty maps extend above the actual error and in general give lower values. This is as expected. Following the theory of normal distributions, roughly 68%, 95%, 99.7% of values are within the boundaries of  $\pm 1, \pm 2, \pm 3$  standard deviations. Therefore to evaluate the quality of uncertainty, the distribution of pixels must be analysed and not just single pixels. Subfigures (b) show a comparison of a cumulative distribution function (CDF) of the used Gaussian distribution (red) in comparison to a CDF of the following ratio between error and uncertainty, called quality of prediction ( $Q$ ):

$$Q = \frac{|P_0 - P_{blurred}|}{U_{pos}} \quad (6.24)$$

Evaluating these two plots (green and blue, last column) it is evident that the quality of prediction can be slightly higher or lower in comparison to the Gaussian CDF (red), depending on the used pattern.

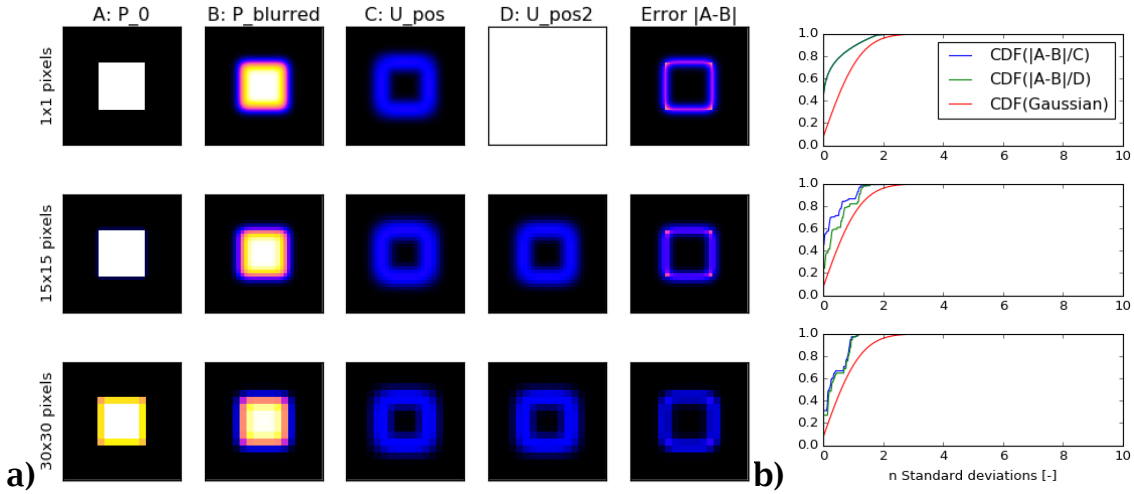


**Figure 6.27:** a) A: 500x500 px square pattern; B: (A) blurred with  $\sigma_{pos}=20$  px; C: Estimated position uncertainty; D: rescaled position uncertainty; E: magnitude difference (A-B); b) Comparison quality of prediction to Gaussian CDF (red); rows: different spatial averages

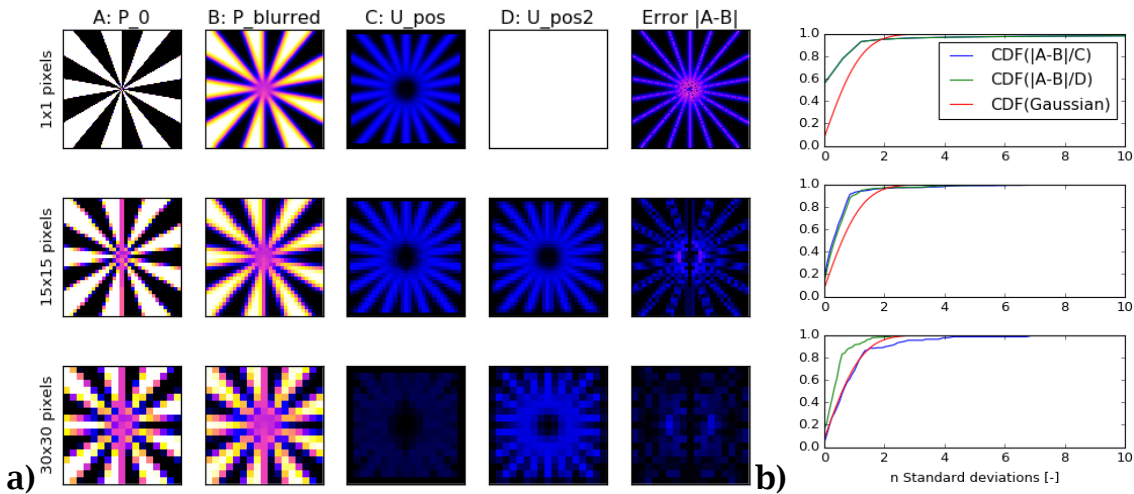


**Figure 6.28:** Same as Figure 6.27 for spoke pattern ( $\sigma_{pos}=10$  px, number of spokes=9)

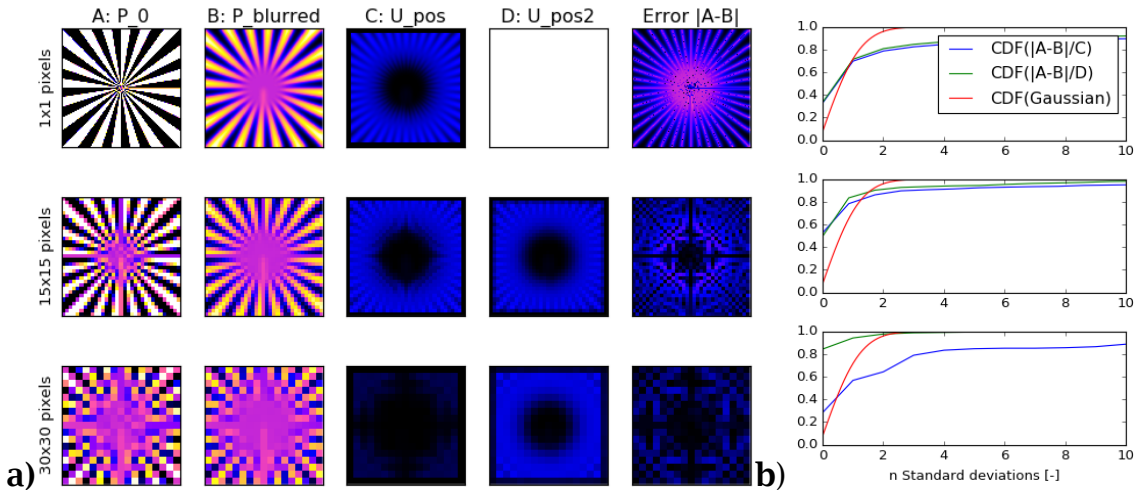


**Figure 6.29: Same as Figure 6.28 (number of spokes=20)**

When the pixel group average such as one cell in a PV module is evaluated, the uncertainty also has to be averaged as well. If a noisy signal is averaged, its intensity uncertainty decreases with the square root of the number of averaged values (Equation 6.16). To evaluate the position uncertainty behaviour when averaged, the three patterns in Figure 6.27-6.29 ( $P_0$ , first column) were additionally averaged with pixel groups of 15x15 and 30x30 pixels. The individual pixels size scales relative to the standard deviation of the PSF. Therefore, to calculate  $U_{pos}$ , ( $\sigma_x, \sigma_y$ ) must be divided by this resolution factor ( $f_{res}$ ). The result of a 1x1, 15x15 and 30x30 px average is shown in the three rows of the following figures.

Remarkably,  $U_{pos}$  only shows a small decrease within the two averaging steps. Column D displays  $U_{pos2}$ . This uncertainty was obtained from a 15x15, respective 30x30 px average of  $U_{pos}$  (1<sup>st</sup> row). In general for each resolution, the generated  $U_{pos}$  and the averaged  $U_{pos2}$  are in good agreement. Only for larger averages (last row),  $U_{pos2}$  overestimates the actual uncertainty.

The three chosen patterns vary in their complexity. Whilst the relatively simple square pattern causes an overestimation of uncertainty (the red plots below other plots in Subfigures (b)), uncertainty can also be underestimated, as shown for the centre of both spoke patterns (Figure

6.28,6.29, first row). Therein, features within  $P_{blurred}$  were smoothed out to such an extent that no uncertainty could be derived.

It can be concluded that (outgoing from  $\overrightarrow{\sigma_{pos}}$ ) a pixel intensity based position uncertainty ( $U_{pos}$ ) can be calculated. For the evaluated cases, the deviations between error and uncertainty were within the expected range of a normal distribution.

When image intensities are averaged, the position uncertainty also averages. If features smooth out due to blur, the position uncertainty will underestimate the actual deviation.

### 6.2.9 SATISFYING OBJECT RESOLUTION REQUIREMENTS

Subsection 3.4.3.3 introduced the smallest resolvable object size ( $s_{obj}$ ) as an image quality parameter and Table 7.17 proposes a minimum  $s_{obj}$  of 1.5 mm to resolve non-disconnecting cracks on PV modules. To ensure this size rule is fulfilled (especially for outdoor imaging), the position uncertainty algorithm (Section 6.2) appears impracticable. Therefore, the following equation can be used as a rule of thumb to ensure minimum object resolution requirements are fulfilled. Equation 3.43 defines the resolution factor ( $f_{res}$ ) approximately as twice the image sharpness ( $\sigma_G$ ). If  $\sigma_G$  is not known, following the comparison of different camera systems in Figure 7.43, a value of 1.5 px can be assumed. Within an image the distance of the smallest DUT edge [px] can be obtained from the magnitude of both DUT corner points ( $\overline{P_1P_2}$ ). Together with the physical module width ( $w$ ) this minimum distance can be obtained using:

$$\overline{P_1P_2} \geq \frac{2 \cdot w \cdot \sigma_G}{s_{obj}} \quad (6.25)$$

For example with a module height of 1000 mm, a given minimum resolvable object size of 1.5 mm and an assumed sharpness of 1.5 px the minimum distance ( $\overline{P_1P_2}$ ) should be larger than  $\frac{1000 \text{ mm} \cdot 2 \cdot 1.5 \text{ px}}{1.5 \text{ mm}}$  or 2000 px.

### 6.2.10 SECTION SUMMARY

Perspective and lens distortion in an EL image can be largely corrected. The resulting corrected image will not have the same quality as a similar EL image without these distortions however. Areas that were expanded during rectification also have a higher position uncertainty because more pixels are used to display the same information. A PV device, imaged with perspective distortion, will have areas closer or farther from the focal range. Depending on the optics used, depth-of-field blur can occur. Every camera lens has a certain camera lens distortion, which can be calibrated and corrected. The quality of correction is described with the re-projection error.

A method to calculate pixel intensity based uncertainty from the uncertainty of position is presented and validated. It was shown that position uncertainty is sensible to high gradient variations. Therefore, the position uncertainty of EL images will be particularly highest along busbars and cell edges.

## 6.3 Uncertainty Estimation

Based on the findings in this chapter, the following procedure gives practical instructions on how to measure the uncertainty of a corrected EL image. It is proposed to store the EL image uncertainty ( $U_I$ ) in three separated two dimensional vector arrays:

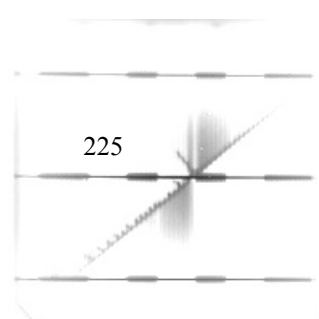
$$\overrightarrow{U_I} = \begin{pmatrix} U_{Noise} \\ U_{EL,corr} \\ \overrightarrow{\sigma_{pos}} \end{pmatrix}; U_{Noise} = \frac{1}{SNR}; U_{EL,corr} = \sqrt{U_{EL-w}^2 + U_{EL-r}^2 + U_{corr}^2} \quad (6.26)$$

The following algorithm can be used to calculate EL image uncertainty:

1. Calculate the signal-to-noise ratio (SNR) map from raw EL image(s) (Subsection 3.2.6).

2. Estimate the EL signal uncertainty from DUT warm-up ( $U_{EL-w}$ ) depending on DUT type and warm-up time between 0.8 - 2.8% (Subsection 6.1.4.1.1).
3. If an uncertainty map of random signal variations ( $U_{EL-r}$ ) exists, scale  $U_{EL-r}$  depending on exposure time of current EL image. Otherwise, assume a homogenous distribution of 1.5% for silicon or 3.5% for a thin-film DUT (Table 6.5).
4. Depending on the quality of the flat field calibration, assume an image correction uncertainty ( $U_{corr}$ ) of approximately 2% (Subsection 6.1.3.3).
5. Measure or estimate the image sharpness as the standard deviation of a Gaussian blur kernel ( $\sigma_G$ , Subsection 3.4.4). Calculate  $\sigma_{lens}$  using Equation 6.21.
6. Depending on the aperture, focal length and DUT distance, neglect or calculate  $\sigma_{DOF}$  (Figure 6.23).
7. Perspective transform the EL image, SNR,  $\sigma_{lens}$  and  $\sigma_{DOF}$  and calculate  $\overrightarrow{\sigma_{pos}}$  using Equation 6.22.
8. Create an uncertainty vector array ( $\vec{U}_I$ ) using Equation 6.26.
9. If a pixel group average is evaluated, average  $U_{Noise}$ ,  $U_{EL,corr}$  and  $\overrightarrow{\sigma_{pos}}$  according to Equation 6.16 and 6.17.
10. Calculate the position uncertainty  $U_{pos}$  from  $\overrightarrow{\sigma_{pos}}$  and the corrected EL image using Equation 6.19.
11. Calculate EL image uncertainty as:

$$|\vec{U}_I| = \sqrt{{U_{Noise}}^2 + {U_{EL,corr}}^2 + {U_{pos}}^2} \quad (6.27)$$



# 7 CASE STUDIES

The following two sections are based on results of studies conducted during this doctoral studentship. In Section 7.1, eight PV modules were imaged with the same camera system at different treatment steps. The analysis focussed on correlating EL images taken to measured performance parameters. To extract the impact of treatment steps, all EL images were corrected, statistically analysed and their features were extracted.

The second case study in Section 7.2 gives a preview on the evaluation of the first international Round Robin based of the EL measurement method. Images submitted from 14 different camera systems are analysed. The result demonstrates a proof of concept of quantitative inter-comparison. The quality of the different camera systems (noise, sharpness, flat field correction) was compared and camera type dependent differences were extracted.

## 7.1 Thermo-Mechanical Load Experiment at NREL

### 7.1.1 MEASUREMENT SETUP

In a combined thermo-mechanical load experiment, eight modules (Table 7.1) were tested. The measurements took place in July 2016 under the guidance of Peter Hacke at the National Renewable Energy Laboratory (NREL) in Golden, Colorado. The aim of that study was as follows:

- Take EL images of those modules after different treatment steps.
  - Correct images and extract features, such as cracks and inactive areas.
- The abilities of the presented image correction and feature extraction

routines were tested and statistical information connecting the applied stress to module performance were obtained.

**Table 7.1: PV modules used in the NREL study**

ID	Type	Manufacturer	Name	Nominal Power	Price per module
M1...M4	Mono	SolarWorld	SW235	235 W	160\$
P1...P4	Poly	Astroenergy	CHSM 6610P	230 W	115\$

Within a 16 day period, the modules were either mechanically stressed or aged in a climate chamber with a humidity-freeze (HF) routine. In the HF routine the modules were cycled 10 times between -40° and +85°C at a relative humidity of 85% according to the procedure described in IEC 61215 [117]. HF was chosen to age the module since it is suitable to develop cracks [118, 119]. In the treatment sequence (Table 7.2), the modules were first stressed and subsequently measured. Measurement methods included EL imaging, as well as dark and light I-V curve measurement (DIV, LIV).

**Table 7.2: Treatment steps executed on modules, listed in Table 7.1**

Date	Treatment step	Test	Measurement
06/07/2016	0	-	EL, DIV
06/07/2016	1	Mech. Stress 1	EL, DIV
8/07/2016	2	HF	EL, DIV, LIV
11/07/2016	3	HF	EL, DIV
12/7/2016	4	Mech. Stress 2	EL, DIV
13/7/2016	5	HF	EL, DIV
15/7/2016	6	HF	EL, DIV, LIV
15/7/2016	7	Rough hand. 1	EL, DIV
18/7/2016	8	2xHF	EL, DIV
20/7/2016	9	Rough hand. 2	EL, DIV
20-22/7/2016	10	HF	EL, DIV, LIV

The aim of the mechanical stress experiments (Table 7.3, 7.4) was to introduce cracks at different positions (module centre, long edge).

**Table 7.3: Setup ‘Mech. stress 1’**

Modules	No. Bags	Final load	Description
M1,P1	6x4	217 kg	Bags dropped on module centre (fall height 23 cm)
M2,P2	6x4	217 kg	Successively stacked bags on module centre (Figure 7.1a,b)
M3,P3	4x4	145 kg	Successively stacked bags on long edge (Figure 7.1c,d)
M4,P4	-	-	-

**Table 7.4: Setup ‘Mech. stress 2’**

Modules	No. Bags	Final load	Description
M1,P1	-	-	-
M2	6x4	217 kg	Same as ‘Mech. Stress 1’
P2	7x4	254 kg	Same as ‘Mech. Stress 1’
M3,P3	4x4	145 kg	Bags successively stacked on opposite long edge
M4	5x4	181 kg	Bags dropped on module centre (fall height 23 cm)
P4	7x4	254 kg	Same as M4

Sand bags were placed successively on the modules. The maximum weight was achieved either when the module frame almost touched the floor or when more than five distinctive cracking sounds were heard. With a weight over 200 kg, the requirements of the mechanical load test (2400 Pa → 411 kg) IEC 61215 [117] were not matched. In contrast to this test, weights were not applied uniformly, but rather localised. Figure 7.1 shows the two different weight positions (centre, long edge).

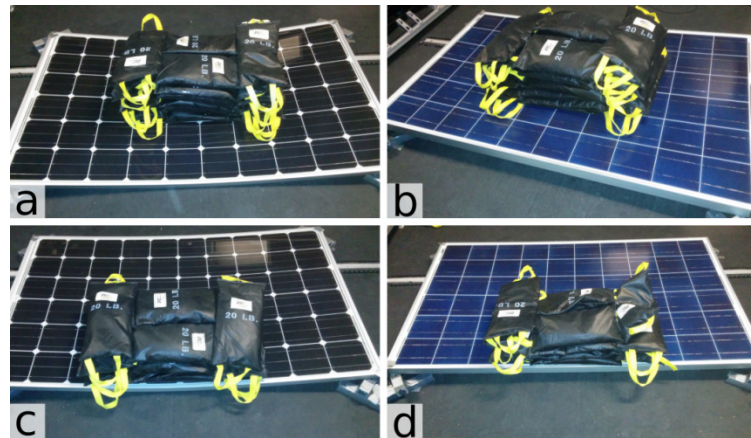


**Figure 7.1: Example weight positions (centre: (a,b), long edge: (c,d)) for 'Mono' (a,c) and 'Poly' (b,d) modules**

'Poly' modules (b, d) bent less due to a more rigid frame. Therefore, the individual load required for these modules was generally higher. A dynamic load was applied to modules M1, P1 and M4, P4 in the first, respective second mechanical load experiment. Each individual bag was dropped from a height of 23 cm above the module surface.

Whilst the mechanical load experiments attempt to emulate wind or snow loads, rough handling tries to imitate stress during module transport and installation [120]. Within 'Rough handling 1,2' the modules were once lifted and released, causing them to fall on a concrete floor (Table 7.5) or on two metal bars (Table 7.6).

**Table 7.5: Setup 'Rough handling 1'**

Modules	Description	Diagram
M1, P1	Short side lifted 114 cm, falling on short side	
M2, P2	Upright on short side, falling on long side	
M3, P3	Upright on long side, falling on opposite long side	
M4, P4	Upright on short side, falling on opposite short side	

**Table 7.6: Setup ‘Rough handling 2’**

Modules	Description	Diagram
M1-4, P1-4	Upright on short side, falling on opposite short side. Two metal bars (4 cm) placed where module corners would hit floor	

## 7.1.2 MEASUREMENT RESULTS

This subsection presents and discusses the results obtained from dark/light I-V curve measurements and EL imaging. During the study, the modules were successively damaged and degraded (Figure 7.2).

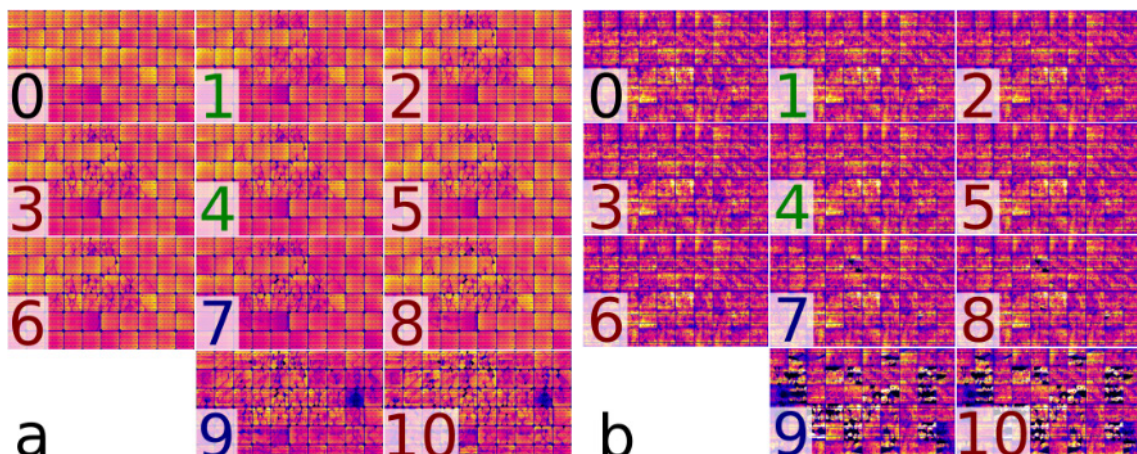


**Figure 7.2: Example corrected EL images of modules ‘M1’ (a) and ‘P2’ (b); numbers correspond to treatment step in Table 7.2; black: initial EL image; green: EL after mechanical load; red: EL after humidity-freeze treatment; blue: EL after rough handling**

### 7.1.2.1 DARK/LIGHT I-V CURVE

After every treatment step, a dark I-V (DIV) measurement was conducted using the same power supply as used for current control during EL imaging. At three treatment steps (2, 6, 10) the illuminated/light IV (LIV) curve was measured by flash test using the NREL ‘Spire 5600SLP IV’ System. Figure 7.4 and 7.4 show the measured DIV and LIV curves for all the modules. For better comparability, the current measured in DIV

conditions ( $I_{Dk}$ ) was referenced relative to the short-circuit current ( $I_{Sc}$ ) obtained from the LIV measurement:

$$I_{Dk*} = I_{Sc} - I_{Dk} \quad (7.1)$$

The only remarkable change occurred in the last LIV measurement (light green). Both remaining LIV and all DIV curves have a similar slope. Due to the inverted view of the DIV curve it is apparent that an open-circuit voltage derived from DIV would be higher than the one obtained with LIV. The offset between both curves is similar amongst all ‘Mono’ and ‘Poly’ modules. In the aim of substituting LIV, this relationship will be later used to generate a pseudo LIV from DIV and EL measurement (Subsection 7.1.2.3).

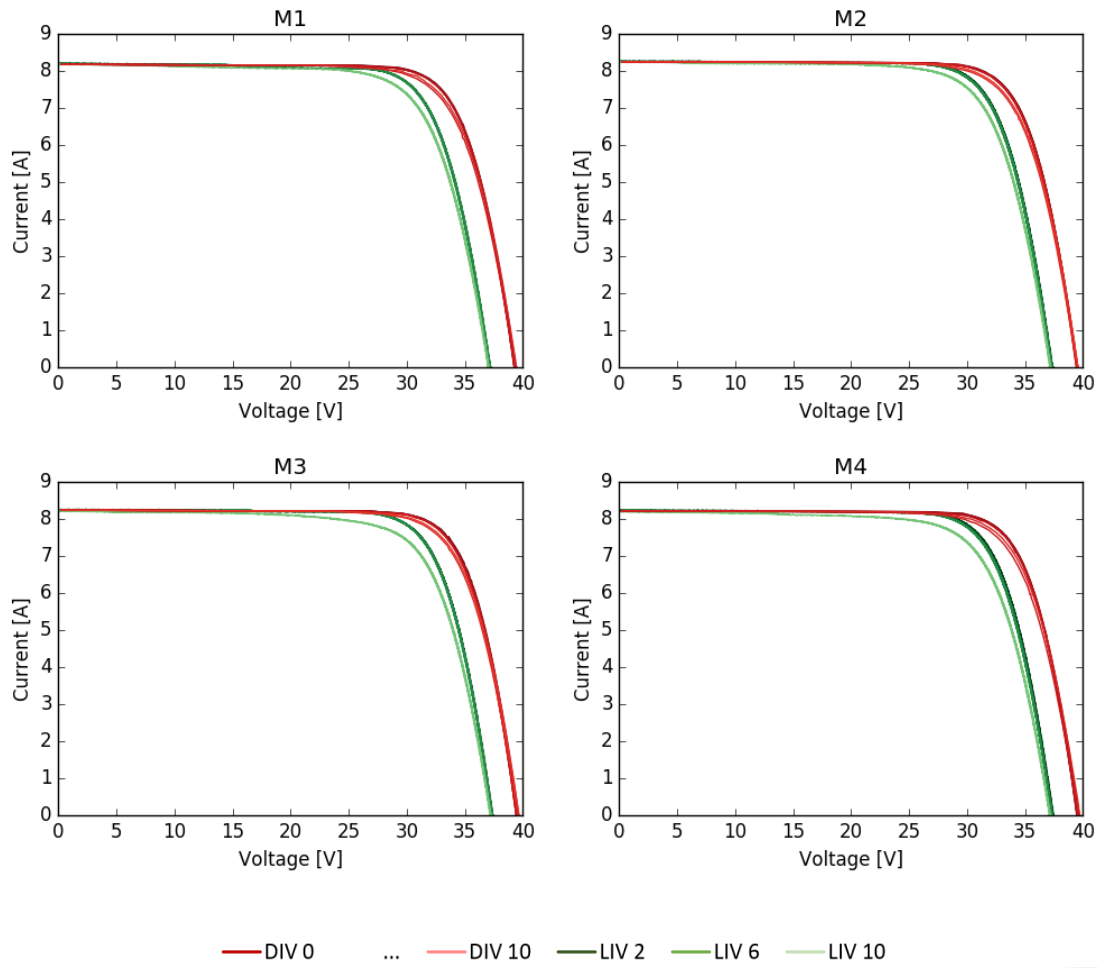


**Figure 7.3: All measured light-IV (green) and dark-IV (red) curves of ‘Mono’ modules**

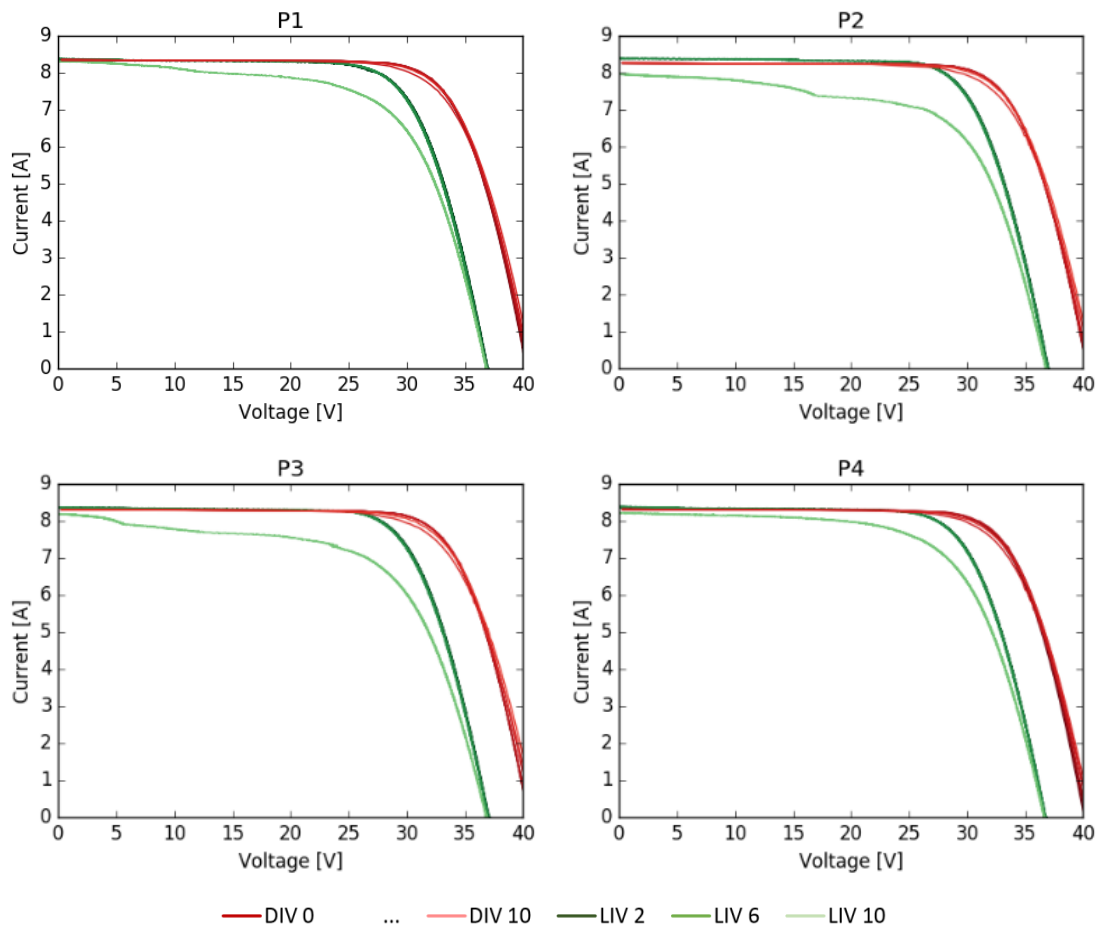


**Figure 7.4: All measured light-IV (green) and dark-IV (red) curves of 'Poly' modules**

#### 7.1.2.1.1 EXTRACTED PERFORMANCE PARAMETERS

The measured LIV curves (Figure 7.4 and 7.4, green) were used to determine common PV performance parameters (description: Table 2.1, values: Table 7.7). LIV measurement at step (2) shows absolute values. Measurement steps (6) and (10) show the change relative to step (2):

$$\#_{6,10} = \frac{\#_{6,10} - \#_2}{\#_2} \cdot 100\% \quad (7.2)$$

**Table 7.7: PV performance values of all examined modules as obtained from LIV measurements**

	Treat. step	$V_{oc}$	$I_{sc}$	FF	$V_{mpp}$	$I_{mpp}$	$P_{mpp}$
M1	2	37.17 V	8.199 A	75.7 %	30.1 V	7.664 A	230.7 W
	6	0.0%	-0.1%	0.1%	0.1%	0.0%	0.0%
	10	-0.3%	-0.3%	-3.4%	-1.7%	-2.4%	-4.0%
M2	2	37.32 V	8.249 A	76.5 %	30.33 V	7.767 A	235.6 W
	6	0.0%	-0.1%	0.4%	0.1%	0.2%	0.3%
	10	-0.3%	-0.1%	-3.4%	-1.5%	-2.4%	-3.9%
M3	2	37.38 V	8.247 A	76.5 %	30.44 V	7.747 A	235.9 W
	6	0.1%	0.0%	0.1%	0.1%	0.0%	0.2%
	10	-0.4%	-0.4%	-4.8%	-1.6%	-4.0%	-5.6%
M4	2	37.43 V	8.238 A	76.4 %	30.39 V	7.751 A	235.6 W
	6	0.2%	0.0%	0.7%	0.5%	0.4%	0.8%
	10	-0.7%	-0.5%	-5.0%	-2.4%	-3.7%	-6.1%
P1	2	36.97 V	8.371 A	72 %	28.79 V	7.74 A	222.9 W
	6	0.2%	-0.1%	0.1%	0.6%	-0.3%	0.3%
	10	-0.3%	-0.7%	-10.3%	-1.9%	-9.4%	-11.2%
P2	2	37.01 V	8.382 A	72.5 %	28.71 V	7.835 A	224.9 W
	6	0.1%	0.0%	0.1%	0.2%	0.0%	0.2%
	10	-0.5%	-5.0%	-11.3%	-1.4%	-15.0%	-16.2%
P3	2	37.07 V	8.358 A	72.1 %	28.62 V	7.8 A	223.2 W
	6	0.1%	0.0%	0.3%	0.3%	0.1%	0.4%
	10	-0.5%	-2.0%	-13.9%	-2.7%	-13.7%	-16.0%
P4	2	36.78 V	8.377 A	71.8 %	28.47 V	7.773 A	221.3 W
	6	0.0%	0.0%	0.1%	0.2%	0.0%	0.2%
	10	-0.3%	-2.0%	-8.4%	-2.3%	-8.3%	-10.4%

Both  $I_{sc}$  and  $V_{oc}$  remain unchanged or decrease less than 5% during the measurements. The greatest changes were observed in FF and  $P_{mpp}$ . Whilst the measured power of ‘Mono’ modules was 4-6% less after all treatment steps, the power decrease was 10-16% for ‘Poly’ modules.

#### 7.1.2.1.2 EXTRACTED DIODE PARAMETERS

Diode parameters were extracted from measured LIV and DIV curves (Figure 7.4 and 7.4) by fitting an I-V curve [14] following the single-diode-

model (Section 2.1). The relatively low RMSE between measured and fitted curves of less than 0.8% for all curves indicates the validity of the model used. Figure 7.5-7.7 show extracted ideality factor, shunt and series resistance. The single and unconnected dots represent values obtained from LIV measurements whilst lines represent values from the respective DIV measurements. Unfortunately, the meaningfulness of these parameters is rather limited. The best agreement between parameters from DIV and LIV measurement can be seen for the ideality factor in Figure 7.5. Therein, all the modules showed a similar trend of increasing values from treatment step (0-10).

Throughout all the treatment steps, the extracted series resistance remains too low. Higher values for ‘Poly’ modules are as expected due to the inferior quality of the bulk material. Whilst values from DIV suggest a positive trend, LIV values remain constant or even decrease. Since only three LIV measurements are available, this contrary trend remains questionable. It is assumed that a full I-V curve, which includes the negative voltage part, would result in values that are more credible.

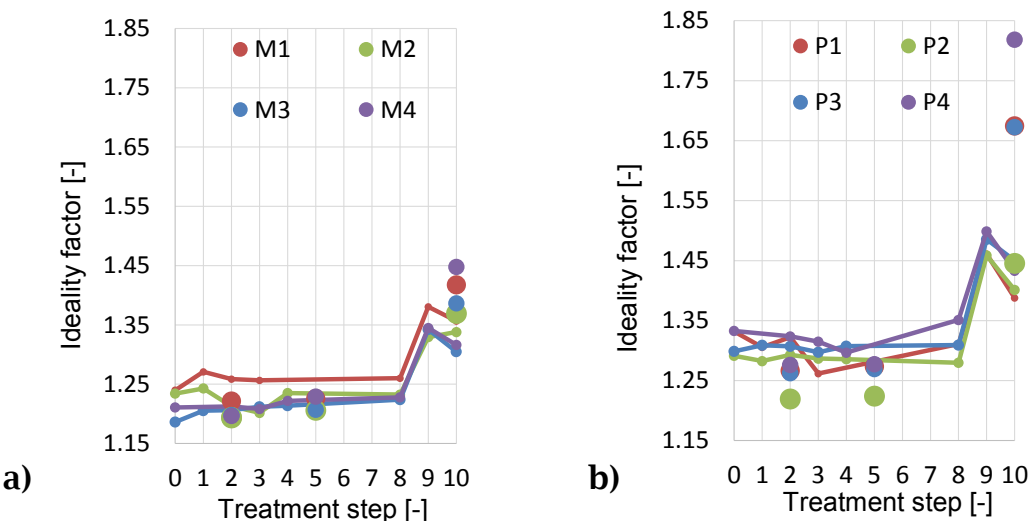


**Figure 7.5: Ideality factor extracted from DIV (lines) and LIV (dots) curves for ‘Mono’ (a) and ‘Poly’ (b) modules**

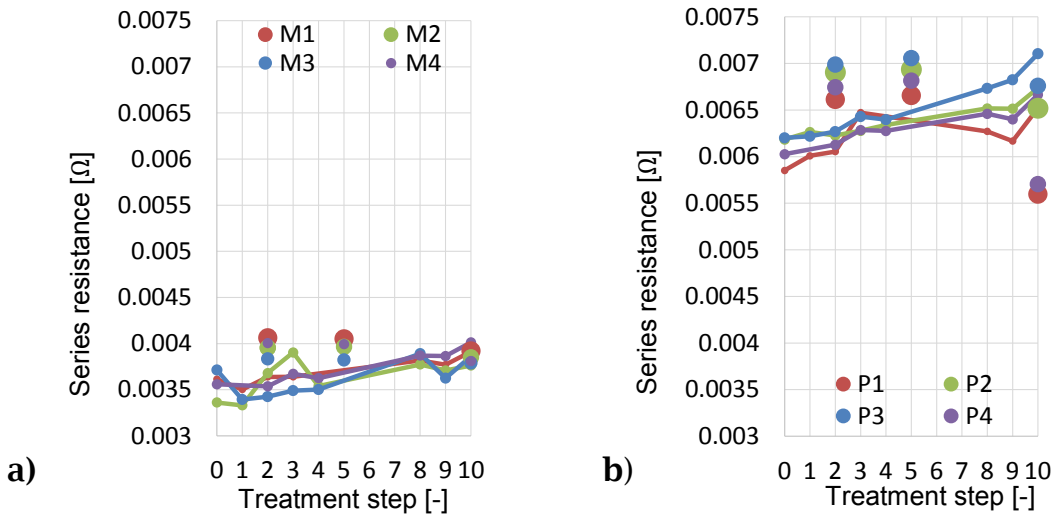


**Figure 7.6: Series resistance for ‘Mono’ (a) and ‘Poly’ (b) modules**

The negative influence of shunt resistances above  $100 \Omega$  is barely noticeable. Therefore, it was decided to use a logarithmic plot in Figure 7.7. Nevertheless, agreement between DIV and LIV is not given and a trend cannot be identified. The results remain inconclusive. It is assumed that this is due to the nature of the single-diode-model were an increased shunt resistance can also be modelled with an increasing ideality factor or decreasing saturation current (not shown).

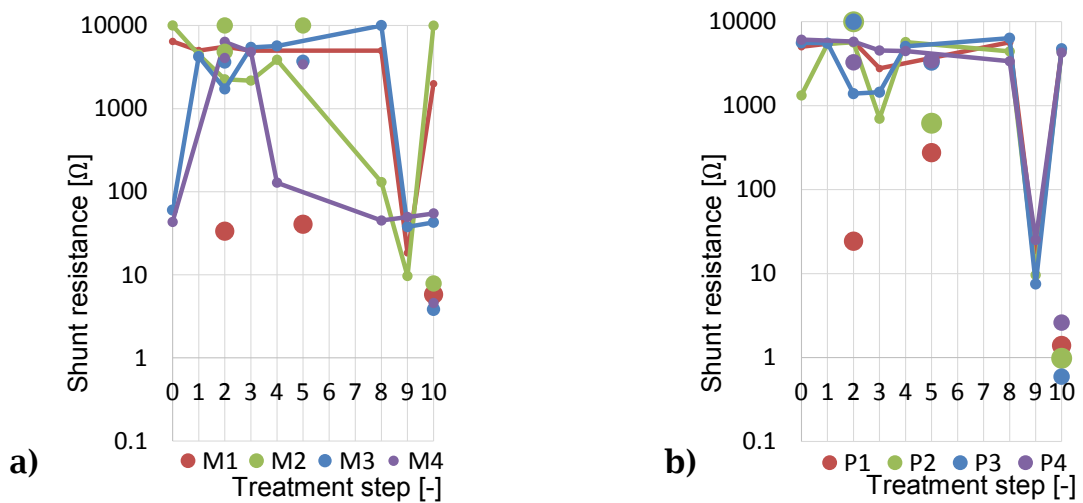


**Figure 7.7: Shunt resistance for ‘Mono’ (a) and ‘Poly’ (b) modules**

### 7.1.2.2 ELECTROLUMINESCENCE IMAGING

Two images were taken at 10% and 100%  $I_{sc}$  for each EL measurement. The exposure time was determined once and allowed signal-to-noise ratios (SNR) around 96 for 100%  $I_{sc}$  and 47 for 10%  $I_{sc}$  measurements. The SNR was measured using two consecutively taken EL images and was calculated with options ‘NLF2’ and ‘xBG’ as described in Section 3.2. The images were corrected as described in Chapter 4. Fully automated image correction, feature extraction and report generation (Appendix 4.1) were carried out.

The initial corrected image 100%  $I_{sc}$  was used to determine cell positions and to rectify perspective (Subsection 4.7.1) for every module. Every cell was rescaled to 400x400 pixel resulting in an image size of 4000x2400. All images were first roughly aligned with its predecessor using pattern recognition (Subsection 4.7.2) and then precisely mapped using sup-pixel alignment (Subsection 4.7.3). Figure 7.8 shows the effect of both image rectification methods on the difference image between two treatment steps. It can be clearly seen that without intensity correction and perspective rectification, the actual differences between two EL images are superimposed by larger deviations next to cell borders, busbars and luminescence variations (especially for polycrystalline cells).

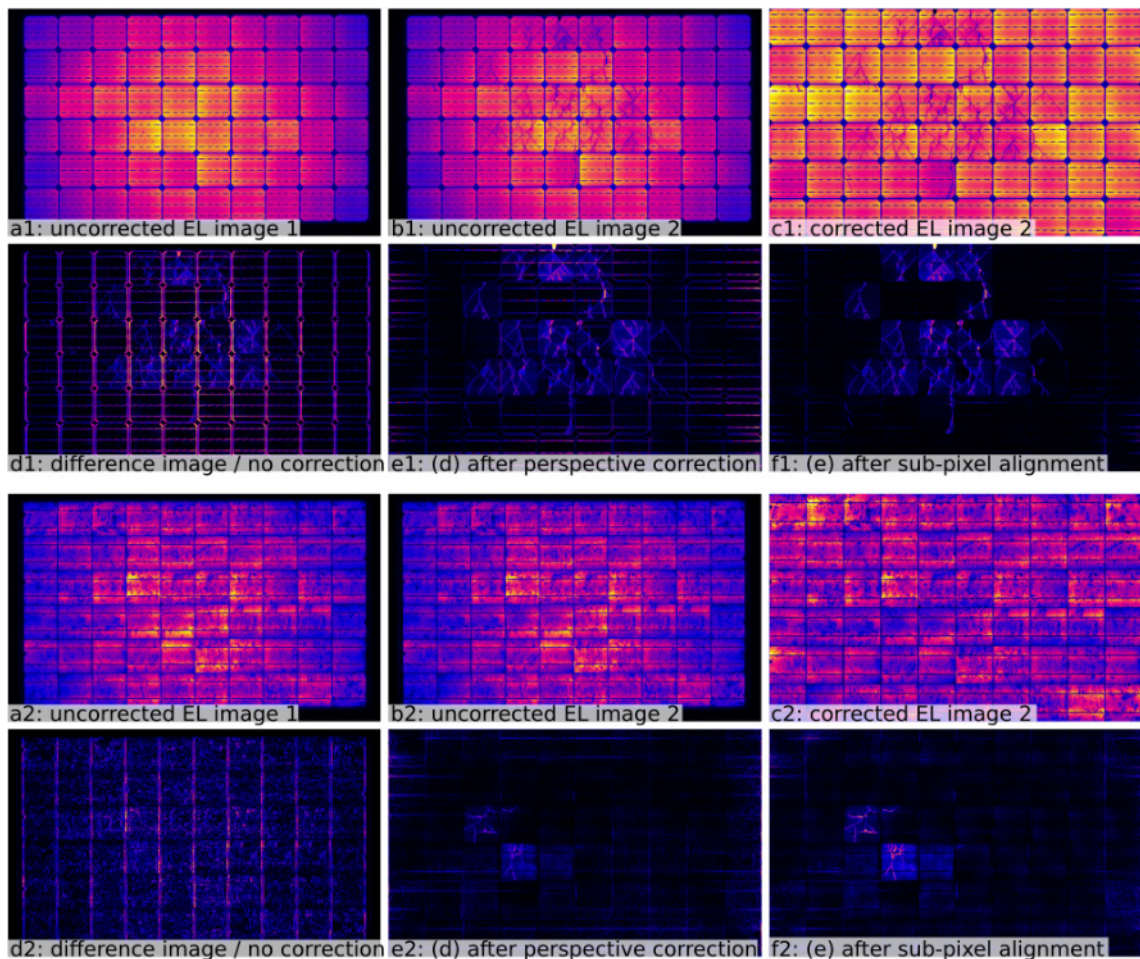


**Figure 7.8: Influence of image correction of EL difference images on a mono (1) and polycrystalline module (2); a-b) Uncorrected EL images (treatment step 0, 1); c) corrected EL image of step (1); d) EL difference images of uncorrected images; e) (d) after perspective rectification; f) (e) after sub-pixel alignment**

Figure 7.9 shows the average operation voltages of all the devices, relative to its initial values. Throughout the entire treatment procedure voltage remained in a narrow range of  $\pm 2\%$ . It can be seen that the trend points slightly upwards for EL measurements at 100%  $I_{sc}$  and slightly downwards for measurements at 10%  $I_{sc}$ .

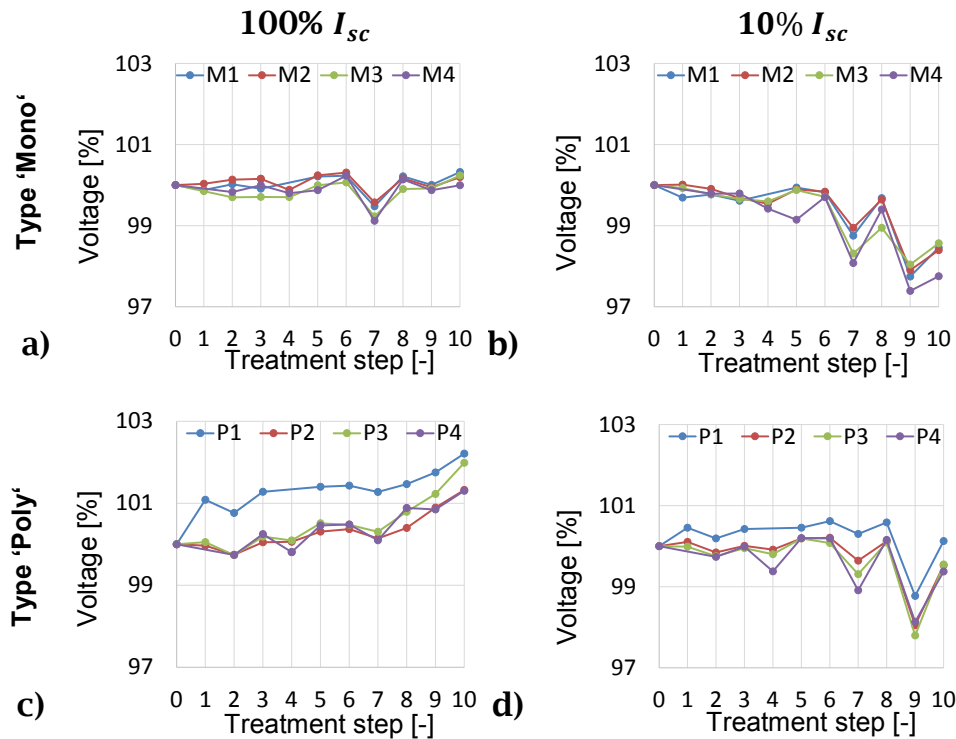


**Figure 7.9: Operation voltage relative to initial EL measurement [%] for every treatment step at 100%  $I_{sc}$  (a,c) and 10%  $I_{sc}$  (b,d)**

The following figures are the result of a statistical evaluation of EL images and therein detected features. It was observed that the brightness of cracked cells decreases. Heavily broken cells were often also the darkest in a module. Figure 7.10 plots the average cell intensity of all modules across all treatment steps over the crack length, relative to cell width (Equation 5.3). In particular for 'Mono' devices (Figure 7.10a,b) a correlation is evident. Subfigure (b) shows that a cell cracked thrice across its entire length (relative crack length=3) will be roughly 30% darker in the 10%  $I_{sc}$  image. In the 100%  $I_{sc}$  image (a), it appears that the same cells only have a 10% decreased intensity.

A contrary trend of negative intensity changes (and thereby brighter cells) over the crack length can be seen as well. This phenomenon is however caused by other (similarly cracked) cells connected in series after the respective cell. These cells caused a higher local voltage decrease and thereby a higher intensity. For 'Poly' modules, the correlation is less clear. Nevertheless for both types it can be observed that the intensity decrease

is about three times higher for EL images taken at 10%  $I_{sc}$ , relative to the images at 100%  $I_{sc}$ .

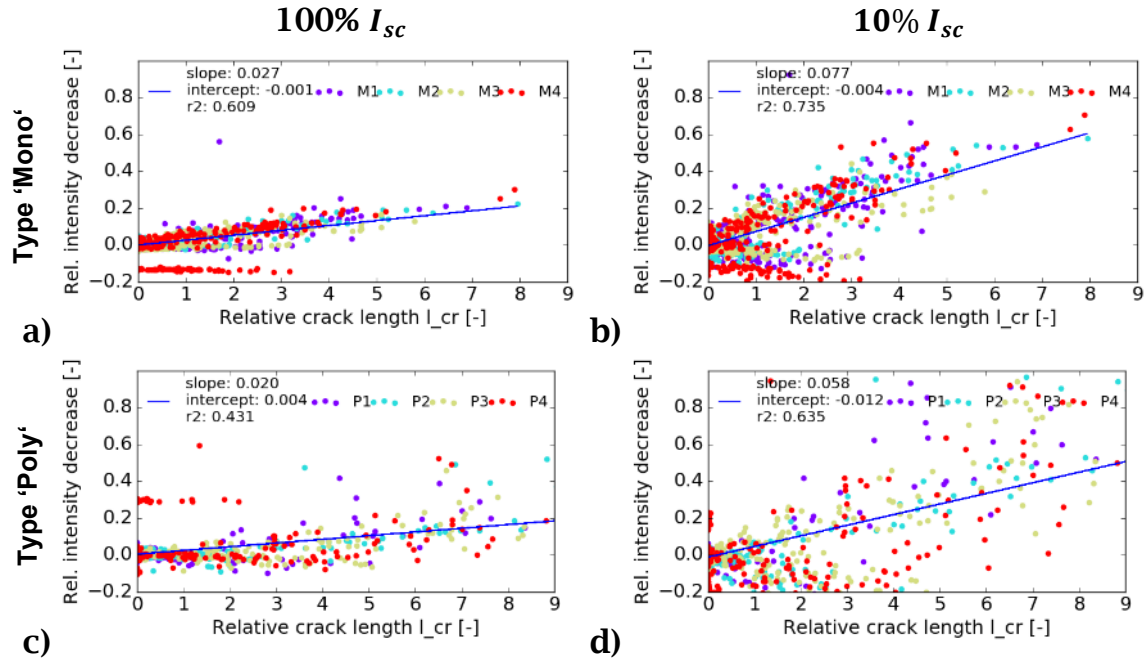


**Figure 7.10: Average cell intensity decrease relative to initial values over relative crack length (Equation 5.3); a,b) 'Mono'; c,d) 'Poly' modules**

With this statement the question arises, whether cell intensity deviations are in general more pronounced in 10%  $I_{sc}$ . Indeed, as Figure 7.11 shows, the same cells will in general occur 3 times (or  $\sqrt{10} = 3.162$ ) darker at 10%  $I_{sc}$  relative to 100%  $I_{sc}$ .

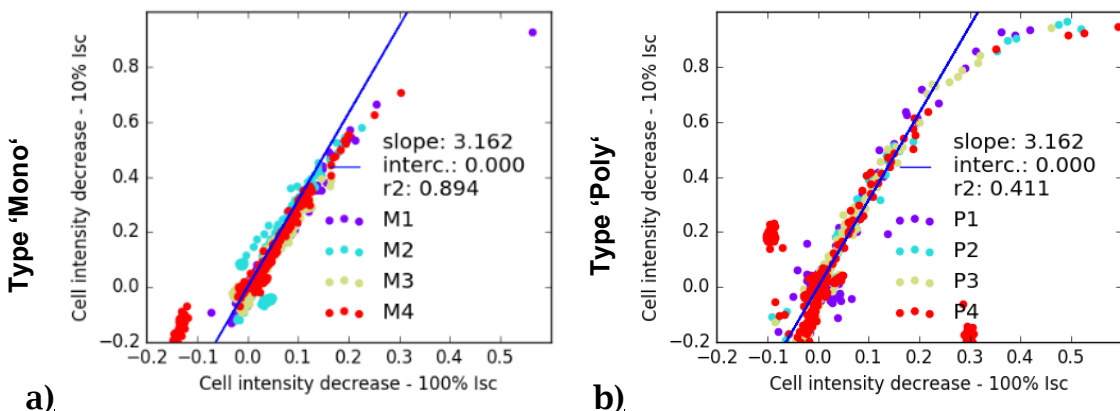


**Figure 7.11: Average cell intensity of all cells in all EL images at 10% and 100%  $I_{sc}$  relative to their initial intensity; a) 'Mono'; b) 'Poly' modules**

When a cell is already broken, will it tend to break again or will the existing crack decrease mechanical stress and thereby stabilise the cell? Figure 7.12 plots the newly introduced crack length relative to the initial one. This initial crack length was defined as the cumulative sum of all new cracks, starting at zero (Table 7.8).

**Table 7.8: Example values for measured ‘introduced’ and derived ‘initial’ crack length**

Treatment step	1	2	3	4	5
Introduced and ...	2	1	4	1	...
Initial crack length	0	2	2+1=3	3+4=7	7+1=8

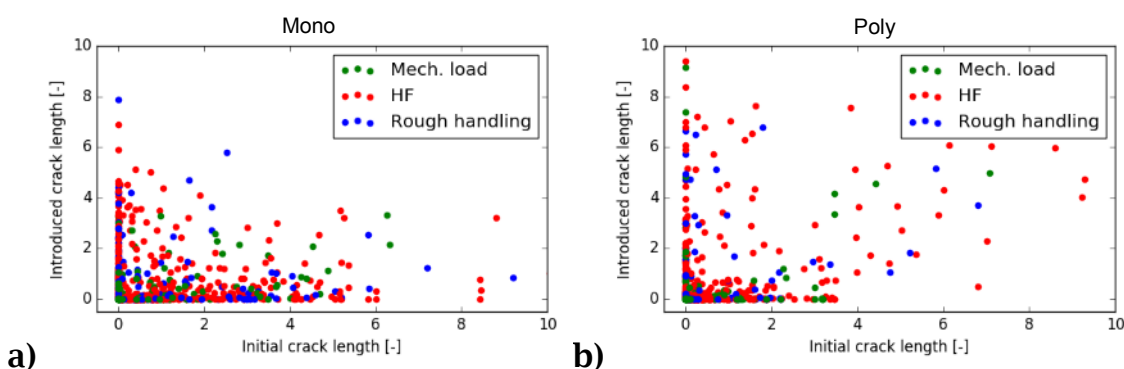


**Figure 7.12: Influence of existing (initial) cracks on newly introduced or extended cracks; a) ‘Mono’, b) ‘Poly’ modules**

Most values in Figure 7.12 accumulate along both axes. This can be interpreted as follows:

- The probability for an unbroken cell to crack is noticeably higher than for a broken cell ( $x=0, y>0$ ).
- If a cell is broken once, is more likely to remain in its state than break again ( $x>0, y=0$ ).

The number of outliers ( $x>0, y>0$ ) is higher for ‘Poly’ modules. This allows the conclusion that cracked ‘Poly’ cells will more frequently break again than ‘Mono’ cells.

On many cells, a similar behaviour was observed in EL:

- Cells mostly broke during mechanical load (1,4) and rough handling (7,9) steps as opposed to the HF treatment steps.

- Humidity freeze treatment often did not develop cracks. It is assumed a wafer-drifting increased the series resistance of the cells. This caused areas next to cracks to darken during the course of all treatment steps.

Figure 7.13 shows corrected EL images of four selected cells for every treatment step. Green boxes indicate breakage introduced. It can be seen that the intensity next to the cracks decreases with every step. In this example, only one area showed increased intensities (step 8, white box).

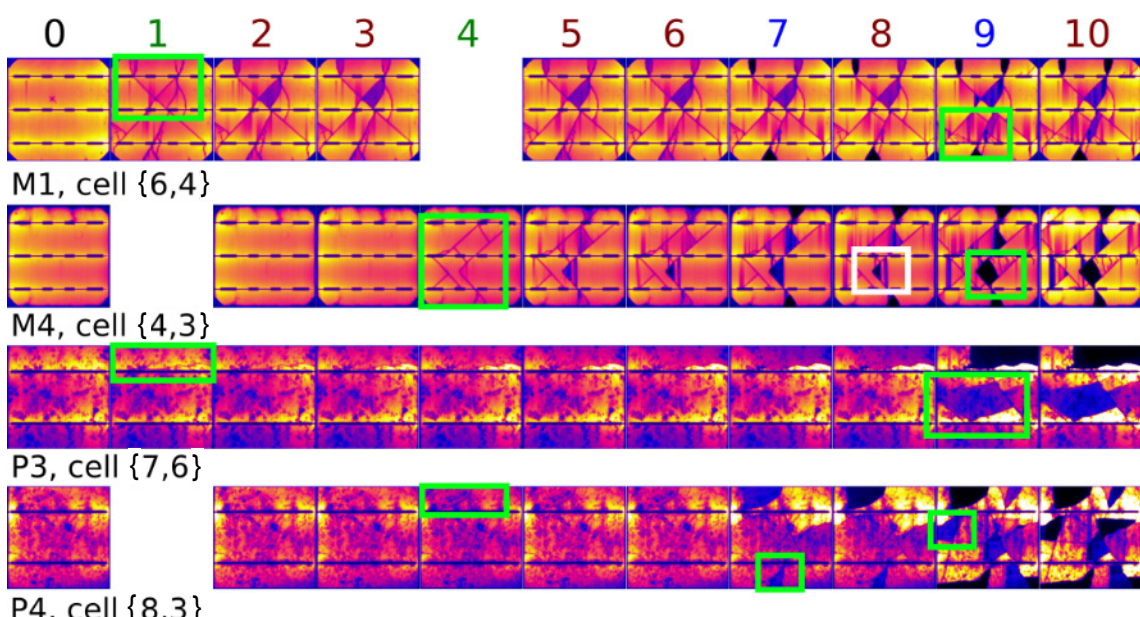


**Figure 7.13: Corrected EL image of selected cells for all treatment steps; green boxes: introduced cracks; white box: EL intensity increase**

An attempt to quantify these observations is shown in Figure 7.14-7.16. Figure 7.14 shows the per-step added inactive area on two different scales (top/bottom). The definition of inactive area can be found in Subsection 5.2. In this section, no distinction is made between partly and fully inactive areas however.

Subfigure (a,b) clearly shows that the mechanical load (1,4) steps and rough handling (7,9) steps were most influential on the results. Thereby loading around 200 kg on a module showed to be much less influential than letting a module fall on the ground. In the latter case, the inactive area was 10 to 30 times larger than after mechanical load. The influence

of the remaining HF treatment (2,3,5,6,10) steps are more evident in Subfigure (c,d). Looking at steps (2->3), (5->6) and (10) it is evident that the amount of additional inactive area decreases successively.

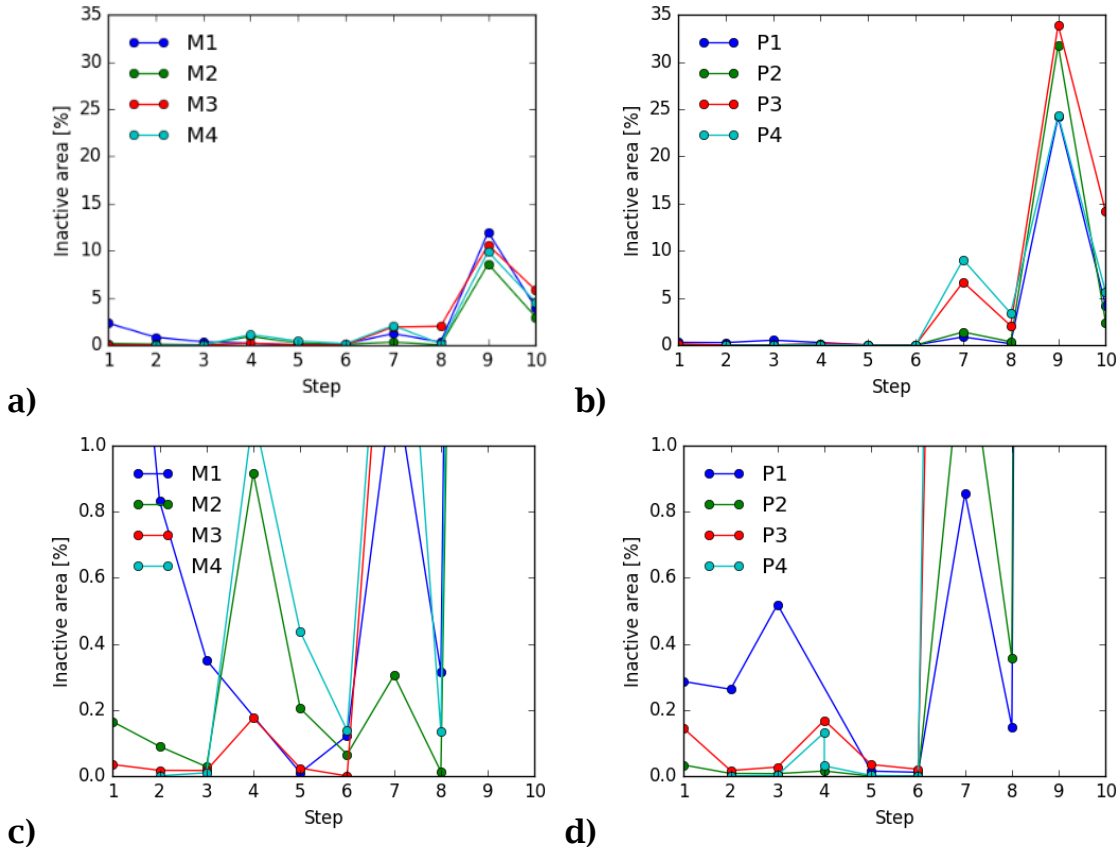


**Figure 7.14: Inactive area vs treatment step scaled 0-35% (top) and 0-1% (bottom) for ‘Mono’ (left) and ‘Poly’ modules (right)**

A similar trend can be seen in Figure 7.15 for introduced crack length.

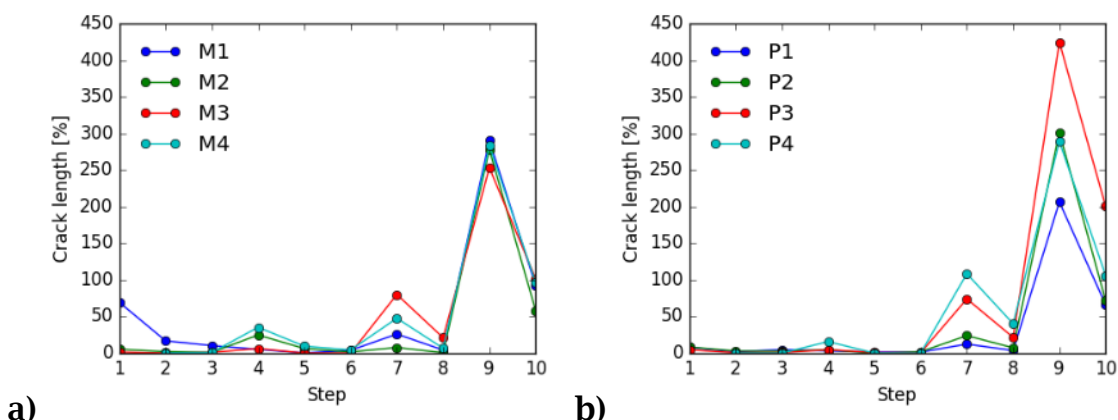


**Figure 7.15: Relative crack length vs treatment step for a) ‘Mono’ and b) ‘Poly’ modules**

The majority of cracks is generated during mechanical load (1,4) but even more during rough handling (7,9). The amount of breakage varied heavily between different modules.

Similar conclusions can be made (Figure 7.16) regarding crack fragmentation (Equation 5.5). Crack fragmentation is largest for rough handling and remarkably not module type dependent.

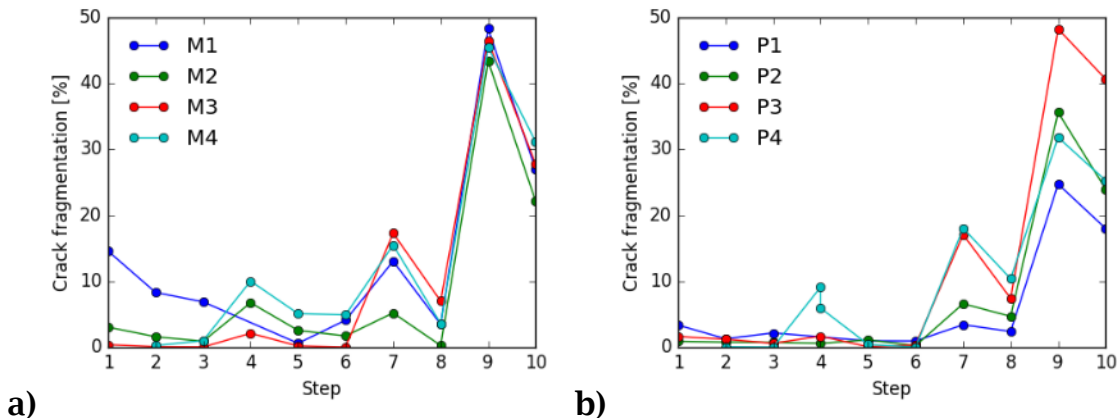


Figure 7.16: Crack fragmentation vs treatment step for a) 'Mono' and b) 'Poly' modules

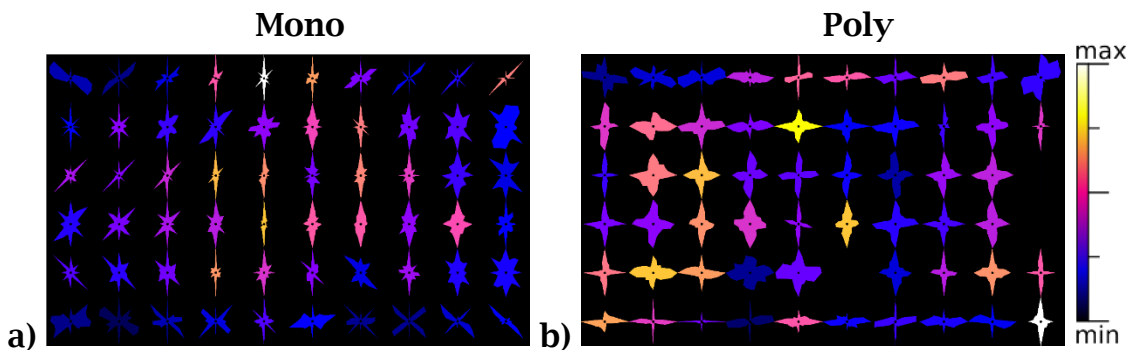
A closer look at the crack lengths generated in step (1,4,7,9) (Table 7.9) shows which treatment was most influential.

Table 7.9: Average crack length [%] generated in the treatment steps (1,4,7,9); values are colour-coded (highest: red, smallest: green)

Mod.	Mech. Load		Rough handling			
	Step 1	Step 4	Step 7	Step 9		
M1	69.48	drop	-	26.18		290.29
P1	8.02			12.46		206.58
M2	5.52	centre	24.95	7.81		278.00
P2	8.35		4.70	24.05		301.35
M3	1.51	edge	6.45	80.21		253.28
P3	4.75		4.84	74.14		424.66
M4		-	35.43	47.77		283.30
P4			15.90	108.52		288.98

In both mechanical stress steps dropping weights on the module centre, even from a small height, introduced most cracks. Stacking weights on the long edge of the module however caused low breakage. Looking at the two rough handling steps (7,9) it is evident that highest damage was created for upright modules falling on their long or short edge (M3,P3,M4,P4). In the second rough handling routine, every module was treated identically, causing similar breakages (excluding P3).

The distribution of crack directions in the final measurement, averaged for all ‘Mono’ and ‘Poly’ modules is shown in Figure 7.17. Therein, the 12 measured crack orientations are shown as polygon, built by all individual crack orientation vectors (Subsection 5.3.2).



**Figure 7.17: Distribution of crack propagation directions; colours correspond to crack length relative to maximum**

A cross-shaped polygon indicates cracks predominantly orientated in two directions. Every polygon is coloured according to the average cracks length at that position. Looking at colour distribution it is apparent that crack length is smallest at the module border and increases towards module centre for ‘Mono’ modules. However, no trend is visible for the more rigid ‘Poly’ modules.

For ‘Mono’ modules cracks close to module edges tend to point towards the module centre. Within the module, centre cracks are in majority horizontal oriented.

Although cracks in individual EL images of ‘Poly’ modules look rather random, most cracks propagate either horizontally or vertically through the cells.

### 7.1.2.3 DERIVING LIV CURVES FROM DIV AND EL

The advantage of DIV to LIV measurement is that no light source (flasher or sun) is required to generate results. Measurements can be conducted outdoors and drones could be used to fully conduct automated scans of entire PV arrays. Though, the modules would have to be disconnected from their strings, or strings from the inverter. However, the current paths travelled in DIV measurement are in the opposite direction to those at normal operation or during LIV measurement (Figure 2.2, 2.5).

During illumination, current is generated in the bulk of the cell and travels to the emitter in the top of the cell. It is then extracted from the cell through the fingers and busbars. In the absence of light (DIV) current is injected into the fingers and then travels towards the back contact. Thereby the travelled distance - and therefore the effective series resistance - is less than that of the illuminated case. Furthermore, electrically isolated areas in a PV module will not influence the DIV since the injected current will find other paths to the back contact rather than dissipating thermally due to high series resistance.

In this section, it was attempted to reproduce LIV measurements using DIV together with EL and initial (such as manufacturers) LIV results. In Figure 7.4 and 7.4, I-V curves from DIV and LIV were plotted together using the short-circuit current ( $I_{sc}$ , from initial LIV) to shift the DIV accordingly. As already discussed,  $I_{sc}$  remained almost constant during all treatment steps. In the next step, the voltage measured in DIV conditions ( $V_{Dk}$ ) will be scaled using the open-circuit voltage obtained from the initial LIV ( $V_{oc}$ ) as follows:

$$V_{Dk}^* = V_{Dk} \cdot \frac{V_{Dk}(I_{sc} = 0)}{V_{oc}} \quad (7.3)$$

This is accompanied by the simplification that  $V_{Dk}$  is overestimated due to a lower series resistance, which is module specific and will not change significantly during degradation.

As discussed, inactive areas cannot be detected in DIV. However, various papers [27, 101, 103, 119] claim that the inactive areas detected by EL reduce PV efficiency [103]. EL images at low current ( $10\% I_{sc}$ ) were found suitable to differentiate between non-disconnecting (type B) and disconnecting cracks (type C) [103]. This is due to the assumption that at low current, series resistance effects can be neglected. The brightness of type C cracks would be around the background level, whilst type B cracks would have an intensity between background and average signal level [101].

Using SPICE (Simulation Program with Integrated Circuit Emphasis) the impact of inactive areas was shown to be significant on the modules power loss [103]. However, a direct comparison between detected inactive area, simulated and measured LIV could not be found. Therefore a bespoke SPICE simulation, based on the Python package ahkab (<https://github.com/ahkab/ahkab>), was developed. It consists of 60 series connected single-diode-modelled cells with three bypass diodes in parallel with cell numbers 1-20, 20-40 and 40-60.

The diode parameters and  $V_{oc}$  were identical for all cells and their values were obtained from the initial LIV measurement from every module (Figure 7.5 et seq.). The generated photo current ( $I_{Ph}$ ) was calculated for every cell individually as a product of the measured short-circuit current ( $I_{sc}$ ) and the ratio inactive area ( $A_{inactive}$ ) versus cell area ( $A_{cell}$ ) as follows:

$$I_{Ph} = I_{sc} \cdot \left(1 - \frac{A_{inactive}}{A_{cell}}\right) \quad (7.4)$$

The second part of Appendix 4.2 shows the corrected low current images of all eight modules at the top-left of every page.

Figure 7.18 shows an example corrected EL image at  $10\% I_{sc}$ . As Figure 7.10 and Figure 7.11 indicate, extrinsic cell defects (such as cracks) lower the respective cell intensity about 3 times more than in the high current EL image. If it can be assumed that the signal peak is higher than the background peak, a simple division by the median cell value is sufficient

to correct for the inhomogeneity of cell intensities. The result is shown in Subfigure (b). A difference image (Equation 5.1) between the intensity corrected EL images at treatment step 0 and 8 is shown in (c).

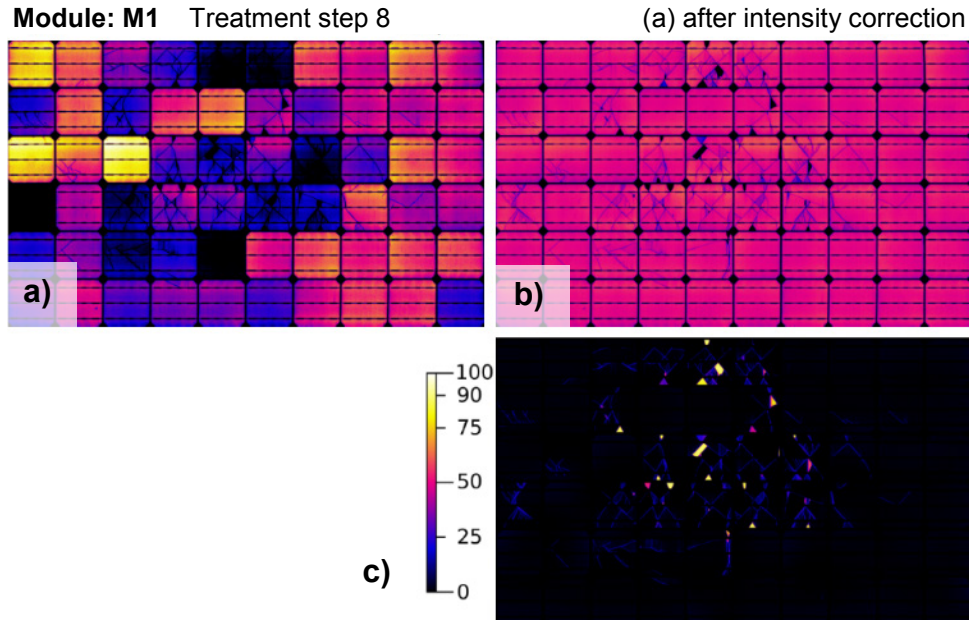


**Figure 7.18:** Example page from Appendix 4.1 displaying the module M1 at treatment step (8); a) Corrected EL image at 10%  $I_{sc}$ ; b) (a) after dividing every cell by its median; c) relative difference image

It can be seen that inactive areas, although shown black in the corrected EL image, become visible at different intensities in the relative EL difference. To find out which threshold is most suitable to determine inactive areas, six different threshold conditions were tested (Table 7.10). Figure 7.20 and 7.20 compare the measured LIV and scaled DIV of the final treatment step (10) to the six different simulation results for every module.

**Table 7.10: Threshold criteria to determine inactive area**

Name	Sim. 0	Sim. 1	Sim. 2	Sim. 3	Sim. 4	Sim. 5
$A_{inactive} = \sum dEL_i > \dots$	-	25%	50%	85%	90%	95%

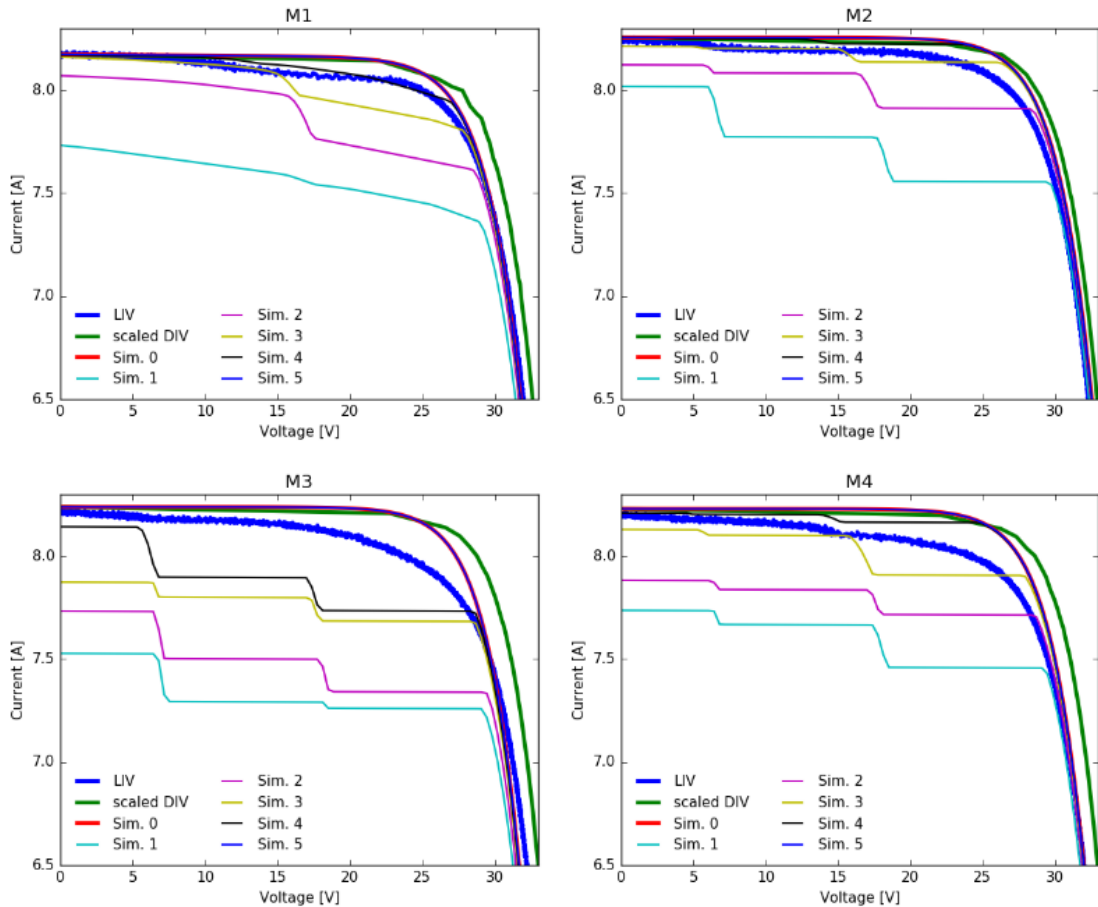


**Figure 7.19: Measured LIV and scaled DIV curve of the last treatment step (10) together with simulated I-V curves following different threshold criteria to determine ‘inactive’ areas for ‘Mono’ modules**

It can be seen that the threshold criterion is decisive for the current in the simulated I-V curve. Overall ‘Sim. 5’ gave results closest to the measured I-V curve. With increasing influence of the inactive areas, the steps in the I-V curve steepen. Although these steps can be found in several LIV curves (M4, P2, P3) the simulated steps are on average more pronounced and much steeper than the ones visible in LIV.

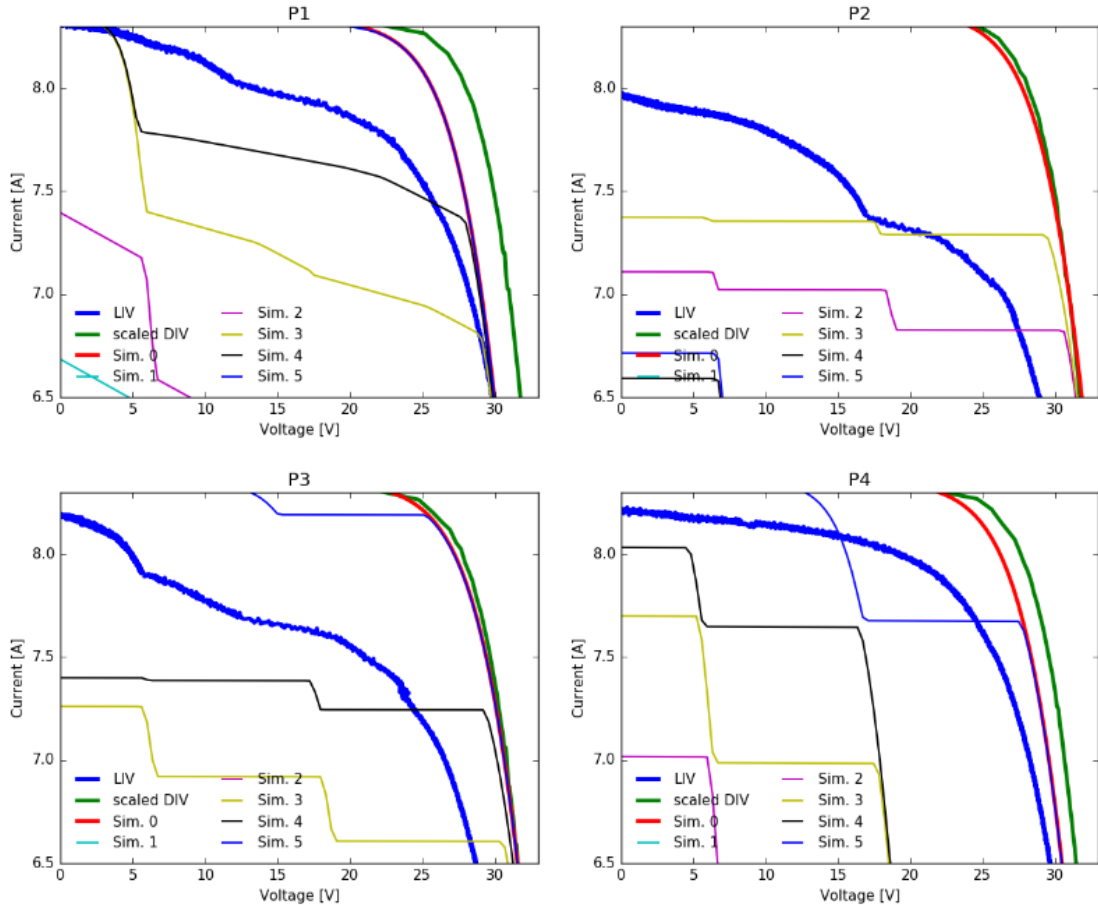


**Figure 7.20: Same as Figure 7.19 for 'Poly' modules**

Therefore, reproducing I-V curves with a SPICE simulation incorporating cell mismatch due to different influence of inactive areas was not successful. Since the measured LIV curves deviate mostly in current, another SPICE simulation tried to establish a link between the measured crack length and decreasing shunt resistance. Similar cell intensity patterns (as observed in the analysed EL) can be found looking at EL images of modules before and after potential induced degradation (PID) tests [121]. Whilst PID is associated with shunting, it can be assumed that introduced cracks cause similar effects.

The photo current was set to  $I_{sc}$  for every cell but the cells shunt resistance ( $R_{sh,i}$ ) was reduced by crack length ( $l_{cr}$ ) as follows:

$$R_{sh,i} = \frac{R_{sh,0}}{(l_{cr,i} + 1)^2} \begin{cases} R_{sh,0} = 15\Omega \text{ for 'Mono'} \\ R_{sh,0} = 5\Omega \text{ for 'Poly'} \end{cases} \quad (7.5)$$

A lower  $R_{sh,0}$  for ‘Poly’ modules was assumed to be due to the influence of grain boundaries. Deriving a cell shunt resistance based on its extracted diode parameters was not possible since their results remain inconclusive (Figure 7.7). Figure 7.22 to 7.24 again show LIV and scaled DIV together with the new simulation results for the second and final LIV measurement step (6, 10). The comparison with the previous Figure 7.20 and 7.20 shows that the deviation of the simulated I-V curve is comparably smaller.

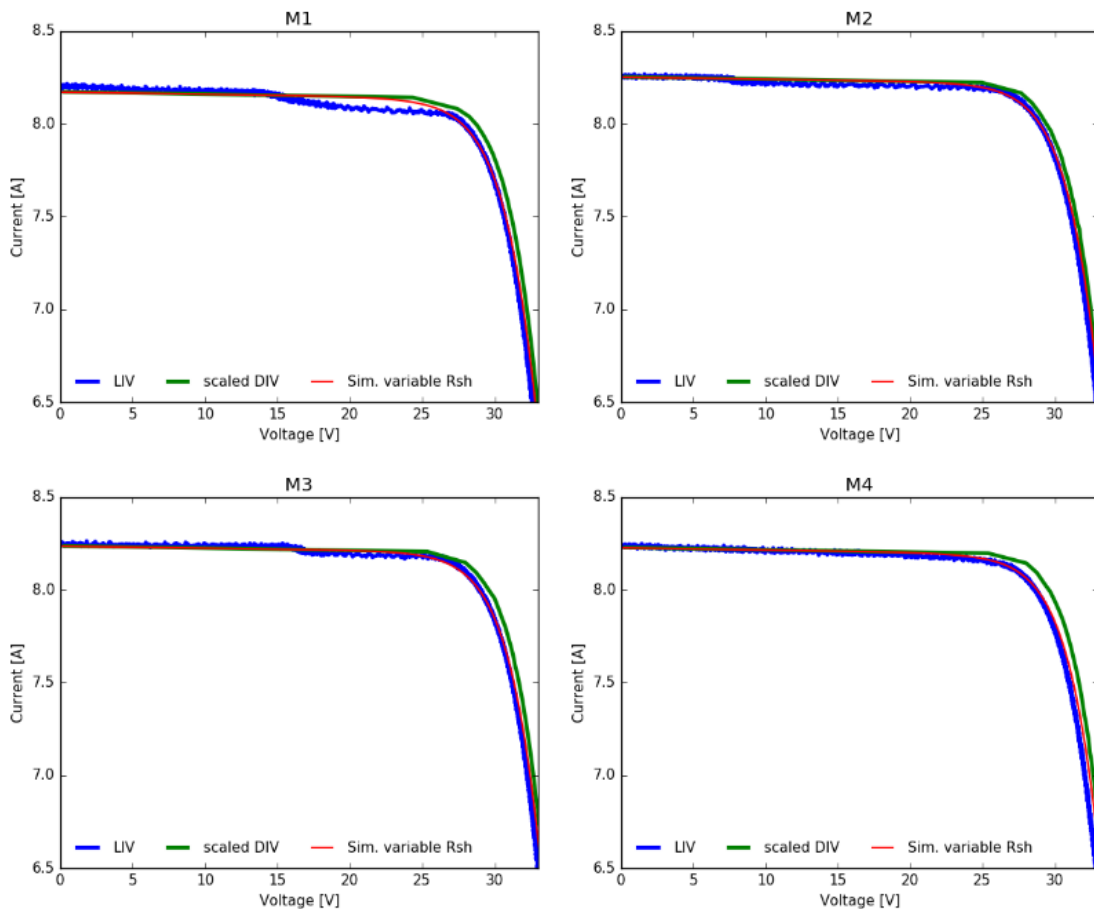


**Figure 7.21: Measured LIV and scaled DIV curve of treatment step (6) together with simulated I-V curves with cell-specific shunt resistance for ‘Mono’ modules**

Chapter 7: Case Studies  
Section: 7.1: Thermo-Mechanical Load Experiment at NREL

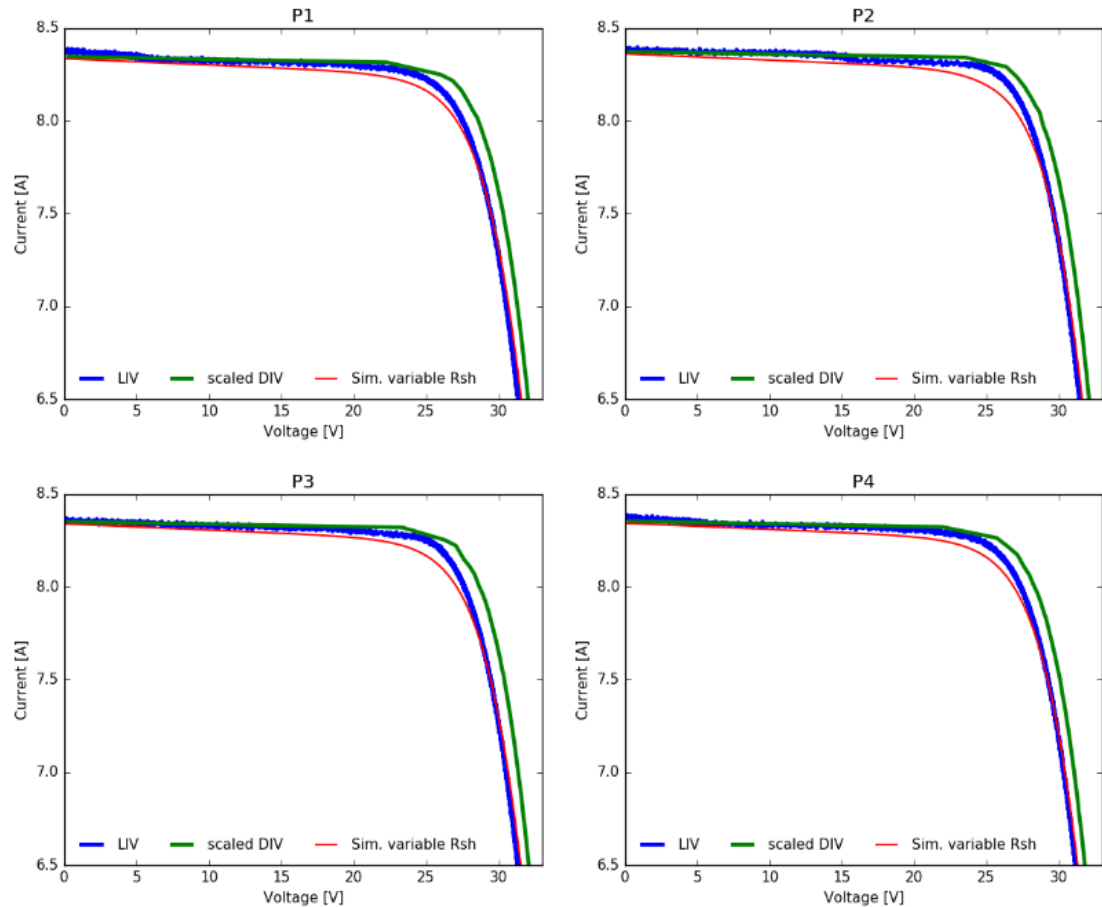


Figure 7.22: Same as Figure 7.21 for ‘Poly’ modules

Chapter 7: Case Studies  
Section: 7.1: Thermo-Mechanical Load Experiment at NREL

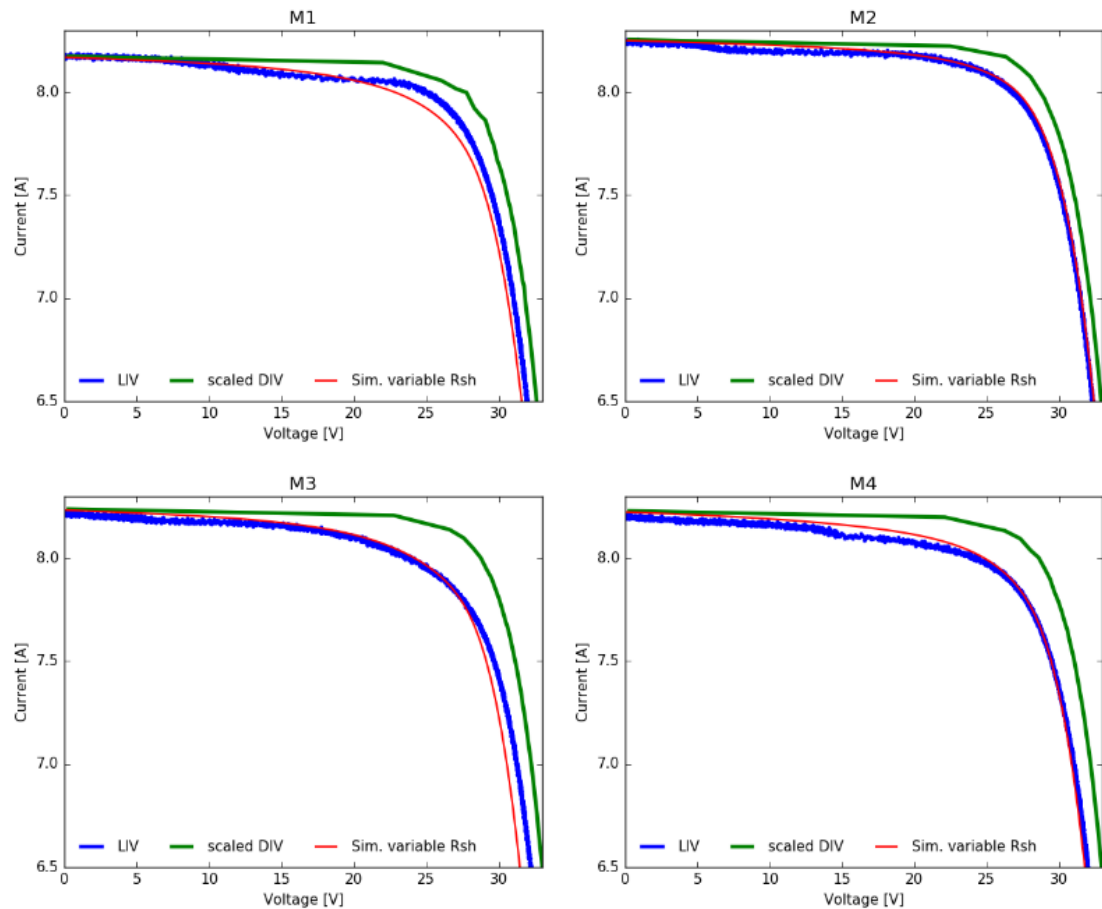
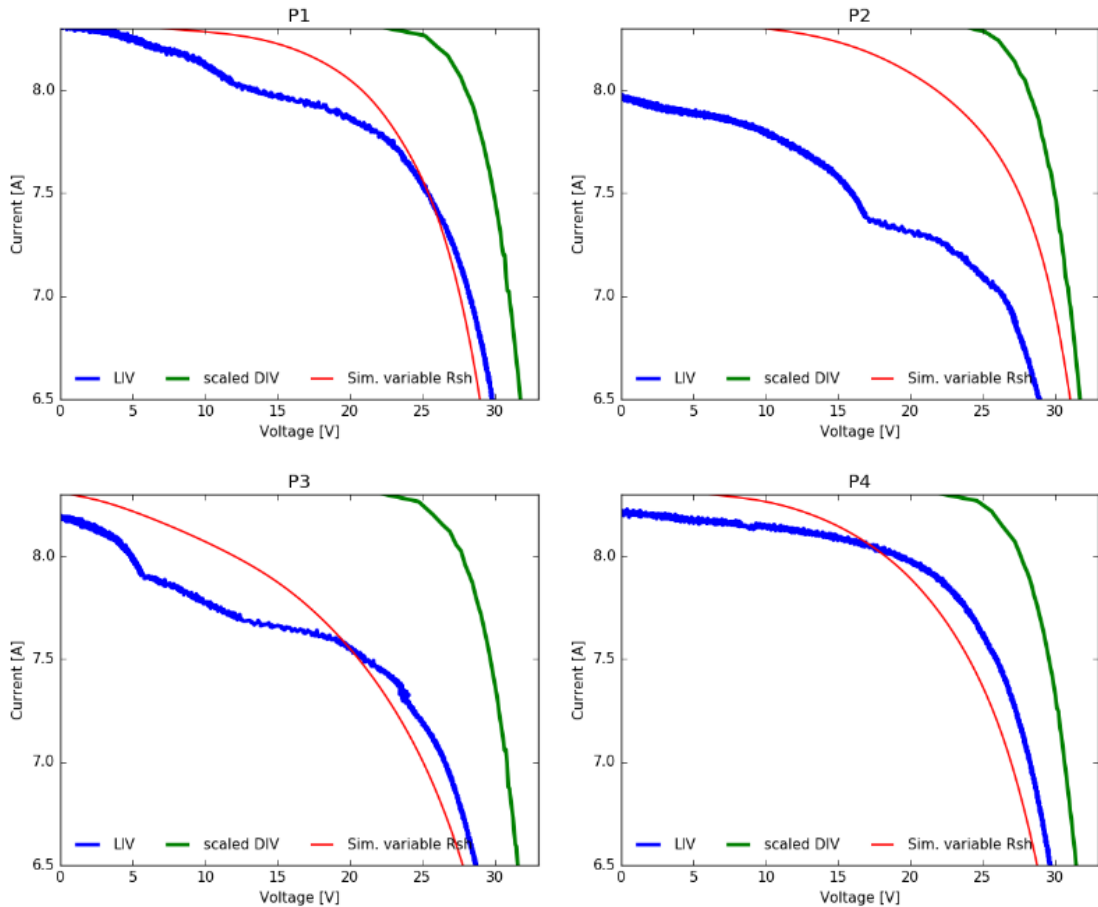


Figure 7.23: Same as Figure 7.22 and 7.22 for last treatment step (10)



**Figure 7.24: Same as Figure 7.23 for ‘Poly’ modules**

The approach to reproduce LIV curves using only DIV and EL can be concluded as follows: Although dark areas in EL images suggest the existence of inactive cell areas, a simulation could not verify that these areas are indeed electrically isolating.

Crozier suggests that cracks also reduce shunt resistance. This causes more injected current to bypass the cells diode junction and therefore to decrease EL intensity [27]. A simulation incorporating this assumption (crack length influencing shunt resistance) shows a better agreement to the measured results. Decreased shunt resistance can also explain the homogenous intensity decrease for cracked cells.

Köntges et al. correlate the number of cracks in a module or number of cracked cells in a module to power loss using only a few data points [103]. This approach does not consider crack length and is based on a rather loose definition of crack quantity, which will often require manual

counting. Since only three LIV measurements were available for every module in this study, Köntges approach could neither be verified nor disproven. It is however hoped that crack length as parameter enabling automated detection and as cause for decreased shunt resistance can be established. However, for more specific statements a spatially resolved SPICE simulation [122] together with a current-mapping method (such as LBIC) would be needed.

### 7.1.3 SNAIL TRAILS

All ‘Mono’ modules showed blue-discolorations (‘snail trails’) after HF tests at areas where cracks were visible in the EL images. This section details the image processing needed, to visualize these defects and will show that snail trails are indeed caused by cracks.

Figure 7.2 shows images of the unbiased but illuminated device, taken with a mobile phone (a) and a high-end consumer camera (b,c). The snail trails were most visible at close distance and high angles of incidence. In order to prepare light image (b) for quantitative comparison, the perspective was corrected, as described in Subsection 4.7.1.

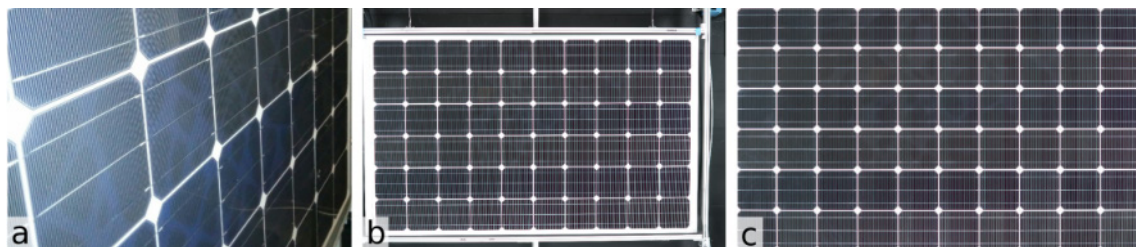


**Figure 7.25: Images of module ‘M4’ after HF treatment step (6);  
a) close up; b) total; c) (b) after perspective correction**

In the following steps the colour channels were separated and a spatial minimum filter (kernel size = 6 px) was applied to remove the disturbing influence of the high reflective fingers (Figure 7.26a-c). It can be seen that every colour layer has a slightly different base intensity. In addition, intensity gradients towards the top-left corner can be identified. This

influence is corrected by subtracting a pseudo-background image (Figure 7.26d-f) from every channel.

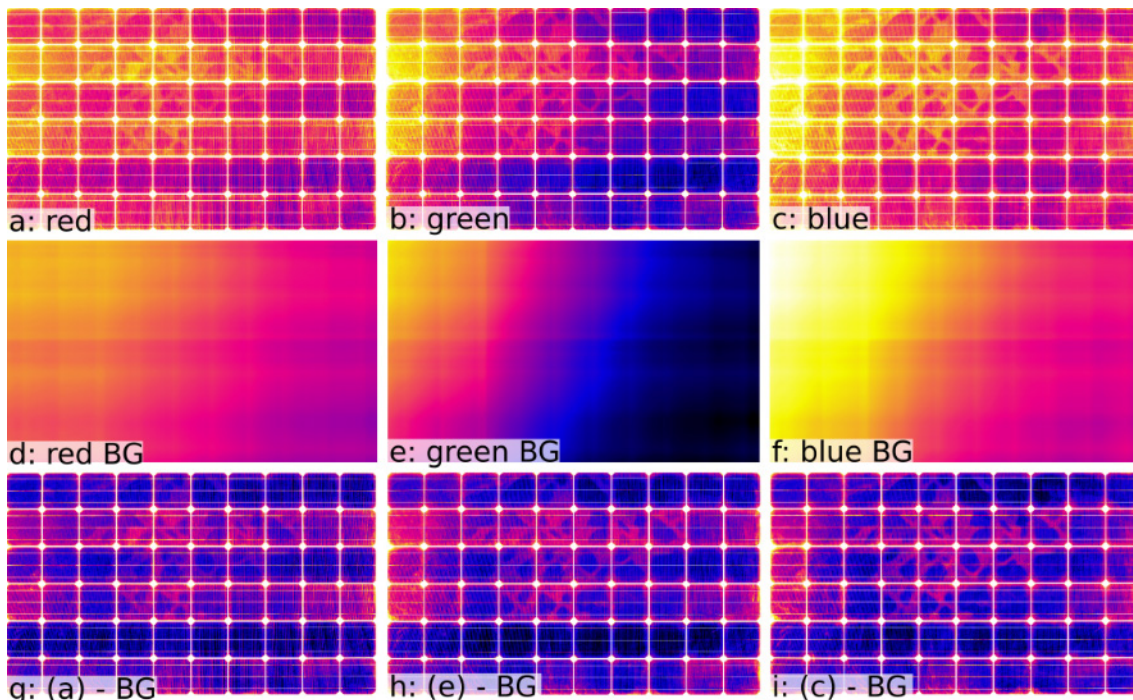


**Figure 7.26:** a-c) Separated colour channels of the light image, shown in Figure 7.2c; d-f) extracted pseudo-background from (a-c); g-i) (a-c) after pseudo-background subtraction; (a-c), (d-f) and (g-i) are scaled identically

The pseudo-background image was generated using a large-kernel median filter (kernel size = 1000 px). To reduce the processing time of a filter at that kernel size only every 30<sup>th</sup> pixel was used for computation. The 'background-corrected' colour layers can be seen in Figure 7.26g-i.

A close-up of these images also indicates that snail trails might be best visible in the blue colour channel (Figure 7.27). This is as expected, since they are seen as blue discolorations.

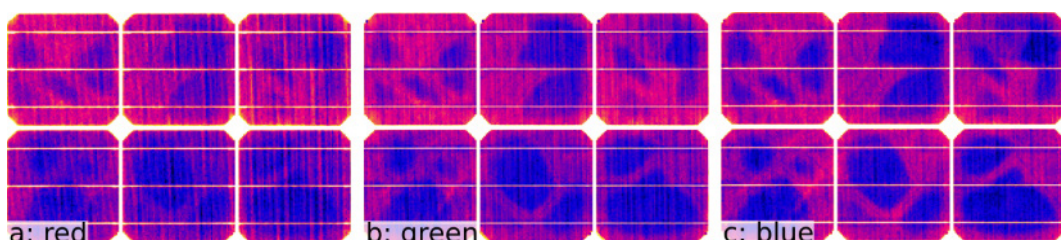


**Figure 7.27:** ROI of cell {5,2}-{7,3} of 'background-corrected' colour channels, shown in Figure 7.26g-i

In order to demonstrate that these features are caused by cracks, an EL difference image was calculated from an initial EL image taken after treatment step (6) (Figure 7.28a,b).

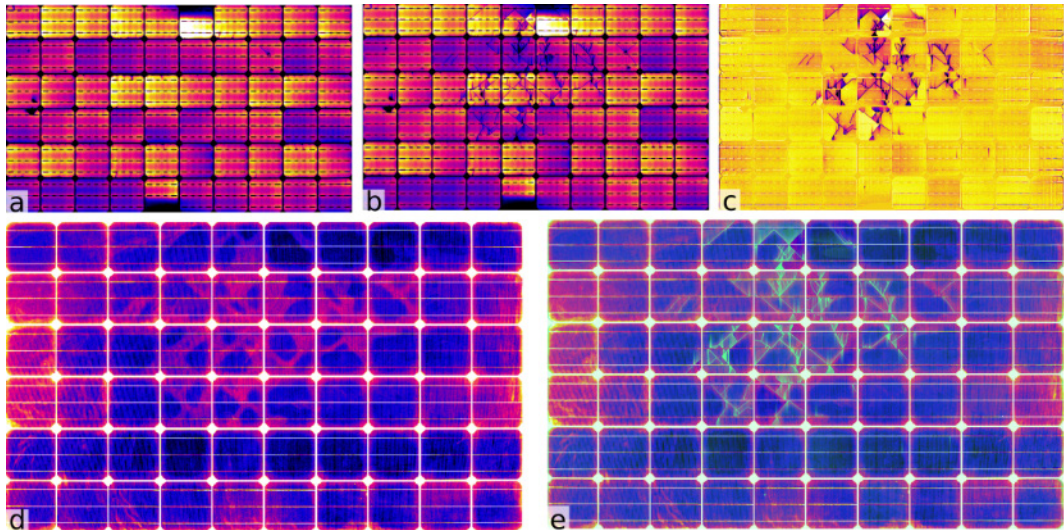


**Figure 7.28:** a,b) Initial EL image and EL image after treatment step (6) of module M4; c) EL difference image (a)-(b); d) blue colour channel of light image; e) same with overlaid EL difference image as semi-transparent green layer

Both images were taken at 100%  $I_{sc}$  and were corrected according to the procedure described in Chapter 4. A transparent-to-green colour map was then applied to the difference image. As the direct comparison of the light image with and without overlaid EL difference image shows, all features, visible as snail trails are also visible as cracks (Figure 7.28d,e). However, snail trails were only observed on ‘Mono’ modules. The ‘Poly’ modules, (although similarly stressed and aged) remained free from visible snail trails.

Meyer et al. linked the formation of snail trails to silver nanoparticles accumulating in the encapsulation foil. It was assumed that this process is caused by environmental moisture, diffusing from the back sheet through cracks and detaching silver from grid fingers [123]. Snail trail imaging relies on specific devices and a sufficiently long ageing time for moisture to cause a visible decolouration. Therefore it is questionable,

whether snail trails (detected by light or UV-fluorescence imaging [109]) can be used as a simple alternative for on-field crack detection by EL.

#### 7.1.4 SECTION SUMMARY

In this case study, eight PV modules (four monocrystalline ‘Mono’ and four polycrystalline ‘Poly’) were exposed to multiple mechanical load, rough handling and humidity-freeze routines.

The quality of images, processed with the presented image correction routine (Chapter 4) was sufficient to allow quantitative analysis of relative difference images. Inactive areas and cracks were extracted. A statistical analysis showed a correlation between crack length and cell intensity. Cells were predominantly broken within mechanical stress routines and inactive areas were generated during HF treatment. In all ‘Mono’ modules, snail trails were visible at cracked locations. A SPICE simulation considering variable photo current generation from detected inactive areas was not able to reproduce the measured I-V curves. Instead, crack length (extracted from EL) was linked to decreasing shunt resistance. A simulation incorporating shunt resistance generated I-V curves similar to the measured ones. If the link between crack length and shunt resistance can be corroborated, PV performance can conceivably be estimated from only EL and DIV measurements.

## 7.2 First International Round Robin on EL Imaging

From January 2016 to April 2017 ten PV modules and five 1-cell mini modules were shipped outgoing from CREST (UK) to 15 other laboratories across Europe and the USA. The number of labs and countries is listed in Table 7.11. Since the results are evaluated anonymous, laboratory names are substituted with letters. Several labs submitted results from multiple camera setups. Every lab-camera setup was assigned a different randomly assigned letter A-X. Setup IDs starting with ‘X’ indicate an InGaAs camera

sensor. In this work, only submitted raw images from 14 camera-setups were analysed. At time of writing, eight laboratories did not submit results.

As the first one of its kind, the Round Robin (RR) aimed to find common criteria for the EL imaging method. This included measurement setup, camera calibration and image quality. Every lab was asked to perform a camera calibration (lens distortion and flat field as described in Section 3.5 and 3.6.2.1). The devices were shipped in a wooden crate (Figure 7.29a). To detect possibly critical impacts during shipment, three shock detectors were attached to the sides of the crate (Figure 7.29b). At crate arrival, every lab was given the task to image every DUT twice at two given currents ( $100\% I_{sc}$  and  $10\% I_{sc}$ ). For every different exposure time, two additional dark current images should be taken. Camera correction and image rectification were optional, since there was no standardised routine available.

**Table 7.11: Number of participant laboratories by country**

Number	Country
1	UK (CREST)
1	Italy
8	Germany
1	Slovenia
1	Cyprus
2	USA
2	Spain

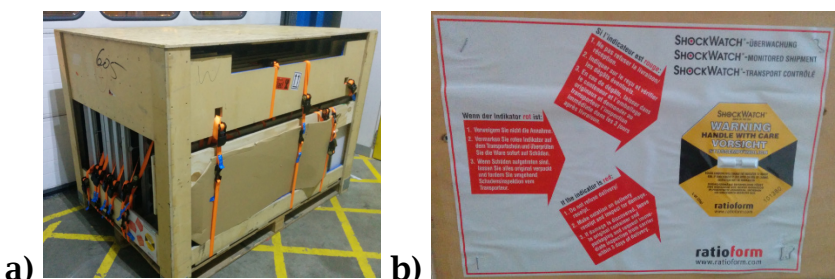


**Figure 7.29: a) Wooden crate, used to transport the ten modules and five mini-modules during the RR; crate dimensions: L185xB125xH132 cm; b) one of three shock detectors**

The devices used in the RR cover five monocrystalline, three polycrystalline and two amorphous modules of dimensions up to 1.68 m (Figure 7.30). The one-cell mini modules were fabricated at CREST. They included one mono- and four polycrystalline cells. The modules were of different ages and tried to cover different defect types. The mini-modules were made from state of the art commercially available cells with different introduced extrinsic defects.

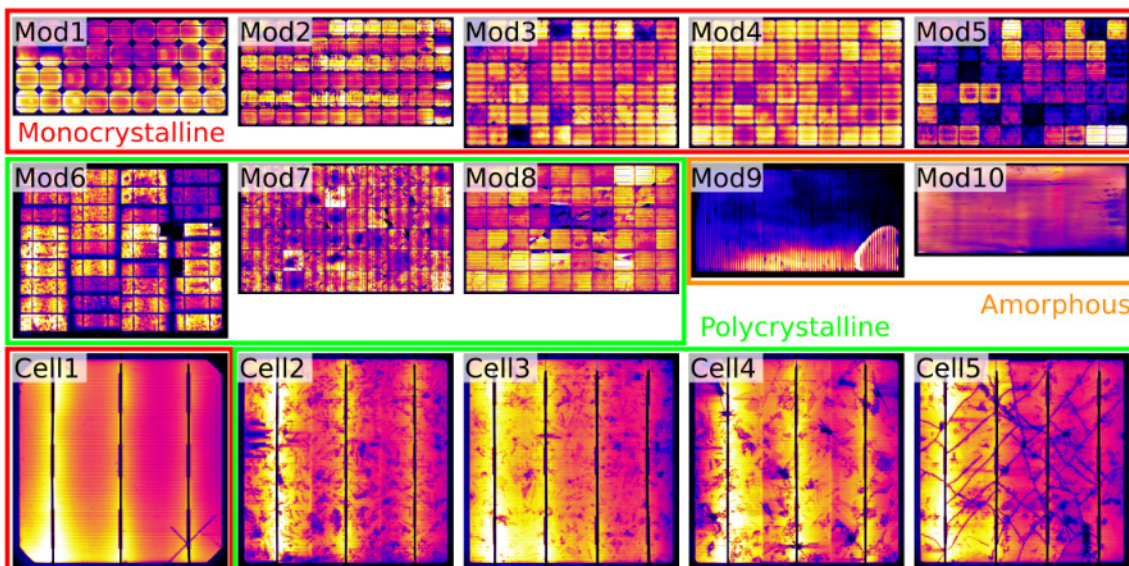


**Figure 7.30: Overview of Round Robin DUT; EL images are from camera system 'B' and are corrected according to Chapter 4**

The following results should be regarded as preliminary. They will focus on image quality (SNR, sharpness) of the submitted EL images as well vignetting and lens calibration. The number of evaluated images is shown in Table 7.12. Different numbers between EL and background images as well as vignetting and vignetting background calibration indicate missing data. Therefore before automated analysis it was attempted to find equivalent replacements for missing images.

**Table 7.12: Number of images evaluated in EL RR**

EL	Background	Lens calibration	Vignetting calibration	Vignetting background
616	579	316	178	70

## 7.2.1 IMAGE QUALITY ANALYSIS

The resolution of submitted images varied from 320x256 (InGaAs) to 4096x4094 pixels. The distribution of camera resolution and aspect ratio is shown in Figure 7.31. It is remarkable that (excluding 8.3 MPixels) no resolution dominates and many less traditional aspect ratios were found.

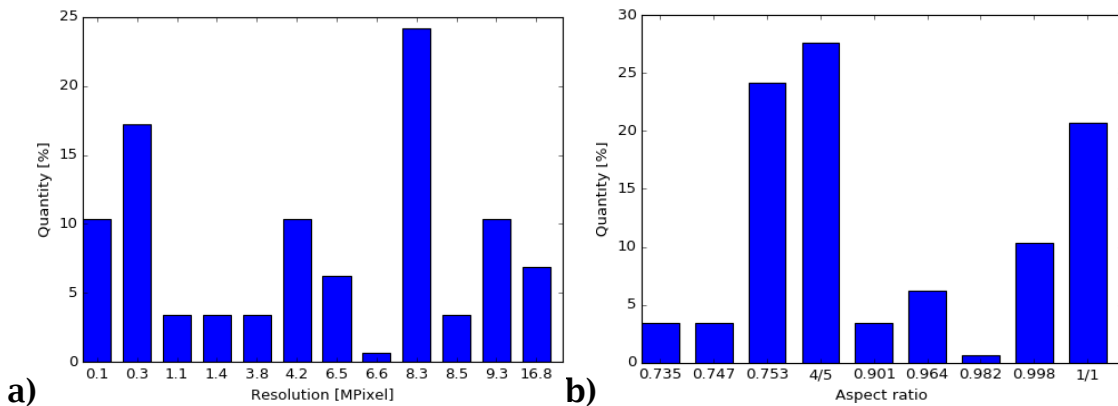


**Figure 7.31: Distribution of resolution (a) and aspect ratio (b) of all submitted images**

### 7.2.1.1 INTENSITY

Most submitted images were of file type TIFF. Images of type FIT and RAW were converted to TIFF before analysis. The depth of all submitted TIFF images was 16 bit. This is not surprising, since TIFF images can only be either 8 or 16 bit. To evaluate whether camera sensors were rather 8 or 14 bit, the maximum value of every image was analysed. If this maximum value was  $\leq 255$  (16383) the bit depth was assumed to be 8 (14) bit.

It was found that only 10% of all images were likely to have been created with a 14 bit camera sensor. The remaining 90% were done with a 16 bit sensor. Noting a probable non-linear charge of the camera sensor well at high fill rates, a maximum image intensity of 75% (for gain = 1) resp. 95% (for gain  $\geq 1$ ) was defined prior to the RR.

To analyse the image intensity distribution, three parameters were extracted from all images: signal peak level (Figure 3.7) as well as lowest (i.e. background level) and highest 2% of image intensities. In Figure 7.32a,b their levels are coloured red, green and blue respectively. They

are plotted relative to their maximum intensity, defined by bit depth ( $2^{depth} - 1$ ).

Only a minority of images utilised the full depth resolution of the camera sensor. In comparison to EL images taken at 100%  $I_{sc}$ , images at 10%  $I_{sc}$  use even less of the available capacity. It is assumed that signal quality is diminished by short exposure times. Subfigures (c,d) analyse the distributions shown in (a,b) where an additional ‘Utilization’ ratio is displayed. It is calculated as follows:

$$Utilization = \frac{Top2\% - BG\ peak}{Max.\ intensity - BG\ peak} \quad (7.6)$$

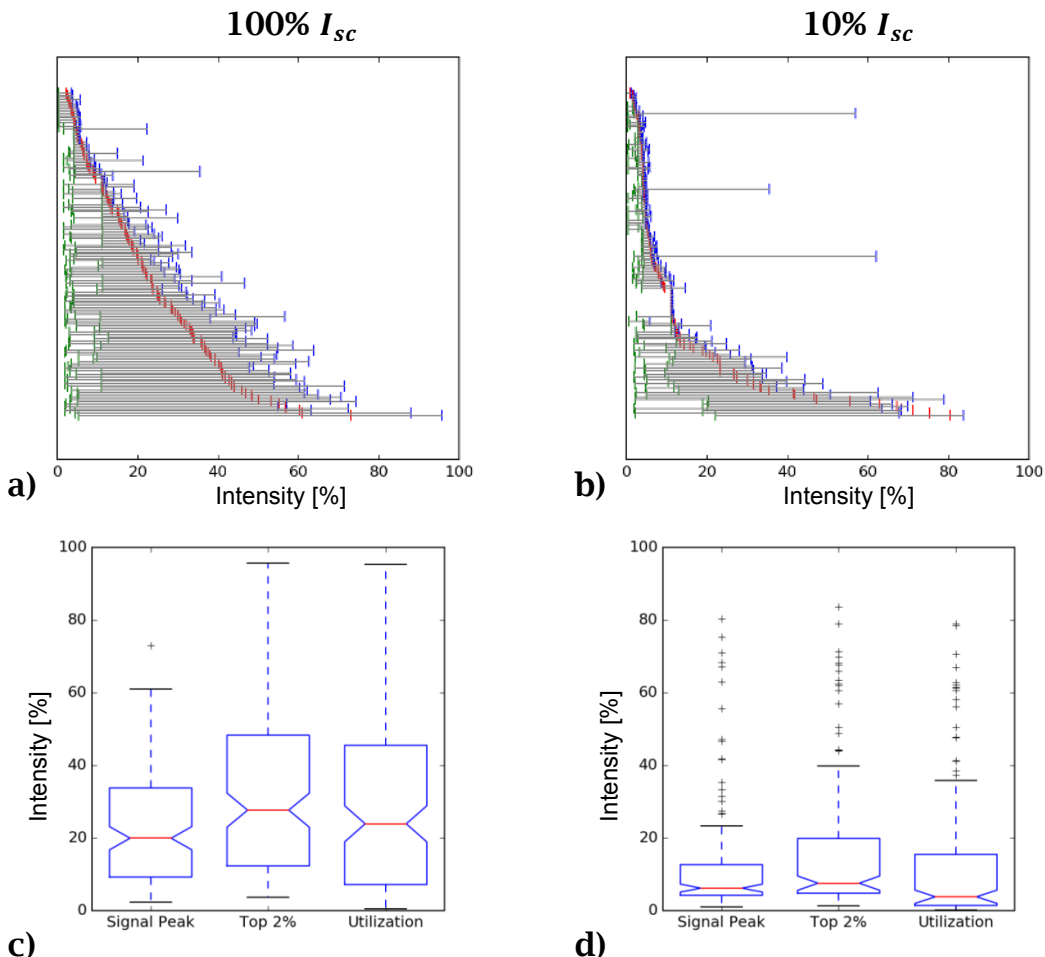


**Figure 7.32: a,b)** Levels of background and signal peaks (green, red) and the highest 2% (blue) relative to maximum image intensity [%]; **c,d)** Distribution of signal peak, highest 2% and utilization [%]

The median utilization of 20% (4%) for 100% (10%)  $I_{sc}$  EL images is lower than expected. Its effect on the signal-to-noise ratio is analysed in the following subsection. Although camera gain was not included in this evaluation, it is shown that the majority of labs did not use the full capabilities of their camera.

### 7.2.1.2 SIGNAL-TO-NOISE RATIO (SNR)

All labs were asked to submit two EL images and one background image per measurement. This had two advantages: single-time-effects could easily be removed (Section 4.1) and the noise-level-function, used to calculate the SNR could be obtained from the difference of both EL images. The used calculation and averaging scheme, named ‘NLF2,xBG’, is detailed in Section 3.2. All labs were asked to adapt gain and exposure time to achieve SNR averages greater than 25. The simplified SNR (Equation 3.16) was provided. The distribution of all individual SNR, listed for every camera system is shown in Figure 7.33. InGaAs based systems are shown separately due to their typically higher quantum efficiency within the emission waveband of EL.

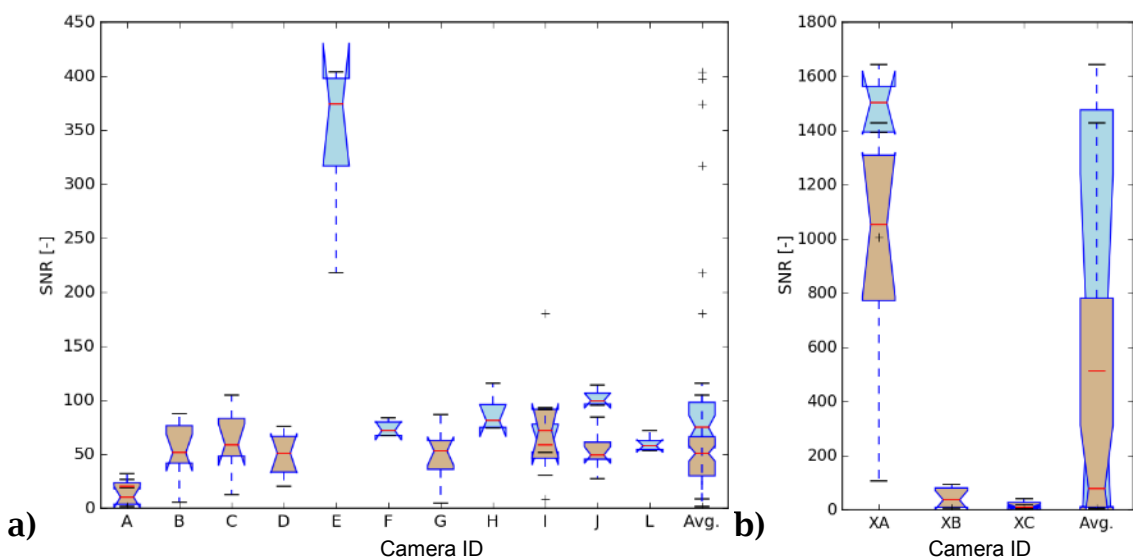


**Figure 7.33: Distribution of signal-to-noise ratios, listed for all camera systems for (a) CCD and (b) InGaAs sensors; light-blue: Cell1-5; brown: Mod1-10**

It can be seen that (excluding camera A) the majority of images exceeded the given SNR minimum. Most SNR were around 70. Far ahead of the others, camera E achieved a median SNR above 370. On average, the SNR of the one-cell mini modules (Cell1-5) had a higher SNR than module based SNR.

All labs were asked to provide the exposure time in the file name of every submitted image formatted for example ‘...\_e20-3\_...’ for an exposure time of 20.3 s. Accordingly, exposure times were extracted only from the submitted EL file names. Their distribution for EL images at 100%  $I_{sc}$  is shown in Figure 7.34.

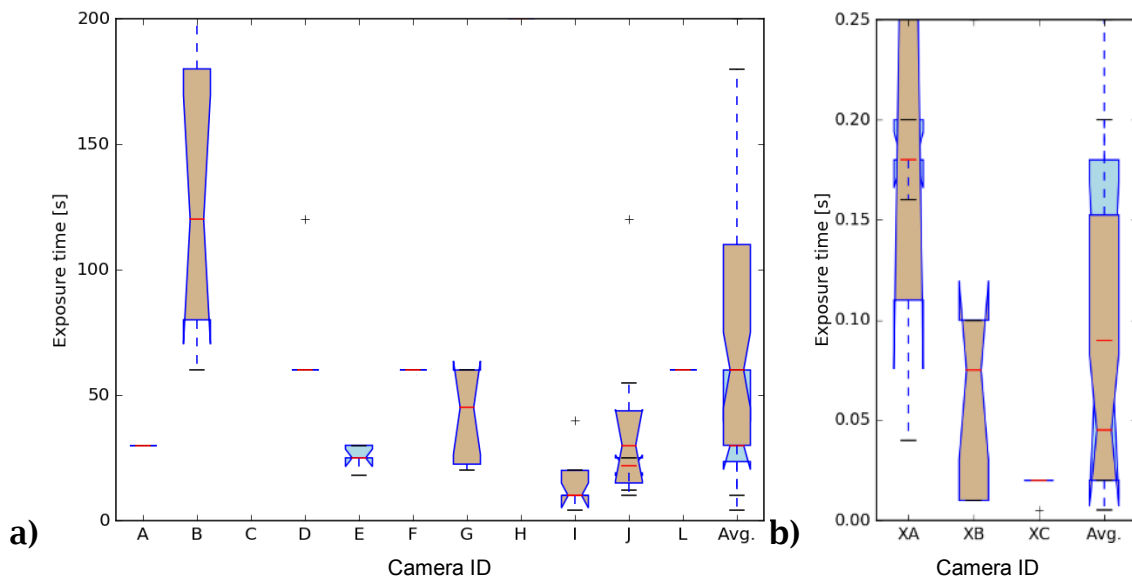


**Figure 7.34: Distribution of exposure times for EL images at 100%  $I_{sc}$ , listed for all camera systems for (a) CCD and (b) InGaAs sensors; light-blue: Cell1-5; brown: Mod1-10**

Remarkably, exposure times for CCD cameras imaging Cell1-5 (A,D,F,L) did not change. Popular times were 30, 60 and 200 s. Otherwise, exposure times were between one and two minutes, but could range up to 10 minutes. Exposure times for InGaAs cameras were generally less than one second. If listed by device, the exposure time distribution appears more homogenous (Figure 7.35).

No discrimination between the different cell-type devices is visible. For module-type devices, the comparably old monocrystalline Mod1 shows the highest spread in exposure times.

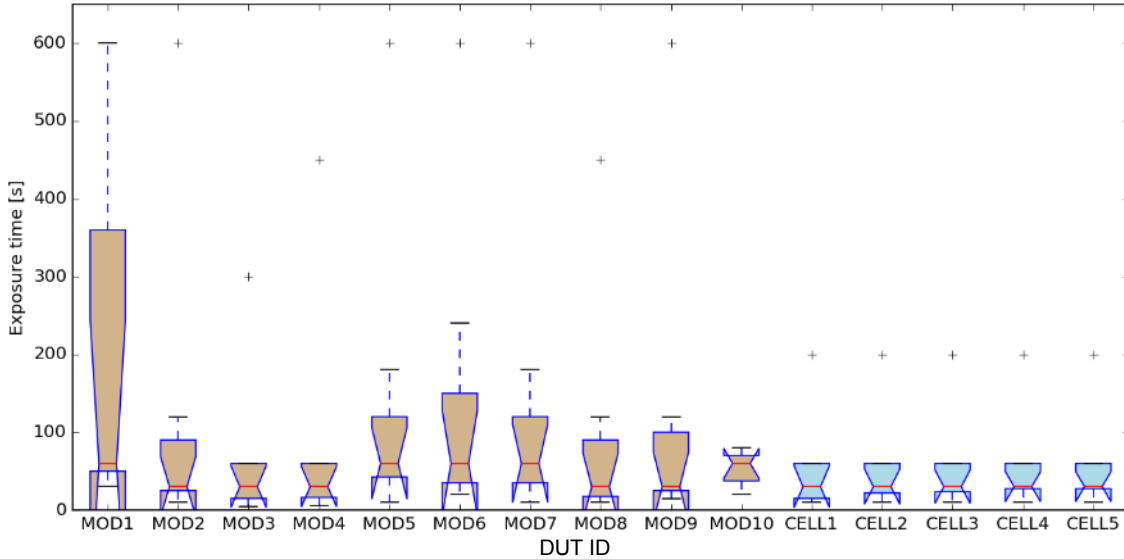


**Figure 7.35: Distribution of exposure times [s] for EL images at 100%  $I_{sc}$ , listed for all devices; only CCD systems are included**

The SNR performance can be evaluated by dividing all SNR values by their respective exposure time (Figure 7.36).

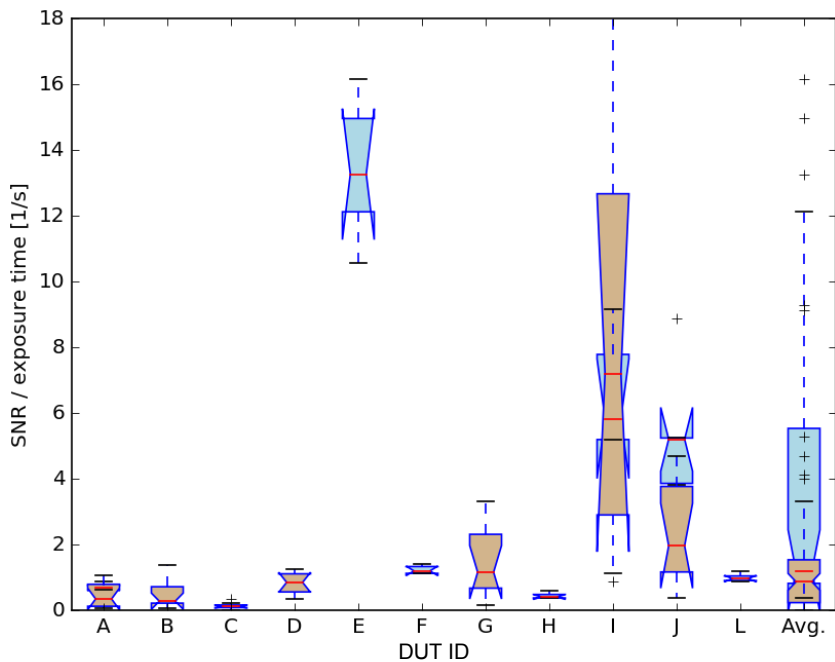


**Figure 7.36: SNR rate per second exposure time, listed for all CCD camera systems**

With an SNR rate of about  $13 \text{ s}^{-1}$ , camera E clearly leads amongst all CCD type cameras. Performance differences can be influenced by camera lens diameter, sensor quantum efficiency and cooling temperature to name just a few. Their analysis however, is out of the scope of this work.

The captured image intensity is roughly directly proportional to the applied current. In order to keep the SNR at the same level, one would expect that the exposure time of a  $10\% I_{sc}$  image would be 10 times longer than the one at  $100\% I_{sc}$ . However, Figure 7.37 gives another impression. Instead of increasing the exposure times 10 fold for the  $10\% I_{sc}$  images, exposure times were only increased twice, whereby devices with generally longer exposure times caused smaller ratios.

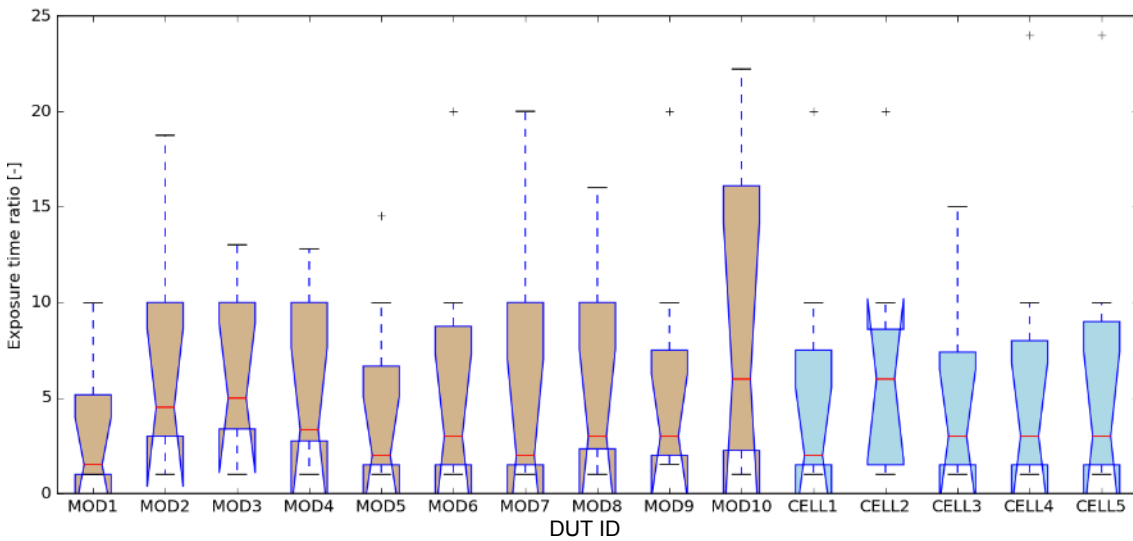


**Figure 7.37: Exposure times ratio  $\frac{10}{100}\% I_{sc}$  images [-] for all CCD cameras, listed by device**

With no further details, the origin of this phenomenon is speculative. It could be that the achievement of short measurement times takes precedence over the aim of recording high quality images. Another reason might be the opinion that  $10\% I_{sc}$  EL images do not require such a high quality. Looking at the distribution of exposure times for  $10\% I_{sc}$  images (Figure 7.38), it is apparent that half of all cameras did not change their exposure time. Most exposure times were less than 600 s (10 min) and 3000 s (50 min) were never exceeded.

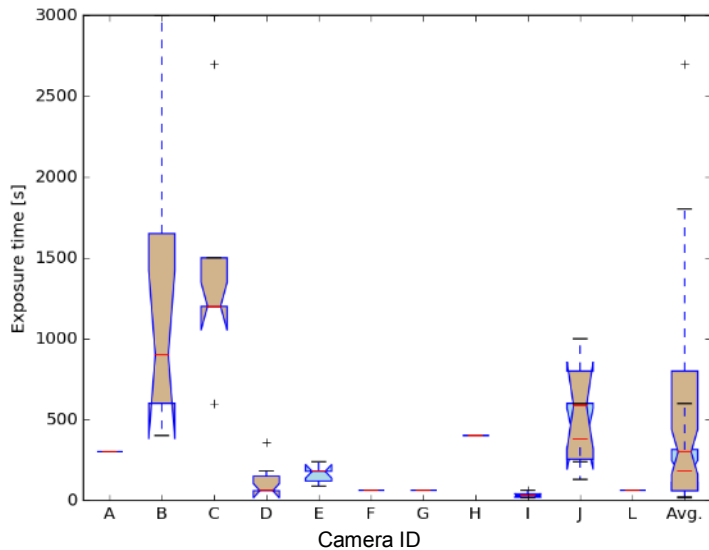


**Figure 7.38: Distribution of exposure times for EL images at 10%  $I_{sc}$  listed for all CCD camera systems**

### 7.2.1.3 SHARPNESS

Knowing the image sharpness enables evaluating whether features (like cracks) can actually be resolved with the imaging system (Section 3.4). Within the context of the Round Robin the determination of image sharpness is also required to rate every imaging system and to calculate the blur-caused part of position uncertainty.

However, labs were not asked to conduct one of the sharpness measurements methods, described in Subsection 3.4.4. To measure sharpness from an image set (Subsection 3.4.7), the sharpest image of the set must be known. To find the imaging system with sharpest images, the Tenengrad operator (Section 3.3) was applied to all corrected EL images. Although this operator is scene dependent, its results can be used for inter-lab comparison because both image content and image intensity are equivalent of the corrected EL images.

The Tenengrad, normalised to the maximum value amongst module- and cell-based imaging systems, is shown in Figure 7.39. At cell level Tenengrad is at maximum for camera A and on module level for camera B (red circle).

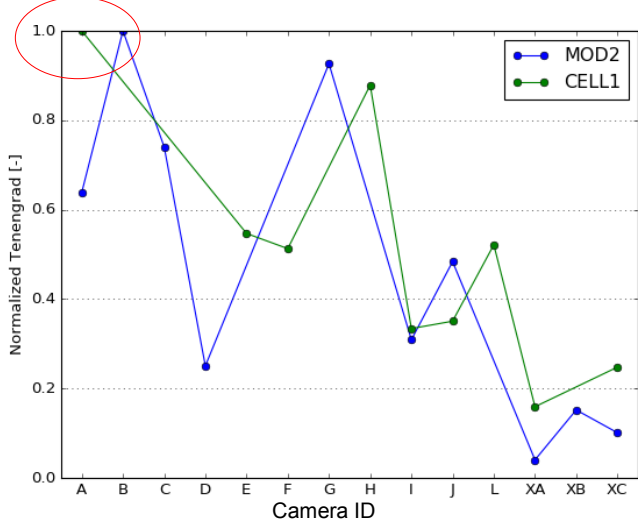


**Figure 7.39: Imaging system comparison of normalised Tenengrad for normalised images of Mod2 and Cell2; Note that lines are only to guide the eye**

After measuring this relative sharpness, the absolute image sharpness was determined. The standard deviation of an equivalent Gaussian blur kernel ( $\sigma$ , [px]) is used as sharpness parameter. For the reference cameras A and B,  $\sigma$  was estimated by measuring the edge spread (Method A, Subsection 3.4.4.2) of four edges along busbars or cell edges of Mod2 and Cell1 (Figure 7.40). These edges were not ideal since they were at the same (vertical or horizontal) angle and the EL signal varied along the edges. Therefore, a precise determination of  $\sigma$  was not possible with this method. Fortunately, when measuring  $\sigma$  using the image comparison method (Subsection 3.4.7), this calculated reference sharpness only offsets the other obtained values. Differences between individual sharpness values remain.

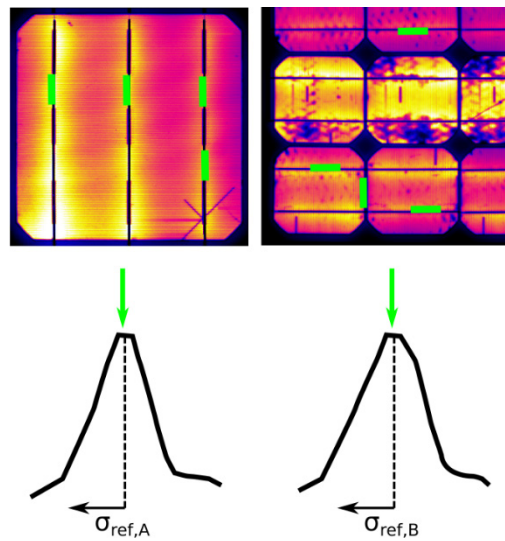


**Figure 7.40: Schematic of sharpness estimation using edge spread measurement method A (3.4.4.2) for the two sharpest camera systems A,B**

The resulting values are 1.1 px (2.3 px) for Cell1 and camera A (Mod2, camera B). The sharpness level of the corrected images of one camera varies, if the ratio between original and corrected image changes as well across all ten modules and five cells. This scale is described by the resolution factor ( $f_{res}$ ). It characterizes the ratio of pixel length and width ( $w_o, h_o$ ) of the DUT within the original image to the resolution of the corrected image ( $w_n, h_n$ ):

$$f_{res} = \sqrt{\frac{w_n \cdot h_n}{w_o \cdot h_o}} \quad (7.7)$$

$f_{res}$  varies between 0.4 and 1, as shown for cameras A and B (Figure 7.41). From  $\sigma_{ref}$  relative to  $f_{res}$ , measured image sharpness of one corrected EL image can be transformed to the other images of a camera system (Table 7.13).

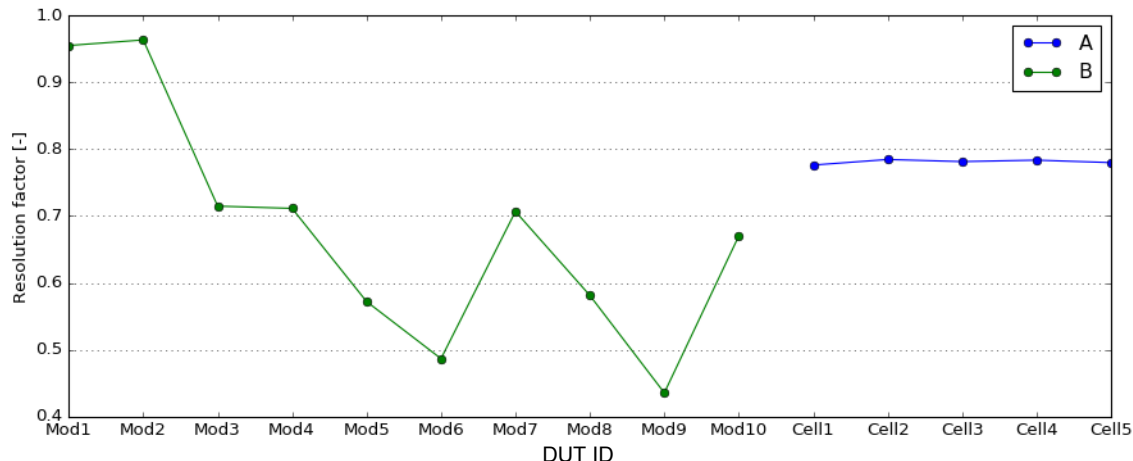


**Figure 7.41: Resolution factor ( $f_{res}$ ) between original and corrected (rescaled) EL images for cameras A and B across all devices**

**Table 7.13: Reference sharpness ( $\sigma_{ref}$  [px])**

Camera B										Camera A				
Mod1	Mod2	Mod3	Mod4	Mod5	Mod6	Mod7	Mod8	Mod9	Mod10	Cell1	Cell2	Cell3	Cell4	Cell5
2.2	2.3	1.7	1.7	1.3	1.1	1.7	1.4	1.0	1.6	1.1	1.1	1.1	1.1	1.1

$\sigma_{ref}$  enables the calculation of sharpness of corrected images from other camera systems using the method described in Subsection 3.4.7. The values obtained are however based on the sharpness of the corrected EL images ( $\sigma_n$ ) and not the imaging system ( $\sigma_o$ ). The imaging system sharpness is obtained from the median of all  $\sigma_{n,i}$  divided by their device specific  $f_{res}$  (Figure 7.42):

$$\sigma_o = \text{median}\left(\frac{\sigma_{n,i}}{f_{res}}\right) \quad (7.8)$$

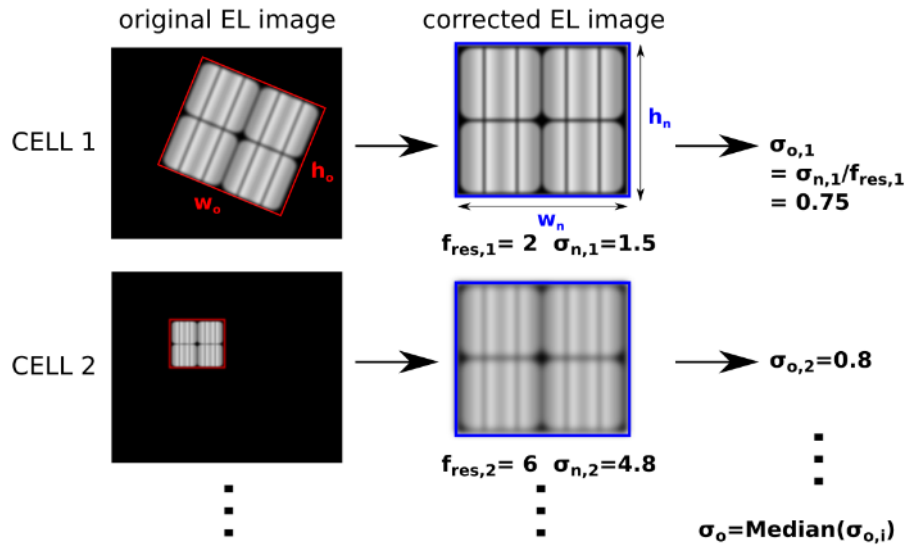


**Figure 7.42: Schematic to obtain imaging system sharpness from image sharpness ( $\sigma_n$ ) and resolution factor ( $f_{res}$ )**

Figure 7.43 shows a sharpness comparison using the example of Mod2 for ten different camera systems (A-XC).

The first row shows the top left corner of Mod2 of the corrected images. To visualize the influence of different resolution factors, row two shows the same area but at the same resolution as in the original image. Row 3 plots the corrected image sharpness and the last row the imaging system sharpness (Equation 7.8).

With a corrected image sharpness  $\sigma_n > 14$  the images with highest blur belong to camera XA. However, noting their low resolution, their imaging system sharpness is actually highest. Amongst all CCD camera based imaging systems lab C, I and A produced the sharpest images.

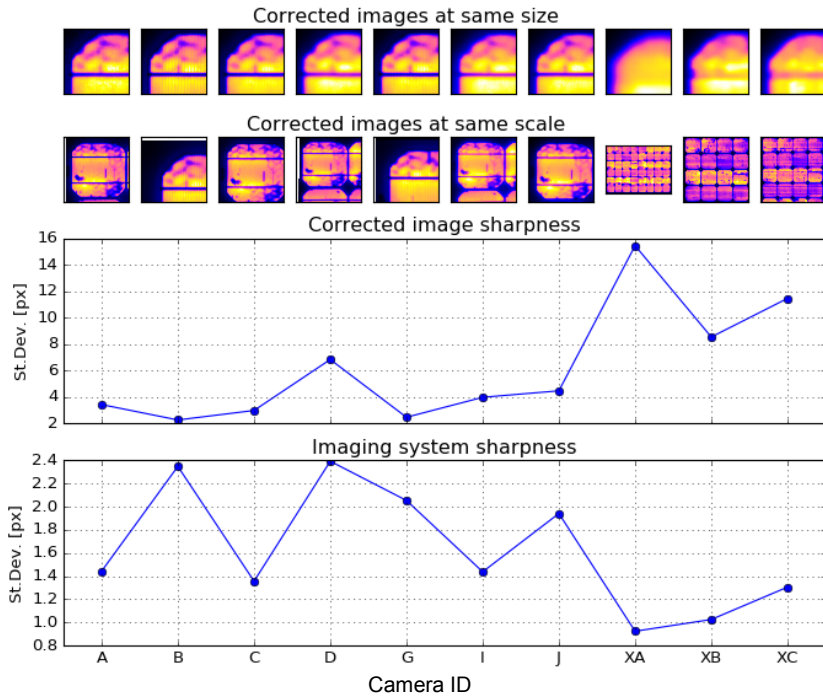


**Figure 7.43: Sharpness comparison for all module-scale imaging systems modules for Mod2; note that values are discrete and lines are to guide the eye**

The same evaluation on cell-scale is shown in Figure 7.44. Therein again lab XA had the sharpest images amongst the InGaAs systems. For CCD-based systems, camera L, A and I produced sharpest results.

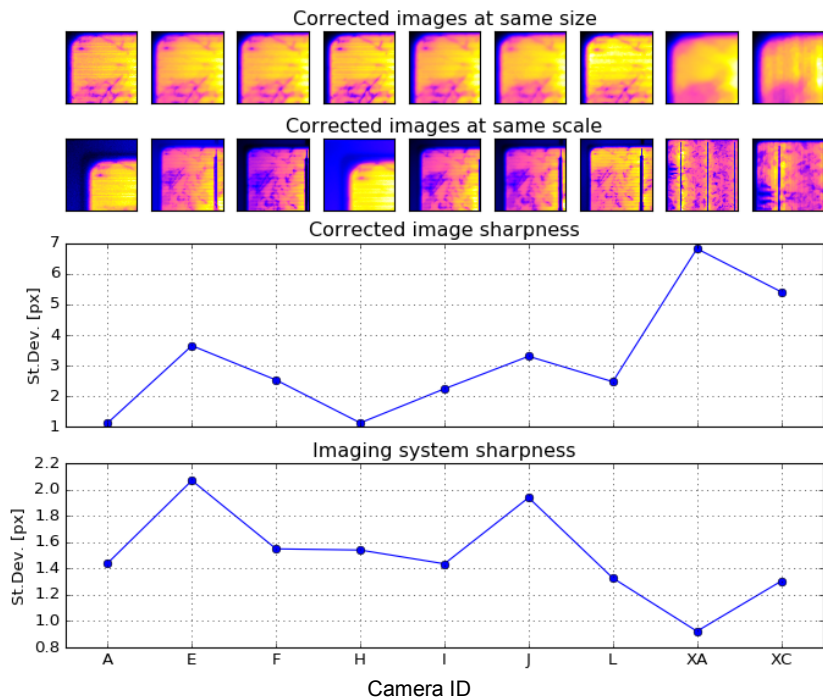


**Figure 7.44: Sharpness comparison for all cell-scale imaging systems modules for Cell2**

#### 7.2.1.4 OBJECT-TO-IMAGE RATIO

The minimum resolvable object size ( $s_{obj}$ ) directly depends on the camera resolution and sharpness but also the size of the imaged object relative to the image plane. This named object-to-image ratio ( $r_{obj}$ ) describes the ratio of the object area as an irregular quadrilateral ( $A_{quad}$ ) vs image resolution ( $s_x, s_y$ ).  $A_{quad}$  can be calculated using by the four clockwise ordered corner points ( $p_0 \dots p_3$ ) using the Shoelace formula:

$$A_{quad} = 0.5 |(p_{2,x} - p_{0,x})(p_{3,y} - p_{1,y}) + (p_{3,x} - p_{1,x})(p_{0,y} - p_{2,y})| \quad (7.9)$$

$$r_{obj} = \frac{A_{quad}}{s_x \cdot s_y} \quad (7.10)$$

The object corner positions were detected in all 100%  $I_{sc}$  images using the algorithm described in Subsection 4.7.1.1. Figure 7.45 shows the distribution of resulting ratios sorted by camera systems. Looking at the narrow distribution, it becomes clear that camera E, F, H and L only imaged Cell1-Cell5. The otherwise wide spread values and low medians indicate that the camera focus was kept constant for all other devices. The majority of labs only used 50% of their cameras pixels to capture the EL signal. At cell-scale and with a median ratio higher than 90%, camera E achieved the best  $r_{obj}$ . For modules, camera H leads with 65%.

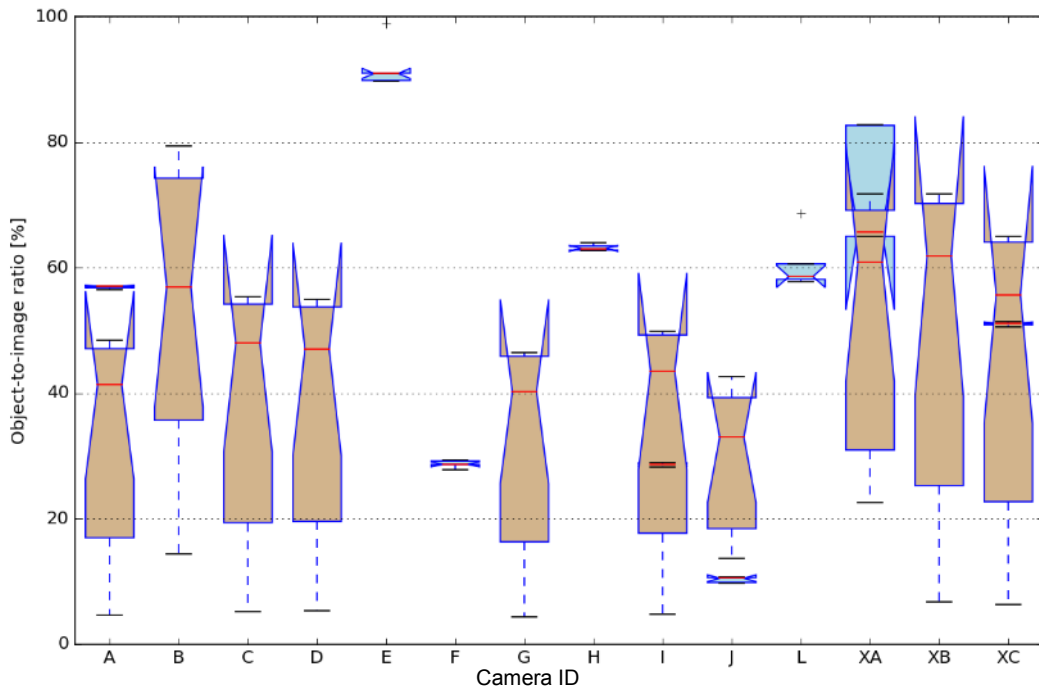
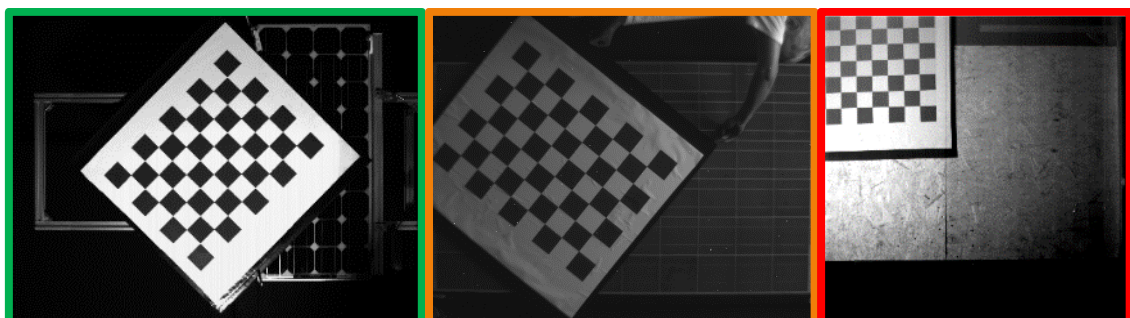


**Figure 7.45: Comparison of object-to-image ratios sorted by camera systems; light-blue: Cell1-5; brown: Mod1-10**

## 7.2.2 CALIBRATION IMAGE ANALYSIS

### 7.2.2.1 LENS DISTORTION

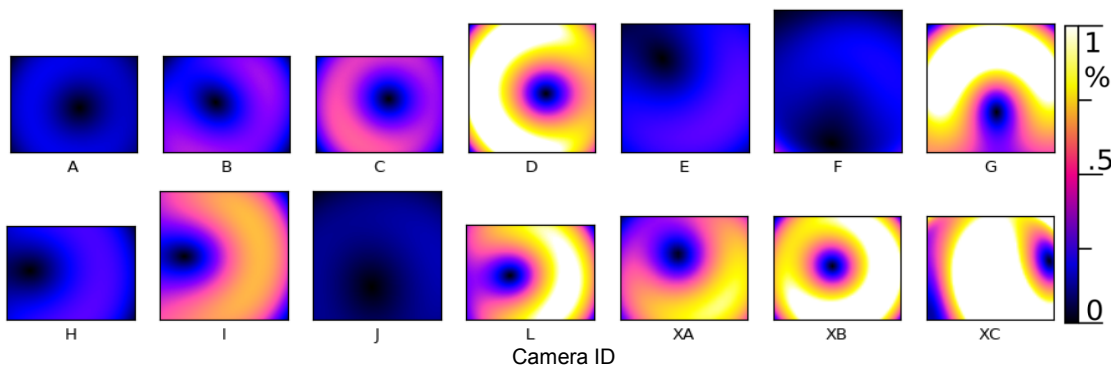
Each lab was given the task to take a minimum of 15 images either of an A1 or A5 chessboard pattern (Figure 7.46) in image plane. In every image, the pattern position and rotation were to be changed slightly. The routine to measure and remove camera lens distortion from these images is described in Section 3.5 and 4.6.



**Figure 7.46: Selection of submitted lens calibration images; green: valid image; orange: chessboard detection might fail; red: chessboard detection will fail because not all squares are visible**

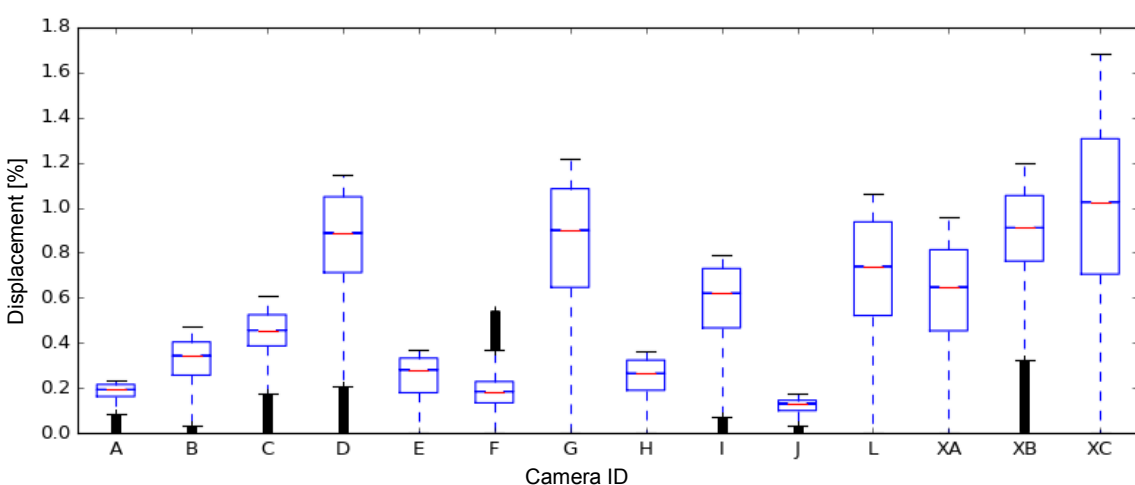
From the lens distortion parameters obtained, the pixel displacement can be calculated with Equation (3.51)-(3.54). The displacement magnitude in x and y-axes is shown in

Figure 7.47. With magnitudes around 0-1.5%, no camera systems have a distortion, which is easily noticeable by the human eye. However, for a resolution of 4000x4000 pixels this distortion can shift features, like busbars up to 60 pixels along its extent. Correction for lens distortion is therefore advisable.



**Figure 7.47: Magnitude pixel displacement, relative to average image size and scaled 0-1%**

Looking at the displacement distribution (Figure 7.48) it is shown that camera J,A,F have the lowest and camera XC,G and D have the highest distortion.



**Figure 7.48: Magnitude displacement distribution sorted by imaging system**

The calculation of both, deflection from lens distortion and re-projection error is described in Subsection 6.2.4 and 6.2.2. An uncertainty, based on these two factors is shown in Figure 7.49. All the camera systems have a position uncertainty far less than 1%. Its homogenous distribution is due to the major influence of the re-projection error. Due to its low values, the uncertainty from lens deflection and re-projection will be neglected for the uncertainty maps calculation.

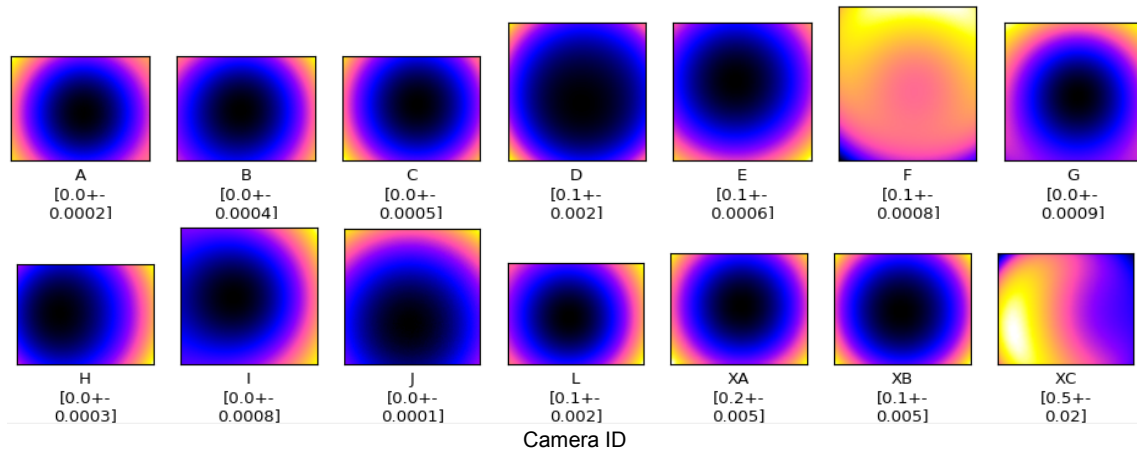


**Figure 7.49: Position uncertainty  $\sigma_{\text{Lens}}$  [%], relative to the image size**

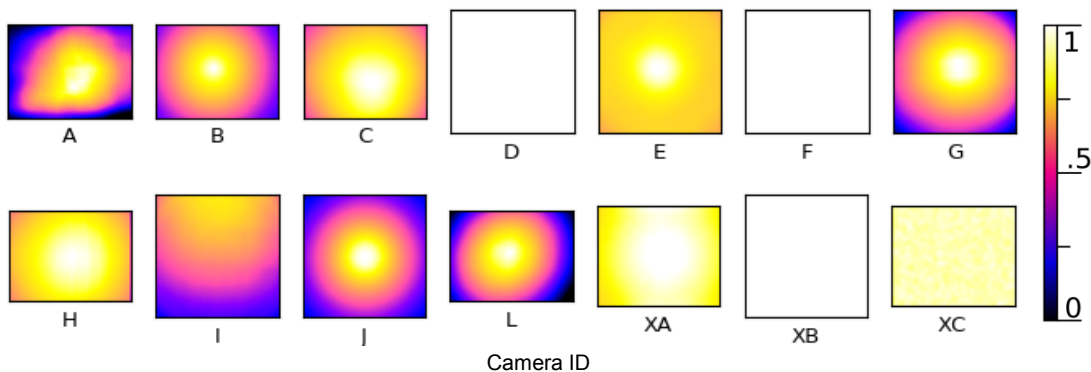
### 7.2.2.2 FLAT FIELD

Of all the submissions, camera XB did not include flat field images and camera D and F delivered heavily overexposed images, which could not be used for flat field correction. Their flat field map was uniformly set to one. For all the other cameras, the flat field was calculated from multiple images of a homogenous red light source, placed directly in front of the camera lens (Subsection 3.6.2.1). Several labs did not deliver dark current images of the same exposure time. In this case, the background level was set to 1% of the cumulative distribution function of the raw flat field image intensities. The results are shown in

Figure 7.50. In comparison to CCD, InGaAs cameras (XA, XB, XC) appear to be less influenced by vignetting. It is assumed that the firmware of those InGaAs cameras already implemented a flat field correction. All the

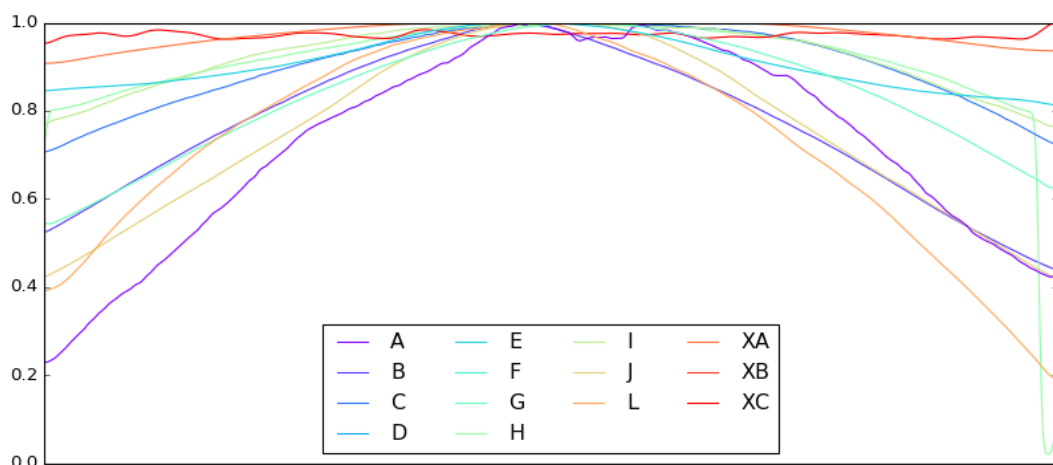
submitted images from camera I show the same vertical gradient as the averaged flat field image in

Figure 7.50. It is assumed that for camera I the flat field measurement itself was executed incorrectly – possibly due to a gap between the imaged light source and the camera lens. Only a few suitable images were submitted by camera A. The resulting flat field map caused a flat field overcorrection to such an extent that flat field correction was omitted for camera A.



**Figure 7.50: Calculated flat field maps**

Figure 7.51 shows line plots taken from the horizontal centre of the vignetting maps. It can be seen that flat field between image centre and edge varies between 0-80%. Camera A especially shows an inhomogeneous trend. This is due to the small number of submitted images and the (probably) missing movement of the light source.



**Figure 7.51: Line plots of the horizontal middle of all flat field maps shown in Figure 7.50**

### 7.2.3 IMAGE COMPARISON

In order to compare EL images of the same DUT (imaged by different cameras) quantitatively, the following correction algorithm (Figure 7.52) was implemented:

1. Remove single-time-effects, dark current, flat field, image artefacts and lens distortion as described in Chapter 4.
2. For all images from camera I, execute grid detection and rectification (Subsection 4.7.1)
3. The resulting rectified images were used as reference image for step 4.
4. Detect common features and calculate homography matrix used to rectify image (Subsection 4.7.2)
5. Improve rectification using sub-pixel alignment (Section 4.8) and normalize intensity level of all rectified images of the same DUT (Section 4.9)
6. Define reference images (camera B for Mod1-Mod10 and camera A for Cell1-Cell5) with measured image sharpness.
  - a. Match the sharpness level of the reference image to every other image of the same DUT (Subsection 3.4.7).
  - b. Create a difference image to that reference image.
  - c. Mask cell edges and busbars using DUT mask obtained from grid detection (step 3).
7. Calculate an intensity uncertainty map (Subsection 6.1.4.3) from original images and rectify the result (step 4).
8. Use the rectified intensity uncertainty image to calculate the position uncertainty (Subsection 6.2.10).

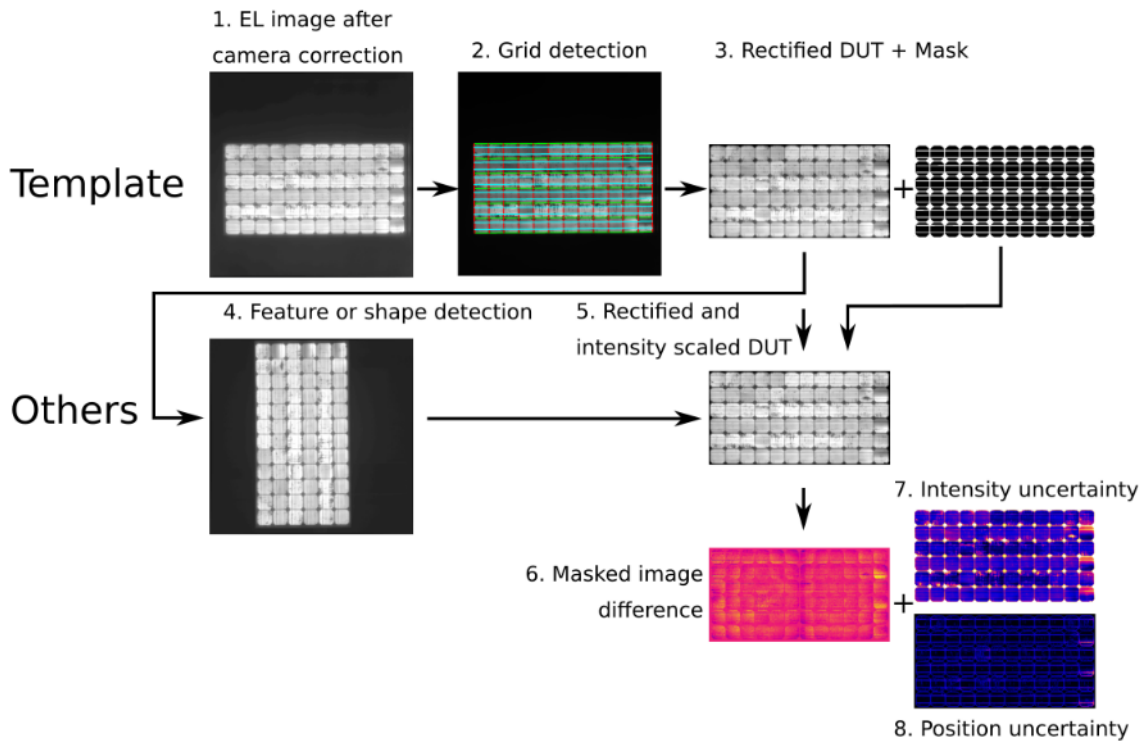
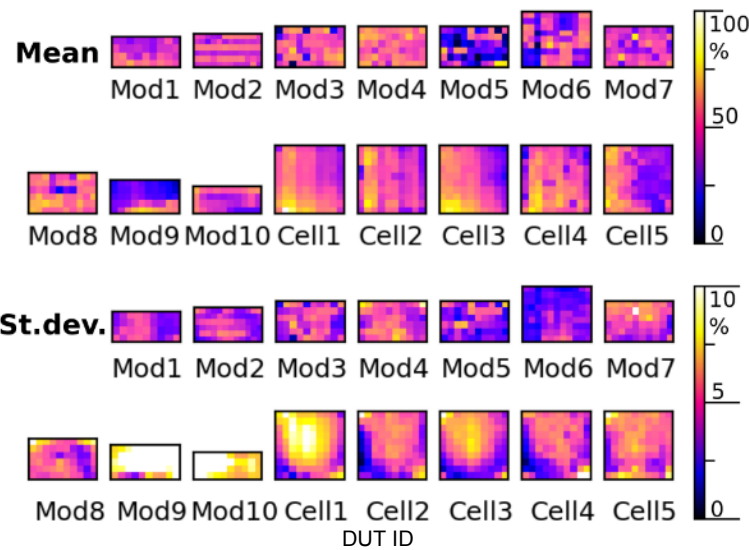


**Figure 7.52: Image correction schematic applied to all the images in the EL Round Robin**

A comparison of all the corrected EL images together with difference image and uncertainty maps can be found in Appendix 4.2.

### 7.2.3.1 CELL INTENSITIES

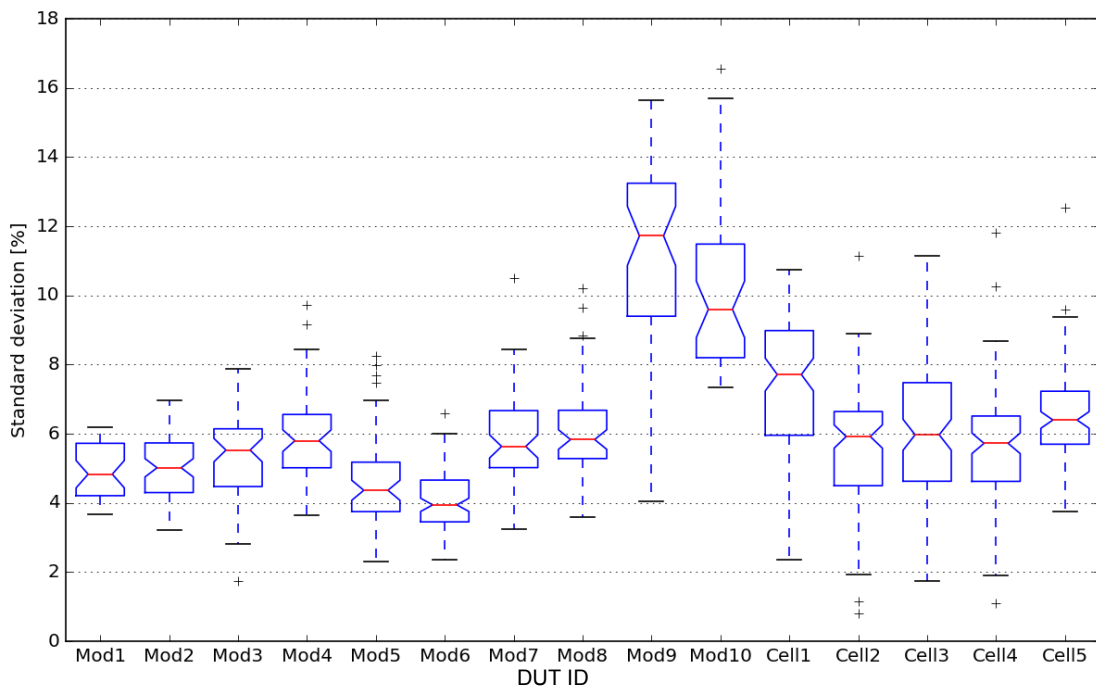
Before focusing on the illustration quality of features (like cracks and broken fingers), the intensity deviations of averaged areas in EL images need to be analysed. For this, average cell intensity was calculated for all crystalline devices Mod1-Mod8. All other DUT were averaged regarding squares of 10% DUT width. The average intensities and standard deviations across all analysed imaging systems are shown in Figure 7.53. The standard deviation maps of Cell1-Cell4 show a similar pattern of highest deviations in the image centre. In addition, Mod9 and Mod10 appear to have the highest deviations across all DUTs.



**Figure 7.53: Mean and standard deviation of all DUT for all camera systems, averaged by cell, respective 10% image width**

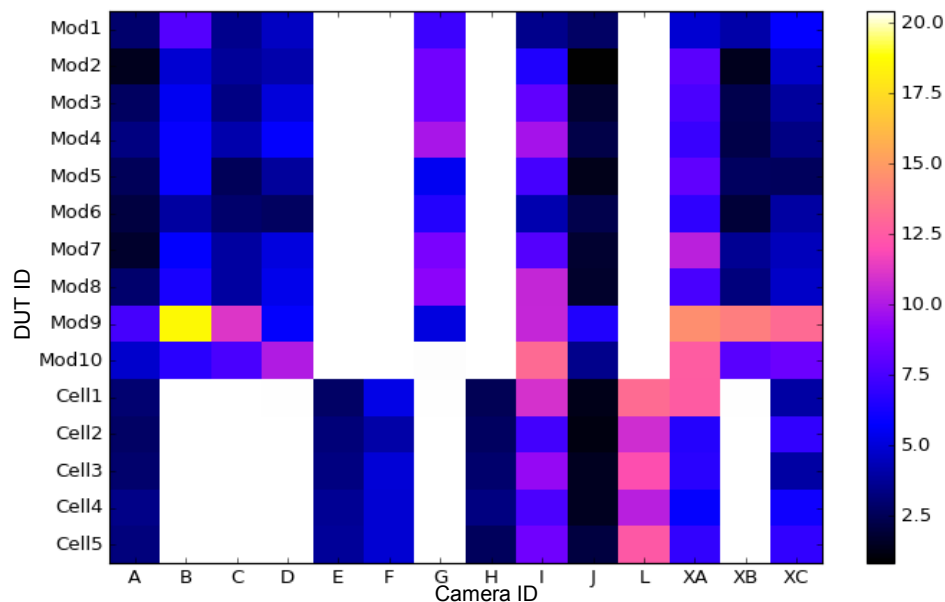
A clearer representation of the range of DUT specific standard deviations is shown in

Figure 7.54. With median values around 10% and 12%, the thin-film Mod9 and Mod10 again show the highest deviations across the different camera systems.



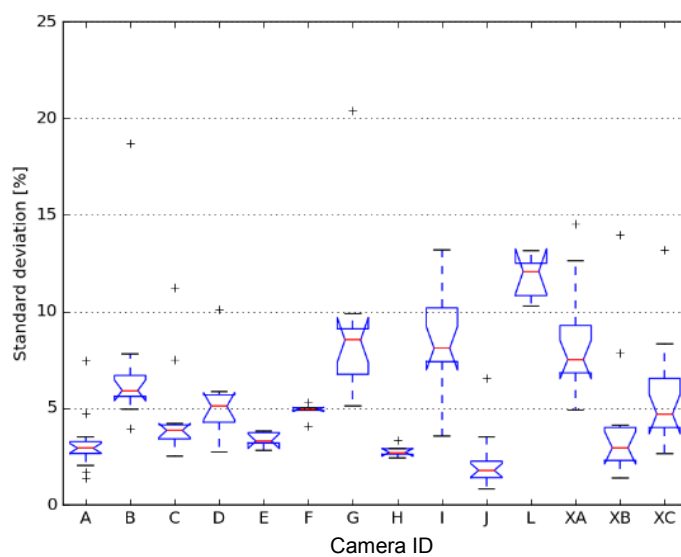
**Figure 7.54: Boxplots of DUT specific standard deviations shown in Figure 7.53**

All the other module-size DUTs deviated by 4-6% followed by the cell sized DUT with values around 6-8%. Using the mean cell intensities in Figure 7.53, a camera and DUT specific standard deviation was calculated (Figure 7.55).



**Figure 7.55: Relative difference [%] between averaged cell intensities imaged by a specific camera to the camera independent average, shown in Figure 7.53**

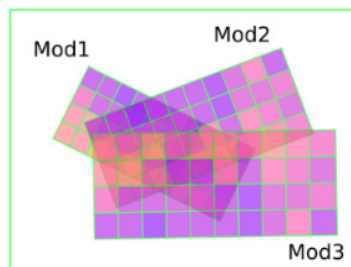
Boxplots generated from this data reveal the camera systems with the smallest and highest deviations, relative to mean (Figure 7.56).



**Figure 7.56: Boxplots of the distribution of standard deviations of averaged cell intensities for all camera systems**

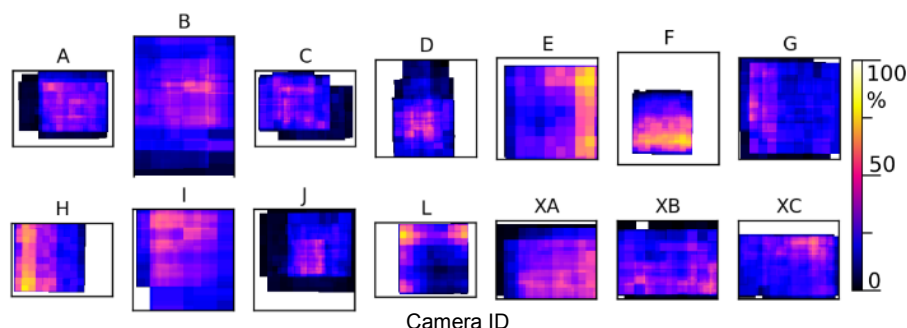
With standard deviations below 4% it is apparent that the average image intensities captured with camera J, H and A are closest to the mean DUT intensities. Their intensity differences agree to the estimated signal uncertainty of  $\sim 3.4\%$  (Subsection 6.1.4). On the other side, camera L,G and I deviate most from the average.

Figure 7.53 encourages the suspicion that part of EL intensity deviations is not due to changed EL signal but rather due to residual flat field distortion from under- or overcorrected vignetting. In order to investigate this theory, for every camera the average DUT intensity grid from the corrected EL image was transformed to the original position of the raw image (Figure 7.57).



**Figure 7.57: Schematic of transforming cell averages of all DUT to their original position in the raw image**

It is assumed that the temporal average of all DUT cell averages cancels out individual cell deviations, similarly to the approach used to extract flat field from a series of images of different devices (Subsection 3.6.2.3). As Figure 7.58 shows, residual vignetting effects can be made visible for the majority of the camera systems, especially for camera E, F and L.



**Figure 7.58: Average of all normalised cell intensities after transformation to the original position in the raw image**

### 7.2.3.2 IMAGE UNCERTAINTY

Figure 7.59 shows an example comparison of corrected EL images and their corresponding uncertainty maps of one cell in Mod3. Images from all the other devices can be found in Appendix 4.2. Due to the erroneous flat field correction (Subsection 7.2.3.1), the correction uncertainty ( $U_{corr}$ ) was set 7%. For improved visibility, intensity uncertainty ( $U_{Noise}$ ) is shown as black-to-red colour layer. Its values are scaled 0-25%. Since EL signal and correction uncertainty were defined as constant throughout the image it is omitted in the displayed uncertainty image. Position-based uncertainty is shown as a black-to-green- colour layer, its values are scaled 0-100%.

The EL uncertainty changes with the area size of the averaged pixels. The uncertainty of one pixel, a 40x40 pixels sized group and a cell average (400x400 pixel) is shown in Subfigure (b). Although pixel intensities deviate between the different analysed camera systems, all the intensities are within a range limited by their individual uncertainty.

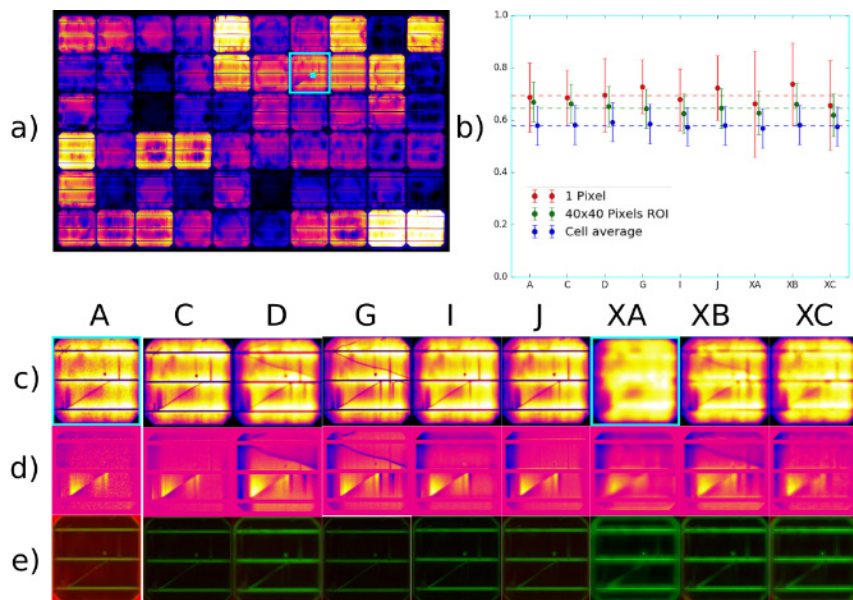


**Figure 7.59:** EL image comparison of Mod3 at 100%  $I_{sc}$  ;  
 a) corrected EL image of camera B; b) Pixel values of single pixel or  
 pixel groups, indicated by blue ROIs in (a);  
 c) corrected EL image detail of blue ROI in (a); d) sharpness corrected  
 difference image to (a); e) combined noise (red) and position (green)  
 uncertainty map of (c)

### 7.2.3.3 FEATURE VISIBILITY

All the corrected EL images for both 10% and 100%  $I_{sc}$  are shown in Appendix 4.2. In this section, only several remarkable differences of the representation of features within the different EL images are discussed. In general, after image correction the appearance of features is a function of:

1. The local noise level
2. Image sharpness
3. Residual vignetting effects
4. The cameras spectral response and
5. Actual changes of the EL signal.

As already discussed in Subsection 7.2.1.2, most images achieved an SNR above 25. The pixel-based image noise was on average less than 4% and can be neglected. To quantify individual changes, the difference images to the reference camera A (for cells) or B (for modules) were calculated. In order to remove the influence of different image sharpness levels, all the reference images were brought to the same sharpness level as the target image (Subsection 7.2.1.3). Residual vignetting effects were found to be a major influence of different intensities (Subsection 7.2.3.1). To reduce this effect in difference images, residual vignetting effects are removed as follows:

- For Cell-Cell5 and Mod9,Mod10: calculate and remove pseudo-background (similar to method in Subsection 7.1.3)
- For Mod1-Mod8 (crystalline modules): divide pixel value of every cell by its cell median.

After these corrections the difference image should only be influenced by EL signal changes and the cameras spectral response. As already mentioned, all the imaging systems were assigned a random letter in order to maintain their anonymity. Therefore difference images shown are not necessarily in chronological order and extrinsic defects, introduced during lab-to-lab transport, cannot be analysed. An example,

based on Mod1, is shown in Figure 7.60. Further examples, together with uncertainty maps are shown in Appendix 4.2.

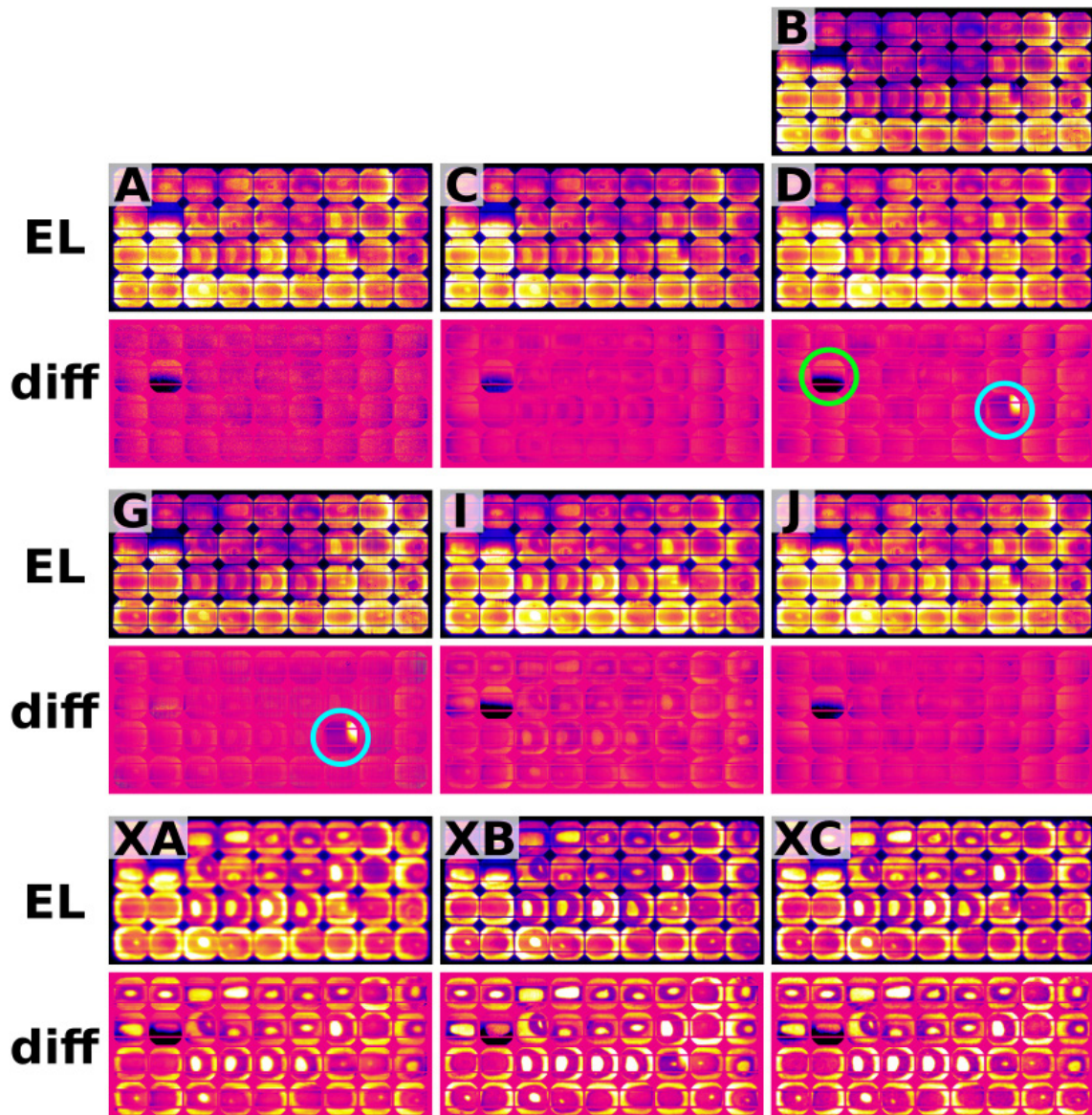


**Figure 7.60: Comparison of EL images ( $100\% I_{sc}$ ) and their (sharpness and flat field) corrected magnitude differences to the top EL image (B)**

Differences between relatively sharp and blurry images ('B' vs 'XC') can be analysed without disturbing high gradient variations due to the sharpness correction (Subsection 3.4.1). In Figure 7.60, the following EL signal changes can be observed:

- Temporary reconnection along the right end of the top busbar in 'D' and 'G' (blue circle).

- Intensity deviations in cell {2,2} (green circle) due to high contact resistance of top busbar.
- ‘Doughnut’-shaped darkenings in most cell centres are more pronounced in InGaAs camera images (XA-XC). It is assumed that these areas occur darker due to spatially limited relaxation of the encapsulation.

In the following qualitative comparison, image sharpness will be evaluated by the ‘smallest resolvable object size’ ( $s_{obj}$ ) as defined in Equation 3.31. This equation is adapted to the known parameters: physical cell width ( $w_{cell}$ ), cell resolution in x-axis ( $r_{cell}$ ) and standard deviation of Gaussian image blur kernel ( $\sigma_G$ ). The calculation of the resolution factor ( $f_{res}$ ) as function of  $\sigma_G$  is described in Equation 3.43. For example camera A and Mod1,  $s_{obj}$  is calculated as follows:

$$s_{obj} = \frac{w_{cell}}{r_{cell}} \cdot f_{res}(\sigma_G) = \frac{125 \text{ mm}}{400 \text{ px}} \cdot f_{res}(2.8 \text{ px}) = 1.51 \text{ mm} \quad (7.11)$$

The following comparison is structured as follows: A figure showing a DUT and a region of interest (cells, for crystalline DUT) as imaged by all different cameras. The following table evaluates the visibility of DUT features, like busbars or non-disconnecting cracks. For every camera and feature, a number (0-2) is assigned in the following Tables 7.14 et seqq.

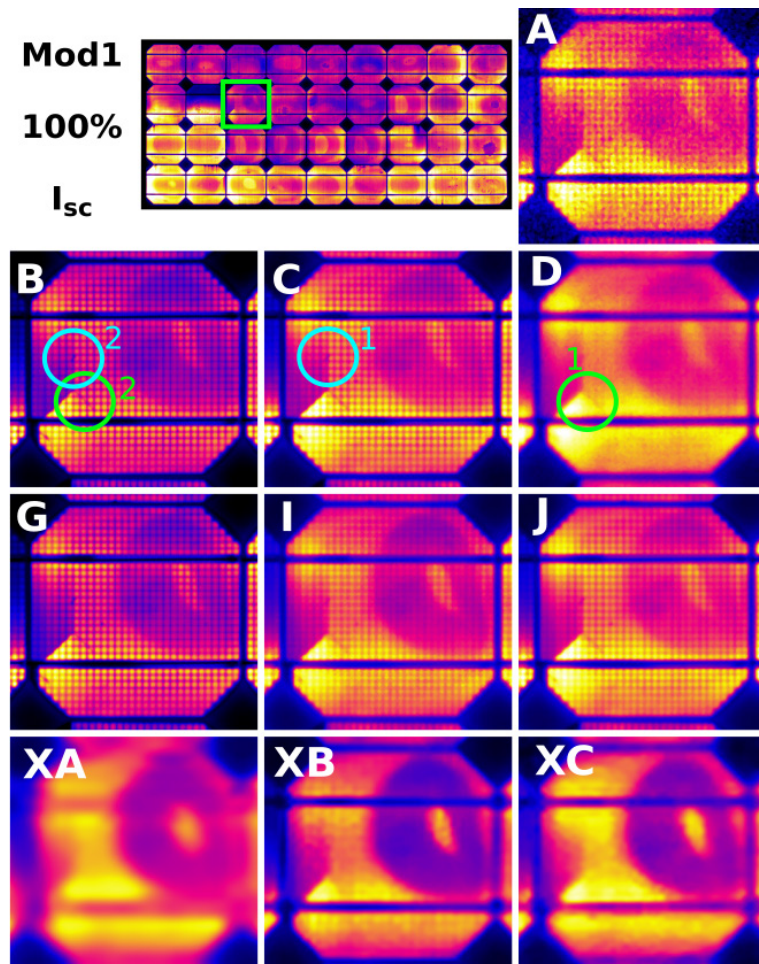
The numbers stand for:

- 0 – Feature not visible
- 1 – Feature ‘poorly’ visible
- 2 – Feature ‘good’ visible

The differentiation between a ‘good’ and ‘poorly’ visible feature is highly subjective. Therefore, for both an example is highlighted in each figure (green/blue circles). A scatter plot finally compares visibility to  $s_{obj}$  with the aim of assigning a minimum  $s_{obj}$  for each feature for every device type (crystalline module, amorphous module, crystalline cell). In this section

only four DUTs at a specific short-circuit current are discussed. All the other images can be found in Appendix 4.2.

A comparison of cell {3,2} from Mod1 is shown in Figure 7.61. In a blue circle, a suspected intrinsic defect is highlighted. Whilst this defect is comparably ‘good: 2’ visible for camera B, camera C shows a ‘poor: 1’ visibility and especially cameras D and XA-XC do not show the feature at all. In the same way, a non-disconnecting crack is highlighted with a green circle.



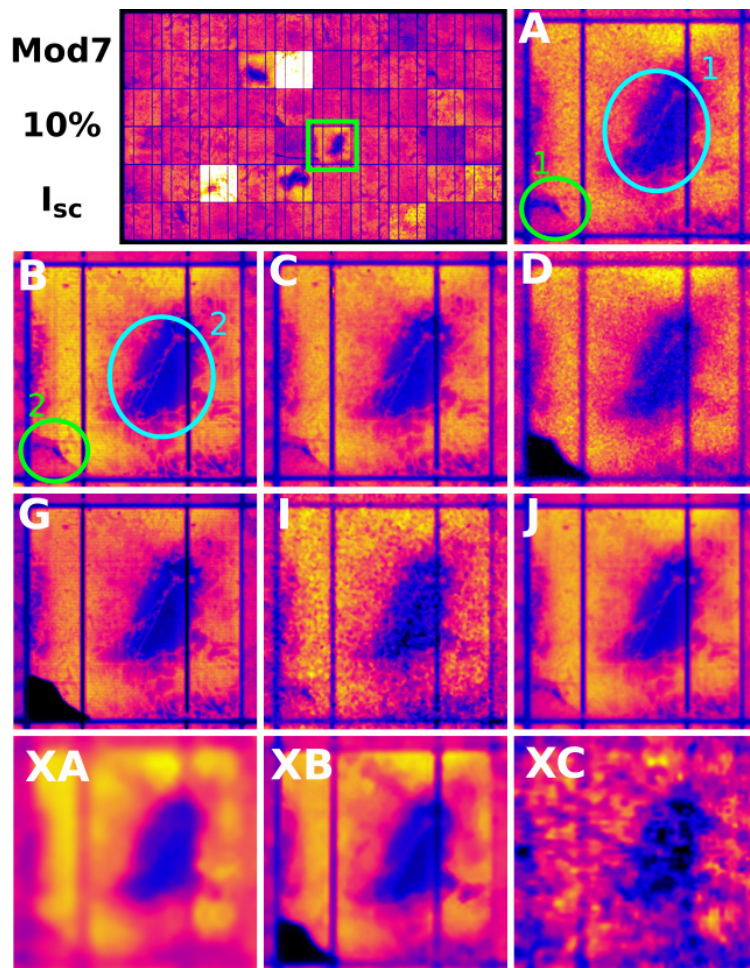
**Figure 7.61: Mod1 imaged at 100%  $I_{sc}$ ; resulting corrected EL images for different cameras shown for cell {3,2}**

Table 7.14 lists the visibility of the two features mentioned together with the visibility of busbars and fingers. On the left side the signal-to-noise ratio (SNR) averaged for the same area is shown. Image noise is clearly visible for camera A (SNR~5).

**Table 7.14: Visibility of different features in cell {3,2} of Mod1**

Cam. ID	SNR [-]	$s_{obj}$ [mm]	Busbar	Finger	Intrinsic defect (blue)	Non-disc. crack (green)
A	5.17	1.51	2	1	0	1
B	45.13	0.98	2	2	2	2
C	32.30	1.17	2	2	1	1
D	17.48	2.88	2	0	0	1
G	45.54	0.73	2	2	2	1
I	39.27	3.11	2	2	1	1
J	33.89	1.90	2	2	1	1
XA	778.91	9.50	1	0	0	0
XB	16.45	2.74	2	0	0	1
XC	22.01	6.88	1	0	0	0

In the same way, Figure 7.62 shows a comparison of different corrected EL images for cell {6,4} of Mod7, imaged at 10%  $I_{sc}$ . A line shaped structure in the middle of a darker cell is highlighted with a blue circle as representative for an intrinsic defect. The images taken by camera D, G and XB show an inactive area at the bottom right of the cell. The crack that caused this electrical isolation can also be found in the other images (green circle). Although at 10%  $I_{sc}$  EL emission is roughly 10% relative to a 100%  $I_{sc}$  image, in most cases the exposure time was only doubled (Subsection 7.2.1.2). As seen for cameras I, D, A and XC the low SNR value impaired feature visibility. Again, Table 7.15 evaluates the visibility of four different features of the highlighted cell.



**Figure 7.62: Mod7 imaged at 10%  $I_{sc}$ ; resulting corrected EL images for different cameras shown for cell {6,4}**

**Table 7.15: Visibility of different features in cell {6,4} of Mod7**

Cam. ID	SNR [-]	$s_{obj}$ [mm]	Busbar	Finger	Intrinsic defect (blue)	Non-disc. crack (green)
A	6.15	1.93	2	0	1	1
B	42.13	0.90	2	2	2	2
C	15.42	1.50	2	1	2	2
D	6.03	3.72	1	0	1	-
G	17.26	0.93	2	2	2	-
I	6.16	3.08	1	0	1	0
J	36.12	2.43	2	1	2	1
XA	1093.53	9.40	1	0	0	0
XB	78.68	5.11	1	0	0	-
XC	2.46	6.90	0	0	0	0

A representative for instable EL signal (due to cracks) is shown in Figure 7.63. Therein, different series resistance along several fingers caused the

EL signal to vary (dark: camera B, bright: camera A). The visibility of these disconnecting fingers (blue ellipse) is evaluated in Table 7.16. The branch of a larger disconnecting crack was selected as being representative of a non-disconnecting crack (green circle).

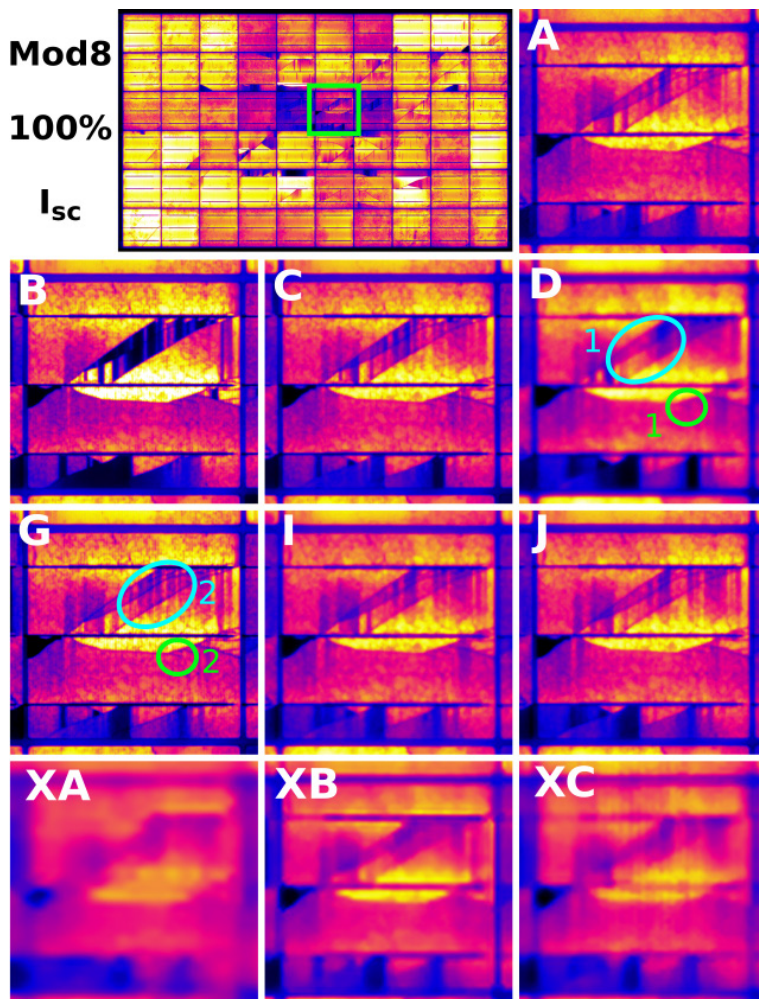
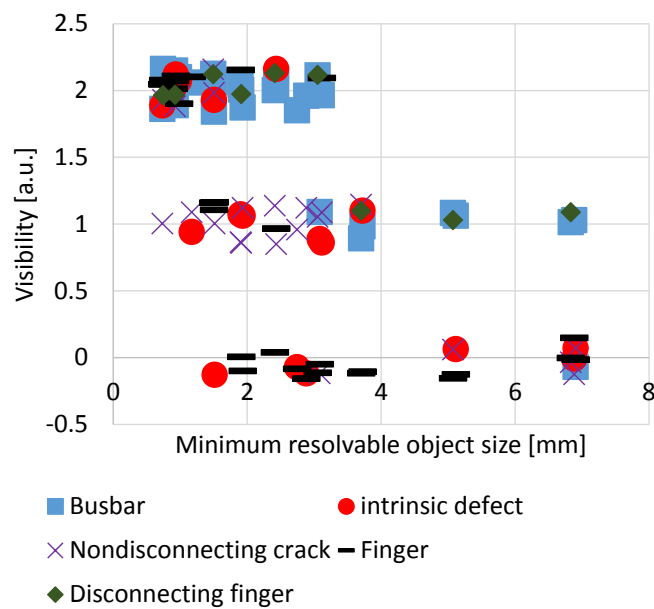


Figure 7.63: Mod8 imaged at 100%  $I_{sc}$ ; resulting corrected EL images for different cameras shown for cell {6,3}

**Table 7.16: Visibility of different features in cell {6,3} of Mod8**

Cam. ID	SNR [-]	$s_{obj}$ [mm]	Busbar	Finger	Disconnecting finger (blue)	Non-disc. crack (green)
A	18.87	1.91	2	0	2	1
B	66.00	0.74	2	2	2	2
C	46.65	1.49	2	1	2	2
D	55.47	3.70	1	0	1	1
G	54.06	0.92	2	2	2	2
I	44.50	3.05	2	0	2	1
J	34.97	2.41	2	0	2	1
XA	996.27	9.32	0	0	0	0
XB	61.01	5.07	1	0	1	0
XC	114.75	6.83	1	0	1	0

The object size and feature visibility of the recent Tables 7.14 - 7.16 were used to generate Figure 7.64. With the low number of evaluated features the trend of improved visibility for smaller object size is not clear (although visible). Therefore, the following minimum object sizes are a proof of concept and not robust guidelines.



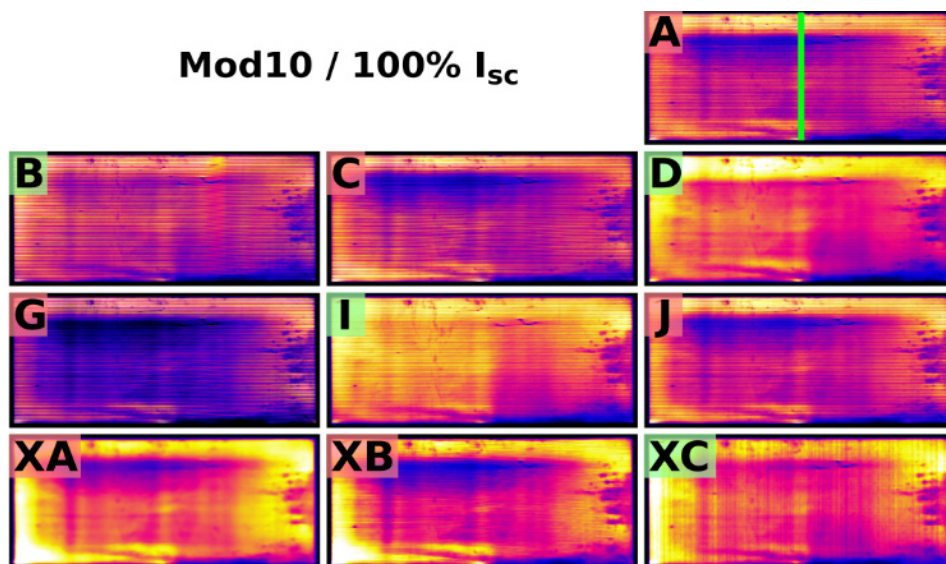
**Figure 7.64: Visibility vs. object size for crystalline modules**

Table 7.17 shows threshold values for a minimum object size ( $s_{Obj,min}$ ), required to resolve a given feature as those size causing an average visibility of 1.5.

**Table 7.17: Minimum object size required to resolve different features in crystalline modules**

Feature	Busbar	Finger	Disconnecting finger	Non-disconnecting crack	Intrinsic defect
$s_{Obj,min}$ [mm]	3	1.3	1.7	1.5	2

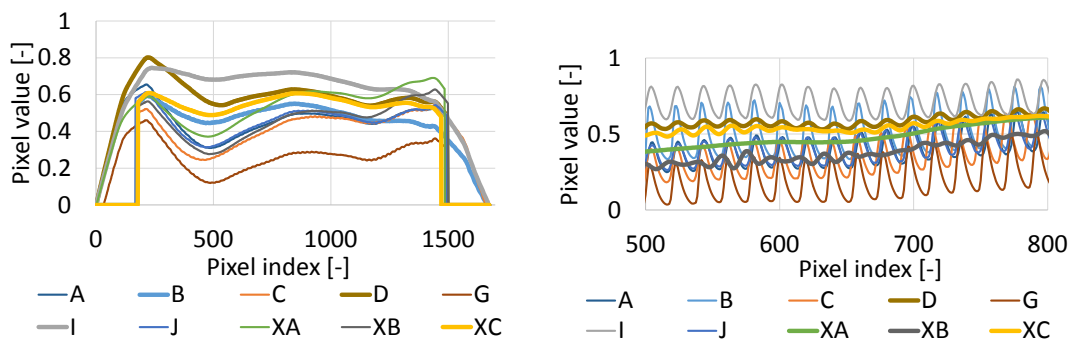
In contrast to crystalline devices, the variations in the EL images of both thin-film modules (Mod9, Mod10) were much more pronounced (Figure 7.65). In the warm-up experiment on a CIGS module (Subsection 6.1.4.1), the spatial homogeneity of EL signal decreased over time. Similar patterns can be seen in Figure 7.65. Whilst every lab was asked to ensure a warm-up time of 10 minutes, the EL images of camera B, D, I and XC (highlighted green) might have been imaged without this warm-up time. Further investigation is required to corroborate this theory.



**Figure 7.65: Comparison of corrected EL images of Mod10 at 100%  $I_{sc}$**

Figure 7.66a shows a moving-average-smoothed line plot (position indicated in Figure 7.65A). The trend of plots B, D, I and XC (bold plots) is steadier. As with most of the EL images in this test case, the image intensities were scaled between 2% and 98% of their cumulative distribution function (Section 4.9). Since all the images in Figure 7.65 display the same device, it should not be expected to see darker (B, G, A) and brighter (I, XA, XB) images.

In contrast to crystalline devices, the module consists of numerous narrow cells, which cause the image to be dominated by high gradient variations. Figure 7.66b shows part of the line plot of Subfigure (a) without smoothing. Depending on the image sharpness, gradients along the cells are barely visible (bold plots) or more pronounced.



**a) Smoothed by moving average   b) Unprocessed middle area of (a)**  
**Figure 7.66: Vertical line plot of green line (Figure 7.65) of Mod10**

The same behaviour can be also observed in the EL images shown in Figure 7.67. When looking at images of the entire module one would guess that these cell-to-cell deviations average out. Since the average of white and purple is not yellow, the colour map used is not suitable however to assign the right colour to an average of extreme differences.

To compare feature visibility in Figure 7.67, the subjective visibility of cells, a line-shaped intrinsic defect (blue, possibly caused by inhomogeneous crystallization) and a shunt (green) is observed. The results are listed in Table 7.18.

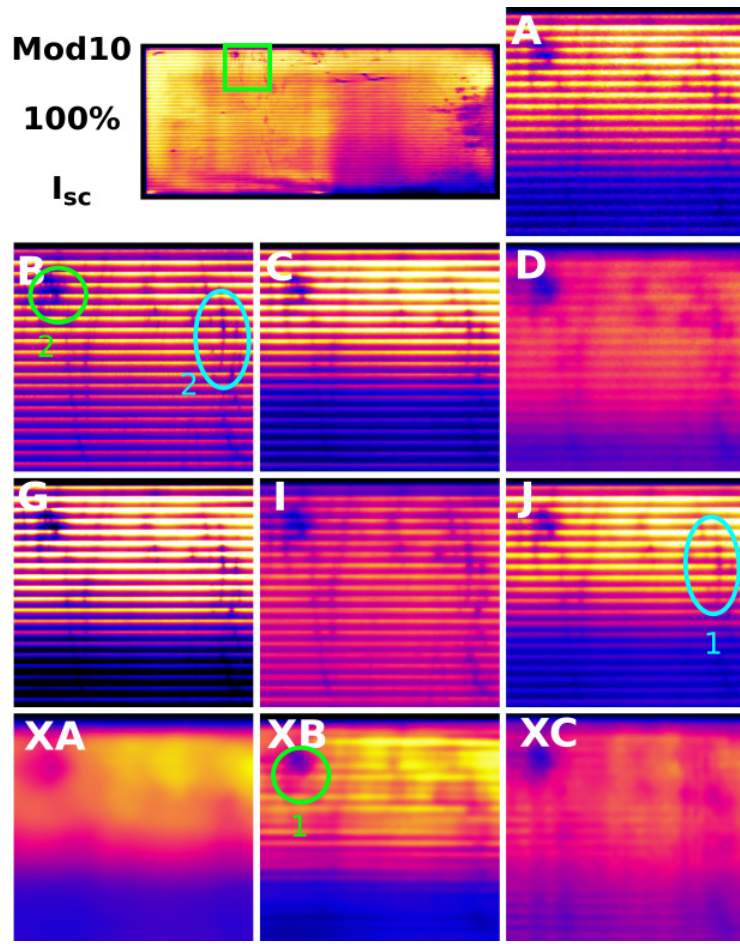


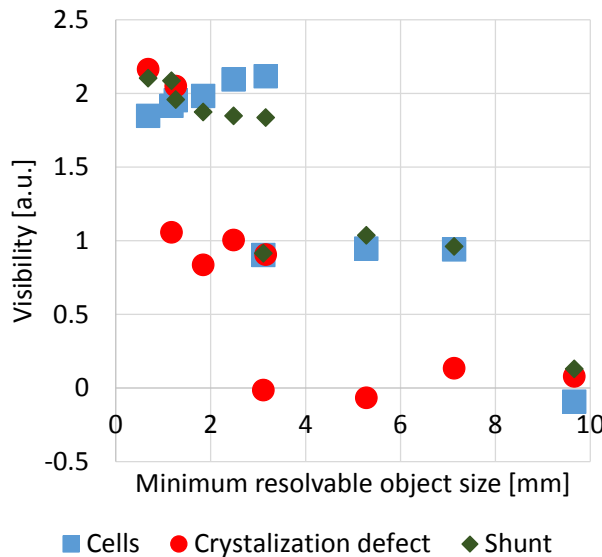
Figure 7.67: Mod10 imaged at 100%  $I_{sc}$ ; the resulting corrected EL images for different cameras are shown for the top-left area of the module (green box)

Table 7.18: Visibility of different features in top right area in Mod10

Cam. ID	SNR [-]	$s_{obj}$ [mm]	Cells	Crystallisation defect (blue)	Shunt (green)
A	11.58	1.84	2	1	2
B	18.41	0.68	2	2	2
C	13.08	1.17	2	1	2
D	18.41	3.11	1	0	1
G	96.72	1.26	2	2	2
I	49.13	3.16	2	1	2
J	37.70	2.48	2	1	2
XA	770.59	9.66	0	0	0
XB	103.35	5.28	1	0	1
XC	153.78	7.13	1	0	1

In the same way, Figure 7.68 and Table 7.19 plot visibility vs  $s_{obj}$  and provide a minimum object size to resolve the features mentioned. Again,

it should be noted that, due to the small number of data points, the results should be only seen as a proof of concept.



**Figure 7.68: Visibility vs. object size for Mod10**

**Table 7.19: Minimum object size required to resolve different features in Mod10**

Feature	Cells	Crystallization defect	Shunt
$s_{Obj,min}$ [mm]	3.5	1.5	4

Features of the polycrystalline Cell4 and Cell5 were analysed at cell-level. Figure 7.69 shows a comparison of a 400x400 pixel array of the bottom-right of Cell4. In this and the following comparison of Cell5, a red box indicates a phenomenon only seen in one camera: reflected EL signal over busbars (camera E). It is assumed that this is due the inner walls of the measurement chamber allowing a back reflection of the emitted EL signal. This can introduce additional blur and distort the EL intensities.

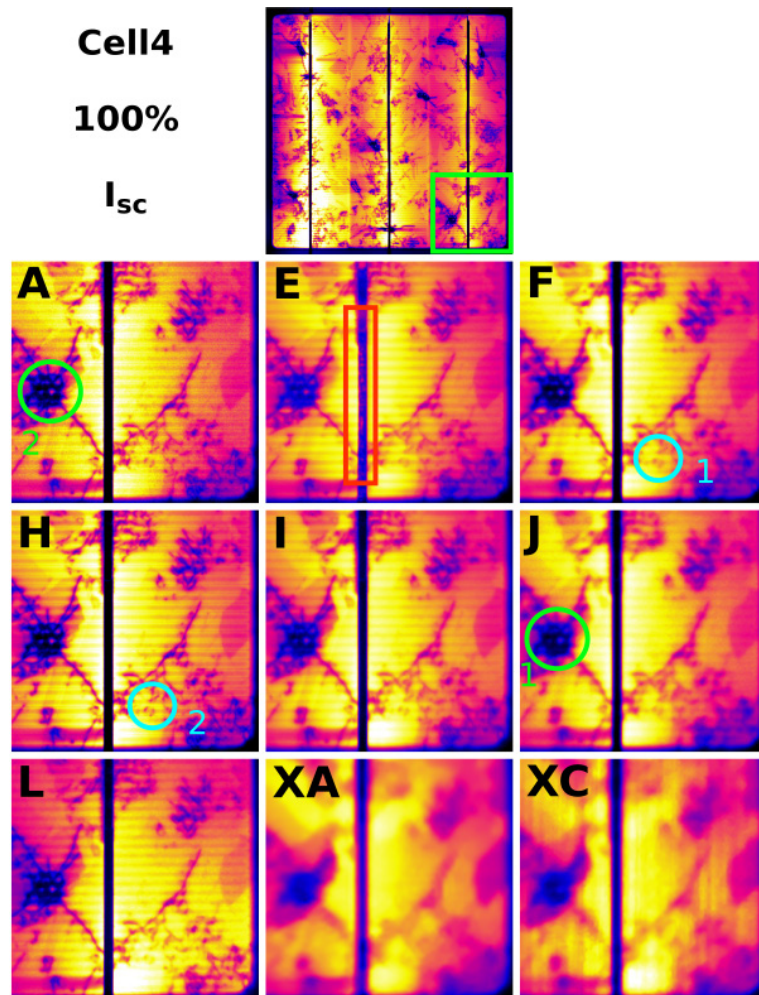


**Figure 7.69: Cell4 imaged at 100%  $I_{sc}$ ; resulting corrected EL images for different cameras shown for bottom right area of the cell (green box); red box: reflected EL signal**

The criteria for feature visibility were adapted to cell-level as follows:

- Busbar: 2 - sharp edge, 1 - blurry edge
- Finger: 2 - print marks visible, 1 - only intensity fluctuation due to fingers visible, 0 - no intensity fluctuations visible
- Dislocations (blue circle): 2 - all structures resolved, 1 - structures generally visible, 0 - no structure visible
- Crack structure (green circle): 2 - two bright spots clearly visible, 1 - spots hardly visible, 0 - no spots visible

**Table 7.20: Visibility of different features in bottom right of Cell4**

Cam. ID	SNR [-]	$s_{obj}$ [mm]	Busbar	Fingers	Dislocations (blue)	Crack structure (green)
A	16.68	0.22	2	2	2	2
E	297.56	0.66	2	1	1	2
F	59.40	0.48	2	1	1	2
H	70.57	0.22	2	2	2	2
I	126.58	0.54	2	1	1	2
J	38.57	0.61	2	1	1	1
L	48.31	0.47	2	1	1	2
XA	1008.97	1.29	1	0	0	0
XC	112.37	1.01	1	0	0	0

Equally, Figure 7.70 and Table 7.21 show a feature comparison for Cell5.

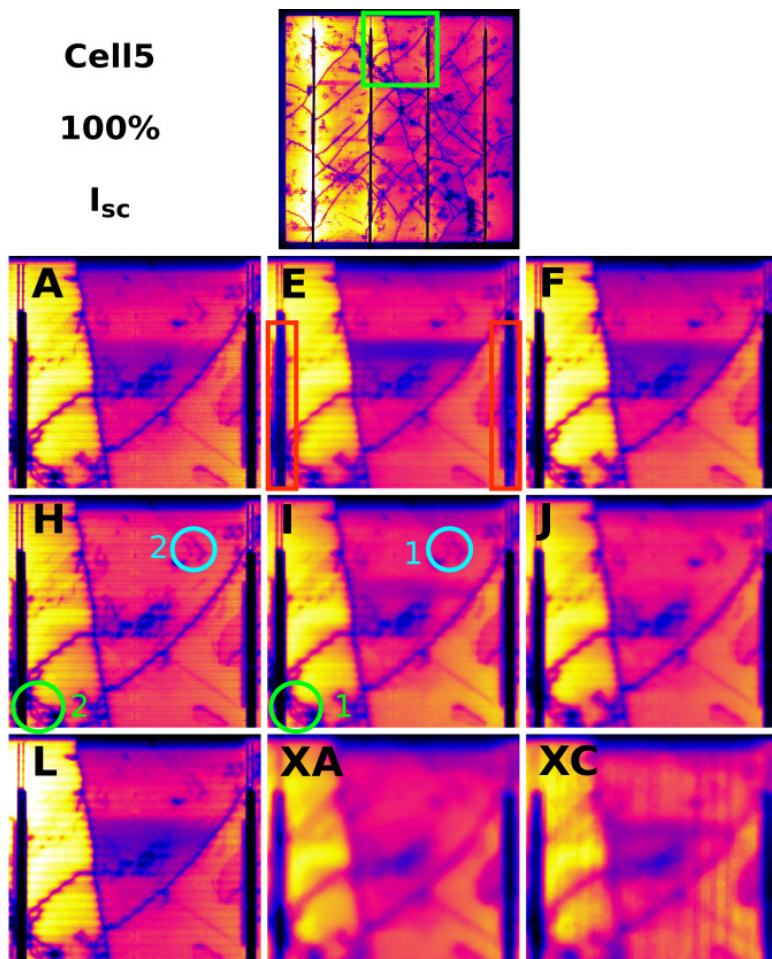


**Figure 7.70: Cell5 imaged at 100%  $I_{sc}$ ; the resulting EL images for different cameras are shown for top middle area of the cell (green box);**

**EL signal in V shaped crack area varies due to changing series resistance**

**Table 7.21: Visibility of different features in top middle area of Cell5**

Cam. ID	SNR [-]	$s_{obj}$ [mm]	Busbar	Fingers	Dislocations (blue)	Crack structure (green)
A	16.82	0.21	2	2	2	2
E	368.05	0.66	2	1	1	2
F	62.01	0.47	2	1	1	1
H	69.71	0.22	2	2	2	2
I	17.12	0.53	2	1	1	1
J	43.47	0.61	2	1	1	1
L	50.01	0.47	2	1	2	2
XA	1002.49	1.29	1	0	0	0
XC	109.54	1.00	1	0	0	0

Again, visibility vs.  $s_{obj}$  and minimum object size are shown in Figure 7.71 and Table 7.22.

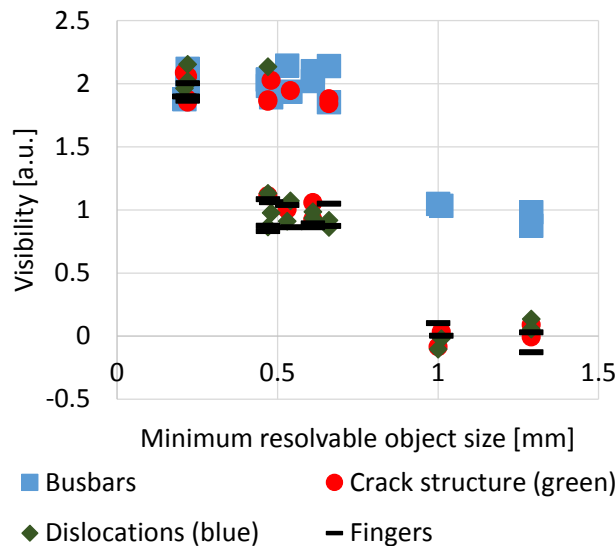


**Figure 7.71: Visibility vs. object size for Cell4 and Cell5**

**Table 7.22: Minimum object size required to resolve different features in Cell4 and Cell5**

Feature	Busbars	Fingers	Dislocations (blue)	Crack structure (green)
$s_{obj,min}$ [mm]	0.8	0.35	0.4	0.45

#### 7.2.3.4 SERIES RESISTANCE MAPS

It is to be expected that the influence of the cameras flat field cancels out, if an EL signal ratio and not the absolute EL signal is analysed. For series resistance imaging, the EL emission at 100%  $I_{sc}$  is corrected by a low current (often 10%  $I_{sc}$ ) calibration image. Its result is usually scaled in [ $\Omega$ ] or [ $\frac{\Omega}{area}$ ] (Subsection 2.4.4.1). This simplifies both camera calibration and image correction because:

- No flat field correction is necessary and
- Brightness and contrast level of images do not need to be adjusted.

The following results were obtained from images, corrected in the same fashion as described in Subsection 7.2.3 but excluding flat field correction and image intensity normalization. Figure 7.72 shows the resulting series resistance maps for Mod2. All images are scaled within the same boundary. Remarkably, for all images a high similarity can be found within the intensity range and distribution. However, the relative difference from the CCD camera average (Subfigure b) reveals that although the influence of flat field caused intensity deviation is reduced, remaining deviations of up to 30% can be seen. Furthermore, the difference image of camera B shows that the EL image must have been stitched together from two sub images, because two separate vignetting trends are visible.

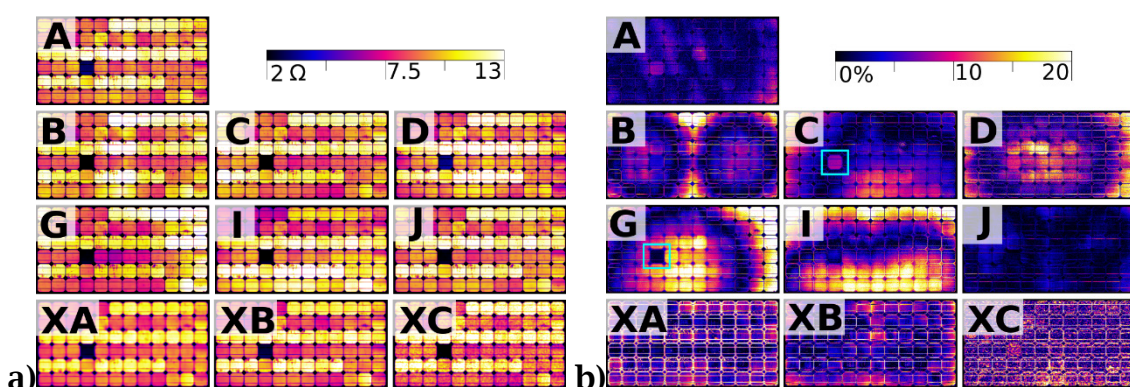


**Figure 7.72: Mod2; a) Series resistance maps; b) magnitude difference to average from camera A-J**

A blue box (Figure 7.72b) highlights a single outstanding cell, which deviates more than its surrounding cells. In particular cells emitting a low or no signal in the low current EL image can cause wrong results in the series resistance map (Figure 7.73).

A physical interpretation of the obtained results is out of the scope of this work, due to the absence of more sophisticated measurement methods.

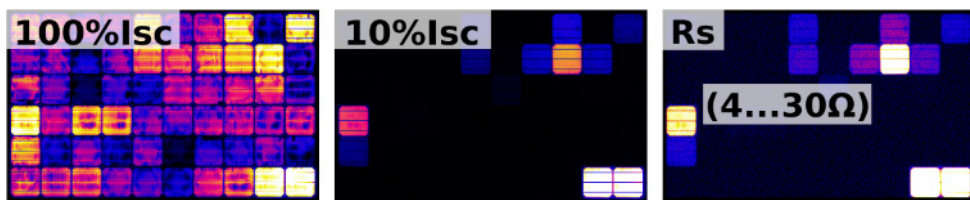


Figure 7.73: Incorrect series resistance map (right) due to inactive areas in low current EL image (middle)

#### 7.2.4 SECTION SUMMARY

At time of writing, this first Round Robin on electroluminescence measurement of PV devices is still ongoing. However, initial results from 14 different camera systems are already presented. It was shown that most labs use a 16 bit CCD camera and EL images at  $100\% I_{sc}$  achieved a signal-to-noise ratio (SNR) of more than 50. In most cases however, maximum intensities were only at a third of the cameras bit depth. In most cases, the need for short measurement times supposedly prevented higher SNR. Hence, for  $10\% I_{sc}$  images exposure times were often only two (and not ten) times longer relative to the ones at  $100\% I_{sc}$ .

All labs were able to successfully image the chessboard pattern, used to determine lens distortion. It was found that deflection caused by lens distortion is on average less than 1.5% (relative to the image size). This lens distortion is not easily visible to the human eye.

The position uncertainty due to lens correction and re-projection error is less than 0.5% (relative to image size). Therefore, it was omitted in the uncertainty analysis. Five labs were not able to provide usable flat field calibration images. As the comparison of averaged cell intensities shows,

deviations for silicon devices (5-7%) were mainly due to residual flat field distortion. Additionally, the instability of the EL signal of the two evaluated thin-film devices caused intensity deviations of 10-12%.

Although image sharpness measurements were not part of the Round Robin, sharpness could be measured by comparison of the corrected EL images. Noting the DUT size in the original image this sharpness could be rescaled accordingly. Interestingly, the sharpest images were generated with low-resolution InGaAs cameras. The otherwise relatively high spread of sharpness levels underlines the need to optimize image focus using quantitative measures rather than the bare eye.

At module-scale, the often constant camera focus caused the DUTs to not fill out the entire image plane. This caused on average 50% of the available pixels to remain unused.

A direct comparison of several corrected EL images showed good agreement. The EL images deviated mostly due to different sharpness levels, residual vignetting, image noise and instable EL signal (mostly next to cracks). Contrast levels of intrinsic defects were also found to be slightly different between InGaAs and CCD cameras.

This first international Round Robin on electroluminescence measurement of PV devices aimed to capture the state of the art and to demonstrate general comparability of results. It was not intended as a competition but rather a comparison. Nevertheless, it was found that amongst the participating camera systems and according to the discussed image quality criteria, camera XA and E produced best results.

Further classification and ranking can be found in Table 7.23 and Table 7.24. It is noted that the chosen criteria were not known to the laboratories and InGaAs and CCD cameras were not evaluated separately. Depending on the position of the best three camera systems within a category, three to one points were assigned.

**Table 7.23: Points assigned to top three camera systems**

	3 points	2 points	1 point
<b>Subsection 7.2.1.2:</b> Signal-to-noise ratio			
Highest average SNR	XA	E	XC
Highest average SNR rate [SNR/s], CCD only	E	I	J
<b>Subsection 7.2.1.3:</b> Image sharpness			
Module-scale - same resolution	C	I	A
Module-scale - same scale	XA	XB	XC
Cell-scale - same resolution	H	A	I
Cell-scale - same scale	XA	XC	L
<b>Subsection 7.2.1.4:</b>			
Highest Object-to-image ratio	E	H	XB
<b>Subsection 7.2.3.1:</b> Lowest EL intensity deviation relative to DUT average	J	H	A

**Table 7.24: EL Round Robin camera ranking from points in Table 7.23**

Camera	XA	E	H	I	A
Position	1	2	3	4	5
Points	9	8	6	5	4

# CONCLUSIONS

In this thesis, a set of tools has been presented to enable quantitative information to be extracted from electroluminescence (EL) imaging. The quantitative electroluminescence imaging (QEL) methods developed during this work aim to standardise and automate image capture, processing and analysis. An introduced signal-to-noise ratio (SNR) definition specifically applicable to EL measurements enables minimum exposure time for target quality thresholds. The metric and thresholds resulting from this work have been incorporated into an IEC standard draft on EL measurement.

Background correction is often done through subtracting a background image from every EL image. To reduce measurement time and cost to the industry and to improve correction quality, different methods for creating one calibration background image rather than an extra image for every measurement have been developed as part of this work.

For image artefact removal (especially for longer exposure times), it is proposed to take two shorter EL images, rather than a longer one.

Image sharpness in EL imaging is currently measured along a slanted edge, created through masking a PV device. If the blur function defining the image sharpness is assumed radially variable, the measurement has to be repeated multiple times and still returns only a radially symmetric blur function. A novel method to measure a spatially resolved blur function is presented.

Novel and precise vignetting measurement methods were presented and their correction quality was quantified. It was shown, that the currently applied vignetting measurement method of imaging a (red) LCD screen in front the camera lens is not suitable for vignetting correction.

Perspective distortion in EL images is a common problem, especially for outdoor imaging. Methods to automatically detect and remove perspective have been discussed and evaluated. The correction algorithm was applied to two case studies, including the first international EL Round

Robin. Quantitative comparison of difference images obtained from PV devices (imaged at different times and with different equipment) became possible due to this work.

For light-IV measurement the determination of measurement uncertainty is a standardised procedure to assess the quality of a measurement system. So far uncertainty was not calculated for EL measurements. This work presents routines to determine noise-, sharpness-, signal- and correction uncertainty. In result, the measurement error of a pixel and a pixel-area within an EL image can be estimated.

Although this work focussed on EL, the majority of routines can also be applied to other scientific imaging techniques, such as photoluminescence and lock-in thermography.

None of the presented methods are overly complex to implement and the source code written by the author and used to calculate and evaluate the results in this thesis is made available to the public. With `dataArtist`, an interactive graphical application for scientific image processing was developed. It focusses on EL imaging and provides tools for determining best focus and exposure time, camera calibration, image correction and comparison as well as feature extraction and series resistance imaging.

Manual EL image analysis on all monitored PV systems in the field and in production is neither reliable nor profitable. This work provides tools to automate the process. Manufacturer and installer-based warranty cases will be detected at almost no time without extra costs for image processing. With this, both physical PV durability and financial reliability will be increased.

# FUTURE RESEARCH AVENUES

This work only discussed briefly possible feature extraction and performance analysis routines. To further validate and refine the results, the larger number of EL images need to be evaluated and correlated to other measurement methods, like laser beam induce current (LBIC). Further, more sophisticated (spatially resolved) simulations need to be conducted. In detail:

Crack propagation within on-field modules need to be measured and modelled for different climate zones. Crack age and -length need to be correlated to performance data to get a better understanding regarding its influence for series- and shunt resistance.

The measurement of inactive areas need to be revised. It was shown that identified inactive areas can reconnect again and that those areas can still be beneficial for current generation. Combined mechanical load and EL measurements might be useful to identify an ‘effective inactive area’.

Moisture ingress in PV devices is a cause for performance degradation. Through evaluating time series of EL images, QEL will be used to model the related physical processes.

# REFERENCES

- [1] EPIA, "Global Market Outlook for Solar Power / 2016 - 2020," no. February, p. 40, 2016.
- [2] T. Fuyuki, H. Kondo, T. Yamazaki, Y. Takahashi, and Y. Uraoka, "Photographic surveying of minority carrier diffusion length in polycrystalline silicon solar cells by electroluminescence," *Appl. Phys. Lett.*, vol. 86, no. 26, p. 262108, 2005.
- [3] K. Bothe and D. Hinken, *Quantitative luminescence characterization of crystalline silicon solar cells*, 1st ed., vol. 89. Elsevier Inc., 2013.
- [4] M. Glatthaar, J. Haunschild, R. Zeidler, M. Demant, J. Greulich, B. Michl, W. Warta, S. Rein, and R. Preu, "Evaluating luminescence based voltage images of silicon solar cells," *J. Appl. Phys.*, vol. 108, no. 1, p. 14501, 2010.
- [5] T. Trupke, E. Pink, R. a. Bardos, and M. D. Abbott, "Spatially resolved series resistance of silicon solar cells obtained from luminescence imaging," *Appl. Phys. Lett.*, vol. 90, no. 9, p. 93506, 2007.
- [6] P. Würfel, T. Trupke, T. Puzzer, E. Schaffer, W. Warta, and S. W. Glunz, "Diffusion lengths of silicon solar cells from luminescence images," *J. Appl. Phys.*, vol. 101, no. 12, p. 123110, 2007.
- [7] B. Li, A. Stokes, and D. M. J. Doble, "Evaluation of two-dimensional electrical properties of photovoltaic modules using bias-dependent electroluminescence," *Prog. Photovoltaics Res. Appl.*, vol. 20, no. 8, pp. 936–944, 2012.
- [8] T. Potthoff, K. Bothe, U. Eitner, D. Hinken, and M. Köntges, "Detection of the voltage distribution in photovoltaic modules by electroluminescence imaging," *Prog. Photovoltaics Res. Appl.*, vol. 18, no. 2, pp. 100–106, Mar. 2010.
- [9] B. Li, A. Stokes, and D. M. J. Doble, "Two Dimensional Mapping of Electrical Properties of PV Modules using Electroluminescence," *26th Eur. PVSEC*, vol. 26, pp. 3285–3289, 2011.
- [10] S. Johnston, "Contactless electroluminescence imaging for cell and

- module characterization," *2015 IEEE 42nd Photovolt. Spec. Conf. PVSC 2015*, 2015.
- [11] L. Stoicescu, M. Reuter, and J. H. Werner, "Daylight Luminescence for Photovoltaic System Testing," *22nd Int. Photovolt. Sci. Eng. Conf.*, p. CD-ROM, 2012.
  - [12] S. Guo, T. M. Walsh, A. G. Aberle, and M. Peters, "Analysing partial shading of PV modules by circuit modelling," *Conf. Rec. IEEE Photovolt. Spec. Conf.*, pp. 2957-2960, 2012.
  - [13] S. R. Wenham, M. A. Green, M. E. Watt, and R. Corkish, *Applied photovoltaics*, 2d ed. Earthscan, 2007.
  - [14] W. De Soto, S. A. Klein, and W. A. Beckman, "Improvement and validation of a model for photovoltaic array performance," *Sol. Energy*, vol. 80, no. 1, pp. 78-88, 2006.
  - [15] D. L. King, B. R. Hansen, J. a. Kratochvil, and M. a. Quintana, "Dark current-voltage measurements on photovoltaic modules as a\ndiagnostic or manufacturing tool," *Conf. Rec. 26 IEEE Photovolt. Spec. Conf.*, no. September, pp. 1125-1128, 1997.
  - [16] Keithley, "Application Note Number 2876: Making I-V and C-V Measurements on Solar/Photovoltaic Cells Using the Model 4200-SCS Semiconductor Characterization System," no. 2876, 2007.
  - [17] European Commission, J. R. Centre, and I. for Energy, *Guidelines for PV power measurement in industry*. 2010.
  - [18] T. Kirchartz, A. Helbig, and W. Reetz, "Reciprocity between electroluminescence and quantum efficiency used for the characterization of silicon solar cells," *Prog. Photovoltaics Res. Appl.*, no. April, pp. 394-402, 2009.
  - [19] P. Würfel, *Physics of solar cells: from principles to new concepts*, no. 2003. 2005.
  - [20] J. Colvin, "Comparative Failure Analysis of Photovoltaic Devices," in *35th International Symposium for Testing and Failure Analysis*, 2009, pp. 149-156.
  - [21] T. Fuyuki and A. Kitiyanan, "Photographic diagnosis of crystalline

- silicon solar cells utilizing electroluminescence," *Appl. Phys. A*, vol. 96, no. 1, pp. 189–196, Dec. 2008.
- [22] M. Israil, S. a. Anwar, and M. Z. Abdullah, "Automatic detection of micro-crack in solar wafers and cells: a review," *Trans. Inst. Meas. Control*, vol. 35, no. 5, pp. 606–618, Oct. 2012.
- [23] R. Stojan, J. Vaněk, and M. Malý, "Progression of Silicon Solar Cells Luminescence Diagnostic Methods," *Univers. J. Electr. Electron. Eng.*, vol. 2, no. 1, pp. 18–22, 2014.
- [24] M. P. Peloso, B. Hoex, and A. G. Aberle, "Polarization analysis of luminescence for the characterization of silicon wafer solar cells," *Appl. Phys. Lett.*, vol. 98, no. 17, p. 171914, 2011.
- [25] M. Köntges, M. Siebert, and D. Hinken, "Quantitative analysis of PV-modules by electroluminescence images for quality control," *Proc. 24th ...*, 2009.
- [26] S. P. Phang, H. C. Sio, and D. Macdonald, "Applications of carrier de-smearing of photoluminescence images on silicon wafers," in *Progress in Photovoltaics: Research and Applications*, 2016, vol. 24, no. 12, pp. 1547–1553.
- [27] J. L. Crozier, "Characterization of cell mismatch in photovoltaic modules using electroluminescence and associated electro-optic techniques," Nelson Mandela Metropolitan University, 2012.
- [28] A. S. H. van der Heide, J. H. Bultmann, J. Hoornstra, and A. Schönecker, "Contact resistance measured using the Corescan: relations with cell processing," *17th Eur. Photovolt. Sol. Energy Conversion, Munich*, p. 1531, 2001.
- [29] B. Moralejo, M. a. González, J. Jiménez, V. Parra, O. Martínez, J. Gutiérrez, and O. Charro, "LBIC and Reflectance Mapping of Multicrystalline Si Solar Cells," *J. Electron. Mater.*, vol. 39, no. 6, pp. 663–670, Mar. 2010.
- [30] J. Carstensen, G. Popkirov, J. Bahr, and H. Föll, "CELLO: An advanced LBIC measurement technique for solar cell local characterization," *Sol. Energy Mater. Sol. Cells*, vol. 76, no. 4, pp. 599–611, 2003.

- [31] H. Kampwerth, T. Trupke, J. W. Weber, and Y. Augarten, "Advanced luminescence based effective series resistance imaging of silicon solar cells," *Appl. Phys. Lett.*, vol. 93, no. 20, pp. 1-4, 2008.
- [32] O. Breitenstein, a. Khanna, Y. Augarten, J. Bauer, J. M. Wagner, and K. Iwig, "Quantitative evaluation of electroluminescence images of solar cells," *Phys. Status Solidi - Rapid Res. Lett.*, vol. 4, no. 1-2, pp. 7-9, 2010.
- [33] D. Hinken, K. Ramspeck, K. Bothe, B. Fischer, and R. Brendel, "Series resistance imaging of solar cells by voltage dependent electroluminescence," *Appl. Phys. Lett.*, vol. 91, no. 18, p. 182104, 2007.
- [34] J. Haunschild, M. Glatthaar, M. Kasemann, S. Rein, and E. R. Weber, "Fast series resistance imaging for silicon solar cells using electroluminescence," *Phys. Status Solidi - Rapid Res. Lett.*, vol. 3, no. 7-8, pp. 227-229, 2009.
- [35] K. Ramspeck, K. Bothe, D. Hinken, B. Fischer, J. Schmidt, and R. Brendel, "Recombination current and series resistance imaging of solar cells by combined luminescence and lock-in thermography," *Appl. Phys. Lett.*, vol. 90, no. 15, p. 153502, 2007.
- [36] T. M. Pletzer, J. I. Van Molken, S. Rissland, B. Hallam, E. Cornagliotti, J. John, O. Breitenstein, and J. Knoch, "Quantitative local current-voltage analysis with different spatially-resolved camera based techniques of silicon solar cells with cracks," in *2014 IEEE 40th Photovoltaic Specialist Conference, PVSC 2014*, 2014, pp. 3473-3478.
- [37] A. R. L. M. Ezquer Mayo, J.M. Cuadra, J. Díaz, J. Moracho, "New Analytical Software for Electroluminescence Results Out of Patterns," in *27th European Photovoltaic Solar Energy Conference and Exhibition*, 2012, pp. 3041-3048.
- [38] T. Trupke, R. Bardos, M. Schubert, and W. Warta, "Photoluminescence imaging of silicon wafers," *Appl. Phys. Lett.*, vol. 89, no. 4, pp. 44107-44107, 2006.
- [39] O. Breitenstein, J. Bauer, K. Bothe, D. Hinken, J. Müller, W. Kwapil, M.

- C. Schubert, and W. Warta, "Can luminescence imaging replace lock-in thermography on solar cells," *IEEE J. Photovoltaics*, vol. 1, no. 2, pp. 159–167, 2011.
- [40] B. P. Rand, J. Genoe, P. Heremans, and J. Poortmans, "Solar Cells Utilizing Small Molecular Weight Organic Semiconductors," *Prog. Photovolt Res. Appl.*, vol. 15, no. February 2013, pp. 659–676, 2007.
- [41] O. Breitenstein, J. Rakotonaina, and Et.al., "Lock-in thermography—A universal tool for local analysis of solar cells," *Eur. Photovolt. Sol. Energy Conf.*, no. June, pp. 590–593, 2005.
- [42] F. J. J.L. Crozier, E.E. van Dyk, "High Resolution Spatial Electroluminescence Imaging of Photovoltaic Modules," *Vor. Nelson Mand. Metrop. Univ.*, 2009.
- [43] M. Bliss, X. Wu, K. Bedrich, T. R. Betts, and R. Gottschalg, "Spatially and Spectrally Resolved Electroluminescence Measurement System for PV Characterisation," in *IET-RPG, accepted 2015*.
- [44] R. Widenhorn, M. M. Blouke, A. Weber, A. Rest, and E. Bodegom, "Temperature dependence of dark current in a CCD," *Proc. SPIE Vol. 4669*, vol. 4669, no. April, pp. 193–201, 2002.
- [45] D. Sankowski and A. Fabijanska, "CCD Camera Instrumental Background Estimation Algorithm," *Instrum. Meas. Technol. Conf. - IMTC 2007*, pp. 1–5, 2007.
- [46] IEC, "IEC TS 60904-13 PHOTOVOLTAIC DEVICES - Part 13: Electroluminescence of photovoltaic modules - draft." 2017.
- [47] D. Kendig, G. B. Alers, and A. Shakouri, "Characterization of defects in photovoltaics using thermoreflectance and electroluminescence imaging," in *Conference Record of the IEEE Photovoltaic Specialists Conference*, 2010, pp. 1733–1736.
- [48] K. Martin, B. Walter, and W. Warta, "Reliable Hot-spot Classification in 10ms Using Ultra-fast Lock-in Thermography," *Prog. Photovoltaics Res. Appl.*, vol. 17, pp. 441–450, 2009.
- [49] M. P. Peloso, P. Chaturvedi, P. Würfel, B. Hoex, and A. G. Aberle, "Observations on the spectral characteristics of defect luminescence

- of silicon wafer solar cells," *Conf. Rec. IEEE Photovolt. Spec. Conf.*, pp. 2714-2717, 2010.
- [50] B. Mitchell, J. W. Weber, M. Juhl, D. Macdonald, and T. Trupke, "Photoluminescence Imaging of Silicon Bricks," *Solid State Phenom.*, vol. 205-206, pp. 118-127, Oct. 2013.
- [51] B. Mitchell, J. Greulich, and T. Trupke, "Quantifying the effect of minority carrier diffusion and free carrier absorption on photoluminescence bulk lifetime imaging of silicon bricks," *Sol. Energy Mater. Sol. Cells*, vol. 107, pp. 75-80, Dec. 2012.
- [52] R. Gupta, O. Breitenstein, J. Zettner, and D. Karg, "in-Line Shunt Detection in Solar Cells By Fast Lock-in Infrared Thermography," *22nd Eur. Photovolt. Sol. Energy Conf.*, no. September, pp. 5-8, 2007.
- [53] D. Hinken, C. Schinke, S. Herlufsen, A. Schmidt, K. Bothe, and R. Brendel, "Experimental setup for camera-based measurements of electrically and optically stimulated luminescence of silicon solar cells and wafers," *Rev. Sci. Instrum.*, vol. 82, no. 3, pp. 1-9, 2011.
- [54] F. D. van der Meer and S. M. de Jong, *Imaging Spectrometry: Basic Principles and Prospective Applications*. Springer Science & Business Media, 2007.
- [55] D. Dussault and P. Hoess, "Noise performance comparison of ICCD with CCD and EMCCD cameras," *Proc. SPIE*, vol. 5563, pp. 195-204, Oct. 2004.
- [56] J. Mullikin, L. van Vliet, and H. Netten, "Methods for CCD camera characterization," in *H.C. Titus, A. Waks (eds), SPIE vol. 2173, "Image Acquisition and Scientific Imaging Systems,"* vol. 2173, 1994, pp. 73-84.
- [57] R. Geary, "The ratio of the mean deviation to the standard deviation as a test of normality," *Biometrika*, vol. 27, no. 3, pp. 310-332, 1935.
- [58] W. T. Freeman and R. Szeliski, "Noise Estimation from a Single Image," *2006 IEEE Comput. Soc. Conf. Comput. Vis. Pattern Recognit. - Vol. 1*, vol. 1, pp. 901-908, 2006.
- [59] H. Faraji and W. MacLean, "CCD noise removal in digital images,"

*Image Process. IEEE Trans. ...*, vol. 15, no. 9, pp. 2676–2685, 2006.

- [60] H. C. Burger, B. Schölkopf, and S. Harmeling, “Removing noise from astronomical images using a pixel-specific noise model,” *2011 IEEE Int. Conf. Comput. Photogr. ICCP 2011*, 2011.
- [61] I. Young, J. Gerbrands, and L. Van Vliet, *Fundamentals of image processing*. 1998.
- [62] A. Buades, B. Coll, and J.-M. Morel, “Non-Local Means Denoising,” *Image Process. Line*, vol. 1, 2011.
- [63] S. Pertuz, D. Puig, and M. A. Garcia, “Analysis of focus measure operators for shape-from-focus,” *Pattern Recognit.*, vol. 46, no. 5, pp. 1415–1432, May 2013.
- [64] G. Bradski and A. Kaehler, *Learning OpenCV: Computer vision with the OpenCV library*. O'Reilly, 2008.
- [65] T. Trupke, R. a. Bardos, M. C. Schubert, and W. Warta, “Photoluminescence imaging of silicon wafers,” *Appl. Phys. Lett.*, vol. 89, no. 4, p. 44107, 2006.
- [66] D. Walter, A. Liu, and E. Franklin, “Contrast enhancement of luminescence images via point-spread deconvolution,” ... (PVSC), 2012 38th ..., pp. 307–312, 2012.
- [67] N. Joshi, R. Szeliski, and D. J. Kriegman, “PSF estimation using sharp edge prediction,” *26th IEEE Conf. Comput. Vis. Pattern Recognition, CVPR*, 2008.
- [68] O. Breitenstein, F. Fruhauf, and A. Teal, “An Improved Method to Measure the Point Spread Function of Cameras Used for Electro- and Photoluminescence Imaging of Silicon Solar Cells,” *IEEE J. Photovoltaics*, vol. 60, no. 5, pp. 1–6, 2016.
- [69] A. Teal, J. Dore, and S. Varlamov, “Photoluminescence imaging of thin film silicon on glass,” *Sol. Energy Mater. Sol. Cells*, vol. 130, pp. 1–5, Nov. 2014.
- [70] M. Delbracio, P. Musé, A. Almansa, and J. M. Morel, “The non-parametric sub-pixel local point spread function estimation is a well posed problem,” *Int. J. Comput. Vis.*, vol. 96, no. 2, pp. 175–194,

2012.

- [71] Albert, "How to Measure Modulation Transfer Function," 2014. [Online]. Available: <http://harvestimaging.com/blog/?p=1294>. [Accessed: 13-Sep-2016].
- [72] R. Szeliski, *Computer Vision : Algorithms and Applications*, Springer. Springer London, 2010.
- [73] Z. Cao, Z. Wei, and G. Zhang, "A no-reference sharpness metric based on the notion of relative blur for Gaussian blurred image," *J. Vis. Commun. Image Represent.*, vol. 25, no. 7, pp. 1763-1773, 2014.
- [74] A. Teal and M. Juhl, "Correcting the inherent distortion in luminescence images of silicon solar cells," in *IEEE PVSC*, 2015.
- [75] C. J. Schuler, M. Hirsch, S. Harmeling, and B. Sch, "Non-stationary Correction of Optical Aberrations," *ICCV - 13th Int. Conf. Comput. Vis.*, no. 1, 2011.
- [76] D. A. Knoll and D. E. Keyes, "Jacobian-free Newton-Krylov methods: A survey of approaches and applications," *J. Comput. Phys.*, vol. 193, no. 2, pp. 357-397, 2004.
- [77] A. H. Baker, J. M. Dennis, and E. R. Jessup, "On Improving Linear Solver Performance: A Block Variant of GMRES," *SIAM J. Sci. Comput.*, vol. 27, pp. 1608-1626, 2006.
- [78] A. Tanbakuchi, "Comparison of OpenCV Interpolation Algorithms," 2016..
- [79] R. P. Brent, "Algorithms for Minimization Without Derivatives," *IEEE Trans. Automat. Contr.*, vol. 19, no. 5, pp. 632-633, 1974.
- [80] J. Weng, P. Cohen, and M. Herniou, "Camera calibration with distortion models and accuracy evaluation," *IEEE Trans. Pattern Anal. Mach. Intell.*, vol. 14, no. 10, pp. 965-980, 1992.
- [81] A. Datta, J.-S. Kim, and T. Kanade, "Accurate camera calibration using iterative refinement of control points," *2009 IEEE 12th Int. Conf. Comput. Vis. Work. ICCV Work.*, pp. 1201-1208, Sep. 2009.
- [82] M. Bokalic, J. Raguse, J. R. Sites, and M. Topic, "Analysis of electroluminescence images in small-area circular CdTe solar cells,"

- J. Appl. Phys.*, vol. 114, no. 12, p. 123102, 2013.
- [83] K. G. Bedrich, M. Bliss, T. R. Betts, and R. Gottschalg, “Electroluminescence Imaging of PV Devices: Camera Calibration and Image Correction,” *IEEE PVSC-43*, 2016.
- [84] S. B. Howell, *Handbook of Ccd Astronomy*. 2006.
- [85] S. B. Kang and R. Weiss, “Can we calibrate a camera using an image of a flat textureless lambertian surface?,” *Eur. Conf. Comput. Vison*, vol. 2, pp. 640–653, 2000.
- [86] M. Topic, J. Raguse, K. Zaunbrecher, M. Bokalic, and J. R. Sites, “Electroluminescence of Thin Film Solar Cells and PV Modules - Camera Calibration,” in *26th European Photovoltaic Solar Energy Conference and Exhibition*, 2011, pp. 2963–2966.
- [87] N. Otsu, “A threshold selection method from gray-level histograms,” *IEEE Trans. Syst. Man. Cybern.*, vol. 9, no. 1, pp. 62–66, 1979.
- [88] S. Lin, “Single-Image Vignetting Correction,” *2006 IEEE Comput. Soc. Conf. Comput. Vis. Pattern Recognit. - Vol. 1*, vol. 1, pp. 461–468, 2006.
- [89] *VDI Heat Atlas*. 2010.
- [90] IEC, *IEC 62446-3 TS: Photovoltaic (PV) systems - Requirements for testing, documentation and maintenance - Part 3: Outdoor infrared thermography of photovoltaic modules and plants*. 2016.
- [91] K. N. Ermakov, N. a. Ivanov, O. V. Lobanov, V. V. Pashuk, M. G. Tverskoy, and S. M. Lyubinskii, “Experimental investigation of the effect of high-energy protons on charge-coupled devices,” *Tech. Phys. Lett.*, vol. 36, no. 7, pp. 610–612, Sep. 2010.
- [92] G. R. Hopkinson, C. J. Dale, and P. W. Marshall, “Proton effects in charge-coupled devices,” *IEEE Trans. Nucl. Sci.*, vol. 43, no. 2, pp. 614–627, Apr. 1996.
- [93] R. Hill, W. Landsman, D. Lindler, and R. Shaw, “Cosmic ray and hot pixel removal from STIS CCD images,” *Calibration Work.*, pp. 120–125, 1997.
- [94] A. N. L. Johnson and B. Y. N. L. Johnson, “Biometrika Trust Systems

- of Frequency Curves Generated by Methods of Translation  
Published by : Oxford University Press on behalf of Biometrika Trust  
Stable URL: <http://www.jstor.org/stable/2332539> Accessed : 26-04-  
2016 11 : 04 UTC Your use of the JSTOR," *Biometrika Trust*, vol. 36,  
no. 1, pp. 149-176, 1949.
- [95] "Scipy.stats - Statistical functions," *The Scipy community*, 2016.  
[Online]. Available:  
<http://docs.scipy.org/doc/scipy/reference/stats.html>.
- [96] H. R. Wu and K. R. Rao, *Digital Video Image Quality and Perceptual Coding (Signal Processing and Communications)*. Boca Raton, FL, USA: CRC Press, Inc., 2005.
- [97] Z.Liu et al, "Luminescence Imaging Analysis of Light Trapping in Crystalline Si PV Modules," *27th Eur. Photovolt. Sol. Energy Conf. Exhib.*
- [98] A.Bijaoui, L. Starck, and F. Murtagh, "Image Processing and Data Analysis , The Multiscale Approach," vol. 94, no. 448, 2014.
- [99] F. Orieux, J.-F. Giovannelli, and T. Rodet, "Bayesian estimation of regularization and point spread function parameters for Wiener-Hunt deconvolution," *J. Opt. Soc. Am. A*, vol. 27, no. 7, p. 1593, 2010.
- [100] E. Rublee, V. Rabaud, K. Konolige, and G. Bradski, "ORB: An efficient alternative to SIFT or SURF," *Proc. IEEE Int. Conf. Comput. Vis.*, pp. 2564-2571, 2011.
- [101] S. Spataru, P. Hacke, D. Sera, S. Glick, T. Kerekes, and R. Teodorescu, "Quantifying solar cell cracks in photovoltaic modules by electroluminescence imaging," in *2015 IEEE 42nd Photovoltaic Specialist Conference (PVSC)*, 2015, pp. 1-6.
- [102] S. Spataru, P. Hacke, and D. Sera, "Automatic Detection and Evaluation of Solar Cell Micro-Cracks in Electroluminescence Images Using Matched Filters," *43rd IEEE Photovolt. Spec. Conf.*, pp. 1602-1607, 2016.
- [103] M. Köntges, I. Kunze, S. Kajari-Schröder, X. Breitenmoser, and B. Bjørneklett, "The risk of power loss in crystalline silicon based

- photovoltaic modules due to micro-cracks," *Sol. Energy Mater. Sol. Cells*, vol. 95, no. 4, pp. 1131-1137, Apr. 2011.
- [104] S. Anwar and M. Abdullah, "Micro-crack detection of multicrystalline solar cells featuring an improved anisotropic diffusion filter and image segmentation technique," *EURASIP J. Image Video Process.*, vol. 2014, no. 1, p. 15, 2014.
- [105] M. Demant, "MICRO-CRACKS IN SILICON WAFERS AND SOLAR CELLS: DETECTION AND RATING OF MECHANICAL STRENGTH AND ELECTRICAL QUALITY," in *29th European PV Solar Energy Conference and Exhibition*, 2014, no. September, pp. 22-26.
- [106] M. Kumar and R. Saxena, "Algorithm and Technique on Various Edge Detection : A Survey," *Signal Image Process. An Int. J.*, vol. 4, no. 3, pp. 65-75, 2013.
- [107] N. Dalai, B. Triggs, I. Rhone-Alps, and F. Montbonnot, "Histograms of oriented gradients for human detection," in *IEEE Computer Society Conference on Computer Vision and Pattern Recognition, 2005. CVPR 2005*, 2005, vol. 1, pp. 886-893.
- [108] Y. S. Chen and W. H. Hsu, "A modified fast parallel algorithm for thinning digital patterns," *Pattern Recognit. Lett.*, vol. 7, no. 2, pp. 99-106, 1988.
- [109] M. Köntges, S. Kajari-Schröder, and I. Kunze, "Cell cracks measured by UV fluorescence in the field," in *27th European Photovoltaic Solar Energy Conference and Exhibition*, 2012, no. September, pp. 3033-3040.
- [110] K. Pearson, "Mathematical Contributions to the Theory of Evolution. XIX. Second Supplement to a Memoir on Skew Variation," *R. Soc.*, 1916.
- [111] M. Pv-testcenter, "MBJ PV-Module Judgment Criteria," vol. 49, no. 0. 2014.
- [112] W. Kester, "MT-001: Taking the Mystery out of the Infamous Formula, 'SNR = 6.02N + 1.76dB,' and Why You Should Care." Analog Devices, pp. 1-7, 2008.

- [113] *Formeln + Hilfen zur höheren Mathematik*, 5. Auflage. Binomi Verlag, 2007.
- [114] T. M. H. Tran, B. E. Pieters, C. Ulbrich, A. Gerber, T. Kirchartz, and U. Rau, “Transient phenomena in Cu(In,Ga)Se<sub>2</sub> solar modules investigated by electroluminescence imaging,” *Thin Solid Films*, vol. 535, no. 1, pp. 307–310, 2013.
- [115] E. W. Weisstein, “Normal Sum Distribution,” *From MathWorld--A Wolfram Web Resource*. [Online]. Available: <http://mathworld.wolfram.com/NormalSumDistribution.html>.
- [116] B. Kubicek, W. Mühlleisen, G. Ujvari, R. Ebner, and L. Neumaier, “Transient electroluminescence imaging and current-voltage characteristics of individual cells within pv-modules,” *27th Eur. Photovolt. Sol. Energy Conf. Exhib.*, pp. 1419–1422, 2012.
- [117] I. Standard, “61215. Crystalline Silicon Terrestrial Photovoltaic (PV) Modules—Design Qualification and Type Approval,” *Int. Electrotech. Comm.*, vol. 3, 2005.
- [118] S. Spataru, P. Hacke, and D. Sera, “In-Situ Measurement of Power Loss for Crystalline Silicon Modules Undergoing Thermal Cycling and Mechanical Loading Stress Testing Preprint,” no. September, 2015.
- [119] M. Paggi, I. Berardone, A. Infuso, and M. Corrado, “Fatigue degradation and electric recovery in Silicon solar cells embedded in photovoltaic modules.,” *Sci. Rep.*, vol. 4, p. 4506, 2014.
- [120] F. Reil and J. Althaus, “Development of a new test standard and experiences of transportation and rough handling testing of PV modules,” in *European Photovoltaic Solar Energy Conference and Exhibition*, 2011, pp. 3270–3274.
- [121] W. Luo, Y. S. Khoo, P. Hacke, V. Naumann, D. Lausch, S. P. Harvey, J. P. Singh, J. Chai, Y. Wang, A. Aberle, and S. Ramakrishna, “Potential-induced Degradation in Photovoltaic Modules: A Critical Review,” *Energy Environ. Sci.*, vol. 10, pp. 4–7, 2016.
- [122] X. Wu, M. Bliss, A. Sinha, T. R. Betts, R. Gupta, and R. Gottschalg,

- “Accelerated spatially resolved electrical simulation of photovoltaic devices using photovoltaic-oriented nodal analysis,” *IEEE Trans. Electron Devices*, vol. 62, no. 5, pp. 1390–1398, 2015.
- [123] S. Meyer, S. Timmel, S. Richter, M. Werner, M. Gläser, S. Swatek, U. Braun, and C. Hagendorf, “Silver nanoparticles cause snail trails in photovoltaic modules,” *Sol. Energy Mater. Sol. Cells*, vol. 121, pp. 171–175, 2014.
- [124] K. Zaunbrecher, “Imaging as Characterization Techniques for Thin-Film Cadmium Telluride Photovoltaics,” *Color. State Univ.*, vol. Dissertati, 2014.
- [125] A. Mansouri, M. Zettl, O. Mayer, M. Lynass, M. Bucher, and O. Stern, “Defect detection in photovoltaic modules using electroluminescence imaging,” *27th Eur. Photovolt. Sol. Energy Conf. Exhib.*, vol. 64617926, pp. 3374–3378, 2012.
- [126] D.-M. Tsai, S.-C. Wu, and W.-Y. Chiu, “Defect Detection in Solar Modules Using ICA Basis Images,” *IEEE Trans. Ind. Informatics*, vol. 9, no. 1, pp. 122–131, Feb. 2013.
- [127] “Electroluminescence Module Inspection: Stand-alone inspection systems for electroluminescence imaging in the laboratory or in the production area.” MBJ Solutions GmbH, 2013.
- [128] B. Mitchell, J. W. Weber, D. Walter, D. MacDonald, and T. Trupke, “On the method of photoluminescence spectral intensity ratio imaging of silicon bricks: Advances and limitations,” *J. Appl. Phys.*, vol. 112, no. 6, 2012.
- [129] M. P. I. of M. Physics, “Description Electroluminescence ( EL ) Imaging Evaluation Software.” Halle, 2012.
- [130] greateyes GmbH, “LumiSolarCell System: Photo- and Electroluminescence Inspection Equipment for Wafers and Solar Cells.” Berlin, 2012.

# APPENDIX

# 1 RESEARCH OUTPUT

During the doctoral studentship from January 2014 to April 2017, the following scientific output was generated:

## Conference Papers

- KG. Bedrich, M. Bliss, TR. Betts, R. Gottschalg, „Electroluminescence Imaging of PV Devices: Camera Calibration and Image Correction“, in IEEE PVSC43, June 2016
- KG. Bedrich, M. Bliss, TR. Betts, R. Gottschalg, „Electroluminescence Imaging of PV Devices: Single-Time-Effect Statistics and Removal“, in PVSAT12, April 2016
- KG. Bedrich, M. Bliss, TR. Betts, R. Gottschalg, „Electroluminescence Imaging of PV Devices: Uncertainty due to Optical and Perspective Distortion“, in EUPVSEC31, September 2015
- KG. Bedrich, M. Bliss, TR. Betts, R. Gottschalg, „Electroluminescence Imaging of PV Devices: Determining the Image Quality“, in IEEE PVSC42, June 2015
- KG. Bedrich, M. Bliss, TR. Betts, R. Gottschalg, „Module Scale Electroluminescence of PV Devices: Measurements and Image Quality“, in PVSAT11, April 2015

## Unpublished Work

- Electroluminescence Imaging of PV devices:  
Determining the Signal-To-Noise Ratio
- Electroluminescence Imaging of PV devices:  
Image Sharpness Measurement and Specification
- Electroluminescence Imaging of PV Devices:  
Advanced Flat Field Calibration
- Electroluminescence Imaging of PV devices:  
Setup dependency of Effective Flat Field

- Electroluminescence Imaging of PV Devices:  
Quantitative Inter-lab Comparison

### Contributions to IEC 60904-13 (draft Jan.2017)

- Added
  - Section 4.2.1.2.2: Sharpness determination and classification
  - Section 4.3 Image correction and analysis' (part Signal-to-Noise ratio)
  - Annex B: Focus
- Modified
  - Section 6: Reporting
  - Annex 1 Lens distortion

### Built Measurement Systems

- Huge Luminescence Chamber 'HuLC' (Appendix 2)

### Produced Software

- `dataArtist` - interactive scientific image analysis and processing (Appendix 3)
- `imgProcessor` - Python-based image processing library (see <https://github.com/radjkarl/imgProcessor>)

### 1<sup>st</sup> International Electroluminescence Round Robin (16 laboratories)

- Planning, implementation and evaluation.

## 2 HUGE LUMINESCENCE CHAMBER ‘HULC’

The ‘Huge Luminescence Chamber’ (HuLC) (Figure 2.1) consists of an aluminium cage, assembled by 40x40 and 80x40 mm profiles. Its walls are built by two layers of 5 mm polypropylene sheeting. On the ceiling of the chamber, a 16 bit CCD camera is mounted on a linear slide. This enables images to be taken at three (or more) different positions. The module mount accepts variable module sizes up to 1.2x2.4 m. Camera, power supply and thermo couple for measuring the chamber temperature are operated using the LabView executable ‘HuLC\_control.exe’. Current and voltage maxima, determined by the power supply, are 34 A and 150 V. Two light sources are mounted in the chamber: Left middle: cold white LED. Bottom middle: IR light bulb

Both lights can be switched on/off manually from the power strip between both monitors.

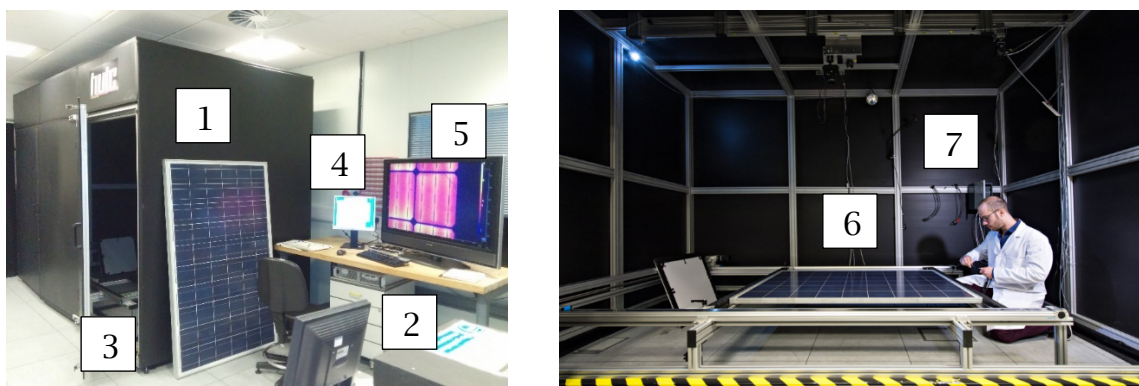


**Figure 2.1:** Equipment: Dark chamber (1); TKD Lambda GEN150-34 (2); Module mount (3); Control PC with software (Labview) ‘HuLC\_control.exe’ (4); ...and Image analysing and processing program, ‘dataArtist.exe’ (5); Temperature sensor (6); Connector cables for clampable, MC3 or MC4 connected modules (7)

## 2.1 Operation

Door open: To open the chamber first pull gently the smaller door handle Figure 2.2(1) until the first two sections build an angle of  $\sim 20^\circ$ . Then take the main door handle (2), lift it gently and push the door open. Door opening and closing should work smoothly without excessive force.

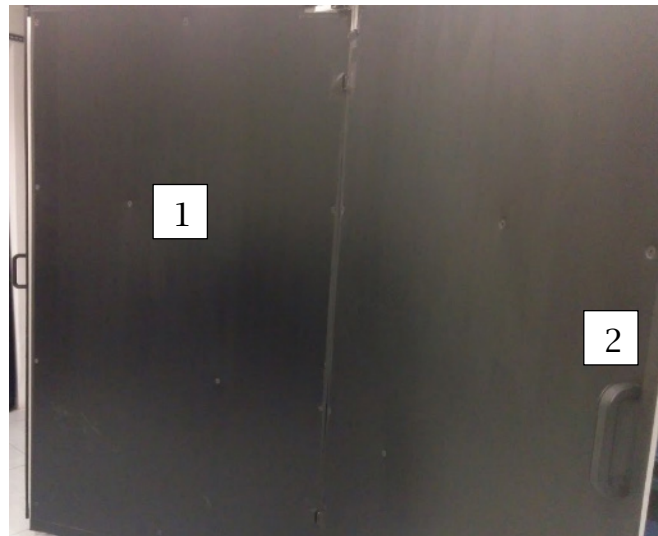


**Figure 2.2: HuLC: Two-hinged folding door**

Mounting a module: The module mount consists of one fixed ledge (Figure 2.3(1)) and one movable ledge (2). The left ledge can be adjusted to the frame length using fixing handles (3a,b).

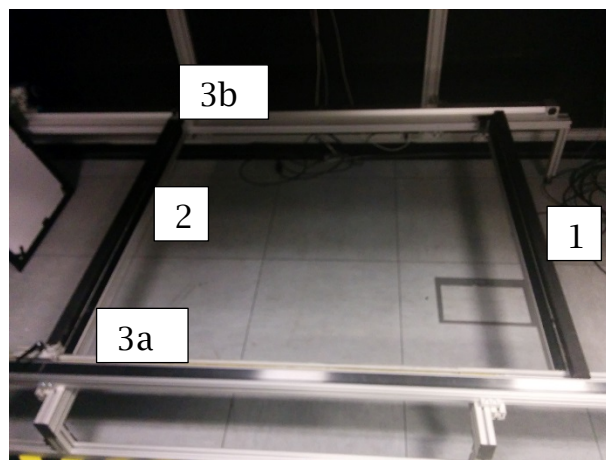


**Figure 2.3: HuLC: Module mount**

The maximum imaged size [in ledge direction] is 1.2 m. If a module exceeds this size it has to be turned 90°. There are two different ways of safely mounting a PV module in HuLC.

1. Open the chamber door completely.
2. Adjust left ledge to roughly match the module length.
3. Take module (two persons, one per end).
4. Walk into the chamber (MIND THE STEP).
5. Place the module on the right mount ledge. The person on the right then walks over to the person on the left, which is still holding the module in place. The former right person brings the left mount ledge into position and the left person puts down the module.

Alternative:

1. Open the chamber door completely
2. The left ledge is set to the exact length of the module (using a ruler at the rear end of the mount).
3. Use fixing handles to fix left ledge.
4. Take module (2 people again)
5. Place the end of the module on both ledges and slide the module in position.

Make sure that the module fits properly. Since EL images for devices wider than 90 cm are stitched together from 2-3 individual images, a remaining rotational angle might impede the later image stitching process.

The imaged area (depending on the camera height) is marked on the outer side of the right arm. Please make sure that the module is within given range.

Module connection: There are currently three different adapters available to connect module and power supply: MC4, MC3 and clamp. These adapters are attached to the rear inner wall (Figure 2.4).



**Figure 2.4: HuLC: PV device adapters**

To connect the module...

1. Make sure that the power supply displays ‘POWER OFF’.
2. Choose the right adaptor cable.
3. Connect the adaptor cable to the universal connector. The connector screws need to be on the same side.
4. Connect the individual connectors to the module. For the clamp connector, check polarity first.

Door close: To close the chamber, take the main door handle, lift it gently and pull it until the first two sections are straight. Then push the smaller door handle till the first two sections lock. Finally push the main door handle until the door is completely closed. There are two clamps for locking the door. Their use is optional - closed clamps can indicate others that the chamber is in use.

## 2.2 Test Procedure

### 2.2.1 DEVICE STORAGE

Store modules as described in ‘CREST AP 05 Handling Calibration and Test Samples’. Ensure that glass-glass unframed modules are never in direct contact with hard floors.

## 2.2.2 PREPARATION (HOURS BEFORE MEASUREMENT)

Clean the modules if necessary (water + non-abrasive cloth).

Bring modules into the measurement room. To stabilize temperature, allow airflow around device.

## 2.2.3 IMAGING

1. Place the module in the chamber (Section 2.1).
2. Switch on main supply for camera, motors, light etc. (“HuLC main”).
3. Switch on control PC.
4. Login using login credentials located under the left monitor.
5. Before starting an imaging routine, make sure that camera (socket ‘camera’) motors of the linear slides (socket ‘motor’) and the proximity switches (socket ‘proxi’) are switched on and all lamps (socket ‘lamp’) in the chamber are switched off.
6. (A) Click on the ‘HuLC’ logo in the task bar to start ‘HuLC\_control.exe’ (Figure 2.5).
7. (B) Change image folder to desired path (for example E\measurements\NAME\DATE)
8. (C) Change image NAME. Images will be saved as for example:
  - o ‘NAME\_e120\_g4\_b1\_V48-362\_I5-280\_T20-062\_p1-2\_n0\_0.tif’
  - o That corresponds to ...
    - 120s exposure time
    - Gain =4
    - Binning =1
    - 48.362 Volt
    - 5.280 Ampere
    - 20.062 °C (Temperature above module)
    - Camera position 1 of 2
    - Image number at current position = 0
    - Absolute image set number = 0

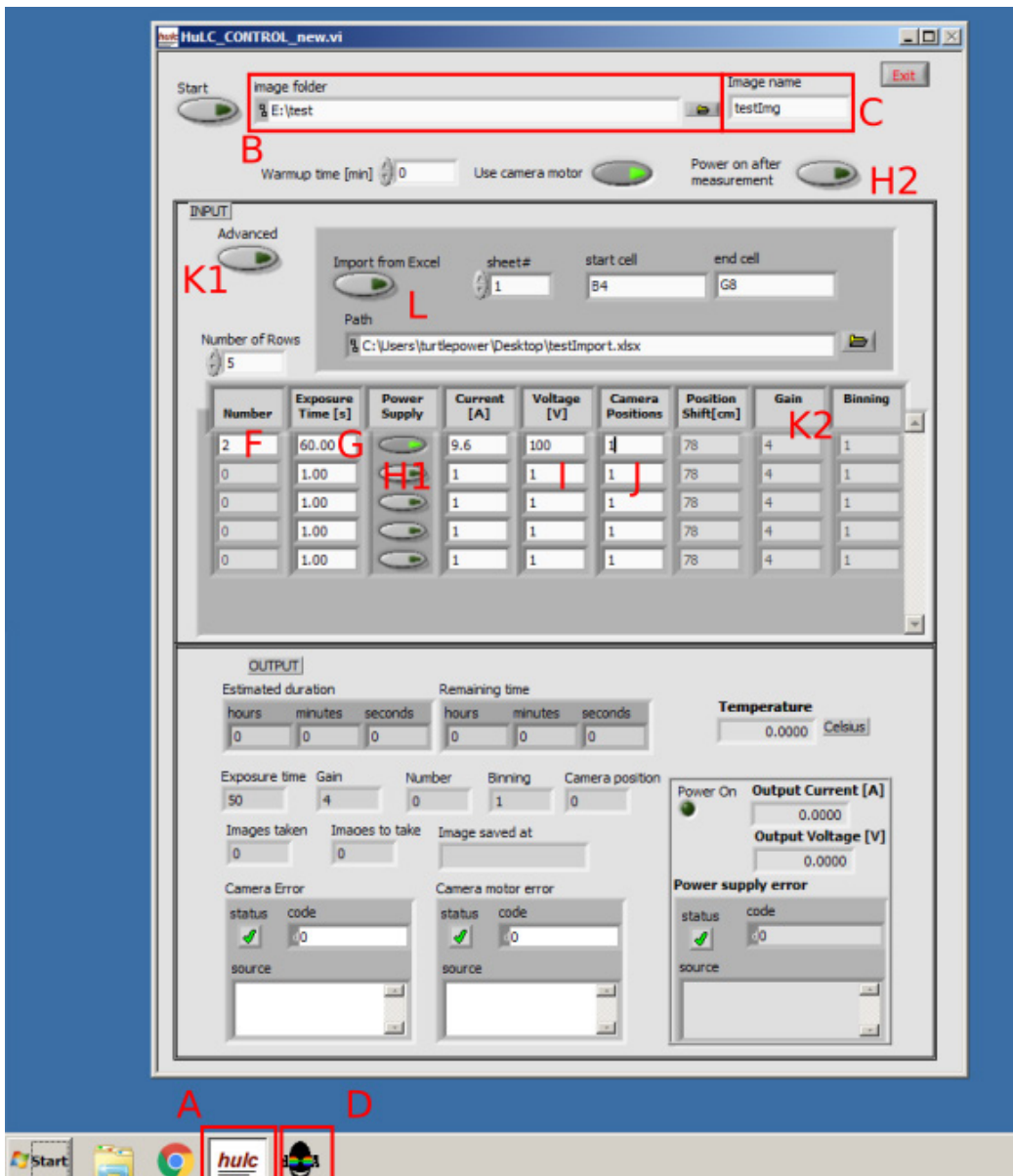


Figure 2.5: HuLC\_control.exe

There are two proposed imaging regimes: 10% of the devices short-circuit current ( $I_{sc}$ ) and 100%  $I_{sc}$ .

- Why 100%  $I_{sc}$ :
  - Shorter exposure time.
  - Series resistance effects are more pronounced.
- Why 10%  $I_{sc}$ :
  - Cell intensity decrease due to shunt resistance  $\sqrt{10}$  times higher, relative to 100%.
  - Negligible series resistance effects, therefore more homogenous EL emission.

- Why both:
  - To calculate a series resistance map.

Exposure time (Figure 2.5 G) should be defined as that time that...

- Results on averaged  $\text{SNR} >= 50 \dots$
- Does not create overexposed areas ...  
...in the captured EL image.

For the used camera an averaged image intensity of 22,000 corresponds roughly to an  $\text{SNR}=50$ . The image processing software ‘dataArtist’ (Appendix 3) provides a tool for determining exposure time.

If exposure time is higher than 2 minutes, respective the averaged  $\text{SNR} < 30$ , consider capturing 2 images (F) at every position and current to enable removal of temporary imaging artefacts (single-time-effects).

Power supply (H1): Switch toggle button to ‘on’ to use power supply. If device should be kept biased after image is taken switch on toggle (H2). This is useful to keep module temperature constant. Be aware to manually switch off power supply if using this feature.

Background image (image under open circuit) is OPTIONAL. Background images can be calculated as  $f_n(\text{exposure time})$  in dataArtist (D).

Positions (J): If a module width  $> 90 \text{ cm}$  the final EL image will be stitched from up to 3 sub-images, between 90-160cm: position 1-2, 160-240cm: position 1-3

Warm-up: To stabilize EL signal, a warm-up time of 10 min in prior to each measurement is suggested.

Voltage (I): Both current and voltage are limited to the respective threshold. It is proposed to set voltage to 120% of the devices open-circuit voltage to ensure that the given current (max. 100%  $I_{sc}$ ) is reached.

Advanced (K1):

Gain (K2): Leave at 4 - this ensures short exposure times and a linear behaviour of the CCD well.

Binning (K2): Leave at 1 - increasing this value reduces exposure time but also image resolution.

**Position shift (K2):** For every imaged position, the camera moves 78 cm by default. If a different distance is required change that parameter.

#### Example setup:

N images	Exp. time [s]	Camera on	Power supply on	Current	Voltage	Binning	Gain	Positions
1	600	0	1	[100%Isoc]	[>120%Voc]	1	4	1
2	30	1	1	[100%Isoc]	[>120%Voc]	1	4	1-2
1	600	0	1	[10%Isoc]	[>120%Voc]	1	4	1
2	300	1	1	[10%Isoc]	[>120%Voc]	1	4	1-2

**Import from Excel (L):** All parameters (Number->Binning) can be imported from an Excel sheet. Start and end cell limit bounding box containing these parameters in the same order as in the program.

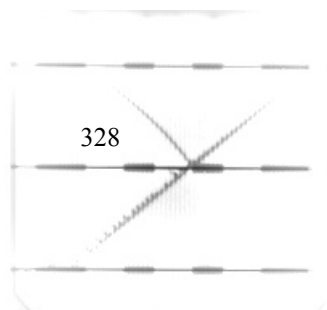
### 2.2.4 IMAGE ANALYSIS AND POST PROCESSING

All image processing (removal of background, flat field, lens distortion, perspective, and image stitching ...) is done in dataArtist (D). In order to auto-import all newly created images into the software, right click on the ‘dA’ icon (black face, coloured glasses) and open the session ‘EL\_imaging.da’. In introduction of dataArtist gives Appendix 3.

The current display in the opened dataArtist session contains various scripts used to execute common image corrections.

#### 2.2.4.1 SHUT DOWN

1. Switch off power supply.
2. Close ‘dataArtist’ and ‘HuLC\_control’.
3. Shut down PC.
4. Switch of both monitors.
5. Switch off ‘HuLC main’ power supply.



# 3 SCIENTIFIC IMAGE PROCESSING WITH ‘DATAARTIST’

The analysis of EL images and similarly photoluminescence images requires dedicated and specialised software. For common image processing problems such as geometric measurements, filtering and edge detection, the Java-based open source program `imageJ`, is frequently used [27, 82, 124]. Others have created own routines based on MATLAB [37] or LabView [43, 47].

The scope of image processing on EL/PL images can be separated into the following problems:

- Images correction (camera calibration, perspective, intensity, artefacts)
- Automated detection of material/electrical defects (such as cracks) [101, 125–127]
- Prediction of electrical properties including localised series resistance and saturation current [37, 128, 129]

Only few programs have their own graphical user interface (GUI) [126] and are commercially available [127, 129, 130].

For EL applications, no software tool could be found dedicated to camera calibration and the removal of EL signal distortions, essential for quantitative analysis and inter-lab comparison. This was the motivation for creating an individual software solution, called `dataArtist`.

`dataArtist` is an interactive program for scientific image processing, specialised on EL imaging (Figure 3.1). It was built to analyse and process EL images created during the doctoral studentship.



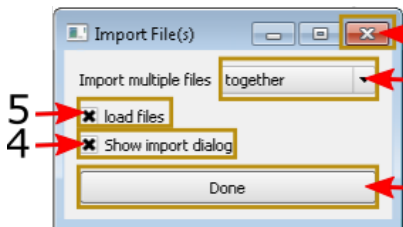
**Figure 3.1: Usage of `dataArtist` to analyse EL images**

Some of its features are...

- Drag and drop file import (local and from internet browser).  
Currently supported file types are:
  - Images: TIF, BMP, PNG, JPG, CSV, TXT, MAT
  - 2D Graphs: CSV, TXT
  - Python ‘Numpy’ arrays, saved as NPY
  - Text and tables for instance from Excel, Word, Notepad
- Auto-import from ‘watched’ folders.
- Commonly used processing algorithms can be accessed by tools in the top of the window.
- Automation and direct access on image data using a built-in Python console.
- Interaction with other programs using RabbitMQ file server.

The source and executables for Windows 7/10 can be found at GitHub (<https://github.com/radjkarl/dataArtist>). A video tutorial can be found at <https://www.youtube.com/playlist?list=PLKyzYL-Q8Rcl6tHN1PjB3FiIfI24pdLLb>.

### 3.1 Importing Data



1 The usual way for importing data is by drag-and-drop one or multiple selected files or folders into `dataArtist`. Alternatively, 2 the file import dialog can be opened using the menu bar: `File`→`Import data`. If not deactivated, the shown window pops up. The selected files are only imported, if the ‘Done’ button {3} is pressed. In import can be cancelled by clicking on the close button {1}. Three options are available when importing multiple files at the same time {2}:

- Together
  - All files are stacked in one display. For this, files need to be of the same type and shape (for images: same resolution).
- Separated
  - Open a new display for every single file.
- In display
  - Add all files as new layers in the current or another display.

Importing many or huge files can take time or slow down the computer. Do avoid this or to change the preferences for importing files in prior it might be useful to not automatically load files into memory {5}. The imported files can be loaded later by clicking on the green ‘update’ button (first button on the left of the tool bar). Some tools also work on unloaded files. For those tools, files can remain unloaded. The shown import dialog will pop up every time when new files are dropped into `dataArtist`. To avoid this and to load files with the last preferences, uncheck {4}.

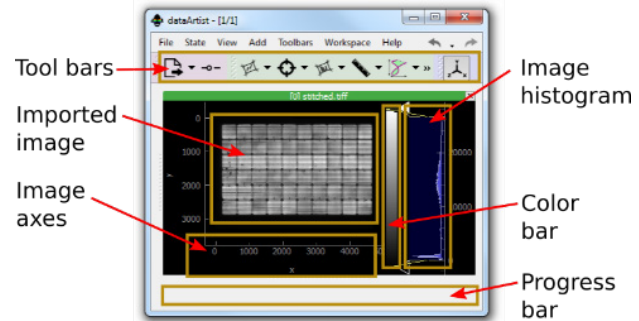
## 3.2 Program Layout

dataArtist starts as an empty window. Through draw/drop files can be imported or a saved session can be loaded (File→Load Session)



An image, imported in `dataArtist`, opens some general-purpose tool bars. At the right side of every display, an image histogram and a colour bar are shown. Both can be used to interactively change contrast, brightness and colour map. If multiple images are imported, a time line at the display bottom enables to slide through every image layer tool bars at the top of the window.

Two sliders on the left and bottom can be used to show the current display preferences (including built-in console) and the output messages.



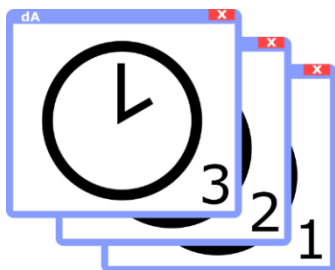
### 3.2.1 PROGRAM COMPONENTS

#### 3.2.1.1 SESSIONS



All imported and displayed input data, visual and layer settings as well as tool parameters built up a dataArtist session. A session can be saved and restored using the Menu bar File→Save Session/Open Session or using the shortcuts CTRL+S or CTRL+O. The file format for dataArtist sessions is DA. A saved session can also be opened by drag-and-drop the DA-file into an opened dataArtist window or directly by double clicking on it. For the latter option, “open \*.da files with dataArtist” must to be checked in the “first-start” window.

#### 3.2.1.2 STATES



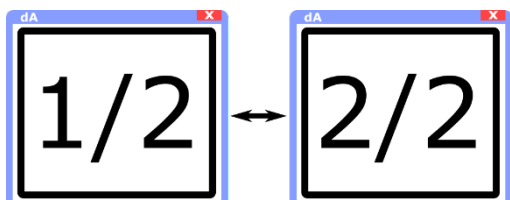
A dataArtist session can contain multiple states (respective temporal version or revision) which display the currently visible data and settings. The maximum number of states to be saved in a \*.da file can be chosen in the preferences menu as follows:

Menu bar→File→Preferences→Session

By default, each state is named with its state number. An individual name can be defined in the Menu bar: State->Rename

When a maximum number of states is reached, new saved states override older ones. When a dataArtist session is opened, the latest state is loaded. To change the currently displayed state, use the Menu bar: State→Set.

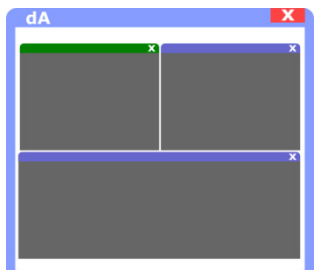
### 3.2.1.3 WORKSPACES



Especially when many different input files are shown, `dataArtist` can look messy. Instead of opening `dataArtist` another time one can add another workspace. A Workspace can be compared with the desktop of your OS. If there are too many windows, you move to an empty (virtual) desktop or you change between desktops, specified for specific tasks. To change between `dataArtist` workspaces, use the menu bar: `Workspaces`→`Next/Previous` or use the shortcuts `Ctrl+PgUp` or `Ctrl+PgDown`.

Workspaces can be added or removed using the menu bar: `Workspace`→`Add/Remove` or using the shortcuts: `Ctrl+W` or `Ctrl+Q`. To move a display to another workspace, use the menu bar: `Docks`→`Move current dock to other workspace`.

### 3.2.1.4 DISPLAY DOCKS



Every dataset loaded into `dataArtist` opens a new display dock. These docks are similar to windows in your OS. Multiple docks are tiled or tabbed on top of each other. The docks position can be changed by clicking on a docks decorator (top label) and drag and drop it to its destination.

Every dock can only represent data of the same file type.

Like windows, docks can be closed, minimised and maximised using the dock decorators on the top-right of each dock. To show a dock in full screen double click on its label on the top of every dock. Press `ESC` to exit full screen. Right click on the dock label to rename the current display dock.

The label colour of a display dock indicates whether it is selected or not. The currently selected display dock also changes the visible display tools

on the top and the display preferences on the left of the window. A new and empty dock can be added in the menu bar: Add→Display.

Right clicking on the dock label gives the options:

- Pop out: show the dock in an extra window in front of other windows.
- Full screen: show the dock in full screen (Press Esc to go back).
- Set name: rename the dock.

### 3.2.2 IMPORT AND REPRESENTATION OF EL IMAGES

Greyscale and colour images of different formats (TIFF, JPEG, PNG, BMP etc.) can be imported by drag and drop. They are shown in ‘displays’ within the program. These displays can be tiled and stacked to allow an intuitive comparison. Multiple images of the same size can also be stacked within one display. Each image layer can be shown individually. Scale, size, aspect ratio and colour map can be chosen freely.

Image analysis and processing can be conducted by tools in the toolbar. Regions of interests (ROI) can be analysed individually or averaged in X or Y dimension, allowing a line cut or spatial averages. In the same way, image histograms can be created. Distances can be measured and used to scale axes to physical dimensions.

Individual routines and process automation can be developed using a built-in Python 3 console with an extended namespace for easy and fast access to the image data. The created scripts can be triggered manually or after changed or added image data. The following examples demonstrate the implementation of common image processing problems within the built-in console:

```
#subtract layer 2 from layer 1 in the
#current display: (d ... display,  l ... layer)
d.11 -= d.12

#set layer 1 on display 4 to the sum of
```

```
#layer 3 and 4 in the current display:
d4.l1 = d.13 + d.14

#average all layers of the current display
d.l = d.l.mean(axis=0)

#print the average of an ROI of the size of
#10x10 pixels at position (100,200) of
#layer 3:
print(d.13[100:110,200:210].mean())

#import and execute a filter from the
#library 'scipy':
from scipy.ndimage.filters import median_filter
d.l = median_filter(d.l, 3)
```

One dimensional plots for instance created from a line cut can be manipulated correspondingly:

```
#add the Y-component of two plots in different displays:
d.l1 = d2.l0 + d4.l2

#print all x-values of all plots within
#the current display:
print(d.l.x)

#divide all plots in the current
#display by their average:
avg = d.l.y.mean()
d.l /= avg
```

Although `dataArtist` can be fully automated, it might be more useful to access certain image processing algorithms directly without using a

graphical interface. Many algorithms are implemented in the Python library `imgProcessor`. A description of their classes and functions can be found at <http://radjkarl.github.io/imgProcessor/>.

### 3.2.3 IMAGE RECTIFICATION USING CAMERA CALIBRATION FILE

This section demonstrates the implementation of the image correction routines detailed in Chapter 4 in `dataArtist`. Data required for dark current-, lens- and flat field removal is stored in CAL files. The generation of these camera calibration files with `dataArtist` is explained in <https://www.youtube.com/channel/UCjjngrC3jPdx1HL8zJ8yqLO>.

Camera correction in `dataArtist` is embedded in the tool `Correct→CorrectCamera`. Tool preferences, as well an EL image before and after correction are shown in Figure 3.2.

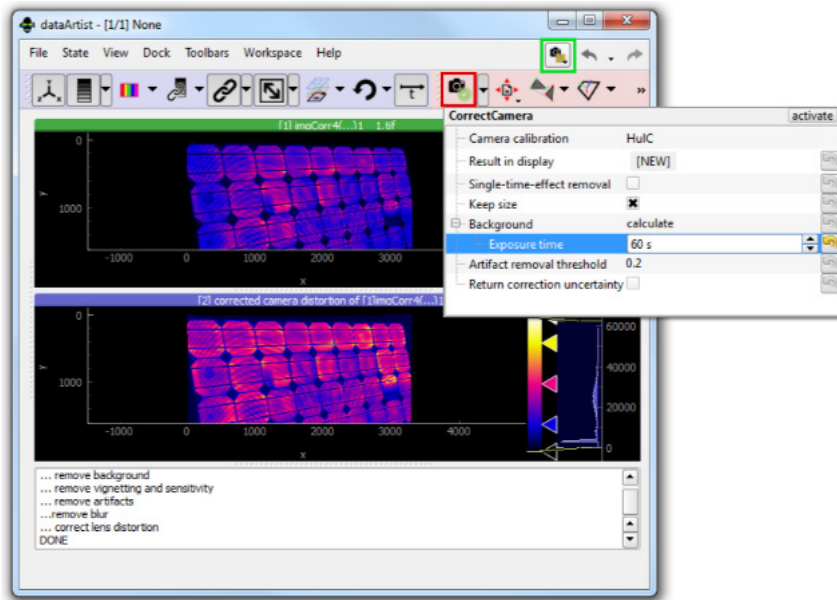


**Figure 3.2:** `dataArtist` screenshot - correction of camera based distortions; Corrected image: bottom; red box: executed tool; green box: tool for managing camera calibrations

Two different tools allow rectifying perspective distortion in EL images. With `Correct→PatternRecognition` images can fitted relative to reference images (Figure 3.3).

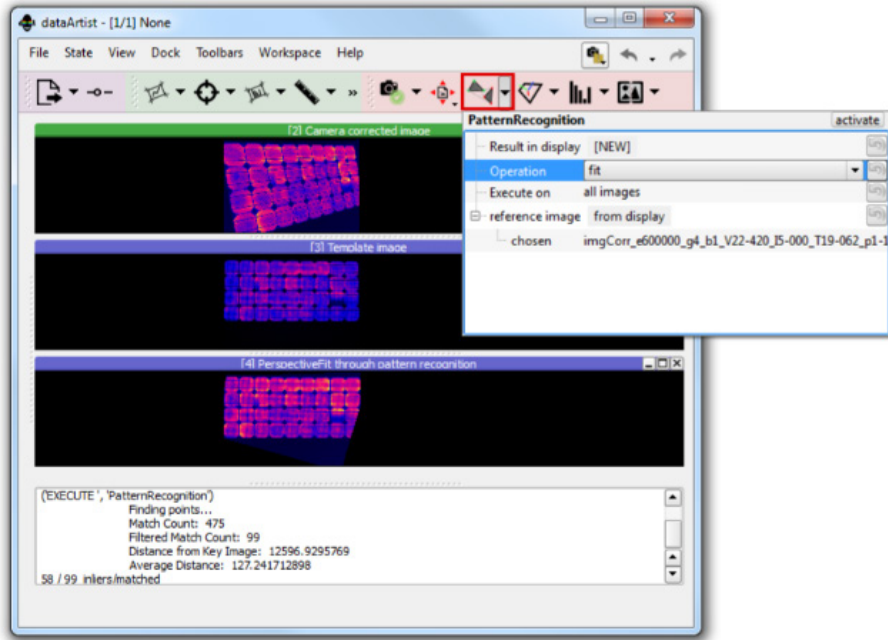


**Figure 3.3: dataArtist screenshot - Perspective correction using pattern recognition; Template image: middle; red box: executed tool; corrected image: bottom**

If no reference image is given, perspective can be determined manually or with automated object corner detection (Subsection 4.7.1.1). Optionally, the intensity of the tilted device can be corrected.

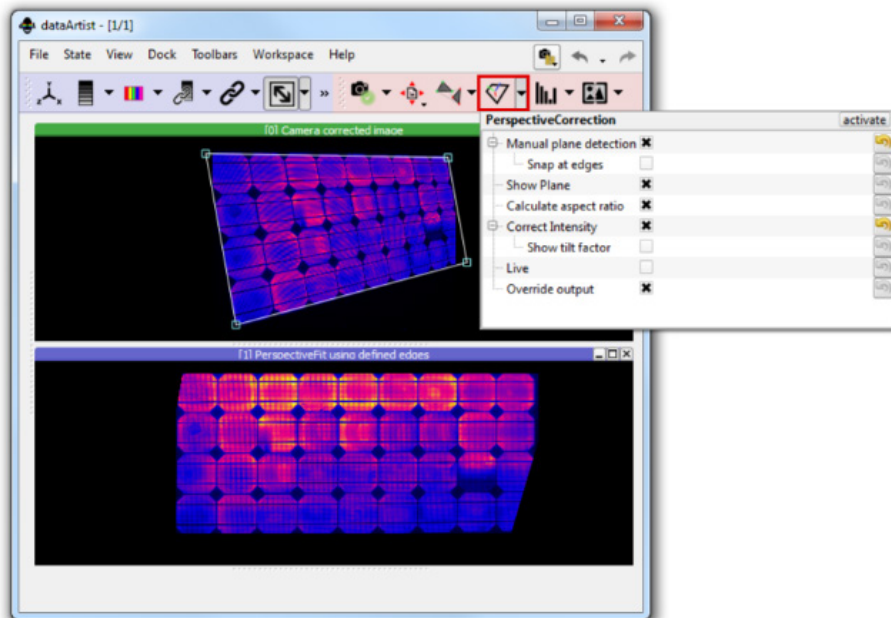


**Figure 3.4: dataArtist screenshot - Perspective correction from detected corners; Red box: executed tool; corrected image: bottom**

# 4 ADDITIONAL MATERIAL

## 4.1 Thermo-Mechanical Load Experiment at NREL

Please see provided files '[NREL\\_EL\\_IMAGES\\_100ISC.pdf](#)' and '[NREL\\_EL\\_IMAGES\\_10ISC.pdf](#)' for a list of corrected images, extracted features and detected inactive areas for modules M1-M4, P1-4 and for all treatment steps (1-10).

## 4.2 First International Round Robin on EL Imaging

Please see provided file '[EL\\_RR\\_init.pdf](#)' for a listing of corrected EL images, their differences to a reference image and uncertainty maps for all modules and 1-cell-mini modules evaluated within the EL Round Robin. Images only include submissions before February 2017.

## 4.3 V-Cut Sharpness Measurement (Method B)

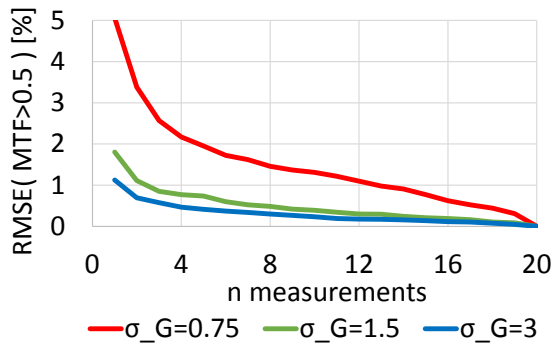
This section is an extension of the sharpness measurement method, introduced in Subsection 3.4.4.3.

The measurement uncertainty of the V-cut method depends on the image signal-to-noise ratio (SNR), the number of measured V-cuts and the V-cut angle. The influence of the latter two factors is evaluated hereinafter. For this purpose, V-cuts in random orientations were synthesised on an image of 501x501 pixels and a SNR of 30. The image was blurred with a Gaussian PSF of a standard deviation of 0.75, 1.5 and 3 px.

### 4.3.1 INFLUENCE OF MEASUREMENT NUMBER

The root mean square error (RMSE) of a MTF generated from the V-cut measurement was compared for 1-20 measurements relative to the final average from 20 measurements. The experiment was then repeated 50 times to average out individual deviations (Figure 4.1). Since the meaningfulness of a MTF generated from the V-cut method below 50% is limited (see Thesis, Subsection 4.3.3) the RMSE was only calculated for  $y_{MTF} > 50\%$ . The opening angle  $\alpha$  was set to  $5^\circ$ .

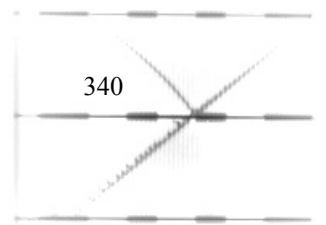
The seceding trend in Figure 4.1 is as expected. If more than 5 measurements are used to calculate the MTF, the deviation relative to a result using 20 measurements is below 2%. Therefore, it is suggested to measure at least five V-cuts.



**Figure 4.1: RMSE of MTF for different number of averaged measurements relative to a result using 20 average V-cut**

### 4.3.2 INFLUENCE OF OPENING ANGLE

In order to determine the best cut opening angle ( $\alpha$ ), the MTF was measured on the same synthetic pattern and averaging 50 measured cuts, each with opening angles ranging from  $0.3^\circ$  to  $14^\circ$ . In contrast to Figure 4.1, the RMSE was calculated relative to the MTF calculated from  $\sigma_G$  using Equation 3.24. Figure 4.2 shows that the opening angle resulting in the lowest error is between  $3-5^\circ$ . This corresponds to a cut-width of 0.5-0.9 cm for a cut length of 10 cm. In particular for sharp images ( $\sigma_G \sim 0.75 \text{ px}$ )  $x_{MTF}$  only consists of a few values. This results in  $\text{RMSE} > 10\%$ .



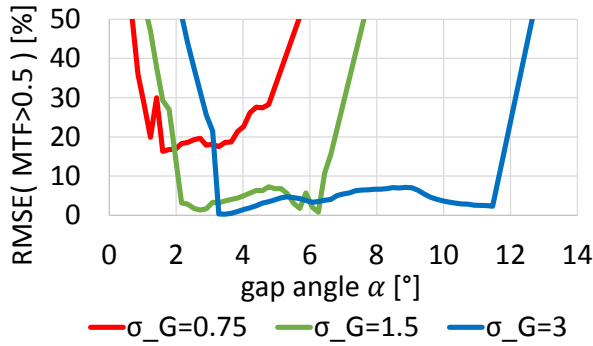


**Figure 4.2: RMSE for an MTF obtained with the V-cut method for different cut angles**

By analysing the influence of measurement number and opening angle, it can be concluded that at least five measurements should be taken at an opening angle ( $\alpha$ ) of 3-5°.

#### 4.3.3 SCALING $x_{MTF}$ TO ALIGN WITH THEORETICAL MTF SLOPE

With only one bright line blurring into its dark surrounding, the V-cut measurement has a different measurement setup than measurements using a spoke target. For V-cut measurements, the image intensity at the actual cut intersection is darker than the mean between bright and dark line. The detected edge lines ( $L_1, L_3$ ) can also deviate from their actual position due to blurring. Unsurprisingly, measured MTF deviate from the ones calculated directly from a Fourier transformed LSF (Thesis, Figure 4.3).

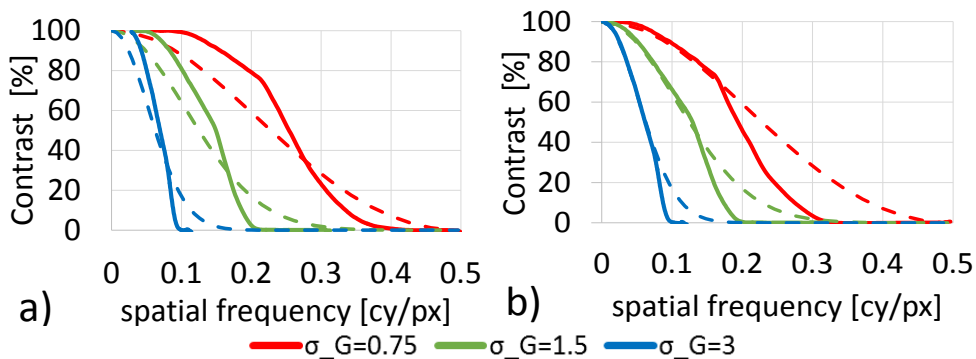


**Figure 4.3: MTF obtained with V-Cut method; a) without correction; b) with scaling  $x_{MTF}$  using Equation 4.1; continuous lines: as measured with V-cut; dashed lines: theoretical MTF, as calculated using Equation 3.24**

It is possible to fit measured and actual MTF by scaling their X values:

$$x_{MTF\_scaled} = \frac{x_{MTF} - a(m)}{b(m)} \quad (4.1)$$

Both scale parameters ( $a, b$ ) are a function of the MTFs slope ( $m$ ) between 90% and 50%, this case defined as:

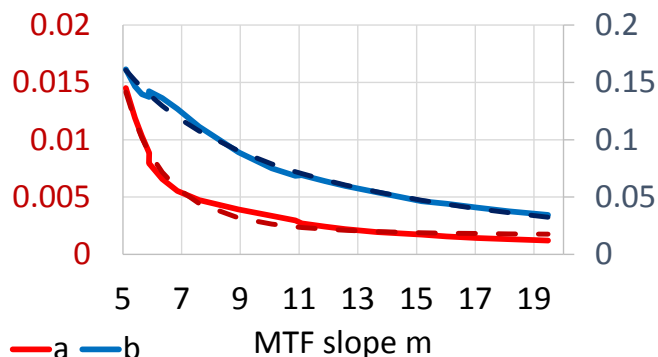
$$m = \frac{0.4}{x_{MTF}(y_{MTF=50\%}) - x_{MTF}(y_{MTF=90\%})} \quad (4.2)$$

Figure 4.4 shows  $a, b$  for different slope values. For an MTF slope ( $m=5\dots19$ ) it is shown that both values can be described by the following function:

$$a(m), b(m) = \frac{i}{m^j} + k \quad (4.3)$$

Where:

	<b>a</b>	<b>b</b>
i	0.1810	1.8029
j	1.8021	1.4615
k	2.560e-4	0.0147



**Figure 4.4: Scale parameters ( $a, b$ ) obtained by fitting measured and actual MTF using Equation 4.1. Dashed lines: Functional fit using Equation 4.3**

Note that this method should only be used to measure the spatial frequency at image contrast levels greater than 50% since values below that threshold will be highly underestimated.